

Structure prediction of nano materials

Inauguraldissertation

zur
Erlangung der Würde eines Doktors der Philosophie
vorgelegt der
Philosophisch-Naturwissenschaftlichen Fakultät
der Universität Basel

von

Deb Sankar De
aus Indien

Basel, 2020

Originaldokument gespeichert auf dem Dokumentenserver der Universität Basel
edoc.unibas.ch



Dieses Werk ist unter dem Vertrag "Creative Commons Namensnennung–Keine kommerzielle Nutzung – Keine Bearbeitung 3.0 Schweiz" (CC BY-NC-ND 3.0 CH) lizenziert. Die vollständige Lizenz kann unter creativecommons.org/licenses/by-nc-nd/3.0/ch eingesehen werden.

Genehmigt von der Philosophisch-Naturwissenschaftlichen Fakultät
auf Antrag von:

Prof. Dr. Stefan Goedecker

Prof. Dr. Stefan T. Bromley

Basel, 11. December 2018

Prof. Dr. Martin Spiess
Dekan

To my family

Acknowledgements

First of all, I would like to acknowledge my supervisor Prof. Dr. Stefan Goedecker for giving me the opportunity to work at the Physics Department of University of Basel. His constant encouragement and inspiration as well as his wise counsels pertaining to my research have been the driving force for me. I would also like to thank Prof. Dr. Stefan T. Bromley for accepting to be the co-referee of this thesis.

Furthermore, I want to thank Dr. Luigi Genovese for providing me continuous support with the problems concerning the BigDFT code. Thank you to Prof. Dr. Thomas Jung for a very fruitful collaboration and has always made time for a chat, however busy he may have been. I am also thankful to Prof. Dr. Raj Ganesh S. Pala for inspiring and motivating me to pursue my interest. I am thankful to Barbara Kammermann and Astrid Kalt, the secretaries of the Physics Department, for being helpful with my official work when I arrived at this new country and continued assisting me for the last four years. Additionally, I thank Martin Jacquot and the SciCORE team for always fixing the problems with the computer clusters, even during weekends. I would also thank Dipanwitta Dutta to bear with me during the collaboration.

Leaving India, took me away from many close friends but over the last four years in Switzerland brought me close to so many wonderful people who I am happy to call, my friends and I am grateful to all of them. My deep gratitude goes to each one of them. A huge thanks to Miglė Graužinytė for being a friend for past four years. Thank you for indulging me in new things and being my constant companion in my adventures. Thanks to José A. Flores-Livas for uncountable helpful discussions, suggestions and all the grilling beside Rhine or on the rooftop. My deepest gratitude goes to Bastian Schaefer for being such a humble friend and always ready to share his knowledge whenever I am stuck. Thank you to Daniele Tomerini for answering all my naive questions and fixing my naive problems. I am thankful to Santanu Saha for a myriad of fascinating discussions and a very effective collaboration. Many

thanks go to my friends and colleagues for the stimulating and pleasant atmosphere: Giuseppe Fisicaro, Marzia, Behnam Parsaeifard, Maximilian Amsler, Shantanu Roy, Augustin Degomme, Melania, Vishal, Francesca. I also like to thank Michael for making my life in Basel musical. Also, I would like to thank Marci and Florent for making my stay in Basel memorable. I would also like to thank all my friends from back home who are living all over the world now: Vishal, Priyanka, Prakash, Sona, Sutapa, Prasenjit, Biswarup, Karuna, Bappa, Sulay, Kishore.

I am also thankful for having such a wonderful dadu and didu. My special thanks go to my mejo jethu, my pishi for their love and support. Finally I would like to thank my Baba, Ma and my brother Raju for their most selfless and deep love and support for me, which gives me the power to fight for the best in life and appreciate all good things in life. Thank you for helping me to believe in myself, and for always being there to walk with me along this path that I have chosen.

Contents

Nomenclature	xi
1 Introduction	7
2 Computational tools to explore a potential energy surface (PES)	11
2.1 The Born-Oppenheimer approximation	11
2.2 Density Functional Theory:	13
2.2.1 Exchange-correlation functional:	16
2.3 Density functional tight binding (DFTB)	17
2.4 Forces:	20
2.5 Stationary Points:	21
2.6 Local geometry optimization:	24
2.7 Overview on global optimization methods	25
2.7.1 Machine learning	26
2.7.2 Simulated annealing	26
2.7.3 Basin hopping	26
2.7.4 Genetic algorithms	27
2.7.5 Minima hopping	27
2.8 Disconnectivity graphs:	31
3 Application to the carbon based fullerene	33
3.1 Introduction	33
3.2 Fullerene Cages	34
3.3 Exohedrally decorated C ₆₀ -fullerenes	35
3.3.1 Alkaline atoms	38
3.3.2 Calcium and scandium	40
3.3.3 Silicon and germanium	41
3.3.4 Beryllium and magnesium	43

3.3.5	Aluminum	44
3.3.6	Single atom on the fullerene surface	44
3.3.7	ELF analysis for decorated fullerene	45
3.3.8	Conclusions	51
3.4	Alkali atom decorated C_{60} in an external electric field	51
3.4.1	Single Li, Na and K atom on C_{60}	52
3.4.2	Li and K on the fullerene surface	54
3.4.3	Conclusions	60
3.5	Decorated $C_{48}B_{12}$ hetero-fullerene	61
3.5.1	Results and discussion	62
3.5.2	Conclusion	64
4	Application to silicon based fullerene	67
4.1	Introduction	67
4.2	Synthesis of $Si_{20}H_{20}$	68
4.2.1	Co-relation between DFT and DFTB	69
4.2.2	Disconnectivity graph	69
4.2.3	Potential energy surface of C_{60}	70
4.2.4	Comparison of PES between different systems	73
4.2.5	Conclusions	79
4.3	Stability of $[Si_{32}Cl_{45}]^-$ and $[Si_{32}Br_{45}]^-$ clusters with Si_{20} core	80
4.3.1	PES of $Si_{32}Cl_{45}^-$	80
4.3.2	PES of $[Si_{32}Br_{45}]^-$	85
4.3.3	Cluster interactions	86
4.3.4	Conclusion	86
5	Applications to the surface and interfaces	87
5.1	Formation of carbon cluster in 4H-SiC/ SiO_2 interface	88
5.1.1	Methods	90
5.1.2	Oxidation models	90
5.1.3	Identification of carbon clusters at the interface	91
5.1.4	Density of states analysis	94
5.1.5	Nitrogen passivation	96
5.1.6	Raman spectra	99
5.1.7	Conclusions	100
5.2	Growth of 2d boron on Si substrates	101
5.2.1	A brief overview of previous work on 2d boron	101
5.2.2	Boron doping in silicon	102
5.2.3	Silicon surfaces	102
5.2.4	B on Si (100) surface:	105
5.2.5	B on Si (111) surface	107
5.2.6	B on Si (110) surface:	109
5.2.7	Si (113) surface:	112
5.2.8	Conclusions:	112

6	Conclusions and outlook	113
A	Minima hopping guided path search (MHGPS)	117
B	Electron localization function (ELF)	118
C	Measuring structural difference	120
D	ELF for all decorated C_{60} configurations	122
E	$Si_{20}H_{20}$ disconnectivity plot for different number of low energy structures	124
F	Lowest energy pathway from the lowest energy structure of one funnel to the global minimum of $Si_{20}H_{20}$	126

Nomenclature

Symbols

k_B	Boltzmann constant	
T	Temperature	[Kelvin]
\mathcal{E}	Electric field	

Acronyms and Abbreviations

PES	Potential Energy Surface
DFT	Density Functional Theory
DFTB	Density Functional Tight binding
LDA	Local Density Approximation
GGA	Generalized Gradient Approximation
PBE	Perdew Burke Ernzerhof
MHM	Minima Hopping Method
MHGPs	Minima Hopping Guided Path Search
MP	Møller-Plesset Perturbation Theory
CISD	Configuration Interaction with all Single and Double substitutions
CCSD	Coupled Cluster using both Single and Double substitutions
LCAO	Linear Combination of Atomic Orbitals
fp	Fingerprint

eV	e lectron- V olt
Ha	H artree
AM	A lkali M etal
AEM	A lkali E arth M etal
a.u.	A tomic U nit
AFM	A tomic F orce M icroscopy
LJ	L ennard J ones
HSE	H eyd S cuseria E rnzerhof
2d	Two dimensional
H-site	Hexagonal site
P-site	Pentagonal site
H-P site	Edge between H and P site
H-H site	Edge between H and H site
T-site	Top of a atom

List of Figures

2.1	A model three dimensional energy surface is shown here	22
2.2	A one dimensional model of a multifunnel energy surface	23
2.3	The schematic diagram of the Bell-Evans-Polanyi principle.	28
2.4	Flow chart of MHM.	29
2.5	The schematic diagram of MHM in a two dimension PES.	30
2.6	Disconnectivity graph for a 1D model energy landscape	32
3.1	Stable fullerene configurations	34
3.2	Maximum number of decorating atoms of the same species that can be homogeneously distributed on the C_{60} surface. For AM a maximum of 12 atom is found for Li, while for Na, K and Rb, it is reduced to 6. For AEM a maximum coverage of 32 atoms forming an outer-shell is achievable by Ca, Sr and Ba. The elements Al, Si, Ti and Ge in contrast do not form homogeneous decoration patterns. Sc (shown) and La (not shown) can form homogeneous distribution with up to 32 atoms.	37
3.3	Low lying energy structures for different Li coverage (n) indicated. For 1 and 2 atoms Li has energy degenerate structures.	39
3.4	Selected optimal structures with different number of Na on the fullerene surface. Similar structures are found for potassium.	39
3.5	Energy order configurations for 32 atoms of Ca and Sc. Selected structures are also shown for comparison. Core-shell type are the most stable structures.	41
3.6	Selected structure with Si (atom depicted on blue) for different coverage.	42
3.7	Selected configurations for Be (upper structures) atoms depicted in green and Mg depicted in yellow.	43
3.8	Selected configuration for aluminum (blue) with different coverage.	44

3.9	Trends in bond lengths for single atom decorating fullerenes. The green circles represent the distance between the probe atom and the nearest carbon atom of the C_{60} for 64 elements sorted by atomic number. The respective average C–C distance in C_{60} is shown for selected elements in blue-triangles. C–C distances do not deviate by more than 5 % and remain thus close to 1.5 Å, the typical C–C distance in a isolated fullerene. Two major trends are: a linear increase in the bond lengths between the decorating atom and the closest carbon for Li, Ca, Sr and Ba and a constant length for Be, Si, and Ge. Note that these same elements also manifest lone electron pairs (see ELF). The typical covalent bond between C and different metals in metallo-organic molecules lies in the range of 1.5 Å to 2.2 Å. [1] Here it is represented by the shaded area in between the black dotted line at 1.5 Å up to the blue line line at 2.2 Å. Hence the elements which are homogeneously distributed over C_{60} have longer bond length than typical metallo-organic molecules.	46
3.10	Different elements considered in this work: top row shows alkali metals, middle row alkaline-earth metals and bottom row other elements. The symbols next to the element symbol indicate the character of the energetically lowest adsorption site: (i) center of the hexagon (hexagon), (ii) center of the pentagon (pentagon) and (iii) On the C–C bond known as the “bridge site” (triangle). The calculated ELF at 0.9 for all the structures is shown for comparison (see text). For each structure the adsorption energy (E_{ads}) is also given.	47
3.11	Periodic table chart summarizing elements that are likely to form homogeneous decorated distributions and have a maximum coverage on the surface. 2 main types of electronic behaviors (ELF) are marked apart from the rest of the elements and those are depicted in orange and green, corresponding respectively to b) and c) in Fig. 3.12. For each atom, the energetically lowest site is indicated together with the difference in energy for other sites.	48
3.12	Electron localization function (ELF) analysis for different atoms: a) isolated C_{60} , b) AM, c) AEM and d) for covalently bonded atoms. In these plots, black lines depicts the single basin (volume) and when it bifurcated, it is represented by blue lines. Yellow lines show the corresponding ELF of the atom considered. Clearly different levels of bifurcation (bonding) are distinguishable via the ELF. Other atoms that follow these patterns are indicated.	49
3.13	Energy of the p-site with respect to the h-site electric field as a function of the electric field	53
3.14	Dipole moment and the ratio of dipole moment and average bond length	53
3.15	Two isomers (a. and b.) found for an electric field of 5×10^{-5} a.u.. The electric filed is along the Z-direction.	54
3.16	Solid lines show the energy of eight isomers Li_2C_{60} as a function of the applied electric field	55

3.17	Theoretical and experimental dipole moments	57
3.18	The free energy for the configurations. The applied electric field is 5×10^{-5} a.u.	57
3.19	The normalized Boltzmann factors as a function of temperature	58
3.20	The dipole moment of the individual structures	59
3.21	The Lowest energy structures for diluted and patched configurations for Be, Ca, Li and Sc decorated $C_{48}B_{12}$	63
4.1	Correlation plot for DFT and DFTB energies	69
4.2	Disconnectivity plot for C_{60}	70
4.3	Disconnectivity plot for $C_{20}H_{20}$	71
4.4	pathways using the MHGPS method and the FP-based method	72
4.5	DE-plots for the investigated C_{60} , $C_{20}H_{20}$ and $Si_{20}H_{20}$ systems	73
4.6	Disconnectivity plot of $Si_{20}H_{20}$	74
4.7	$Si_{20}H_{20}$ and $C_{20}H_{20}$ dodecaheadron configuration.	75
4.8	Pathway between the lowest energy structure of a funnel and the global minima	77
4.9	Energy correction of the ground state w.r.t T to the configurational entropy	77
4.10	DE plots for $Si_{32}Cl_{45}^-$ and $Si_{32}Br_{45}^-$ cluster.	82
4.11	Energy spectrum of $Si_{32}Cl_{45}^-$ and $Si_{32}Br_{45}^-$	83
4.12	Charge density difference and ELF	84
4.13	Boltzmann probability distribution for $Si_{32}Cl_{45}^-$ and $Si_{32}Br_{45}^-$	85
5.1	Different polymorph of SiC.	89
5.2	Computationally predicted atomic structures of the interface	92
5.3	Side and top view of shifted carbon cluster in the SiO_2 matrix.	93
5.4	Computed structures of the characteristic carbon nucleates obtained by an oxygen-rich process (Model A)	94
5.5	MH-DFTB simulations of a carbon chain exposed to ozone.	95
5.6	DOS of SiC/ SiO_2 interface structures with different carbon nucleates .	96
5.7	pDOS for the carbon from 5/6-atom carbon nucleates in the new state is shown here.	97
5.8	Side and top view of nitrogen passivated SiC/ SiO_2	97
5.9	Silicon surfaces reconstruction obtained in this work (top and side views).	103
5.10	Electronic band structure of silicon surfaces reconstruction considered in this work.	104
5.11	Formation energy of different number of boron atom	106

5.12	Boron monolayer with maximum number of boron on different Si surfaces. If we add more boron atoms, they transform into layered configuration or icosahedral boron surfaces. a. 20 boron atoms on Si (100) surface with P12/m1 symmetry b. 20 boron atoms Si (111) surface with Pm symmetry. c. 18 boron atoms on Si (110) surface with P1m1 symmetry d. 16 boron atoms on Si (113) surface with P1 symmetry.	106
5.13	Band structure of boron monolayers with Si substrates. Here the boron contribution to the different bands is also shown.	107
5.14	Convex hull for 2d boron. The convex hull as defined by the hole concentrations. The blue line represents the lowest energy 2d boron configurations at particular hole concentrations. The other points represents the formation energy of exfoliated 2d Boron stabilised on different Si surfaces.	107
5.15	different Boron monolayers on different Si surfaces. a. 20 boron atoms on Si (100) surface with P1 symmetry b. 20 boron atoms Si (100) surface with Pm symmetry. c. 20 boron atoms on Si (100) surface with P2/m symmetry d. 20 boron atoms on Si (111) surface with P1 symmetry. e. 18 boron atoms on Si (110) surface with P222_1 symmetry.	108
5.16	Icosahedral boron surfaces on Si (110) surface. The Lowest energy structure by a. 20 boron atoms b. 22 boron atoms c. 24 boron atoms on Si (110) surface. d-f. metastable boron icosahedral sheets on Si (110) surface.	109
5.17	Band structure of the boron icosahedral layers (from Fig. 5.16a-c) on Si (110) surface.	110
5.18	Calculated phonon spectra of monolayer (from Fig. 5.12c) and icosahedral layers (from Fig. 5.16a-c) on Si (110) surface.	111
5.19	DOS and COHP curves 18, 20, 22, 24 boron atoms on Si(110) surface All curves are shifted so that the Fermi level lies at 0 eV. For COHP, we plotted the surface Si and B interactions.	111
A.1	MHGPs approach for reaction pathway sampling. The shaded region represents MHM algorithm.	117
D.1	different ELF-prints we have found for different single atom adsorbed on C ₆₀	122
E.1	Disconnectivity plot for different number of low energy configurations.a) 900 b) 1600 c) 8000 configurations are considered. The green funnel represents the biggest funnel and the global minimum is in the red funnel.	125

-
- F.1 A possible reaction pathway path from the hydrogenated Si_{20} global minimum structure of Si_{20} to the dodecaheadron $\text{Si}_{20}\text{H}_{20}$ ground state configuration found by BMHPGS. The shown energies are the energies from the physical potential energy surface without the bias. 127
- F.2 Pathway from 8 different local minima to the ground state configuration of $\text{Si}_{20}\text{H}_{20}$. All the initial structures are in the energy difference range of 0.05-0.1 Ha and are the bottoms of different superbasin. Only the orange path was started in the superbasin containing the global minimum. For this reason this path does not have to overcome the higher barriers between superbasins, that have a height of 0.08 Ha or more. In each case the system goes through a flat region of potential energy surface before it reaches to global minimum funnel. 128
-

List of Tables

3.1	Summary of absorption energies (E_{ads}), tendency for lone pair formation, ELF type and charge transfer for selected single atom-decorated C_{60} . The ELF type is determined through visual inspection, as to Fig. 3.12. n is the maximum number of decorating atoms that can homogeneously be distributed on a C_{60} as shown in Fig. 3.2. Non-homogeneous (NH) distributions are also indicated. The ELF type for d)* systems is given in the appendix D.	38
3.2	Dipole moment of the lowest energy structure for different number of K atoms decorated C_{60} . The applied electric field is 5×10^{-5} a.u.	60
3.3	Energy of the first 10 K_2C_{60} structures at different electric field. The energies are given with respect to the lowest energy structure at that particular electric field in eV.	60
3.4	Largest adsorption energies (E_{ads}) for different types of decorating atoms	62
4.1	Properties of different isomers of $[\text{Si}_{32}\text{Cl}_{45}]^-$	81
4.2	Dissociation energy of SiCl_2 from $[\text{Si}_{32}\text{Cl}_{45}]^-$, $\text{Si}_{32}\text{Cl}_{45}$ and $\text{Si}_{32}\text{Cl}_{44}$ in PBE and PBE0.	82
4.3	Properties of different isomers of $[\text{Si}_{32}\text{Br}_{45}]^-$	85
5.1	Main physical and electronic properties of bulk 4H-SiC and Si. The bulk moduli for 4H-SiC and Si result from different ab-initio calculations. [2, 3]	89
5.2	Comparison of experimental and theoretical Raman signals with literature values and the corresponding, most plausible undesired/defective carbon bonds	99

CHAPTER 1

Introduction

The fundamental physical and chemical properties (*e.g.* band gap, dissociation energy, etc.) of a system depend on its atomic arrangement. Targeted engineering of a material for a specific application is possible if we have an idea of its basic configuration. X-ray diffraction techniques (XRD) or High-resolution transmission electron microscopy (HRTEM) imaging for periodic systems and mass spectra for clusters provides this information from the experiments. However, experimental design and synthesis procedures are time consuming and without any guaranteed outcome and in some cases they are uneconomical. Whereas, recent developments in computational physics allow us to identify the atomic arrangement of such systems with less effort and uncertainty in an affordable price. One of the most important concepts of computational physics is the potential energy surface (PES). A potential energy surface is a mathematical function that returns the energy of an assembly of atoms as a function of its geometry. A local optimization of a structure will lead to a local minima of a PES. By exploring the PES, more precisely by sampling the low energy configurations, we can easily identify what the global minima represents, with just the knowledge of chemical composition and the external environment. Starting from this idea, a huge number of computational algorithms for global optimization has been developed in the past decade: particle swarm [4, 5, 6], genetic algorithms [7, 8], simulated annealing [9, 10, 11, 12, 13], minima hopping method (MHM) [14, 15, 16], and more. The application of such methods are not only important for material science but also in the field of biology and pharmacy.

The knowledge of a collection of minima is not enough to comprehend if a global minimum is experimentally accessible, other minima might be entropically favored, or there are multiple kinetically stable states. To understand the dynamical behavior, one should have the information about the minima as well as the transition states

between them. Algorithms as the dimer method, the nudged elastic band method, MHGPS has been developed for unbiased sampling of complex reaction pathways at a sophisticated level of theory, *i.e.* density functional theory (DFT) [17, 18, 19, 20, 21, 22, 23, 24, 25]. This knowledge provides a complete picture of the PES of a system and the reaction pathways between any configurations of the system which can be manipulated by external factors.

Minima hopping is an efficient algorithm, released in 2004 for molecular system, and extended in 2010 for periodic systems, to explore the high dimensional PES of complex systems, while proceeding towards the global minimum structure [14, 15]. MHGPS is a MHM based method for the efficient, automatized and unbiased sampling of complex reaction pathways [25]. MHM and MHGPS has been successfully used for global geometry optimization and constructing their reaction pathways in a large variety of applications, such as molecules and clusters (Lennard-Jones, silicon, fullerene materials, complex biological molecules and large gold clusters) [26, 27, 28, 29, 30, 31, 32] and crystals (cold compressed graphite, Cubine) [33, 34, 35].

In this thesis, we have successfully applied MHM and MHGPS methods to different systems and understand their chemical properties. The applications that we studied, are listed below:

- **Exohedrally decorated atoms on C_{60} :** We investigated exohedrally decorated atoms on C_{60} by employing for the first time a structure prediction method, namely MHM at *ab initio* level. The energetically lowest configurations for exohedrally metal decorated $C_{60}M_n$ with ($2 \leq n \leq 32$) was found for alkali metals, alkaline-earth metals and some other elements. We identified some structures which are found experimentally as well as new putative ground states. Furthermore, we derived a predictive rule for the behavior of a larger number of decorating atoms, by analyzing the bonding characteristics (type and topology) of a single atom via the ELF (electron localization function).
- **Exohedrally decorated C_{60} in the presence of the electric field:** In the previously mentioned work, we have found that Li and K atoms prefer to be homogeneously distributed over C_{60} up to 12 and 6 atoms respectively in the absence of an external electric field. With this knowledge in hand, we wanted to observe the modification of PES for these systems under an external electric field. In this application, we present an unbiased PES scan for Li and K decorated C_{60} at the DFT level in the presence of an electric field. We observed changes in the stability ordering with varying the strength of an electric field. Moreover, we proposed that the measured experimental dipole moment at room temperature is the composite effect of several configurations.
- **Metal decorated $C_{48}B_{12}$:** Next, we scanned the PES of metal decorated $C_{48}B_{12}$ which are considered to be stable and extremely good for hydrogen storage. Using MHM, we performed a comprehensive structural search, decorating both diluted and patched $C_{48}B_{12}$ fullerenes. Almost in every case (except for Li), the ground state structure was massively distorted by the

decoration and the metal decorated patched configurations are much lower in energy than their diluted counterpart.

- **Exploration of $\text{Si}_{20}\text{H}_{20}$ cluster PES:** Despite experimental efforts, the dodecahedron configuration of $\text{Si}_{20}\text{H}_{20}$, that is the most stable configuration calculated on the PES, has not yet been observed. To propose a solution, we employ a fingerprint distance (FP)- based exploration of the PES of $\text{Si}_{20}\text{H}_{20}$, using a recently developed method [36, 37], and we compare it to an analogue calculation on the C_{60} and $\text{C}_{20}\text{H}_{20}$ fullerene. The similarities and differences between the PES of the two systems are used to discuss why the global minimum is observed only for C_{60} and $\text{C}_{20}\text{H}_{20}$. The lowest energy pathways from MHGPS and the FP-disconnectivity method for C_{60} and $\text{Si}_{20}\text{H}_{20}$ has also been analyzed. We hypothesize that the coalition of the effects of complex pathways between the configurations, the fractal shaped funnel and configurational entropy prohibit $\text{Si}_{20}\text{H}_{20}$ to reach its global minima (dodecahedron configuration of $\text{Si}_{20}\text{H}_{20}$).
- **Unbiased search of $[\text{Si}_{32}\text{Cl}_{45}]^-$ and $[\text{Si}_{32}\text{Br}_{45}]^-$:** Recently, it has been developed a one step synthesis procedure to synthesize $[\text{Si}_{32}\text{Cl}_{35}]^-$ cluster which consists of a Si_{20} dodecahedral core with an (endohedral) Cl^- ion. We have re-investigated this system by performing a systematic and unbiased search for low-energy minima for the stoichiometries of $[\text{Si}_{32}\text{Cl}_{45}]^-$ and $[\text{Si}_{32}\text{Br}_{45}]^-$. Although, we have observed different low energy structures, the previously found low energy configuration remains most stable configuration. The charge analysis suggests that negatively charged $[\text{Si}_{32}\text{Cl}_{45}]^-$ provides stability to the system. Our analysis also suggests that Br decorated system should provide more stability than Cl decorated system.
- **Analysis of carbon defect assessment at the SiC/SiO₂ interface:** Silicon carbide (SiC), a wide-bandgap semiconductor, is considered as the major enabling material for advanced high power and high temperature electronic applications. However, the efficiency of SiC decreases with time due to the surface oxidation and hence carbon accumulation at the interface of SiC/SiO₂. We theoretically analyzed the SiC/SiO₂ interface considering different carbon removal pathways and the effects that interfacial defects, such as dangling bonds and carbon clusters, have on the electronic properties (*i.e.* generation of intra-gap trap levels). We found that during the thermal oxidation of Si-terminated SiC (0001) surface, just between the SiO₂ layer and bulk SiC, carbon atoms tend to align in chainlike configurations or in connected 6-member or 5-member rings at the interface of SiO₂/SiC. These stable interface structures in turn generate intra-gap states. We found that when NO/N₂O is used as an oxidizing agent, it inhibited the formation of bigger carbon chain like clusters.
- **Growth of 2d B structures on Si substrates:** Since boron forms boride compounds with most of the elements, only a few metal surfaces have been considered as a substrate, until now. Boron atoms have high solubility limit

in Si, but they tend to segregate on the surface of the Si atom at very high concentration, due to their high diffusivity. Motivated by this fact, we considered a semiconductor, *i.e.* Si, as a substrate to grow boron 2d structures. Depending on the choice of the Si surface and the concentration of the boron atoms, we can have different types of boron layers. It is possible to obtain not only metallic boron layers but also semi-conductor layers. By controlling the concentration of boron, we can also grow monolayer, icosahedral sheets or layered configurations, a wide range of 2d configurations.

The thesis is sketched out in the following way. In the Chapter 2 we provide a brief summary of DFT and DFTB method. We also discuss the characteristics of PESs and a short introduction of different methods that are used to explore it. At the end, we provided a short review of MHM and disconnectivity plot which has been a major part of this thesis. Chapter 3 is subdivided into three sections: the first section is about exohedrally decorated atoms on C_{60} ; the second section is about modification of the PES of exohedrally decorated C_{60} by an electric field; the last section is about the stability of metal decorated heterofullerene $C_{48}B_{12}$. In Chapter 4 we discuss the PES of Si_{20} decorated with hydrogen as well as Cl^- core and eight chloro substituents and twelve trichlorosilyl groups on the surface. Chapter 5 tackles the issues of the shape and size of carbon clusters at the interface of SiC/SiO₂, as well as the synthesis of different types of boron 2d configurations on various Si surfaces. The summary and the outlook of this thesis is provided in Chapter 6.

CHAPTER 2

Computational tools to explore a potential energy surface (PES)

The potential energy landscape (PES) is a fundamental property in computational modeling for a compound. The PES depends on its energy as function of its internal degrees of freedom. It is also referred to as the Born-Oppenheimer surface. Many important concepts which might be mathematically challenging can be comprehended fully, intuitively, with the insight provided by the idea of the PES. The detailed knowledge of the PES topology allows the prediction of the equilibrium conformations, thermodynamic and dynamic properties of multiatomic systems, *e.g.* molecules, clusters, or bulk [38, 39, 40, 41]. The Born-Oppenheimer approximation is an essential element to understand PES of different systems.

2.1 The Born-Oppenheimer approximation

The time-independent non-relativistic Schrödinger equation is given by

$$\hat{H}_{\text{tot}}\psi_i(\mathbf{x}_1, \dots, \mathbf{x}_N, \mathbf{R}_1, \dots, \mathbf{R}_{N_A}) = E_{\text{tot},i}\psi_i(\mathbf{x}_1, \dots, \mathbf{x}_N, \mathbf{R}_1, \dots, \mathbf{R}_{N_A}) \quad (2.1)$$

where the \mathbf{x}_i are the coordinates of all N electrons and \mathbf{R}_i represent the coordinates of all the N_A nuclei. ψ_i represents the wavefunction of the i -th quantum state. For simplicity, we also consider that all wavefunctions are normalized. The Hamilton operator is a sum of the operators of the electronic kinetic energy (\hat{T}_e), nuclear kinetic energy (\hat{T}_n), the Coulomb attraction of the electrons and nuclei (\hat{V}_{en}), the

electronic Coulomb repulsion (\hat{V}_{ee}) and the nuclear Coulomb repulsion (\hat{V}_{nn}) respectively as it given in Eq. 2.2. The full \hat{H}_{tot} can be written as

$$\hat{H}_{\text{tot}} = \hat{T}_e + \hat{T}_n + \hat{V}_{en} + \hat{V}_{ee} + \hat{V}_{nn} \quad (2.2)$$

where,

$$\begin{aligned} \hat{T}_e &= -\frac{1}{2} \sum_{i=1}^N \nabla_i^2 \\ \hat{T}_n &= -\frac{1}{2} \sum_{A=1}^{N_A} \frac{1}{M_A} \nabla_A^2 \\ \hat{V}_{en} &= -\sum_{i=1}^N \sum_{A=1}^{N_A} \frac{Z_A}{|\mathbf{r}_i - \mathbf{R}_A|} \\ \hat{V}_{ee} &= \sum_{i=1}^N \sum_{j<i}^N \frac{1}{|\mathbf{r}_i - \mathbf{r}_j|} \\ \hat{V}_{nn} &= \sum_{A=1}^{N_A} \sum_{B<A}^{N_A} \frac{Z_A Z_B}{|\mathbf{R}_A - \mathbf{R}_B|} \end{aligned} \quad (2.3)$$

Here i and j run over the N electrons, whereas A and B run over the N_A nuclei. For convenience, atomic units are used, where $\hbar = m_e = e = 4\pi\epsilon_0 = 1$.

The electronic and the nuclear states are coupled in the Hamiltonian, which prevents us to obtain any analytical solution by in a full quantum mechanical framework. So in general we have to deal with $(3N + 3N_A)$ coupled degrees of freedom. However, the rest mass of a proton is approximately 1836 times greater than the rest mass of an electron. Born and Oppenheimer suggested the following approximations [42]:

- *The nuclear motion is so much slower than electron motion that they can be considered to be fixed.*
- *A smeared out potential from the speedy electrons is observed by the nuclear motion (e.g., rotation, vibration).*

Hence, they considered an approximation of the total wavefunction:

$$\psi(\mathbf{x}_i, \mathbf{R}) = \psi_e(\mathbf{x}_i, \mathbf{R}) \psi_n(\mathbf{R}) \quad (2.4)$$

The nuclei are treated as classical particles, such that the kinetic nuclei energies are neglected. The last term in the Hamilton is independent of the electronic coordinates and can be treated separately. Therefore, the electronic Hamiltonian can be written as:

$$\hat{H}_{ee} = -\frac{1}{2} \sum_{i=1}^N \nabla_i^2 - \sum_{i=1}^N \sum_{A=1}^{N_A} \frac{Z_A}{|\mathbf{r}_i - \mathbf{R}_A|} + \sum_{i=1}^N \sum_{j<i}^N \frac{1}{|\mathbf{r}_i - \mathbf{r}_j|} = \hat{T}_e + \hat{V}_{en} + \hat{V}_{ee} \quad (2.5)$$

Since \hat{H}_{ee} have to be solved for a particular nuclear geometry $\psi_e(\mathbf{x}_i, \mathbf{R})$ is a function of the electronic coordinates \mathbf{x}_i and the nuclear positions \mathbf{R} . Hence $\psi_e(\mathbf{r}_i, \mathbf{R})$ and $\hat{V}_e = (\hat{V}_{en} + \hat{V}_{ee})$ represents different wavefunctions and energies for different nuclear configurations which will give rise to electronic surfaces. These \hat{V}_e define as Born-Oppenheimer surfaces. The coupling of different electronic states depends inversely on the gap between the electronic surfaces. Hence, one should be careful to tread if two electronic surfaces are separated by a small energy gap. An important assumption of the Born-Oppenheimer approximation is

- *There are no excitations of the electrons among the various surfaces.*

The excitations comprise non-adiabatic effects which are neglected. If the electrons are in their ground state and the ground state energy is $\mathcal{E}_0(\mathbf{R})$ and if the excited state energy for those electrons is $\mathcal{E}_1(\mathbf{R})$ then at temperature T there will be no excited state if,

$$\mathcal{E}_0 - \mathcal{E}_1 \gg k_B T \quad (2.6)$$

for all nuclear configurations. It is not possible to know beforehand if this condition will be satisfied without complete knowledge of these surfaces. There could be regions where the surfaces proceed towards each other with an energy spacing close to $k_B T$. If the system visits such nuclear configurations, then the Born-Oppenheimer approximation will break down.

2.2 Density Functional Theory:

Despite the simplicity of the the Schrödinger equation under the Born-Oppenheimer approximation (Eq. 2.5), an analytical solution exists only for a few cases, such as the hydrogen atom. Rather than analytical methods, numerical methods must be used to solve the Eq. 2.5. In principle, by searching for an appropriate wavefunction which minimizes the expectation value of energy, the ground state solution can be obtained:

$$E[\psi] = \frac{\langle \psi | \hat{H}_{ee} | \psi \rangle}{\langle \psi | \psi \rangle} \quad (2.7)$$

However, it is computationally too expensive in practice and strongly limited by the system size. For example, the prerequisite memory to simply discretized a $3N$ dimensional wave function into M points for each degree of freedom is M^{3N} . To obtain an accurate solutions, a very flexible description of the spatial variation of the wavefunction is also required. This implies that it is essential to have a substantial number of basis set. This contributes to the expense for practical calculations. Many correlated methods have been emerged for molecular calculations such as,

MP2, CCSD, CCSD(T) etc. For most cases, a sufficient accuracy to compute the chemical properties *i.e.* stability, reaction rates etc of a system can be acquired by CCSD(T) calculations. However, due to the calculation for a realistic system is computationally expensive, this method is impractical to use in reality. The computational cost of the most commonly used methods, for instance, MP2, MP3, MP4, CISD, CCSD, CCSD(T), formally scales with the number of electrons raised to the power of 5, 6, 7, 6, 6, 7 respectively [43]. Despite the fact that there is a rapid advances in computer technology, still these strategies do not appear to be useful for realistic systems in near future.

To circumvent this problem, one can use the electronic density $\rho(\mathbf{r})$ as basic quantity to express the energy within the density functional theory.

$$\rho(\mathbf{r}) = N \int \cdots \int |\psi(\mathbf{x}_1, \cdots, \mathbf{x}_N)|^2 d\mathbf{s}_1 d\mathbf{x}_2 d\mathbf{x}_3 \cdots d\mathbf{x}_N \quad (2.8)$$

This gives the probability of finding an electron $\rho(\mathbf{r})d\mathbf{r}$ in a volume element $d\mathbf{r}=dx dy dz$ around \mathbf{r} . N is the total number of electrons in the system.

In 1964, Hohenberg and Kohn published two theorems, which replaced the electronic wavefunction by electron density [44]. The theorems are:

- Theorem I: *"The external potential is determined, within a trivial additive constant, by the ground-state electron density ρ ."*
- Theorem II: *"The electron density that minimizes the energy of the overall functional is the true electron density corresponding to the full solution of the Schrödinger equation."*

The first theorem suggests that for a system consisting of electrons in an external potential, the total energy can be written as a sum of the energy arising from the electronic density and other external terms.

$$E_{\text{total}} = E_e[\rho] + E_{\text{ext}}[\rho] + E_{nn} \quad (2.9)$$

$$\begin{aligned} E_{\text{ext}}[\rho] &= \sum_A^N \int \frac{\rho(\mathbf{r})Z_A}{|\mathbf{r} - \mathbf{R}_A|} d^3\mathbf{r} \\ &= \int \rho(\mathbf{r})\hat{V}_{en} d^3\mathbf{r} \end{aligned} \quad (2.10)$$

$$E_{nn} = \sum_{A < B}^N \frac{Z_A Z_B}{|\mathbf{R}_A - \mathbf{R}_B|} d^3\mathbf{r} \quad (2.11)$$

The nuclei are assumed to be a point charge. E_{ext} is the external potential and E_{nn} is the internuclear interactions. $E_e[\rho]$ is split into kinetic energy term, a Hartree term and a exchange correlation term. The exchange correlation term contains all the quantum mechanical effects that are not included in the "known" terms.

$$\begin{aligned} E_e[\rho] &= E_{kin}[\rho] + E_H[\rho] + E_{xc}[\rho] \\ &= F_{HK}[\rho] \end{aligned} \quad (2.12)$$

E_e independent of external potential. Hence it is a universal functional. This suggests that if the form of $E_{xc}[\rho]$ is known, it could be used for any many electron system. From the second theorem, we can say that for any many electron system, a true ground state density can only minimize the functional $E_{total}[\rho]$. Hence, together with variational principle and trial density $\tilde{\rho}$ to fix the Hamiltonian for its corresponding ground state wavefunction, we can write

$$\begin{aligned} \langle \tilde{\psi} | \hat{H} | \tilde{\psi} \rangle &= F_{HK}[\tilde{\rho}] + \int \tilde{\rho}(\mathbf{r}) V_{en} d^3\mathbf{r} \\ &= E[\tilde{\rho}] \geq E[\rho] \\ &= \langle \psi | \hat{H} | \psi \rangle \end{aligned} \quad (2.13)$$

These theorems are the cornerstone of Density Functional Theory (DFT).

The problem is that the exact form of energy functional on which the variational principle to be applied, is unknown. The kinetic and electron-electron functionals are unascertained. Direct minimization of the energy would be possible, if a good approximations of these functionals could be found.

To solve the above problem, Kohn and Sham introduced an auxiliary system of non-interacting electrons in 1965 [45]. This non-interacting system is characterized by a single Slater determinant constructed from Kohn-Sham orbitals ϕ_i . For simplicity we will hereon restrict ourselves to closed shell systems. Now the total energy functional can be rewritten as

$$E[\rho] = T_s[\rho] + E_H[\rho] + E_{en}[\rho] + E_{XC}[\rho] \quad (2.14)$$

where

$$T_s[\rho] = -\frac{1}{2} \sum_i^{occ} \langle \phi_i | \nabla^2 | \phi_i \rangle \quad (2.15)$$

$$E_H[\rho] = -\frac{1}{2} \iint \frac{\rho(\mathbf{r})\rho(\mathbf{r}')}{|\mathbf{r} - \mathbf{r}'|} d^3\mathbf{r} d^3\mathbf{r}' \quad (2.16)$$

$$E_{en}[\rho] = \int \hat{V}_{EN}(\mathbf{r}) \rho(\mathbf{r}) d\mathbf{r} \quad (2.17)$$

The terms on the right are, in order, the electron kinetic energies of a non interacting system. The second term is Hartree energy. This potential describes the Coulomb interaction between an electron which is considered in one of the Kohn-Sham equations and the total electron density defined by all electrons in the system. This also includes self interactions. This is due to the electron interacts with its own mean-field and hence it is a nonphysical quantity. The last term is the exchange and correlation term. All the nonphysical quantities and corrections, *i.e.* self interactions, the correction to the independent kinetic energy term due to the interacting system, are grouped together into the final potential E_{xc} . This is considered as exchange and correlation term to the single electron equation. The exchange and correlation potential can be defined as the functional derivative of exchange correlation energy:

$$\hat{V}_{xc} = \frac{\delta E_{xc}(\mathbf{r})}{\delta \rho(\mathbf{r})} \quad (2.18)$$

In practice, the Kohn-Sham equations are solved self-consistently to obtain the ground state density. The basic algorithm is given below:

1. Define an initial, trial electron density, $\tilde{\rho}(\mathbf{r})$.
2. Using the trial electron density, solve the Kohn-Sham equations to find the single-particle wavefunctions, $\phi_i(\mathbf{r})$.
3. Calculate the electron density from the wavefunction obtained from solving Kohn-Sham equations.
4. Compare the new calculated electron density, with the electron density used in solving the Kohn-Sham equations. If the two densities are within the cutoff limit of the two density difference ($|\tilde{\rho}(\mathbf{r}) - \rho(\mathbf{r})| \leq \Delta\rho_{cutoff}$), then this is the ground-state electron density $\rho(\mathbf{r})$, and it can be used to compute the total energy. If the two densities are different, then the trial electron density must be updated in some way. Once this is done, the process begins again from step 2.

2.2.1 Exchange-correlation functional:

The correction terms due to the independent particle approximation are included in the exchange-correlation term. Although the exact form of exchange correlation term is unknown, there exist a large number of ways in which the functional can be constructed. A well constructed functional will lead to accurate results of physical quantities (*i.e.* Band gap, ionization potential, lattice parameter etc) which are comparable with the experimental results. In most of the functionals, the exchange (E_x) and the correlation (E_c) part are separated. This allows easy construction and incorporation of different effects. Among the most common functionals we find:

- LDA
- GGA: PW91, PBE, PBE-sol

The local density approximation (LDA) only depends on the local charge density [46, 47].

$$E_{xc}[\rho] = \int \rho(\mathbf{r}) \epsilon_{xc} d^3\mathbf{r} \quad (2.19)$$

The LDA exchange-correlation functional works best for slowly varying electron densities or homogeneous electron densities. The drawback of the LDA functionals is that they describe poorly the lattice parameters, binding energy, atomization energy etc. A more accurate description, in particular for systems with a more rapidly varying electron density, is available with the exchange-correlation functionals of the generalized gradient approximation (GGA) family [48]. GGA also takes into account the local gradients of the charge density.

$$E_{xc}^{GGA}[\rho] = \int \rho(\mathbf{r}) \epsilon_{xc}(\rho(\mathbf{r}), \Delta\rho(\mathbf{r})) d^3\mathbf{r} \quad (2.20)$$

The functional form of GGA are usually chosen such that they coincide with LDA in the limit of a homogeneous electron gas. Usually they are constructed in the form of a correction term which is added to the LDA functional. Meta-GGA is basically an extension of GGA functional which contains all the properties of GGA as well as a non-interacting kinetic energy density is used as a input [49]. Hybrid functional includes a fraction of exact Hartree-Fock exchange energy with the exchange part of the GGA functional. PBE0, HSE, B3LYP are some hybrid functional that are widely used [50, 51]. Even though this type of mixing leads to an improvement different physical quantities for different systems, the calculations are computationally expensive. Hence as Perdew explained, as one climbs up the "Jacob's ladder" of functionals to reach the heaven of chemical accuracy the computational cost increases significantly [52].

2.3

Density functional tight binding (DFTB)

Kohn-Sham Density-functional theory (DFT) is a very powerful method for the calculation of physical and chemical properties of molecules, clusters and condensed matter systems. Unfortunately, DFT simulations that go beyond a few hundred atoms quickly become computationally intractable. At the loss of accuracy, one can restore to significantly faster methods such as semi-empirical tight-binding methods, or even to the completely empirical force fields. Classical force field methods are several orders of magnitude faster than DFT, allowing one to treat millions of atoms and to follow their dynamics beyond the nanosecond time scale [53, 54]. The draw

back of this method is that it is very accurate for the system for which it has been parametrized. The parameters might suffer from a limited transferability. It also misses quantum effects (*i.e.* tunneling) in such types of simulations. On the other hand, DFTB is an approximate quantum chemical method derived from density functional theory (DFT) based on Taylor series expansion of the DFT total energy expression until a second-order.

Tight binding (TB) approaches work on the principle of treating electronic wavefunction of a system as a superposition of atom-like wavefunction (known as LCAO approach) [55]. Here, valence electrons are tightly bound to the cores and not allowed to delocalize beyond the confines of a minimal LCAO basis. TB energy for N electrons, M atoms system can be expressed as:

$$E_{TB} = \sum_i^N \epsilon_i + \frac{1}{2} \sum_{j \neq k}^M \nu_{j,k} (|R_j - R_k|) \quad (2.21)$$

This separation of one-electron energies and interatomic distance-dependent potential $\nu_{j,k}$ constitutes the TB method. Foulkes and Haydock showed that the TB methodology can be understood as an approximation to DFT, critically depending on the choice of an appropriate input density [56]. The input density ρ_0 has to be optimized in order to minimize the error of the TB total energy with respect to the true ground state energy.

To do Taylor series expansion of the DFT, we need to choose proper reference density $\rho(r)$. Here an approximation is done. We consider a system where atoms are free and neutral. The total density of the system is $\rho_0(r)$ which is composed of atomic densities. Thus the density does not contain charge transfer (artificially). The density $\rho_0(r)$ does not minimize the functional $E[\rho(r)]$. Instead the minimization is done with an reference density which is $\rho_0(r)$ with some perturbed density fluctuation $\rho(r) = \rho_0(r) + \delta\rho(r)$. The exchange-correlation energy functional is then expanded and the total energy can be written as

$$\begin{aligned} E = & \sum_i^{occ} \langle \psi_i | \hat{H}_0 | \psi_i \rangle - \frac{1}{2} \iint \frac{\rho_0 \rho'_0}{|\mathbf{r} - \mathbf{r}'|} d^3\mathbf{r} d^3\mathbf{r}' \\ & + E_{xc}[\rho_0] - \int \hat{V}_{xc}[\rho_0] \rho_0 d^3\mathbf{r} + E_{\alpha\beta} + \frac{1}{2} \iint \left(\frac{1}{|\mathbf{r} - \mathbf{r}'|} + \frac{\delta^2 E_{xc}}{\delta\rho\delta\rho'} \bigg|_{\rho_0} \right) \delta\rho\delta\rho' d^3\mathbf{r} d^3\mathbf{r}' \end{aligned} \quad (2.22)$$

Here we have considered $\delta\rho$ is very small. The linear terms in $\delta\rho$ vanish. The first term does not contain any charge transfer. The last term contains the energy from the charge fluctuations due to the Coulomb interaction and exchange correlation. The rest is considered as repulsive energy because of ion-ion repulsion term. $E_{\alpha\beta}$ is the same quantity as in Eq. 2.11.

The above Equation is the starting point for further approximations leading to the DFTB model. The approximations are given below:

- The Hamiltonian matrix elements in the first term of Eq. 2.22 are represented in a minimal basis of optimized pseudo-atomic orbitals ϕ_μ . Hence the ψ_i can be represented as

$$\psi_i = \sum_{\mu} c_{\mu i} \phi_{\mu}(\mathbf{r} - \mathbf{R}_{\alpha}) \quad (2.23)$$

The non diagonal elements are calculated within the two centered approximation [57, 58]. Whereas the diagonal elements of the matrix are taken from the atomic eigenvalues of free spin-unpolarized atoms. The non diagonal elements are tabulated together with the overlap matrix elements with respect to the interatomic distance $R_{\alpha\beta}$.

- The charge density fluctuations in the last term of Eq. 2.22 can be written as

$$\delta\rho = \sum_{\alpha} \rho_{\alpha} \quad (2.24)$$

Here ρ_{α} is the superposition of atomic contributions. This due to the monopolar charge fluctuations at the atoms α which is given by $\Delta q_{\alpha} = q_{\alpha} - q_{\alpha}^0$. q_{α}^0 represents the number of electrons of the neutral atom α and the q_{α} are determined from a Mulliken population analysis. Hence the last term of Eq. 2.22 can be written as

$$\frac{1}{2} \iint \left(\frac{1}{|\mathbf{r} - \mathbf{r}'|} + \frac{\delta^2 E_{xc}}{\delta\rho\delta\rho'} \bigg|_{\rho_0} \right) \delta\rho\delta\rho' d^3\mathbf{r} d^3\mathbf{r}' \approx \frac{1}{2} \sum_{\alpha\beta} \Delta q_{\alpha} \Delta q_{\beta} \gamma_{\alpha\beta}(R_{\alpha\beta}) \quad (2.25)$$

The analytical solution from the Coulomb interaction of two atom-centred spherical charge distributions located at R_{α} and R_{β} will provide $\gamma_{\alpha\beta}$ for $\alpha \neq \beta$ [59]. The onsite contributions $\gamma_{\alpha\alpha}$ are computed by taking second derivatives of the total atom energy with respect to the charge and the occupation number, respectively from the spin-unpolarized atomic DFT calculations. This approximation allows to treat charge transfer in a self consistent way.

- Finally, the remaining terms (Eq. 2.22) and the ion-ion repulsion ($E_{\alpha\beta}$) are summarized as a short-range repulsive energy.

$$E_{\text{rep}} = \sum_{\alpha\beta} U_{\alpha\beta} \quad (2.26)$$

$U_{\alpha\beta}$ is an atom-type specific pair potentials. In practice, $U_{\alpha\beta}$ is fitted as the difference of total energies from DFT and the electronic part of DFTB with respect to the bond length of certain bonds in reference molecules [57].

Hence, the final approximate DFTB total energy reads as:

$$E_{\text{tot}} = \sum_{i\mu\nu} c_{\mu}^i c_{\nu}^i H_{\mu\nu}^0 + \frac{1}{2} \sum_{\alpha\beta} \Delta q_{\alpha} \Delta q_{\beta} \gamma_{\alpha\beta} (R_{\alpha\beta}) + E_{\text{rep}} \quad (2.27)$$

2.4 Forces:

The forces on the atoms can be obtained by the negative gradient of the PES. As we discussed before, the stationary points are most interesting sites. Here the forces on the atoms vanish. Hellmann and Feynman showed that the forces can be derived from the electronic charge density. Consider a system with a Hamiltonian $H(\lambda)$ that depends on some parameters λ .

$$\hat{H}(\lambda)|\psi(\lambda)\rangle = E(\lambda)|\psi(\lambda)\rangle \quad (2.28)$$

where $\psi(\lambda)$ be an eigenvector of $H(\lambda)$ with eigenvalue $E(\lambda)$. We also assume that $|\psi(\lambda)\rangle$ is normalized so that

$$\langle\psi(\lambda)|\psi(\lambda)\rangle = 1 \quad (2.29)$$

The force can be written as:

$$\begin{aligned} \frac{\partial E}{\partial \lambda} &= \frac{\partial}{\partial \lambda} \langle\psi(\lambda)|\hat{H}|\psi(\lambda)\rangle \\ &= \left\langle \frac{\partial \psi(\lambda)}{\partial \lambda} | \hat{H} | \psi(\lambda) \right\rangle + \langle \psi(\lambda) | \frac{\partial \hat{H}}{\partial \lambda} | \psi(\lambda) \rangle + \langle \psi(\lambda) | \hat{H} | \frac{\partial \psi(\lambda)}{\partial \lambda} \rangle \\ &= E \left\langle \frac{\partial \psi(\lambda)}{\partial \lambda} | \psi(\lambda) \right\rangle + \langle \psi(\lambda) | \frac{\partial \hat{H}}{\partial \lambda} | \psi(\lambda) \rangle + E \left\langle \psi(\lambda) | \frac{\partial \psi(\lambda)}{\partial \lambda} \right\rangle \\ &= \langle \psi(\lambda) | \frac{\partial \hat{H}}{\partial \lambda} | \psi(\lambda) \rangle + E \frac{\partial}{\partial \lambda} \langle \psi(\lambda) | \psi(\lambda) \rangle \end{aligned} \quad (2.30)$$

Since the wavefunction is normalized, the last term vanishes.

$$\frac{\partial E}{\partial \lambda} = \langle \psi(\lambda) | \frac{\partial \hat{H}}{\partial \lambda} | \psi(\lambda) \rangle \quad (2.31)$$

This is known as Hellmann-Feynman theorem. Now if we consider, $\lambda = R_A^{\alpha}$, which is the cartesian component α of the position of nucleus A, and by inserting Eq. 2.5

and \hat{V}_{nn} in Eq. 2.31, we obtain an expression for the corresponding force component F_A^α :

$$\mathbf{F}_A^\alpha = -\frac{\partial E}{\partial \mathbf{R}_A^\alpha} = -\int \rho(\mathbf{r}) \frac{\partial \hat{V}_{en}}{\partial \mathbf{R}_A^\alpha} d\mathbf{r} - \frac{\partial E_{nn}}{\partial \mathbf{R}_A^\alpha} \quad (2.32)$$

Hence the force only depends on the charge density.

2.5 Stationary Points:

Stationary points are the most interesting points on a PES. In the absence of a field, the potential energy of a molecule does not change if it is translated or rotated. Hence it only depends on the internal coordinates of the molecule. Mathematically, a stationary point is one at which the first derivative of the potential energy with respect to each geometric parameter is zero:

$$\frac{\partial V_e}{\partial \mathbf{R}_1} = \frac{\partial V_e}{\partial \mathbf{R}_2} = \dots = 0 \quad (2.33)$$

where each derivative is with respect to just one of the variables \mathbf{R} of which V_e is a function. $(\mathbf{R}_1, \mathbf{R}_2, \dots)$ are the internal co-ordinates of atoms in a molecule. Since the forces vanish at the stationary points, in the Taylor expansion, the leading terms of the potential are quadratic. If the internal co-ordinates are transformed to normal coordinates (q_α) , V_e can be expressed as

$$V_e(q_\alpha) = \frac{1}{2} \sum_{\alpha=1}^{3n} \omega_\alpha^2 q_\alpha^2 + \mathcal{O}(q_\alpha^3) \quad (2.34)$$

where $\mathcal{O}(q_\alpha^3)$ denotes higher-order terms that are neglected in the harmonic approximation.

A displacement along a normal coordinate q_α either raises or lowers the potential energy depending upon whether ω_α^2 is positive or negative. The characteristics of any stationary point are therefore determined by the Hessian eigenvalues which are represented by ω_α^2 .¹ Based on this, we can define three types of stationary points:

- **Minima:** Correspond to stable or quasi-stable species; reactants, products, intermediates. Here

$$\omega_\alpha^2 > 0 \quad (2.35)$$

At a local minimum, the eigenvalues of the Hessian matrix are positive. This means that the curvature into all direction is positive. Hence the local minimum can be identified if the energy rises due to the small displacements into arbitrary directions.

¹if $\omega_\alpha^2=0$, then it corresponds to global displacement of the system.

- **Transition states:** Saddle points which are minima in all dimensions but one; a maximum in that dimension. Here

$$\omega_{\alpha}^2 > 0 \quad (2.36)$$

except along the reaction coordinate and

$$\omega_{\alpha}^2 < 0 \quad (2.37)$$

along the reaction coordinate.

- **Higher-order saddle points:** A minimum in all dimensions but n , with $n > 1$; maximum in the other n dimensions. For this case the Hessian will have n negative eigenvalues. The stationary point is considered as the saddle point of index n .

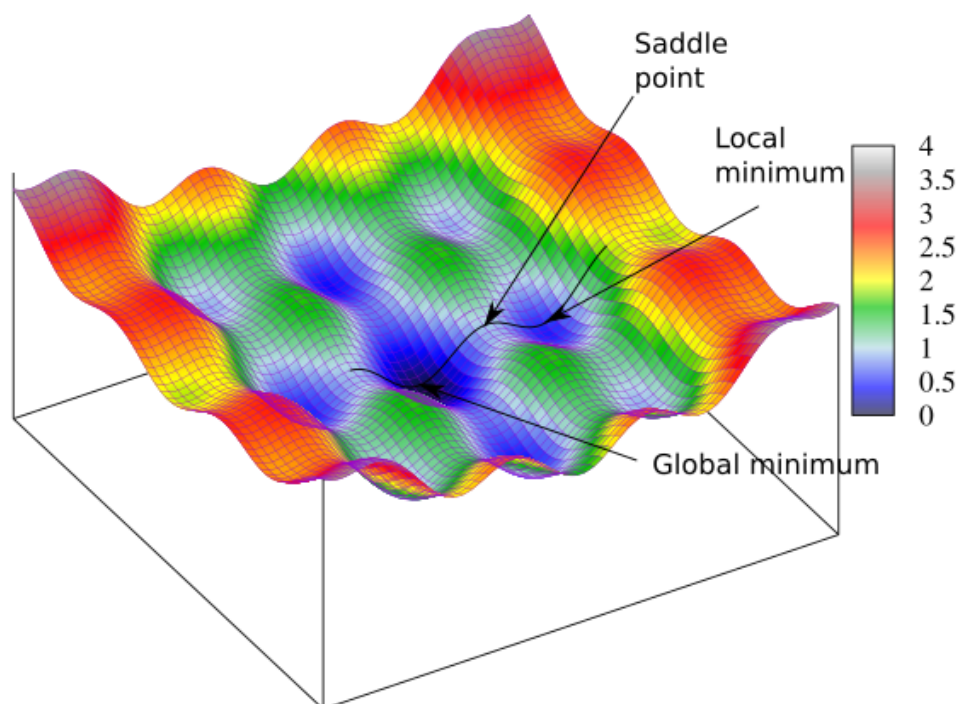


Figure 2.1: A model three dimensional energy surface is shown here. The global minimum, the saddle point and the local minimum is shown in the figure with an arrow. These features have interesting physical significance. Local minima correspond to (meta)stable states. The first order saddle points can be identified with transition states of chemical reactions. The black line correspond to the reaction pathways from local minimum to the global minimum or vice versa through the transitions states.

In Fig. 2.1 A is the global minimum, since it is the lowest-energy minimum on the whole PES, while B is a local minimum, *i.e.* a minimum compared only to its nearby points on the surface. The lowest-energy pathway linking the two minima is the reaction coordinate or intrinsic reaction coordinate (IRC, depicted as a solid line in Fig. 2.1). This is the idle path that would be followed by a molecule in going from one minimum to another because of the lowest barrier height. It should acquire just enough energy to overcome the activation barrier, pass through the transition state, and reach the other minimum. Not all reacting molecules follow the same path exactly: a molecule with sufficient energy can stray outside the path to some extent. Inspection of Fig. 2.1 shows that the transition state linking the two minima represents a maximum along the direction of the IRC, but along all other directions it is a minimum.

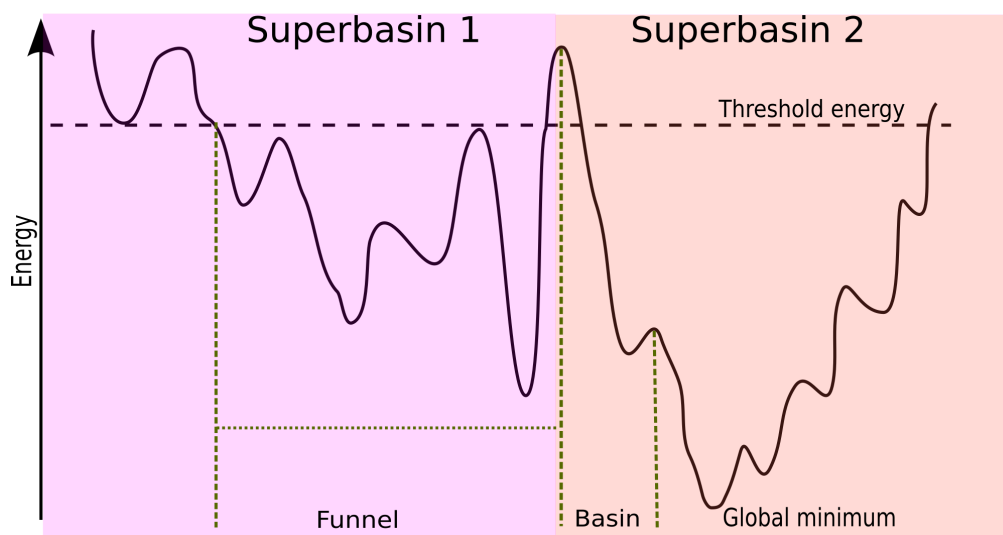


Figure 2.2: A one dimensional model of a multifunnel energy surface to visualize the concept of basins and global minima. It is very difficult to find the global minimum of a multifunnel energy landscape. In this case, if one starts to explore the landscape from a configuration in the funnel which does not contain the global minimum (*i.e.* any minimum from superbasin 1), it will take long time to get out of this funnel and go to superbasin2 where the global minimum is located.

There are few terminologies used to explain the PES during the exploration. This are defined below:

- **A catchment basin (CB):** The set of points from which steepest descent pathways converge to this minimum for each minimum on a PES. The transition states are situated at the edge from where different minima can be explored [60].
- **Superbasins:** If a threshold energy is introduced, the minima of a set of basins are mutually accessible without crossing the threshold energy. These sets of mutually accessible basins are known as superbasins [61].

- **Funnel:** If the lowest minimum of the superbasin can be achieved by never exceeding a barrier that is significantly larger than the average energy differences of the minima in this superbasin then the superbasin will be considered as a funnel. [38, 14]

The global optimization becomes extremely difficult when systems have several funnels. The system might never cross the barrier between two superbasins which will lead to a wrong ground state. For this reason, the majority of the methods are insufficient and also in some cases incapable of finding the global minimum if the starting point is not in the funnel containing the global minima. For example the model energy landscape represented in Fig. 2.2 contains two funnels. If one starts to explore the landscape superbasin 1, it will find the lowest minima of the funnel but the global minimum of the system is in the superbasin 2. The global minima is only accessible after crossing the high barrier between the two funnels. An algorithm will only try to cross the barrier after exploring a large number of local minima in the funnel, in which it starts in. Hence a good global optimization algorithm which is discussed in chapter 2, also needs to have the mechanism to climb up the high barrier to access the funnel containing global minimum. Thus a PES can be partitioned into mutually accessible regions for a given set of different energies. This idea can be used to visualize the PES of arbitrary dimensions. On this basis, Becker and Karplus introduced disconnectivity graphs [37].

2.6 Local geometry optimization:

Exploration of PES required to perform local geometry relaxations so that the local minimums can be found. Since the dynamical properties can be deduced from the energies and the connectivity of minimum and transition states, an efficient determination of the stationary points of PESs is required. Several iterative optimization techniques have been developed throughout the years. This resulted in a number of highly sophisticated methods. Few of them are listed below:

- **Steepest Descent:** The most simple optimization scheme is the steepest descent method. Although not very efficient, it is the most stable method available. A function $f(x)$ is minimized by taking small steps along the negative gradient given at the current coordinate x_t . The iterations of the steepest descent method are given by

$$x_{t+1} = x_t - \alpha_t \nabla E(x_t) \quad (2.38)$$

where the positive real number α_t is denoted as the “step size”. The step size α_t must be chosen such that the energy decreases in all steps.

- **Newton’s method:** The Newton algorithm is an iterative scheme where the Hessian matrix A is used to determine the step-size and descent direction instead of using a constant scalar α as in the steepest descent method. This

approach converges in one single step for any initial configuration if the potential is harmonic.

- **The fast inertial relaxation engine (FIRE):** FIRE belongs to the class of optimization schemes based on damped dynamics [62]. In such schemes the Newtonian equation of motion is iteratively integrated, including a damping factor to reduce the velocity along the trajectory as the potential energy decreases. In this way the system will eventually relax to a close-by local minimum.
- **Quasi-Newton methods, e.g. Broyden-Fletcher-Goldfarb-Shanno (BFGS)** : Determining Hessian matrix A is computationally extremely expensive. A quasi-Newton algorithm such as BFGS is very useful for this purpose [63, 64, 65, 66]. This method employs an approximate Hessian, which is gradually improved as the minimization progresses. The sequence of approximated inverse Hessian matrices C_t should therefore converge towards the true inverse Hessian A^{-1} at the minimum. Importantly, since the true Hessian at the minimum must be symmetric and positive definite, the update mechanism should ensure that the approximate Hessian also preserve these properties.

2.7 Overview on global optimization methods

Distinctive minimization methods, for example, steepest descent, conjugate gradient, and so on or the blends of them is considered to locate the minima of a PES. Tragically, there is no numerical approach to find or to check if a minima is a global minimum. Henceforth the only solution is to consider the lowest minimum of all previously found minimum as a global minimum.

The task of global optimization methods is to find the lowest among all local minima. Regrettably, the quantity of such nearby minima on the high dimensional PES increments exponentially with the system size. For an example the number of local minimum of molecules of the hydrocarbon family (C_NH_{2N+2}) is of the order of 3^N . Because of the constrained measure of computational resources, a small fraction of local minima is investigated and among them, the lowest energy structure is considered as a putative ground state. It is difficult to demonstrate that the genuine ground state has been accomplished.

On the basis of the ideology, global optimization methods can be divided into a few different groups:

- **Empirical correlations:** Machine learning/data mining approach and periodic-graph approach.
- **Thermodynamic approach:** Simulated annealing, metadynamics and basin hopping.

- **Non-Thermodynamic approach:** Genetic algorithms, particle swarm optimization, random search and minima hopping.

A few of these methods are explained in the next sections:

2.7.1 Machine learning

Machine learning is an intensely data-centric technique. A lot of information are gathered and analyzed and trained by a prescient model [67, 68, 69]. If now similar inputs as of the trained data set are provided to the model, it will anticipate probabilistic outcomes dependent on the prepared information. Prediction of crystal structure through machine learning relies upon the capacity to isolate the information of precious crystal structure of all types. The algorithm will only make predictions, and some of these could correspond to completely unstable or even physically impossible compounds. Therefore, chemical intuition will still need to be utilized to determine what is valuable and what to ignore.

2.7.2 Simulated annealing

In experimental physics, to reduce defects and obtain larger single crystals, a sample is heated to high temperatures and then slowly cooled down. Simulated annealing method mimics this process [9, 10, 11, 12, 13]. Starting from an initial configuration, the atoms are usually equilibrated at a high constant temperature through molecular dynamics or with a Monte Carlo method on which periodic local quenching is performed. At high temperature, the Boltzmann distribution exhibits uniform preference for all the states, regardless of their energy. When temperature approaches zero, only the states with minimum energy have nonzero probability of occurrence. This is however true only for systems with simple energy landscapes.

2.7.3 Basin hopping

The basin hopping method is a thermodynamical method [70, 71, 72, 38]. The PES is transformed into a stepwise constant staircase function representing the energies of the local minima of the corresponding basins of attraction. This modified PES is sampled using a Monte Carlo simulation at a constant temperature. The system is moved by a random displacements of the coordinates from a uniform distribution in the range of $[-1, 1]$, times the step size. The step size is dynamically calibrated to give an acceptance ratio of 0.5 and to make certain that the system will not get stuck in the local minima. A local geometry relaxation is then performed. The trial structure is always accepted according to the metropolis algorithm which is if $E_{\text{trial}} < E_{\text{init}}$, and only if a random number drawn from a uniform distribution in $[0, 1]$ is less than the Boltzmann factor $\exp(-\frac{E_{\text{trial}} - E_{\text{init}}}{k_B T})$. If the trial structure is

accepted, the current configuration and the energy is updated, else a new trial step is performed from the previous configuration. Crossing a barrier, using ordinary Monte Carlo simulations is a rare event. It might take long time to reach a global minima.

There is one free parameter, namely the temperature, that can be lowered successively during a simulation. Consequently basin hopping can be used within simulated annealing method.

2.7.4 Genetic algorithms

A genetic algorithms [7, 73, 74, 75, 76, 77, 78] is inspired by Charles Darwin's theory of natural evolution. This algorithm reflects the process of natural selection where the fittest individuals are selected for reproduction in order to produce offsprings of the next generation. Five phases are considered in a genetic algorithm.

- **Initial population:** The process begins with a set of individuals which is called a Population. Each individual is a solution to the problem you want to solve.
- **Fitness function:** The fitness function determines how fit an individual is. The fitness of the individual solutions is usually given by the (free) energy or enthalpy of the structures.
- **Selection:** The selection phase is to select the fittest individuals and let them pass to the next generation.
- **Crossover:** A crossover point is chosen at random from the parents and the offsprings are created by exchanging the genes of parents.
- **Mutation:** New off spring are created by mutation with low random probability.

In each of the main operations in each generation, one makes sure that the configurations with the lowest energies always survive. This method has been implemented and available as software packages *i.e.* GASP [79] or USPEX [76].

2.7.5 Minima hopping

The Minima Hopping (MH) method is a non-thermodynamic global optimization method and depends on the fact that by exploring the low energy part of the PES as fast as possible the global minimum will be revealed at some point [14]. It is based on the two basic principles (Fig. 2.5 and Fig. 2.3):

- A built-in feedback mechanism excludes the trapping and recognizes the regions that are already visited previously.
-

- It exploits the Bell-Evans-Polanyi principle for the moves from one catchment basin to other [80, 13].

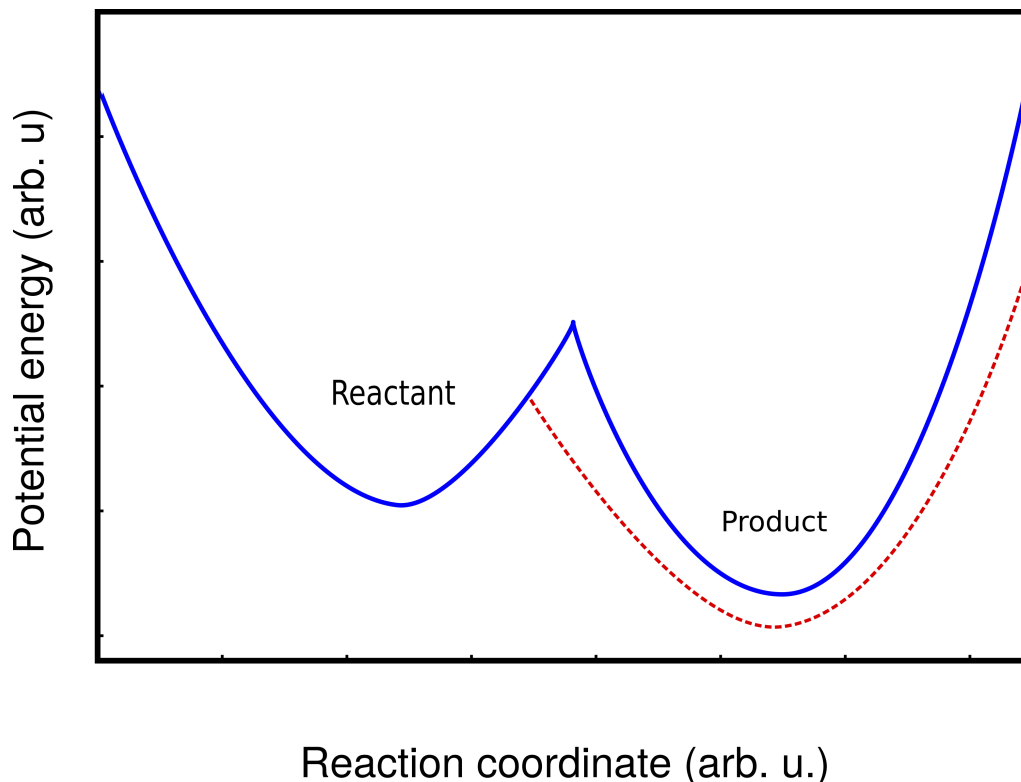


Figure 2.3: The schematic diagram of the Bell-Evans-Polanyi principle.

Bell-Evans-Polanyi (BEP) principle suggests that exothermic reactions typically have low barrier energies. This suggest that the product and the reactant of a chemical reaction is the two local minimums connected by a transition state. A simple one dimensional representation of two local minimums along with reaction coordinate is presented in Fig. 2.3. The two local minimum is represented by the blue curve. Now if the energy of the product is lowered, the barrier height in between them also reduces. However it is a very crude approximation and the curvature of the PES might change due to the shift. Also a high kinetic energy can lead to a lot of undesirable local minimums.

The MHM algorithm is based on two parts as can be observed in the Fig. 2.4:

- the inner part is responsible for the jumps into a neighboring local minimum
- the outer part is used to accept or reject this minimum

As we can see from the flow chart of MH in Fig. 2.4, a molecular dynamics simulation (MD) is performed in the inner part of MH. The system has a random Boltzmann distribution with a kinetic energy E_{kin} to perform the escape moves. During the MD moves the potential energy is monitored as a function of time. The MD trajectory is stopped at the n th minimum as it encounters on the potential energy surface.

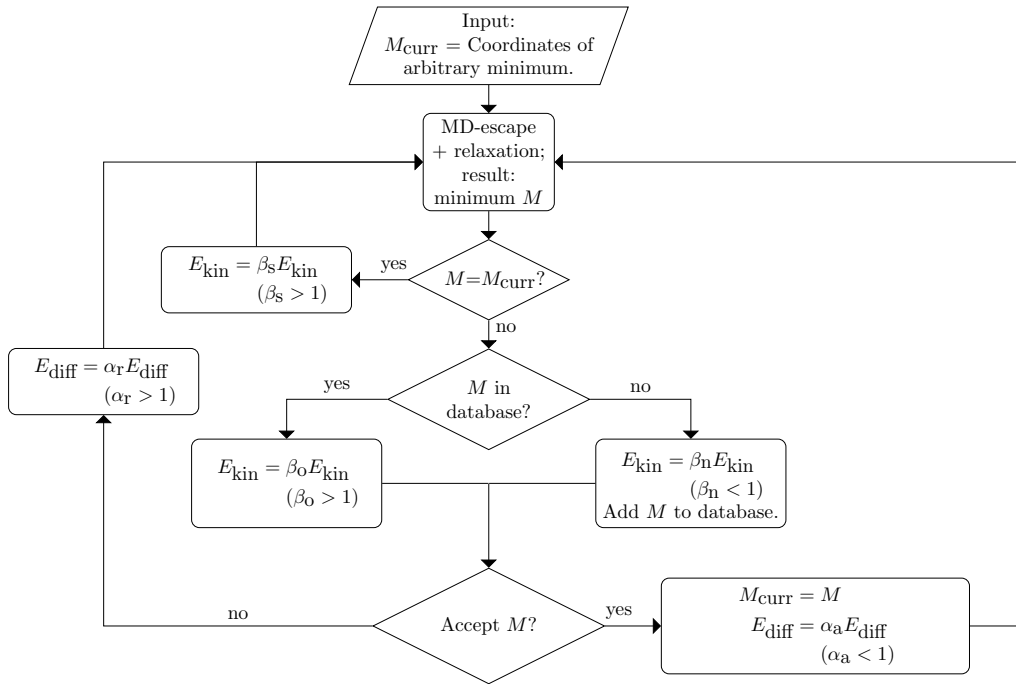
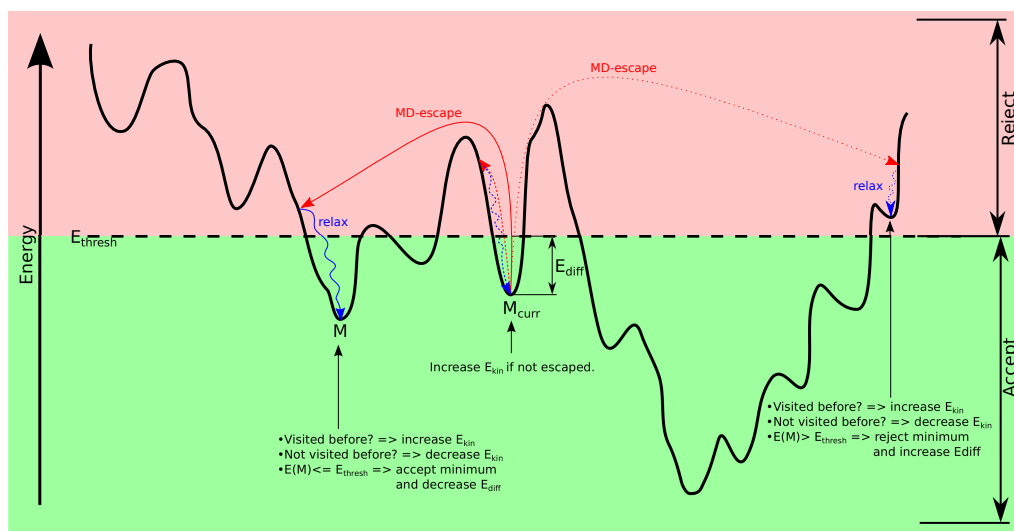


Figure 2.4: Flow chart of MHM. There are five parameters. α_r and α_a determine how rapidly E_{diff} is increased or decreased in the case where a new configuration is rejected or accepted. Depending on the outcome of an escape trial β_s , β_o , and β_n determines that how rapidly E_{kin} is modified .

The final MD configuration is used as a starting point for a standard local geometry optimization. There are three possible scenarios, which are detailed in Fig. 2.4. If a random direction of velocity vector is used at the start of MD simulation then we have to follow the MD trajectory over many oscillations within the catchment basin before it crosses into any other catchment basins. This method is very inefficient and can be avoided by starting an MD simulation with the velocity vectors in a *soft* directions. The soft direction is defined as the direction where the curvature of the potential energy surface is small. Along that direction the probability of finding low energy barrier is higher and can be done with fewer force evolution by the dimer method.

The outer part of the MH accepts or rejects a minimum based on threshold energy (E_{diff}) or on a Metropolis step. The new minima is always accepted if the energy of the new minima is not higher than the energy of the current minima by E_{diff} . The parameter E_{diff} is continuously adjusted during the simulation by a factor α_r , if the new minima is rejected or by a factor α_a if the new minima is accepted. By choosing $\alpha_a = 1/\alpha_r$, roughly half of all the minima are accepted on average during a MH run.

Amsler *et al.* extended MHM for the periodic systems [15]. Initially MHM was developed for an isolated molecule, or a periodic system in a rigid box. To perform structure prediction for a periodic system, not only the atomic positions are required to be optimized, but also the cell shape, especially when external constraints are



- Acceptance / Rejection based on simple thresholding: Accept new minimum M if $E(M) < E(M_{\text{curr}}) + E_{\text{diff}}$
- Feedback on E_{kin} and E_{diff}

Figure 2.5: The schematic diagram of MHM in a two dimension PES. The black broken line indicates the threshold energy. The dotted red arrows represent the rejected moves whereas the unbroken red arrows represent allowed moves. The escape moves generally bring the system to a new basin. The acceptance and rejection of a structure depends on the condition which is $E_{\text{diff}} > E(M) - E(M_{\text{curr}})$. Hence MHM not only accepts the lower energy minimum than the current state but also a energetically high local minimum can also be accepted. This option of accepting higher energy minima is the most important requirement to explore a multi-funnel energy landscape.

imposed. Hence, to generalize the MHM method for periodic systems with variable cell shape, the degrees of freedom are augmented by the three variable cell vectors \mathbf{a} , \mathbf{b} and \mathbf{c} and the angles between the corresponding vectors. The atomic positions can be expressed by vectors in lattice coordinates and the potential energy is replaced by the configurational enthalpy. For the escape step, the MD needs to be performed which should also consider the additional cell parameters. Hence, both the atomic positions in lattice coordinates and the lattice vectors are time-dependent. Parrinello and Rahman proposed a Lagrangian to perform variable cell shape MD at constant pressure P [81]. This method is used for the escape step.

Our implementation of MHM is coupled with different codes at different level of theory. In this thesis, we used MH at tight binding density functional theory level (DFTB) as implemented in DFTB+ [82] and at density functional theory (DFT) as implemented in BigDFT [83] (wavelet basis set) and VASP (plain wave basis set) [84].

2.8 Disconnectivity graphs:

Becker and Karplus suggested an alternative way to visualise a multi-dimensional PES using disconnectivity graphs [37]. This technique has been frequently used and illustrated by Wales *et al.* [85, 38, 86, 87]. A disconnectivity graph analysis focuses on local minima and transition states. By the choice of the threshold energy a number of superbasins are constructed. To construct the disconnectivity graph, the superbasin analysis is performed at a discrete series of total energy. Each superbasin is represented by a point at a horizontal axis. This point is called node. The vertical axis represents total energy. This axis is discretized with a number of equidistant energy threshold levels E_i . Two nodes, *i.e.* E_i and E_{i+1} where $E_{i+1} > E_i$, are connected by a line if they belong to a same basin. Finally, all the single minima at the bottom of the superbasins are represented separately by drawing lines down to their respective energies. For an example, a disconnectivity plot of an one-dimensional PES can be visualized in Fig. 2.6. The disconnectivity plot has been constructed on the basis of the model PES shown in Fig. 2.2. All disconnectivity graphs in this thesis were generated using the disconnectionDPS software [88].

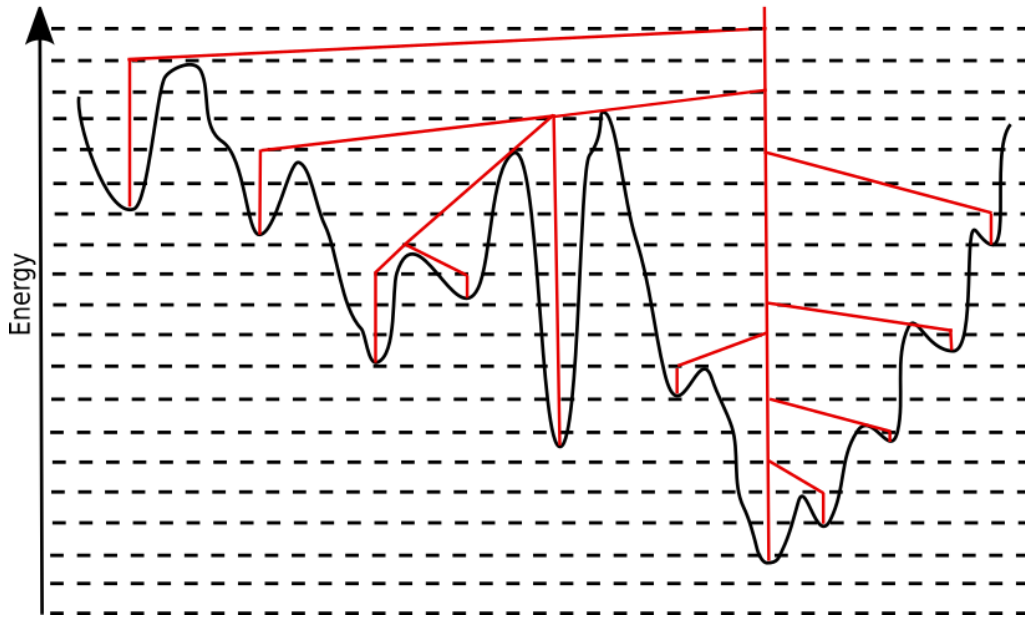


Figure 2.6: The construction of a disconnectivity graph (red tree-like graph) for a one-dimensional model energy landscape which is shown Fig. 2.2, is visualized here. Threshold energies are given by the equidistant horizontal black dashed lines.

CHAPTER 3

Application to the carbon based fullerene

3.1 Introduction

In this chapter we present three different applications related to carbon based fullerene configurations. This chapter is structured as follows.

In the first section(3.3)¹, we attempted to comprehend the geometric configurations of exohedrally decorated C_{60} fullerene structures. For this purpose, we investigated exohedrally decorated atoms on C_{60} by employing for the first time a structure prediction method, namely minima hopping method (MHM) [14] at ab initio level. The energetically lowest configurations for exohedrally metal decorated $C_{60}M_n$ with ($2 \leq n \leq 32$) is thus found for alkali metals, alkaline-earth metals and some other elements. Furthermore, we can predict the behavior of a larger number of decorating atoms by analyzing the bonding characteristics (type and topology) of a single atom via the ELF (electron localization function).

Based on the section3.3, we have observed that the maximum number of alkali atoms required to homogeneously distribute over C_{60} in the absence of an external electric field. In the next section(3.4)², we manipulated the PES of Li and K decorated C_{60} at the DFT level with different external electric fields.

¹The results presented in this section was published in: D. S. De, J. A. Flores-Livas, S. Saha, L. Genovese, and S. Goedecker “*Stable structures of exohedrally decorated C_{60} -fullerenes*” Carbon 129, 847 - 853 (2018).

²The results presented in this section was published in: D. S. De, S. Saha, L. Genovese, and S. Goedecker “*Influence of an external electric field on the potential energy surface of alkali decorated C_{60}* ” Phys. Rev. A 97 (6), 063401 (2018).

Modifying the original carbon fullerene by substitutional doping using boron and nitrogen are a very popular choice. These arrangements and their embellishments with various type of atoms can be used as a novel motif for different periodic configuration and in addition can be utilized in various applications. In the last section^{3.5³}, we addressed the issue of the stability of decorated $C_{48}B_{12}$ heterofullerene. Homogeneously distributed Be, Ca, Li and Sc decorated $C_{48}B_{12}$ clusters are predicted to be stable and a very good candidate as a hydrogen storage material. We revisited the configurations through an unbiased PES search at DFT level. We present a solid confirmation of the precariousness of those hand made structures and legitimize the prerequisite of PES investigation.

3.2 Fullerene Cages

Before we go into our results, in this section we will give a small introduction about fullerene Cages. A fullerene is any molecule in the form of a hollow sphere, ellipsoid or tube, generally composed of carbon atoms (Fig. 3.1).

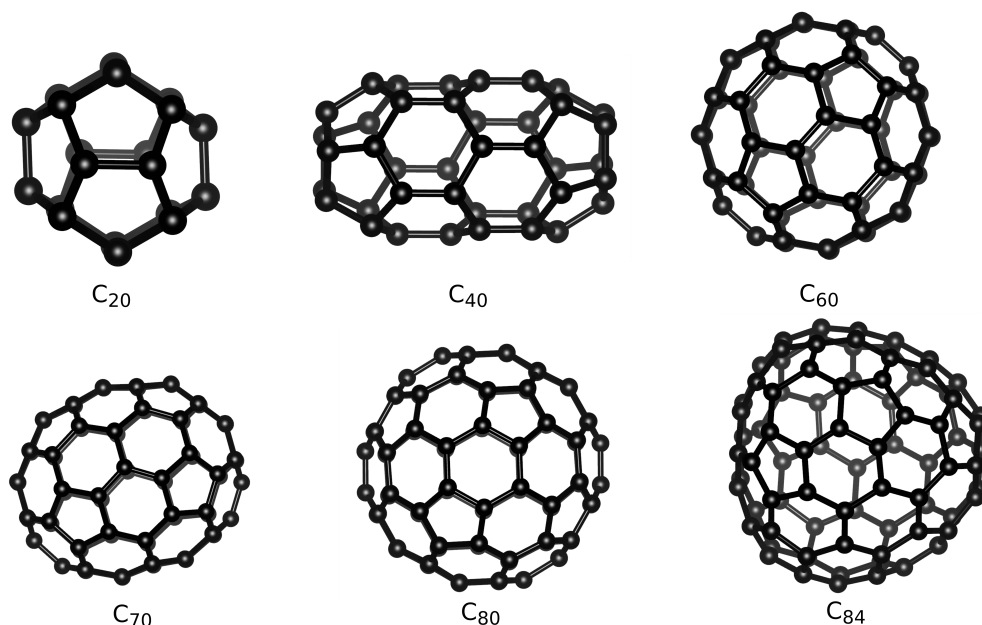


Figure 3.1: Stable fullerene configurations of different shapes and with different number of carbon atoms.

Spherical fullerenes are also called Bucky-balls, and they resemble the football in an atomic scale. The first fullerene, buckminsterfullerene (C_{60}), was prepared in 1985 by Richard Smalley *et al.* at Rice University [89]. In mathematical terms, this

³The results presented in this section was published in: D. S. De, S. Saha, L. Genovese, and S. Goedecker “*Comment on the stability of decorated $C_{48}B_{12}$ hetero-fullerene*” arXiv preprint arXiv:1802.03763.

structure of the fullerene is consists of a trivalent convex polyhedron with pentagonal and hexagonal faces. According to the graph theory, the term fullerene refers to any 3-regular, planar graph with all faces having 5 or 6 vertices which follows from Euler's polyhedron formula, $V - E + F = 2$ (where V , E , F are the numbers of vertices, edges, and faces respectively). There are exactly 12 pentagons in a fullerene and $(V/2 - 10)$ hexagons.

3.3 Exohedrally decorated C_{60} -fullerenes

Certain decorated C_{60} fullerene structures have been assessed for its potential to meet specific hydrogen storage target properties so that fossil fuels can be replaced in practice. [90, 91, 92, 93, 94, 95, 96]. In particular, decorated fullerenes with alkali metals (AM) or alkaline-earth metals (AEM) enhances the hydrogen adsorption capacity [94, 96]. This is due to the charge transfer from the metal atom to the fullerene cage, that leaves the metal atom in a cationic state, where it can bind H_2 molecules due to polarization forces [97]. It is clear that the geometry and type of coverage of the decorating atoms play a key role in determining the H_2 adsorption mechanism. Because of the technical challenges of theoretical structure predictions, metal decorated C_{60} fullerenes has been mainly studied experimentally. At the experimental level, as well, only a few decorating elements has been studied, due to the complexity of the experiments. In previous literature, semi-empirical methods and hand-made geometries were frequently used [98, 99]. Only a few attempts were made at the density-functional theory (DFT) level, but without fully exploring the potential energy landscape of decorated fullerenes [100, 101, 102, 99, 103, 104, 105, 106, 96, 95, 107, 108, 109, 110]. A comprehensive and unbiased exploration of the potential energy surface at the *ab initio* level requires special computational tools and methods that allow to calculate energies and ionic forces extremely rapidly. [111] Typically a simulation include between 60 to 100 atoms, and the study of all the possible configurations (hand-made geometries) is not possible.

We present here a fully *ab-initio*, unbiased structure search of the configurational space of decorated C_{60} fullerenes and report that many of the hitherto postulated ground state structures are not in fact the lowest energy structures. We determine the energetically lowest configurations for decorations with a varying number of decorating atoms ($2 \leq n \leq 32$) for alkali metals, alkaline-earth metals as well as some other elements. All the energy and force calculations were evaluated at the level of DFT using the PBE exchange-correlation functional [112] as implemented in the wavelet basis based BIGDFT code [111]. The grid spacing of 0.4 Bohr was used along with tight electronic parameters such that the total energy difference are converged below 10^{-4} eV for all stable configurations and geometry relaxation until forces on atoms are below 1 meV/Å. The electron localization function (ELF) [113] was calculated on geometry relaxed structures using a plane wave basis-set with cutoff energy of 820 eV within the projector augmented wave (PAW) method as

implemented in the Vienna Ab Initio Simulation Package VASP [114] and in uniform boxes with size of $20 \times 20 \times 20 \text{ \AA}$ for all the systems studies in this work. The adsorption energy is defined as:

$$E_{\text{ads}} = E_{\text{C}_{60}} + n \times E_{\text{atoms}} - E_{\text{Total}}$$

Where $E_{\text{C}_{60}}$ is the energy of C₆₀, E_{atoms} is the energy of an atom, n is the number of atom and E_{Total} is the total energy of the system. Here, the charge transfer is defined as the difference between the amount of electron present on an isolated atom and the total amount of charge present on the atom after the adsorption. This we obtained from the Bader charge analysis [115, 116, 117].

The ELF one-dimensional axis represents,

$$\eta(r) = 1/(1 + (D_P/D_h)^2) \quad (3.1)$$

where D_P is the difference between the positive local kinetic energy of non-interacting electrons, having same density as the real system, and the von Weizsaecker kinetic energy functional and D_h is the local kinetic energy of a homogeneous electron gas. This function takes the values between 0 and 1. $\eta(r) = 1/2$ for instance represents a typical free-electron pairing. On the contrary, values close to 1 are typical of fully localized electron pairing. The important term D_P represents the excess local kinetic energy density due to the Pauli repulsion. The details is given in the appendix B. Though the ELF has density-functional dependence, in this work we aim to capture first general trends over the periodic table treated within the same level of theory (GGA-PBE).

In the following we present the predicted stable configurations of the decorating atoms of different type on the surface of the fullerene. Three main scenarios have to be distinguished:

wetting The decorating atoms are uniformly distributed over the entire surface of the fullerene, maximizing their mutual distances.

clustering The decorating atoms strongly attract each other and form clusters, *i.e.* decorating atoms are clumped at a particular site on the surface with other atoms of the same species aggregated on top it.

patching The decorating atoms form patches, *i.e.* a compact monolayer covers a part of the surface of the fullerene. The atoms of same species never accommodate themselves on top of each other.

Fig. 3.2 summarizes the maximum number of atoms for all the elements considered that the surface of C₆₀ can host before the system starts to show “clustering” or “patching”. During the simulation of each system, several hundred configurations

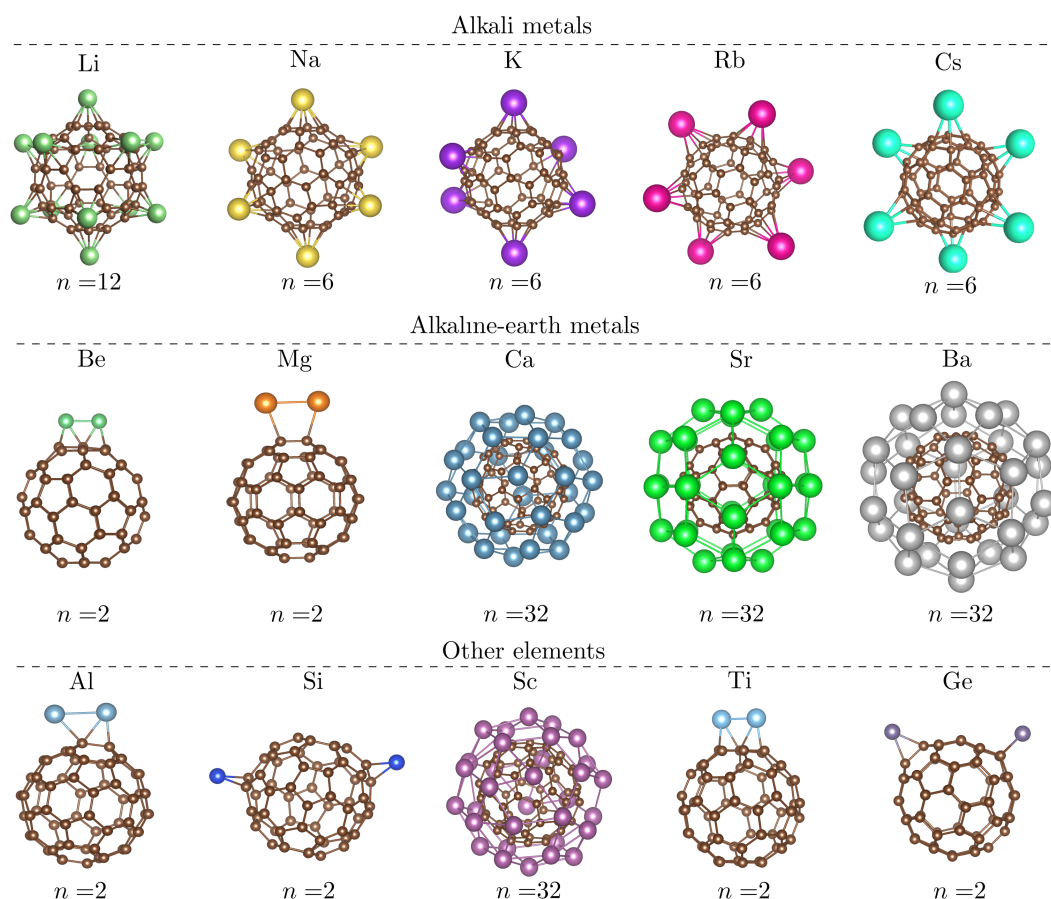


Figure 3.2: Maximum number of decorating atoms of the same species that can be homogeneously distributed on the C_{60} surface. For AM a maximum of 12 atom is found for Li, while for Na, K and Rb, it is reduced to 6. For AEM a maximum coverage of 32 atoms forming an outer-shell is achievable by Ca, Sr and Ba. The elements Al, Si, Ti and Ge in contrast do not form homogeneous decoration patterns. Sc (shown) and La (not shown) can form homogeneous distribution with up to 32 atoms.

Table 3.1: Summary of absorption energies (E_{ads}), tendency for lone pair formation, ELF type and charge transfer for selected single atom-decorated C₆₀. The ELF type is determined through visual inspection, as to Fig. 3.12. n is the maximum number of decorating atoms that can homogeneously be distributed on a C₆₀ as shown in Fig. 3.2. Non-homogeneous (NH) distributions are also indicated. The ELF type for d)* systems is given in the appendix D.

Atom	E_{ads} (eV)	Lone pair	ELF type	n	Charge transfer(e^-)
Li	1.79	✗	b)	12	1.00
Na	1.53	✗	b)	6	1.00
K	1.88	✗	b)	6	1.00
Rb	1.59	✗	b)	6	1.00
Cs	1.70	✗	b)	6	1.00
Be	0.29	✓	d)*	2 (NH)	1.50
Mg	0.07	✓	d)*	2 (NH)	0.12
Ca	1.37	✗	c)	32	1.42
Sr	1.03	✗	c)	32	1.48
Ba	1.85	✗	c)	32	1.40
Sc	2.67	✗	c)	32	1.48
Y	2.38	✗	c)	32	1.59
La	3.37	✗	c)	32	1.50
Zr	3.46	✗	c)	32	1.51
Ti	3.26	✓	d)*	2 (NH)	1.62
Si	2.77	✓	d)	2	2.20
Ge	2.28	✓	d)	2	1.80
Al	1.95	✓	d)*	2 (NH)	1.68

were visited. The MH runs were terminated either when we observed that the energy of the system was significantly reduced, when the system started to form clusters or when the basic structure of the fullerene was destroyed. Systems with a preference for homogeneously distributed configurations and highly symmetric patterns rapidly reach an energy that is much lower than the energy of competing configurations.

3.3.1

Alkaline atoms

First we studied the M_nC_{60} structures for an increasing number n of Li, Na and K atoms and observed that they wet C₆₀ up to a limit of 12 atoms for Li and 6 for Na or K (Fig. 3.2).

Fig. 3.3 summarizes the lowest energy structures for Li coverage from 1 to 32 atoms. In our calculations, we found that from 2 Li atoms onward, these atoms start to distribute far from each other, and take hexagonal sites (see $n = 4$). When the number of Li atom reach 5 they, however, they prefer to go to the pentagonal sites.

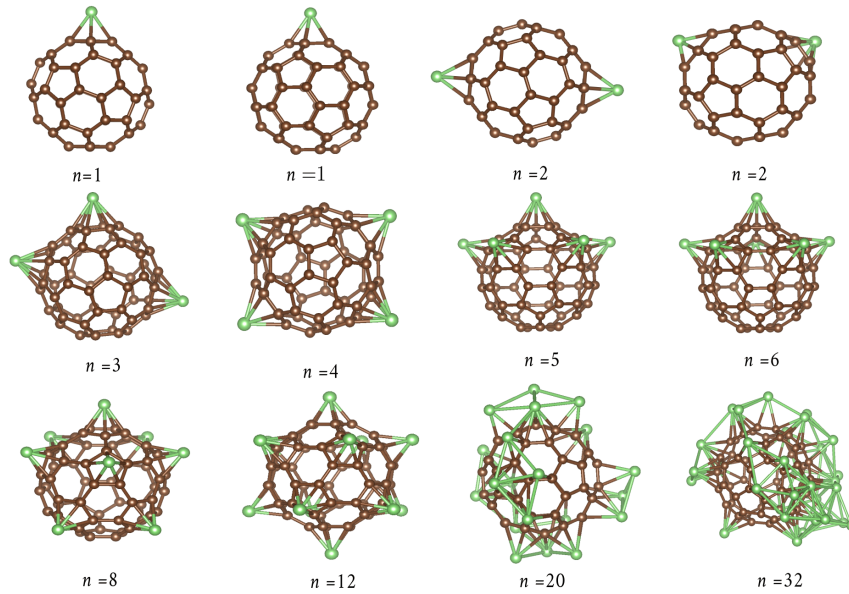


Figure 3.3: Low lying energy structures for different Li coverage (n) indicated. For 1 and 2 atoms Li has energy degenerate structures.

As the number of atoms further increases, Li atoms start to occupy nearest P-sites and for 12 Li atom, they distribute themselves homogeneously on C_{60} . As the ionic interactions dominate for a small number of Li atoms, they organize far from each other. For more than 12 atoms, covalent interaction starts to dominate and Li atoms start to cluster on top of each other (see $n = 32$).

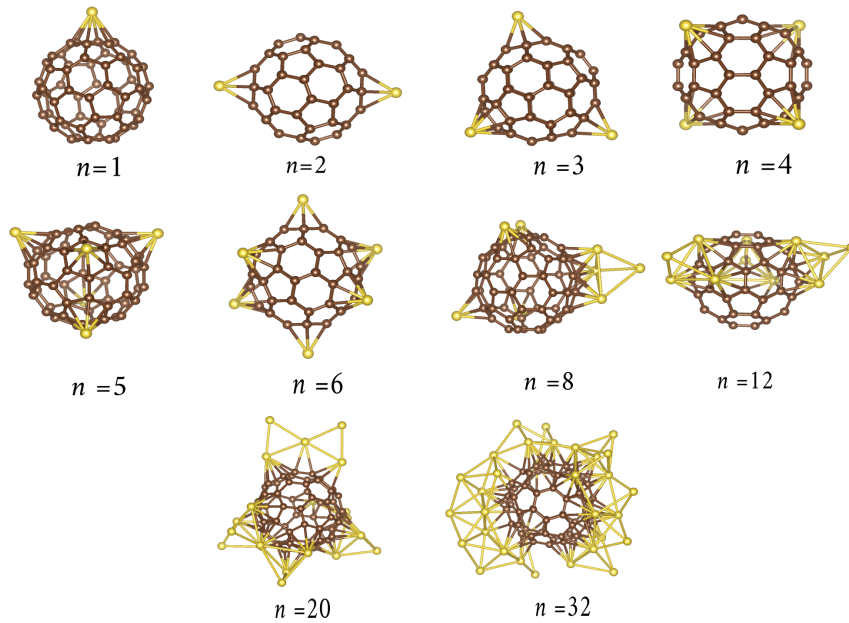


Figure 3.4: Selected optimal structures with different number of Na on the fullerene surface. Similar structures are found for potassium.

Na and K behave similarly to Li when the atom number is increased from 1 to 5. They prefer to take hexagonal sites and show clustering for more than 6 atoms, as shown in Fig. 3.4. 12 Na atoms will tend to form several clusters on the fullerene's surface; interestingly, these clusters are more stable than a single Na cluster.

Rb and Cs atoms also wet C_{60} up to 6 atoms (Fig. 3.2) and for a larger number of atoms they start to form clusters. This is in agreement with previously observed experimental results. [118]

3.3.2 Calcium and scandium

Interestingly, from 2 atoms onward Ca gives rise to many different configurations. Ca adsorption at the closest pentagon-site is less favorable by 0.1 eV, whereas for Sc the two cases are degenerate with an energy difference of 0.006 eV. A third Ca or Sc atom prefers to sit on nearest hexagon-site. Further increasing the number of Ca and Sc atoms, the atoms prefer to occupy close by H-site and P-sites. To further prove that Ca and Sc atoms do not form a cluster on the C_{60} surface, we carried out separate calculations on two selected conformations: in the first we placed four Ca and Sc atoms on the neighboring hexagonal and pentagonal sites of the C_{60} surface. In the second, we placed the four atoms to form a tetrahedron. The configuration where the Ca and Sc atoms form a tetrahedron is 0.83 eV and 0.73 eV higher in energy than when they occupy the H or P sites on the C_{60} surface respectively. This clearly evidences that Ca and Sc atoms do not form clusters on C_{60} , but rather form patches. As we increased the number of atoms to 8, 12 and 20, they homogeneously distributed over the surface. During our structure exploration runs, Ca and Sc atoms aggregated and form patch-type structures. This is in stark contrast to the alkali metals, where we rather see clustering. As we increased the number of atoms to 20, the patches extent over the fullerene surface, covering large areas. For 32 Ca and Sc atoms, C_{60} is completely covered (Fig. 3.5).

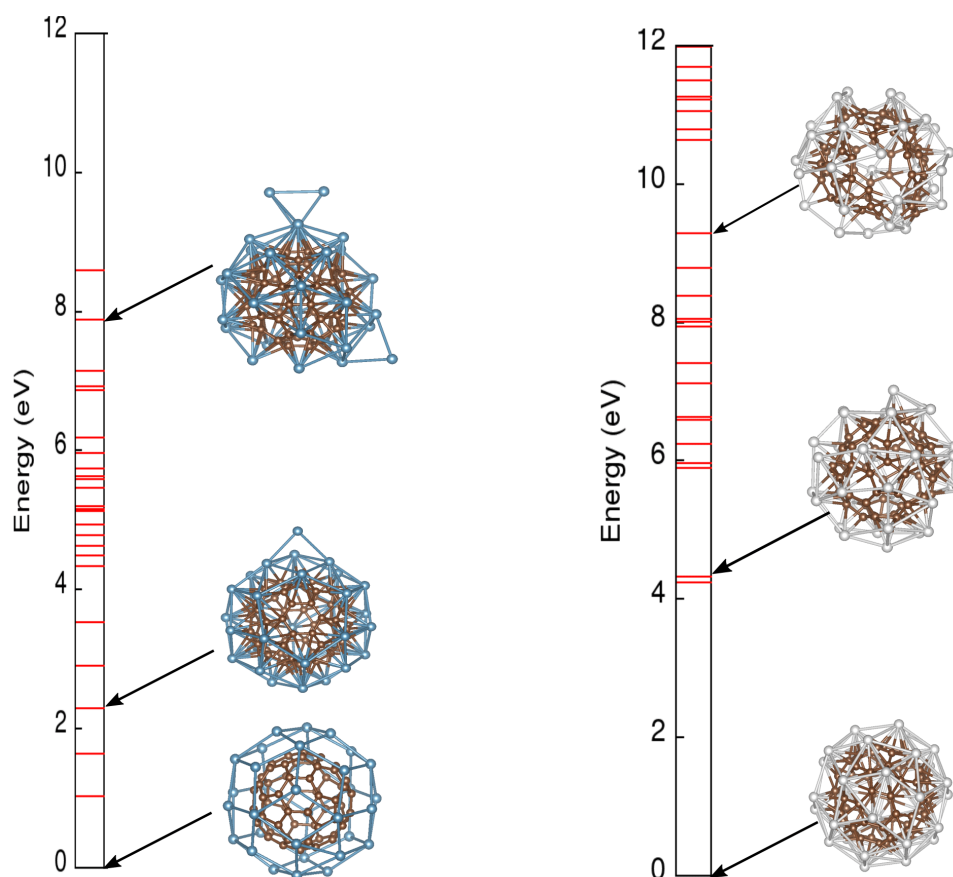


Figure 3.5: Energy order configurations for 32 atoms of Ca and Sc. Selected structures are also shown for comparison. Core-shell type are the most stable structures.

12 Sc atoms do not wet the surface, as obtained in previous theoretical results, [107], but they rather form a patch. We scanned the PES using MH and found out that the patched configuration is 10.66 eV lower in energy than the homogeneously distributed configuration. As we increase the number of atoms, Ca and Sc also prefer to form patches. Ca and Sc can adsorb the largest number of atoms on the C_{60} . They can homogeneously cover C_{60} with up to 32 atoms and form a core-shell type structure (Fig. 3.2). These results are in good agreement with experimental evidences. [118]

3.3.3 Silicon and germanium

If more than two atoms are present, Si and Ge starts to form cluster on the C_{60} surface. It is not surprising that silicon, germanium and carbon behave in a similar way and most other elements which form covalent bonds with carbon, show indeed a similar behavior.

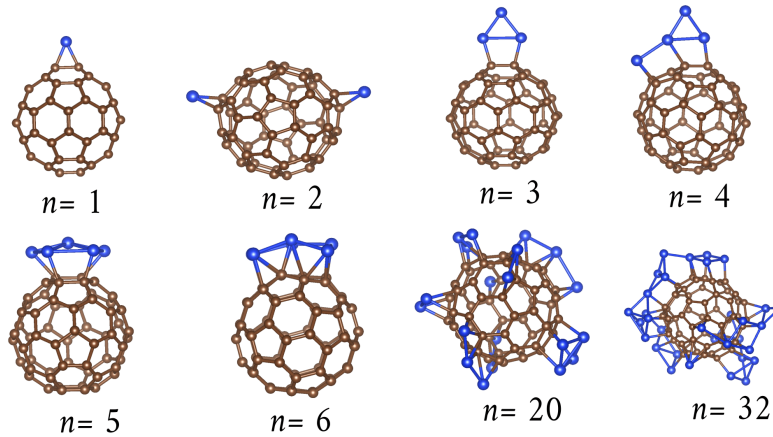


Figure 3.6: Selected structure with Si (atom depicted on blue) for different coverage.

Fig. 3.6 depicts selected configurations for silicon atoms. From two Si atoms, they occupy bridge sites and separate distance far from each other. The Si–C bond length is 1.92 Å. In spite of the strong bonding, there is only a weak deformation of the fullerene cage. With three Si atoms the most stable configuration is with the atoms gathering together, forming a small cluster (see $n = 3$). Two of them occupy a T-site and the C–Si bond is 2.03 Å. Five Si atoms do not stay on top of each other, but get adsorbed on hexagonal and bridge sites. As we increase the number of Si atoms, 12, 20 and 32 do not form core-shell structures. Our findings for Si and Ge are supported by experimental findings [119].

3.3.4

Beryllium and magnesium

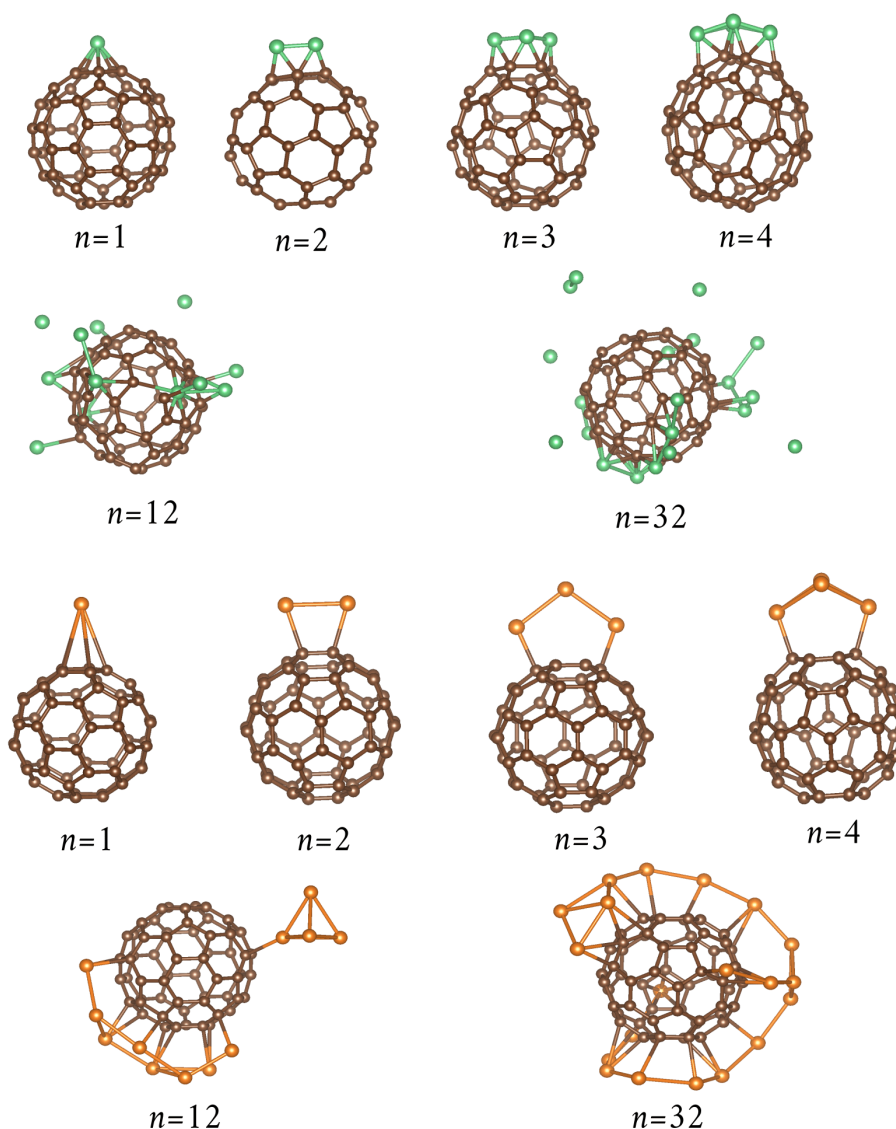


Figure 3.7: Selected configurations for Be (upper structures) atoms depicted in green and Mg depicted in yellow.

For two Be atoms, Be prefers to occupy nearest H–H and H–P site. The C–C bond length close to the H–H site is 1.60 Å whereas it is 1.53 Å at the H–P site. The Be atoms form a patch and the Be–Be distance is 1.90 Å. The bond length of this adsorbed Be dimer is much shorter than for a free dimer in vacuum (2.42 Å). The charge transfer from Be to the nearest C, leads to this decrease in bond length. Increasing the number of adsorbate atoms, it is observed that Be starts to accumulate, occupying alternatively H–H and H–P sites. The bond length in between nearest C–Be is 1.72 Å. For more than 12 atoms Be stay on top of C₆₀ and form

patches. In some other configurations Be atoms prefer to break into the C_{60} cage and destroy the cage structure of C_{60} . Similar effects have been observed for 20 and 32 Be atoms in our structure explorations. Two Mg atoms get adsorbed on close by T-sites. The bond length in between C and Mg decreases to 2.5 Å. Introducing more Mg atoms increases the size of the area of the patches; also, small clusters appear on the C_{60} surface. A few selected stable configurations are given in Fig. 3.7 for Be and Mg atoms on C_{60} .

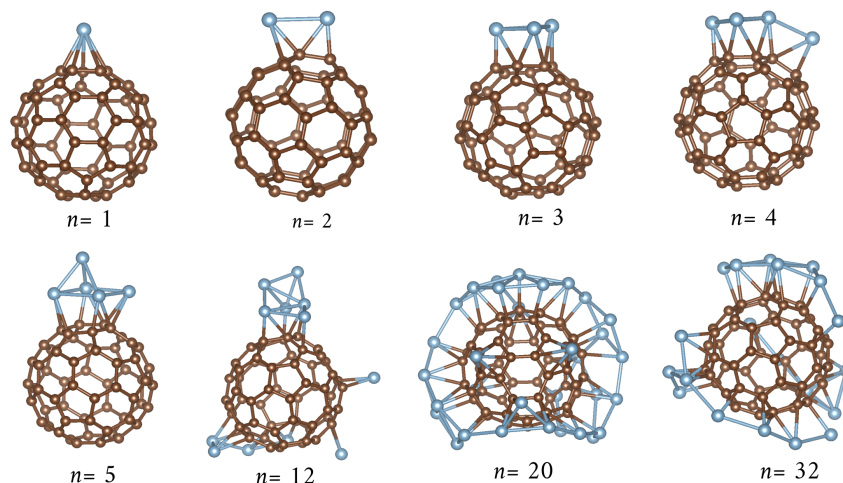


Figure 3.8: Selected configuration for aluminum (blue) with different coverage.

3.3.5

Aluminum

As we increase the number of Al atoms, covalent Al–Al bonds start to dominate and clusters are formed. Two Al atoms prefer already to be close to each other. One atom is at a P-site whereas the other atom prefers to be at H–H site. Four Al atoms form a patch whereas 12, 20 and 32 atoms, pack either in clusters, or patches located near H–H, H–P, or T sites, as shown in Fig. 3.8.

3.3.6

Single atom on the fullerene surface

To obtain further insights into the stability of decorated fullerenes, we summarized the energetically lowest binding site for a single atom on the surface of the fullerene which we observed above. We carried on this exploration also for 54 other elements. Fig. 3.10 shows the geometry optimized structures obtained with a single atom of AM, AEM and Al, Si, Sc, Ti, and Ge. We found that the AM (with the exception of Li) adopt the center of the hexagonal face as the lowest energy binding site. Lithium is the only element of this row with two degenerate sites. The calculated adsorption energy of a Li atom on the center of a pentagon or an hexagon site differs only by a few meV. A previous study reported very similar structures but a

different energetic ranking. This is presumably due to different exchange-correlation functionals employed. [100]

For the AEM family, only Be and Mg prefer to sit on the C–C bond (“bridge” site), whereas Ca, Sr and Ba are most stable on the hexagonal face. Other elements considered in this study, which prefer the “bridge” site are Si and Ge. Moreover, we found that a single Al atom prefers the pentagon site whereas a single Sc and Ti prefers the hexagonal site. The calculated electron localization function (ELF) at a value of 0.9 for all the systems is also shown Fig. 3.10.

Table 3.1 shows important properties for selected single atom-decorated C_{60} . Some trends are evident when comparing the adsorption site and the corresponding ELF (see adsorption values for each system). For instance, Be and Mg atom shows a lone pair electron and do not follow the behavior of the rest of their AEM family. Al, Si and Ge also display lone pair structures in their corresponding ELF. Especially for Na and K atoms the calculated adsorption energy is comparable to hybrid-functional (B3LYP) results. [120, 121] Single Be and Mg atoms occupy bridge-sites and are weakly adsorbed. The binding is probably weak due to the high ionization potentials of Be and Mg, that hinders the donation of metal valence s electrons to the fullerene. The adsorption energies for single atoms also correlate well with the ELF shown in Fig. 3.10. Higher adsorption energies imply higher stability and therefore lower total energy. Hence they are more likely to be accessible experimentally.

Fig. 3.9 shows the distance (y -axis) between a single atom of a certain type and the nearest carbon atom of C_{60} (green circles). The average C–C distance obtained after full geometry relaxation is also shown. It is interesting to observe some trends in the evolution of atom-carbon distance as function of the elements tested. The linear increase in distance between Li–, Ca–, Sr– and Ba–C can be explained by the increasing ionic radii for these elements. For other elements (Ti, Si, Ge), which are strongly bound to the fullerene, the distance of interaction shrinks to 2.1 Å. The distance of Sc, Y and La, also correlates well with the increase of their ionic radii. Be and Mg have a relatively large metal-carbon distance. This is simply due to their weak bonding energies, as described before. The elements, with a interaction distance greater than 2.5 Å (Na, Mg, Al, K, and Rb) have one unpaired electron and behave differently from the rest of the elements of the periodic table. It is noticeable that most of the d -block elements are found around the typical covalent distance lying between 2.0 Å to 2.4 Å.

3.3.7

ELF analysis for decorated fullerene

In the previous section, we have already given indication of the characteristic emerging for the different elements. More detailed information can be obtained by an ELF analysis. In particular the ELF analysis will allow us to predict whether the decorating atoms form a homogeneous distribution or undergo clustering or patching.

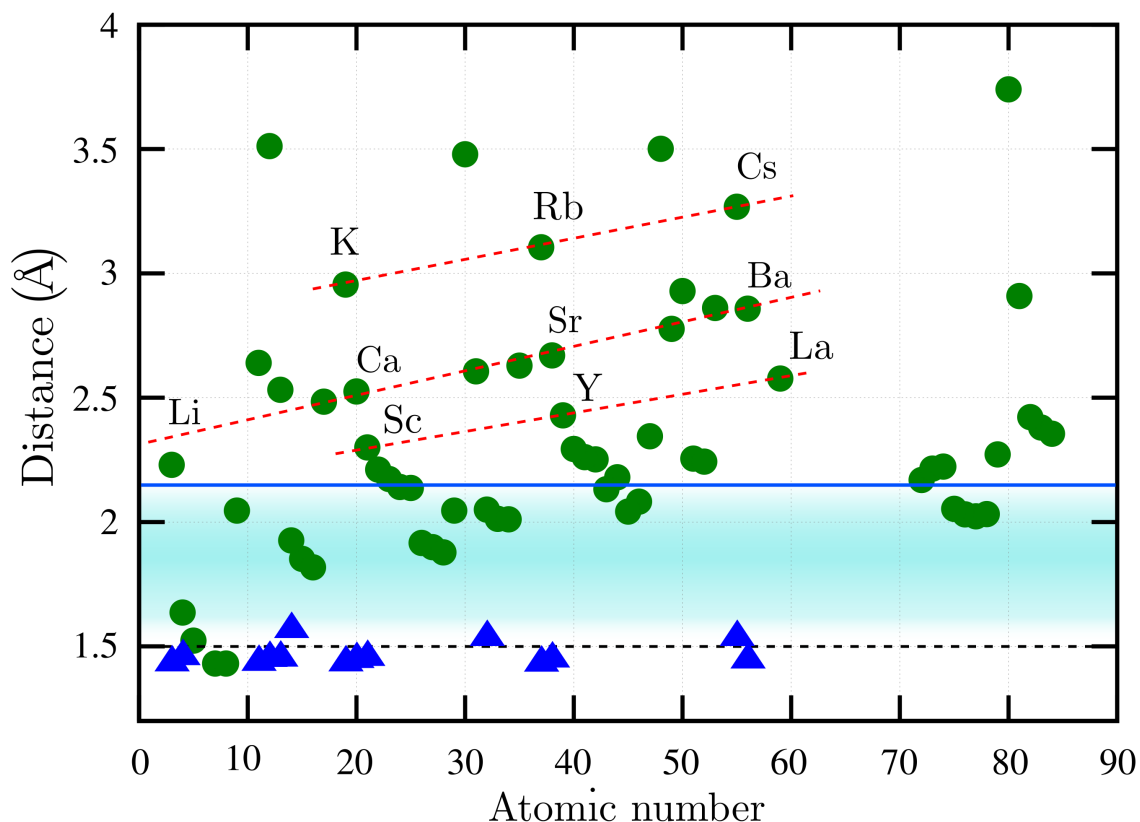


Figure 3.9: Trends in bond lengths for single atom decorating fullerenes. The green circles represent the distance between the probe atom and the nearest carbon atom of the C_{60} for 64 elements sorted by atomic number. The respective average C–C distance in C_{60} is shown for selected elements in blue-triangles. C–C distances do not deviate by more than 5% and remain thus close to 1.5 Å, the typical C–C distance in a isolated fullerene. Two major trends are: a linear increase in the bond lengths between the decorating atom and the closest carbon for Li, Ca, Sr and Ba and a constant length for Be, Si, and Ge. Note that these same elements also manifest lone electron pairs (see ELF). The typical covalent bond between C and different metals in metallo-organic molecules lies in the range of 1.5 Å to 2.2 Å. [1] Here it is represented by the shaded area in between the black dotted line at 1.5 Å up to the blue line line at 2.2 Å. Hence the elements which are homogeneously distributed over C_{60} have longer bond length than typical metallo-organic molecules.

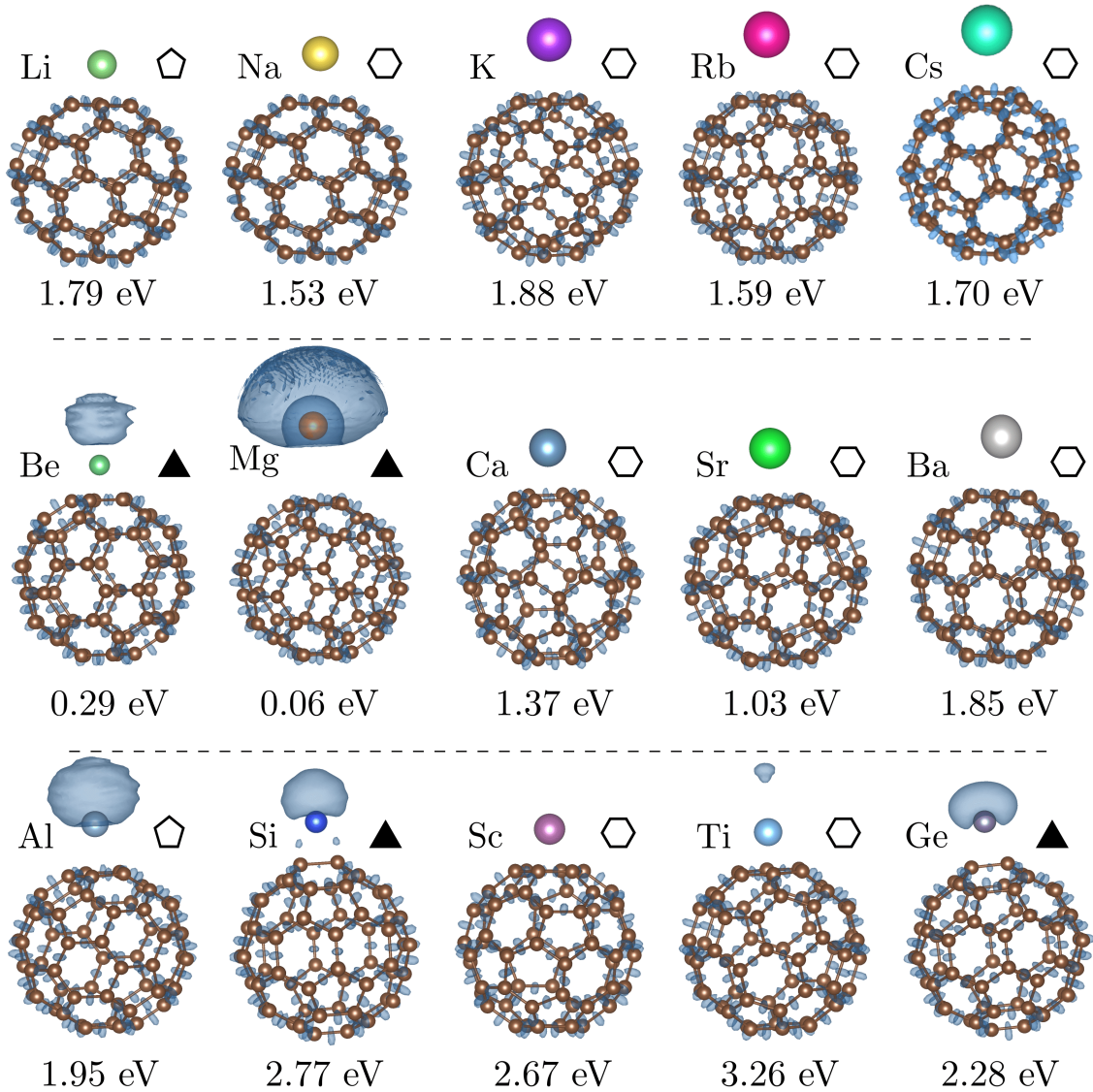


Figure 3.10: Different elements considered in this work: top row shows alkali metals, middle row alkaline-earth metals and bottom row other elements. The symbols next to the element symbol indicate the character of the energetically lowest adsorption site: (i) center of the hexagon (hexagon), (ii) center of the pentagon (pentagon) and (iii) On the C–C bond known as the “bridge site” (triangle). The calculated ELF at 0.9 for all the structures is shown for comparison (see text). For each structure the adsorption energy (E_{ads}) is also given.

Fig. 3.12 shows the different ELF volumes obtained for single atoms of different type on the surface of C_{60} . ELF values (η) vary from 0.5 for free electrons to 1 for a fully localized electrons. Values in the range 0.7–0.8 indicate a covalent bond character. The analysis of the topology of the electronic structure by bifurcation hierarchies has been successfully used in many other systems. [122, 123, 124] According to their nature, core and valence domains of bonding can be distinguished: core domain

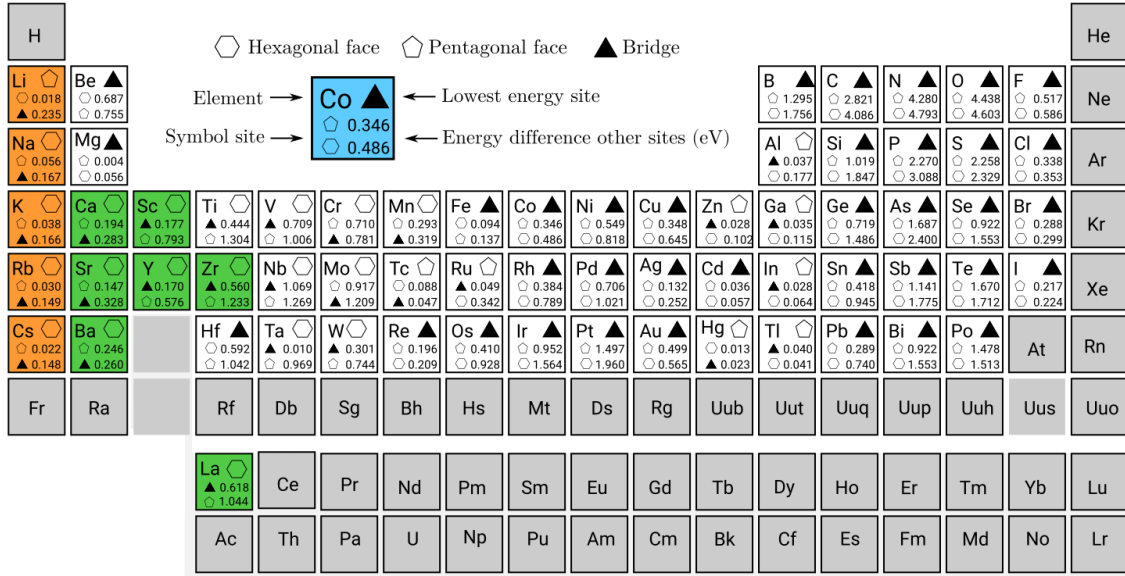


Figure 3.11: Periodic table chart summarizing elements that are likely to form homogeneous decorated distributions and have a maximum coverage on the surface. 2 main types of electronic behaviors (ELF) are marked apart from the rest of the elements and those are depicted in orange and green, corresponding respectively to b) and c) in Fig. 3.12. For each atom, the energetically lowest site is indicated together with the difference in energy for other sites.

denoted as $C(C)$ and $C(M)$ for carbon and considered atom, respectively. Valence domains $V(M)$ for atom on the surface or $V(C)$ for carbon fullerene. A valence overlap composed of both the carbon and the considered atom domains, is denoted as $V(C,M)$.

The periodic chart of Fig. 3.11 summarizes the results of the ELF analysis carried out for 64 different elements decorating the surface of C_{60} . Despite the widely varying different nature of the 64 elements, a large number of atoms share a quite similar behavior, and can be classified in three classes, that we will define. These classes are marked by different colors in Fig. 3.11. For each atom, the energetically lowest site is indicated together with the difference in energy to other sites. The vast majority of elements will seat on “bridge” (indicated with solid triangles) sites forming covalent interactions. Only the orange and green color coded elements are predicted to form homogeneous decorated distributions that have a maximum coverage on the surface.

Both the ELF and Bader (not shown) analysis for single atoms on C_{60} reveal two distinct and general behaviors:

- Atoms with either covalent or ionic bonding do not show any lone pair electron.
- Atoms that do form lone pairs electrons, weakly interact with the C_{60} .

From Fig. 3.10i, we observe that the elements which have a lone pair (*i.e.* Be, Mg, Al) also prefer to form clusters.

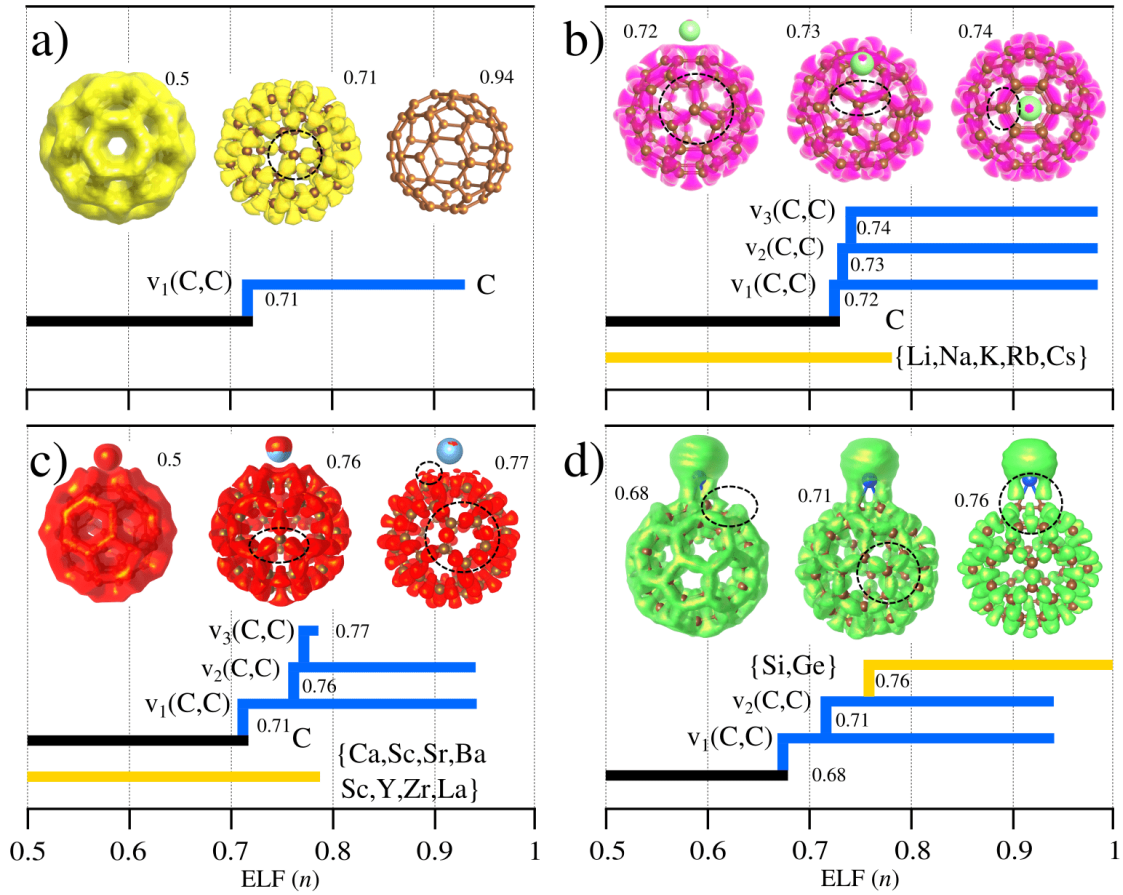


Figure 3.12: Electron localization function (ELF) analysis for different atoms: a) isolated C_{60} , b) AM, c) AEM and d) for covalently bonded atoms. In these plots, black lines depicts the single basin (volume) and when it bifurcated, it is represented by blue lines. Yellow lines show the corresponding ELF of the atom considered. Clearly different levels of bifurcation (bonding) are distinguishable via the ELF. Other atoms that follow these patterns are indicated.

Let us analyze in more detail what is different for AM and AEM from the rest of elements. In all panels in Fig. 3.12 the black solid line represents the main domain (continuous volume) and the blue lines are drawn only after a volume has bifurcated (discontinuous). Different bifurcations (blue lines) can be tracked and do correspond to the valence contributions (V_1 , V_2 and V_3). Yellow lines represent the atom probe on the surface of the fullerene. To further understand the bifurcation diagram, we should mention that the variation of η is simply a measure of the number of the pairing electrons participating in the bonding (here depicted as the ELF volume). The variation of η and consequently the volume variation, *i.e.* topology of the bonding, leading to either continuous or discontinuous volumes depending on the ELF values, represent an reliable indicator for the behavior of a given decorating atom type. In this way ELF can be used to classify the different elements into two classes that share similar behavior as decorating atoms and remainder.

- The first class comprises the alkali atoms Li, Na, K, Rb and Cs, (panel b. of Fig. 3.12). An ELF analysis of the alkali elements suggests that they form strong ionic bonds with C_{60} [125]. The orange part in the periodic table (Fig. 3.11) represents this class of atoms. The ELF volume splits at 0.72, 0.73, and 0.74 values of η , representing three different valence electron contribution for C–C bonds, respectively for ($V_1(C,C)$), ($V_2(C,C)$), and ($V_3(C,C)$). The first volume arises from the C–C bonds which are far from the alkali atom. The second bifurcation is ($V_2(C,C)$) which represents bonding between next nearest carbon atom and nearest carbon atom to the alkali atom. The valence basin ($V_3(C,C)$) is induced by nearest carbon atoms and the alkali atom.
- The second class comprises Ca, Sc, Sr, Ba, Sc, Y, La and Zr and is represented in green in the periodic table (Fig. 3.11). The ELF for these elements is characterized by three volume discontinuities at $\eta = 0.71$, 0.76 and 0.77. This implies a similar bonding pattern as in the case of alkali atoms, except that for these metals, the third discontinuity is localized in space only for small η -values. This feature is visible in panel c) of Fig. 3.12 for a value of 0.77 (small volumes are indicated by a circle on the top of the fullerene).
- The remaining elements shown in white in the periodic chart of Fig. 3.11 exhibit different ELF behavior, but share the property of not homogeneously distributing over the C_{60} surface.

Most of the p -block elements have similar ELF behavior and up to two elements can be accommodated on the C_{60} surface before they start to form cluster.

We also include as reference the diagram for carbon, panel (a) in Fig. 3.12). The ELF analysis shows only one main discontinuity in the volume, occurring at 0.71, which arises due to the purely covalent C–C bonding in the isolated fullerene.

3.3.8

Conclusions

Fullerenes, exohedrally decorated with the alkali metals, alkaline-earth metals and other elements, were studied in a systematic, unbiased fashion with a structure search algorithm at the density-functional level. Our exploration of the potential energy surface resulted in new putative ground states and low energy configurations for a large number of elements and for a varying number of decorating atoms. We determined in particular the maximum number of atoms that can homogeneously be distributed on the fullerene surface. The ELF analysis helped to understand the behavior of AM and AEM and other elements when decorating fullerenes.

By scanning the ELF of 64 elements, we were able to determine: Li, Na, K, Rb, Cs, Ca, Sr, Ba, Sc, Y and La as the sole elements that will favor homogeneous distributions. This picture explains the previous experimental findings for the elements Li, Na, K, Rb, Cs, Ca, Sr and Ba. And for elements on which experimental results are absent, we predict that Y, Sc and La should also homogeneously cover C_{60} .

3.4

Alkali atom decorated C_{60} in an external electric field

Electric dipole measurements provide a convenient way to determine the electronic and geometrical structures of metal decorated C_{60} [126, 127]. Structural changes induced by an electric field have been observed for various systems such as polycrystalline pentacene-based organic transistors [128], pentacene single crystals [129] and polar or non-polar molecules in a dodecahedral water cage [130]. Uncoated fullerenes are prone to structural changes in the gas phase in the presence of an electric field [131, 132].

Rayane *et al.* measured the polarizability and the permanent electric dipole moment of isolated KC_{60} molecules using molecular beam deflection [133]. Their results suggested that the polarizability of KC_{60} is induced by the free skating of the potassium atom on the C_{60} surface. Antoine *et al.* extended the work to different alkali decorated C_{60} 's [134]. They observed that the dipole moment increases steadily for the elements from top to bottom of the 1st column of the periodic table. A strong charge transfer between a single alkali atom and the C_{60} cage has been reported resulting in a large electric dipole moment. Dugourd *et al.* observed a high electric susceptibility of Na_nC_{60} (n is the number of Na atoms) [135]. The results were attributed to a high electric dipole arising from the aggregation of Na_n on the C_{60} . Antoine *et al.* also measured electric susceptibilities for Li_nC_{60} and Na_nC_{60} clusters containing up to $n = 20$ alkali atoms [99]. From the experimental data, they concluded that for more than seven Na atoms all atoms aggregate into a single cluster, whereas for Li not all atoms on C_{60} participate in such a clustering if more than 12 atoms are present.

Antonio *et al.* also explained their experimental results by using a parameterized many body force field in combination with basin hopping [71] to find the most stable structures for Li and Na decorated C_{60} [99]. However, the calculated electrostatic dipole moments for the previously known ground states for different n did not match with the experimental results. Rabilloud *et al.* computed the dipole moments of C_{60} structures decorated with a few Li and Na atoms at the DFT level [120]. By comparing the dipole moments with the experimental value, it was suggested that the configurations whose dipole moments are closer to the experimental values, might be present in the experiment, even though they are energetically higher than other structures.

In this section we present an unbiased PES scan for Li and K decorated C_{60} at the DFT level in the presence of an electric field. The wavelet basis set of the BigDFT code is highly suitable for such a calculation. One can use free boundary conditions which allow for a constant electric field throughout the simulation box. In addition the basis set is systematic and adapts itself fully to the distortion of the wavefunction induced by the electric field. In this way results of identical high quality can be obtained with and without electric field.

In previous work, we have observed that Li and K atoms prefer to homogeneously distribute over C_{60} up to 12 and 6 atoms respectively in absence of an external electric field [136]. For this reason we have limited the present PES scan to this maximum number of atoms.

3.4.1 Single Li, Na and K atom on C_{60}

From our previous calculations, we know that alkali atoms, except for Li, prefer to adsorb on the hexagonal site [136]. The potential energy surface can be altered by applying an external electric field and desired configurations can be stabilized. In the presence of a sufficiently strong electric field, the pentagonal site can however become energetically preferable as shown in Fig. 3.13.

Alkali atoms make strong ionic bonds with C_{60} acting as an electron donor for the C_{60} . The donated charge is strongly localized on the carbon that is closest to the metal atom. As the strength of the electric field increases, the positively charged alkali atom move in the direction of the electric field while the negatively charged C_{60} moves in the opposite direction. This increase in the distance between the positive and negative charge leads to a mainly linear increase of the dipole moment with respect to the field strength since the charges remain more or less constant as shown in Fig. 3.14.

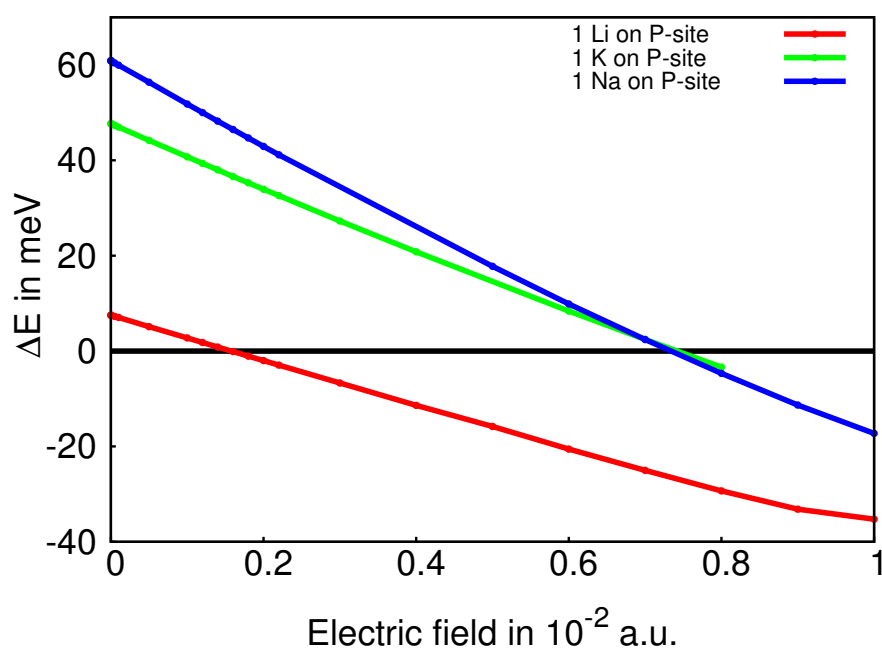


Figure 3.13: Energy of the pentagonal site with respect to the hexagonal site for one Li, K or Na atom on C_{60} as a function of the electric field strength. C_{60} .

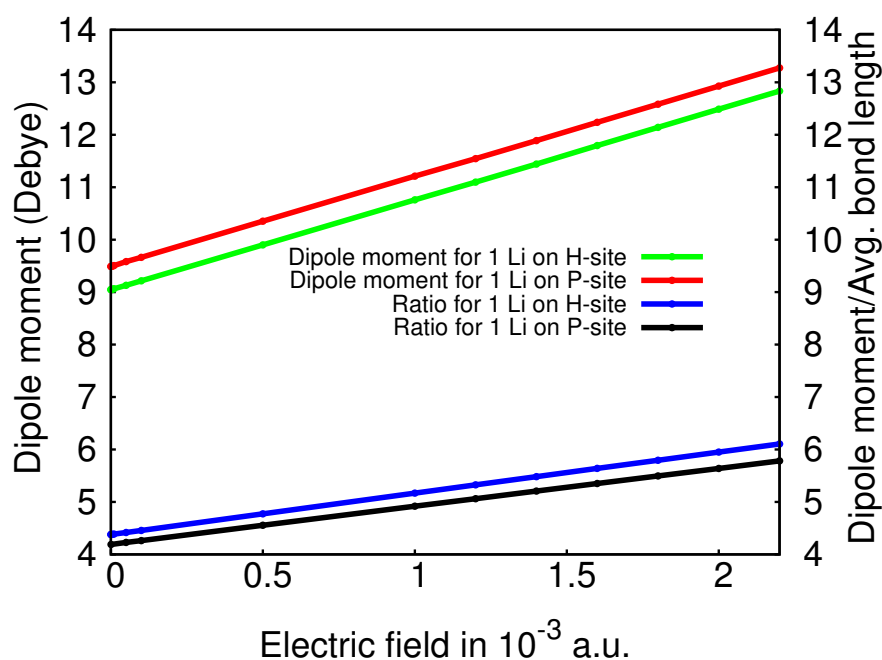


Figure 3.14: Dipole moment and the ratio of dipole moment and average bond length between the alkali atom and the carbon atom from the C_{60} vs electric field for one Li atom on the surface of a C_{60} .

3.4.2 Li and K on the fullerene surface

In this section, we provide further insight into the behavior of C_{60} 's decorated with more than one Li in the presence of an electric field. The number of atoms on the C_{60} surface is stepwise increased from 2 to 12 for Li and from 2 to 6 for K. The electric field used for these calculations was 5×10^{-5} atomic unit (a.u.) which is comparable to the strength of the experimentally applied electric field (7×10^2 V/m) [99]. We also performed another MH run with an electric field of 1×10^{-3} a.u. which corresponds to a strong experimental field reached for instance in the tip of a scanning microscope. We started our calculations with the lowest energy structure at zero electric field. Fig. 3.15 presents two energetically quasi degenerate meta stable structures in absence of an electric field. In one structure, one of the two Li atoms is on P-site (Fig. 3.15a) whereas both Li atoms are on H-site in the other structure (Fig. 3.15b). At low electric field (5×10^{-5} a.u.) they are still energetically degenerate. As we increase the electric field, the energy difference between these structures increases strongly (4th and 5th lowest energy structure of Fig. 3.16). A similar situation arises for more than two Li atoms.

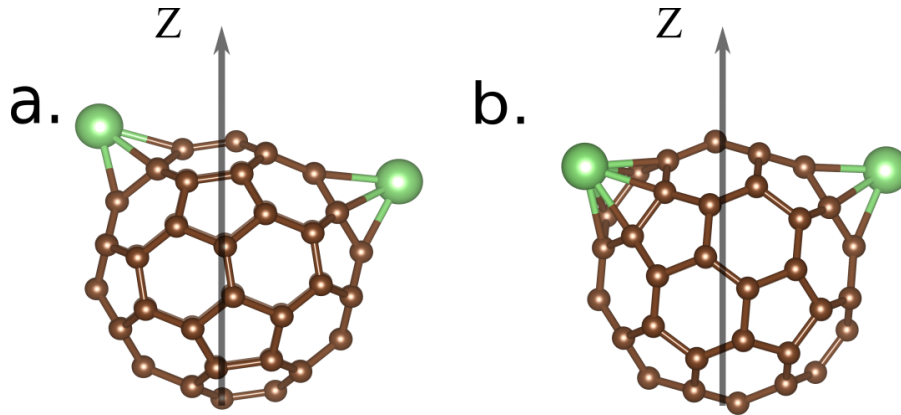


Figure 3.15: Two isomers (a. and b.) found for an electric field of 5×10^{-5} a.u.. The electric field is along the Z-direction.

To establish the energetic ordering of the structures as a function of the field strength, we relaxed the 20 lowest energy structures from minima hopping runs at different electric field strengths and first eight of them are plotted in Fig. 3.16. The two structures that were initially the lowest energy structures are not any more energetically favorable at a strength of 4×10^{-4} a.u. while other structures are lowered in energy.

Different energetic orderings at different electric field are also observed for more than 2 Li atoms on the C_{60} surface. In addition to the total energies E_{tot} calculated consistently in the electric field, we have plotted in Fig. 3.16, also the energies from

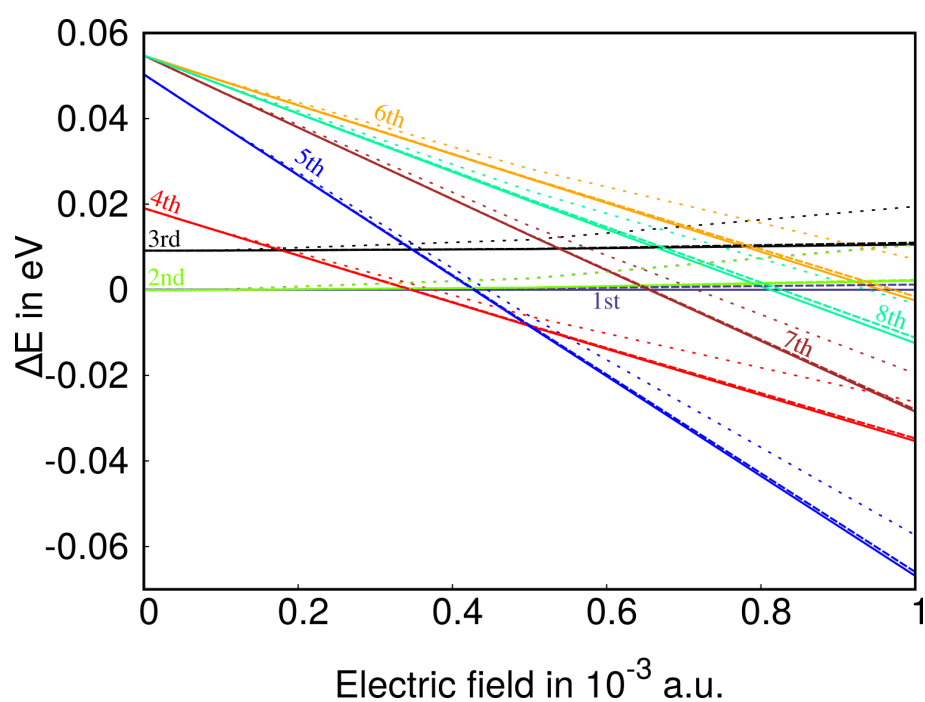


Figure 3.16: Solid lines show the energy of eight isomers Li_2C_{60} as a function of the applied electric field, whereas the dotted lines show their energies obtained from the first order perturbation theory and the dashed lines give their energies obtained from the second order perturbation theory. All energies are calculated with respect to the lowest energy structure at zero electric field.

first and second order perturbation theory which are given by,

$$E = E(\mathcal{E} = 0) - \sum_i P_i \mathcal{E}_i - \frac{1}{2} \sum_i \sum_j \alpha_{ij} \mathcal{E}_i \mathcal{E}_j \quad (3.2)$$

where \mathcal{E} is the applied electric field, P_i and α_{ij} are the static dipole moment and polarizability respectively and $E(\mathcal{E} = 0)$ the energy of the system without electric field. At low electric field the dotted and solid lines overlap, but at higher electric field strengths they deviate, showing that first order perturbation theory cannot predict the correct energetic ordering for strong experimental fields. This is because the change in dipole moment is not considered. As we add the second order perturbation term to the energy, the energies almost overlap with the actual energy. This shows that the second order variation in energy due to the first order variation of the dipole moment (i.e. linear polarizability term) is necessary for an accurate description of this system in the strong electric fields.

The dipole moments for different numbers of Li atoms are plotted in Fig. 3.17 for a field strength of 5×10^{-5} a.u. The experimental values [99] are intrinsically Boltzmann averages over low energy configurations whereas the theoretical value is only obtained from the lowest energy configuration, because it would be computationally too expensive to calculate the energies of a large number of structures for many different field strengths. If there is an energetically degenerate state for a particular number of Li atoms, we have taken the one with the highest dipole moment. In contrast to the experimental results which were obtained at room temperature, our results are at zero temperature, since it would also be computationally too expensive to calculate the required large number of free energies. In spite of these differences between the experimental and theoretical dipole moments, Fig. 3.17 shows similar trends such as a peak of the dipole moment for six Li atoms.

In order to study the stability of some selected configurations at finite temperature, we calculated free energies. We calculated in the standard way [137] the vibrational frequencies ω_i and the zero point energy E_{ZP} to obtain the free energy F

$$F = E_0 - E_{ZP} + k_B T \sum_i \ln[\exp(\frac{\hbar \omega_i}{k_B T}) - 1] \quad (3.3)$$

Fig. 3.18 shows that the lowest energy structure at zero temperature is still lowest in energy at room temperature and highly populated. There is however a high probability of populating the higher energy structures (Fig. 3.19).

The dipole moment for fifth and sixth configuration is quite high (~ 10 Debye). These structures will be present during the measurement of dipole moment at room temperature and contribute to the total dipole moment. In Fig. 3.20, we have calculated the total dipole moment as a sum of the dipole moments of different structures weighted by their Boltzmann probability factors. As we include more isomers the total dipole moment tends towards the experimental value (10.2 Debye) at room temperature. Reproducing exactly the experimental value is however illusive

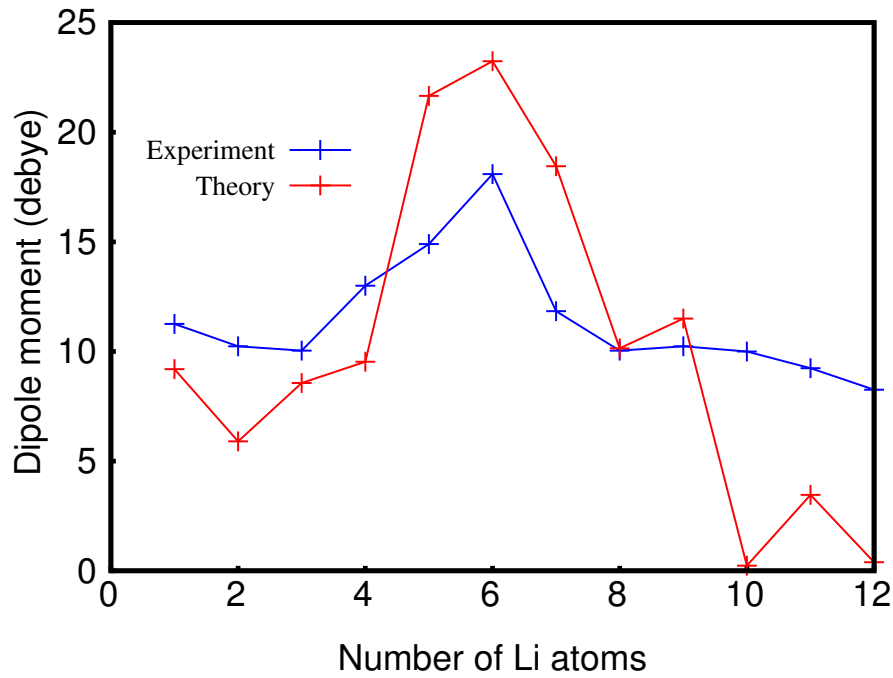


Figure 3.17: Theoretical and experimental [99] dipole moments for the lowest energy structure for different number of Li atoms decorated C_{60} . The experimental data is obtained from the article by Antonio et. al. [99]. For theoretical calculation, the applied electric field is 5×10^{-5} a.u. and for experiment, 3×10^{-5} a.u.

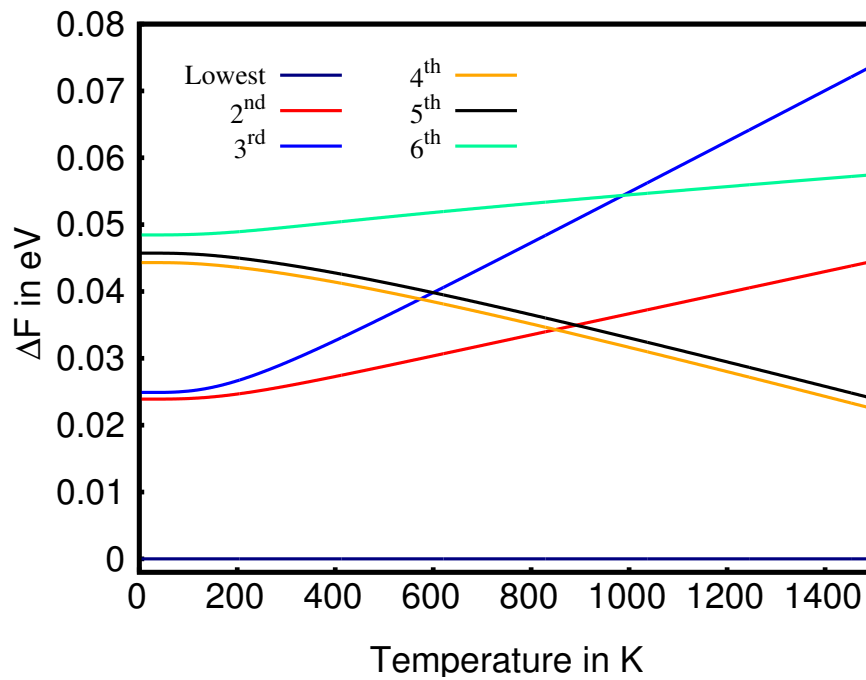


Figure 3.18: The free energy for the six lowest energy configurations. The free energies are plotted with respect to the energy of the lowest energy configuration at 0 K. The applied electric field is 5×10^{-5} a.u.

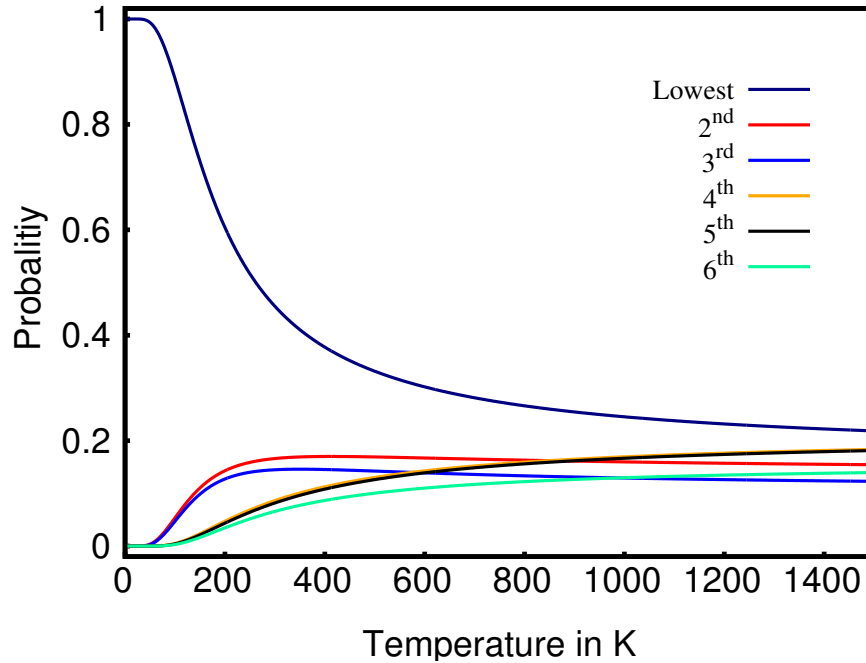


Figure 3.19: The normalized Boltzmann factors as a function of temperature for the six low energy configurations. The applied electric field is 5×10^{-5} a.u.

since the intrinsic errors of density functional theory are larger than $k_B T$ at room temperature and hence it is not possible to obtain reliable Boltzmann probabilities.

C_{60} does not have double bonds within the pentagonal rings. Hence one electron is missing to obtain an additional stabilization by aromaticity. As a result, C_{60} behaves like an electron deficient alkene and readily reacts with electron rich species. The estimated electron affinity and ionization potential values for C_{60} are 2.7 eV and 7.8 eV respectively [138]. The neutral C_{60} can take six extra electron to achieve higher aromaticity. Even additional six electrons can be accommodated [139]. Such a C_{60}^{n-} (where $n=2,3,4$) structure is short lived [140, 141], but can be stabilized by $n Li^+$ [120, 142]. This explains the experimentally observed [143] and theoretically confirmed [136] homogeneous absorption of up to 12 Li atoms on C_{60} . Hence, to alter this distribution pattern, a high electric field is required. The configurations that are provided in our previous work [136] are the most stable configurations up to a field strength of 1×10^{-3} a.u. for Li_4 and 3×10^{-3} a.u. for Li_6 and Li_{11} . For even stronger fields the Li atoms are detached from the C_{60} , but clustering is never observed.

The PES of the K atom decorated C_{60} slowly changes with an increasing electric field. Table 3.3 contains the energy ordering for the first 10 lowest energy structures of K_2C_{60} at different electric fields. The lowest energy structure which is observed at very low electric field is different from the lowest energy structure in the absence of an electric field. As the number of K atom is increased, the structures are even more stable and require high electric field to alter the energy ordering for example

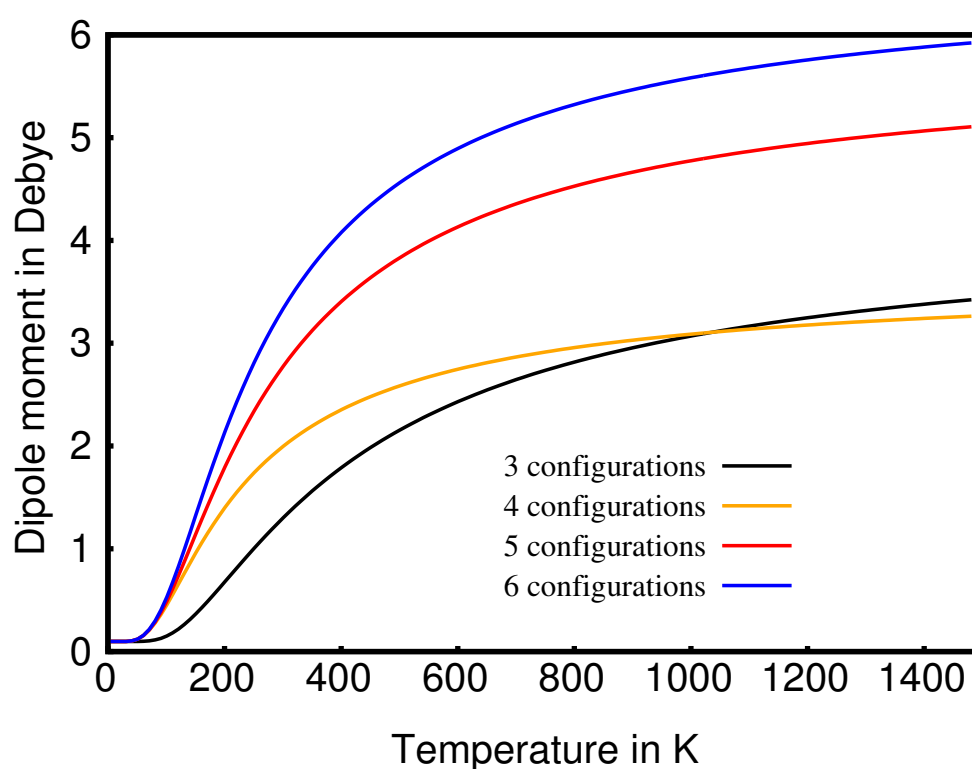


Figure 3.20: The dipole moment of the system at different temperatures obtained by weighting the dipole of the individual structures by their Boltzman factor. The applied electric field is 5×10^{-5} a.u.

for K_6C_{60} , the PES alters at the electric field of 1×10^{-3} a.u.

Table 3.2: Dipole moment of the lowest energy structure for different number of K atoms decorated C_{60} . The applied electric field is 5×10^{-5} a.u.

Number of K-atoms	1	2	3	4	5	6
Dipole moment (Debye)	15.38	10.19	5.73	0.35	11.09	0.21

Table 3.3: Energy of the first 10 K_2C_{60} structures at different electric field. The energies are given with respect to the lowest energy structure at that particular electric field in eV.

Structure ordering	$5.e10^{-5}$ a.u.	$1.e10^{-4}$ a.u.	$5.e10^{-4}$ a.u.	$1.e10^{-3}$ a.u.
1	0.000	0.0371	0.055	0.096
2	0.009	0.074	0.000	0.000
3	0.019	0.097	0.107	0.221
4	0.021	0.104	0.139	0.289
5	0.068	0.000	0.106	0.028
6	0.068	0.000	0.107	0.026
7	0.072	0.095	0.113	0.127
8	0.088	0.164	0.158	0.252
9	0.119	0.201	0.263	0.438
10	0.138	0.201	0.179	0.208

In Table 3.2, we have shown the dipole moment of the lowest energy structures of K decorated C_{60} at the electric field of 5×10^{-5} a.u. Our calculated dipole moment for one K atom on C_{60} is 15 Debye in an electric field of 5×10^{-5} a.u. The arrival time distribution (ATD) profile with an electric field of 1.5×10^7 V/m is in good agreement with the profile simulated for a permanent (and rigid) dipole moment of 17.7 Debye which is very close to the theoretical value [133]. If we increase the number of K atoms, many energetically degenerate structures appear as we increase the applied electric field (Table 3.3). We have not found the experimental dipole moment for C_{60} with more than one K atom in the literature.

3.4.3

Conclusions

We have explored the PES of Li and K decorated C_{60} in the presence of electric fields of varying strength by an unbiased search method at the DFT level. The experimental field strengths, that can for instance be obtained near the tip in a scanning microscope, induce considerable changes of the PES and alter the energetic

ordering of C_{60} isomers decorated with a small number of metal atoms. Some structures which are metastable in absence of an electric field can become ground states by varying the strength of the electric field. In this way one can switch between two structures by increasing or weakening the electric field. A correct calculation of measured dipoles requires to use all those configurations which are the lowest in energy at the given electric field. Since these configuration are frequently virtually degenerate in energy, several configurations can make significant contributions to the dipole moment. Accurate results in strong experimental fields cannot be obtained by perturbation theory but require a fully self consistent electronic structure calculation for the given field strength.

3.5 Decorated $C_{48}B_{12}$ hetero-fullerene

Among the fullerene based structures, the boron substituted fullerene $C_{48}B_{12}$ was predicted theoretically by Manna *et al.* [144]. This structure was constructed by substituting 12 C atoms by B atoms homogeneously in the fullerene such that there are no B-B bonds. This structure will be referred to as “diluted” $C_{48}B_{12}$ in the following. However, in an unbiased minima hopping (MH) structure prediction Mohr *et al.* found a patched configuration, where all the B atoms are close together in a two-dimensional patch, that is considerably lower in energy than the homogeneously distributed arrangement [145]. This structure will be referred to as a “patched” configuration.

Based on DFT calculations, metal decorated $C_{48}B_{12}$ has recently been predicted to have superior H_2 adsorption capabilities compared to pure $C_{48}B_{12}$. Through a systematic search, Sun *et al.* found that that 12 Li atoms that are homogeneously distributed on the surface of the fullerene form the most stable configuration [146]. Gao *et al.* constructed two microporous frameworks consisting of organic linkers and exohedral metallofullerene nodes. They showed through the calculation that the both frameworks can store H_2 with a gravimetric density up to 8–9.2 wt % [147]. The patched configurations was not considered as a basic unit in this study. Zhao *et al.* reported that a structure, that is homogeneously coated with 12 Sc atoms, is stable and also suitable for H_2 adsorption but no structural stability search was performed [148]. Er *et al.* found that homogeneously distributing 6 Ca atoms on the fullerene is stable with respect to decomposition into the fullerene molecule and Ca bulk metal [149]. Most recently a similar study was conducted by Qi *et al.* on the same 6 Ca atom decorated diluted configuration to study the hydrogen uptake mechanism [150]. Lee *et al.* constructed a few hand made structures by adding 6 diluted Be atoms on the surface and they concluded that homogeneously distributed Be atoms on $C_{48}B_{12}$ give rise to the most stable configuration [151].

In these studies of metal decorated $C_{48}B_{12}$, two major factors were overlooked: (a) only diluted structures were decorated with different elements whereas the patched structure, that is lower in energy by 1.8 eV, was not considered and (b) the inves-

Table 3.4: Largest adsorption energies (E_{ads}) for different types of decorating atoms

Type of Structure	E_{ads} in eV			
	Li	Be	Ca	Sc
Patch	3.20	3.41	3.62	5.28
Dilute	2.88	2.66	2.89	4.22

tigated structures were obtained through chemical intuition and local relaxation. Without knowing the true ground state of these systems, it has been conjectured that they are good for hydrogen adsorption. A thorough unbiased search of the PES is necessary to obtain reliable conclusions on their stability and their resulting capacity for hydrogen storage.

3.5.1 Results and discussion

Using the Minima Hopping Method (MHM) [14], we performed a comprehensive structural search, decorating both diluted and patched C₄₈B₁₂ fullerenes. Almost in every case (except for Li), the ground state structure was massively distorted by the decoration and the metal decorated patched configurations are much lower in energy than their diluted counterpart. This is in contrast to C₆₀ whose structure remains stable under decoration as was previously shown [136].

We first adsorbed single atoms on both diluted and patched configurations. There are 8 possible sites to adsorb a single atom on the diluted configuration and 10 on the patched configuration. We have considered all of them and report the largest adsorption energy in Table 3.4. The adsorption energy of n decorating atoms on C₄₈B₁₂ is calculated by the following equation:

$$E_{ads} = E_{C_{48}B_{12}} + n \times E_{atoms} - E_{n_{atom}C_{48}B_{12}} \quad (3.4)$$

For the diluted configuration, single Be, Ca and Sc atoms prefer the hexagonal site which has two neighboring boron atoms. A single Li atom prefers the hexagonal site where the hexagon has a single boron atom. For the patched configuration, Be atoms prefer the pentagon site with 3 neighboring borons, Li prefers the hexagon site with one boron, Ca prefers the hexagon site with two borons and Sc prefers to be on top of boron when boron is in the middle of a hexagonal site with four neighboring boron atoms.

We next present our results for the cases where the C₄₈B₁₂ fullerene is decorated with several metal atoms, namely 12 for Li and Sc and 6 for Ca and Be. Fig. 3.21 summarizes the results.

A structure consisting of six Be atoms which are homogeneously distributed on C₄₈B₁₂ was proposed as a good H absorber [151]. MH runs revealed that even for the diluted fullerene cage there are many different structures which are lower in

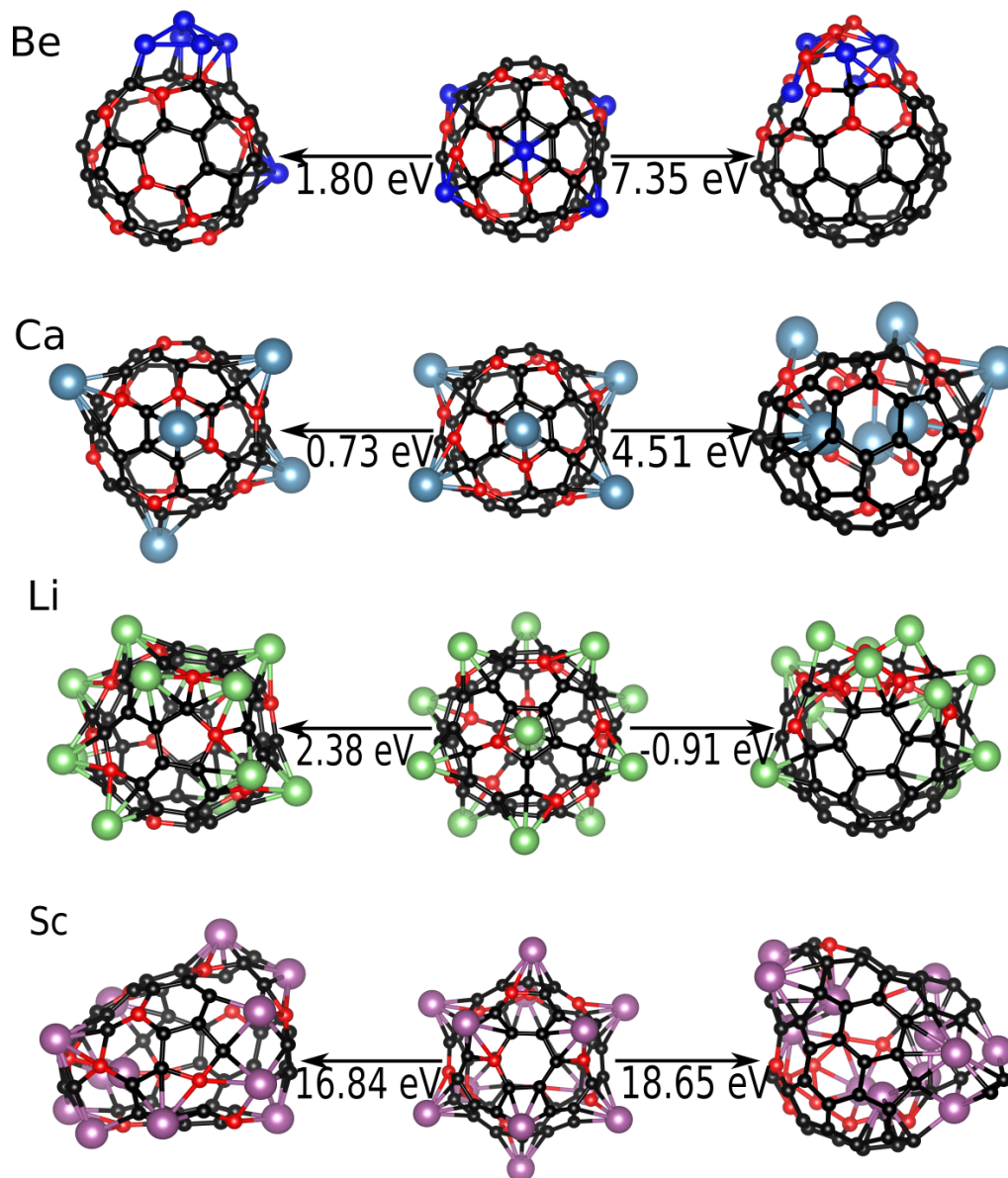


Figure 3.21: The Lowest energy structures for diluted and patched configurations for Be, Ca, Li and Sc decorated $C_{48}B_{12}$. The column in the center shows the previously predicted structures. The column on the right the lowest energy structures for decorations of the diluted fullerene and the left column the lowest energy structures for the patched fullerene. The energy difference is given with respect to the middle structure for each type of decoration. It shows that for all types of atoms except Li the patched configurations are the most stable ones.

energy than this previously proposed one. We observed that the most of the Be atoms form lusters and that a single Be atom prefers to stay on an hexagonal-site far from the Be-cluster. The underlying diluted fullerene structure is however not destroyed by the decoration.

Even lower energy configurations can be obtained if one decorates the patched fullerene structure. The patched configuration is broken during the MH runs and a few of the Be atoms go inside the $C_{48}B_{12}$. This suggests that though the patched configuration is more stable than the diluted configuration, it is more reactive to Be atoms.

The hitherto known lowest energy structure consists of 6 homogeneously distributed Ca atoms on the H-sites of the diluted configuration [149] [150]. We found a new structure based on a diluted fullerene that is 0.73 eV lower than the previously predicted configuration. In contrast to C_{60} , where the Ca atoms form a patch [136] they remain homogeneously distributed on the dilute $C_{48}B_{12}$. The patched configuration with clustered Ca atoms is however also in this case by far the lowest in energy. In these configuration some Ca atoms again enter into the cage of the patched fullerene.

Zao *et al.* proposed a configuration where 12 Sc atoms are homogeneously distributed over surface of the dilute $C_{48}B_{12}$ as the most stable configuration [148].

For the Ca decorated dilute $C_{48}B_{12}$ configuration, we have again observed several lower energy configurations than the previously predicted configuration. In the lowest energy configuration the diluted $C_{48}B_{12}$ the cage structure is broken and a few Sc atom went inside the cage, resulting in a drastic energy lowering.

Similarly, in the patched $C_{48}B_{12}$ configuration decorated with Sc, the cage gets partially destroyed. This configuration is again the lowest one.

12 Li atoms regularly distributed on the P sites of the diluted $C_{48}B_{12}$ structure were proposed to be most stable configuration [146]. The energy can however be lowered by distributing the Li atoms in a more random way, resulting in some Li-Li bonds. This was the lowest energy configuration found in our study. Decorations of the patched $C_{48}B_{12}$ fullerene resulted in this case in higher energy configurations. So decoration with Li atoms stabilizes the diluted configuration.

3.5.2 Conclusion

In conclusion, we have shown that the ground state of different metal decorated boron-carbon heterofullerenes is fundamentally different from previously published structures [149, 146, 148, 151]. The metals considered in our study are not able to homogeneously coat the dilute $C_{48}B_{12}$ cage. With the exception of Li, the decoration actually destroys the cage. The bonding character in all these configurations is quite complicated and there is no simple rule available to predict the type of distribution of different elements on the $C_{48}B_{12}$ surface. Our results give also valuable information

for experimental synthesis efforts of such heterofullerenes. Our investigation reveals that most previous computational studies on metal atom decorated fullerenes for hydrogen storage are based on unrealistic structures.

Application to silicon based fullerene

4.1 Introduction

Carbon-based nanostructures, like trans-polyacetylene, graphene, bucky tubes, and more, are very common in the realms of nanoscience [152, 153, 154]. Similar structures do exist for Si as well, like linear polysilanes, silicon nanosheets and nanotubes [155, 156]. Therefore it does not come as a surprise that the discovery of C_{60} triggered the quest for analogous Si structures. The chemistry of C and Si is not identical, anyway: while carbon atoms can readily adjust their valence states to participate in single, double and triple bonds, silicon strongly prefers sp^3 hybridization and single bonds. Therefore, although C_{20} is the smallest stable fullerene structure, quantum chemical calculations predict Si_{20} fullerene to be highly unstable [157].

The stability of a cage structure can be enhanced by modifications aimed at fulfilling the valence of the silicon atoms. One possibility is endohedral doping with a metal atom, due the nearly ideal size of the Si_{20} cluster cavity [158]. However for most $M@Si_{20}$, this strategy fails [29]. A second approach is to exohedrally bond the silicon atoms; with this method, the dodecahedral configuration has been identified as the global minimum of $Si_{20}H_{20}$ [159, 160]. The third, hybrid approach is a combination of both ideas, which would lead to a stable $X@Si_{20}H_{20}$ where X =metal/(halide) [161, 162, 163]. It is observed that the combination of metal and hydrogenated Si interaction is significantly weaker than the metal-encapsulated silicon cages $M@Si_{20}$ [164]. It is also predicted that the halide ions, especially Br^- , should be ideally suited to the synthesis of $Si_{20}H_{20}$ [162]. In contrast to the theoretical findings, no experimental data is present for this compound (Si_{20} , $Si_{20}H_{20}$,

$\text{M}@\text{Si}_{20}$ etc.) to the best of our knowledge. Nonetheless, the Si_{20} dodecahedron is a recurring structural motif within the expanded covalent frameworks of face-sharing polyhedra in the silicon clathrates M_8Si_{46} and $\text{M}_x\text{Si}_{136}$ (M = alkali metals; $x \leq 24$) [165, 166]. These alkali-metal doped clathrates are accessible through thermal treatment of the corresponding Zintl phases and MSi in an inert atmosphere [167]. In this chapter we present two different studies related to the stability of Si based fullerene (Si_{20}) configurations decorated with different elements.

The dodecahedron of $\text{Si}_{20}\text{H}_{20}$ has long been known to be the energetically most stable structure among the possible configurations but it has never been experimentally observed. In section 4.2,¹ we investigate the complexity of the reaction pathways and the configurational entropy of the cluster as the reason behind the inaccessibility of the global minimum. To propose a solution, we employ a fingerprint distance (FP)- based exploration of the PES of $\text{Si}_{20}\text{H}_{20}$, using a recently developed method [36, 37], and we compare it to an analogue calculation on the C_{60} fullerene and $\text{C}_{20}\text{H}_{20}$ fullerene.

Recently, Tillmann *et al.* stabilized Si_{20} fullerene with Cl^- core and eight chloro substituents and twelve trichlorosilyl groups on the surface [168]. In section 4.3, we investigate the structural stability with an unbiased and systematic global geometry optimization method within density-functional theory. We have provided reasons for the stability of the symmetric configuration of $[\text{Si}_{32}\text{Cl}_{45}]^-$. We have also shown that $[\text{Si}_{32}\text{Br}_{45}]^-$ is more stable than $[\text{Si}_{32}\text{Cl}_{45}]^-$.

4.2 Synthesis of $\text{Si}_{20}\text{H}_{20}$

Despite experimental efforts, the dodecahedron configuration of $\text{Si}_{20}\text{H}_{20}$, that is the most stable configuration calculated on the PES, has not yet been observed. Moreover, structurally similar $\text{C}_{20}\text{H}_{20}$ has been synthesized more than two decades ago [169, 170]. However, the synthesis procedure for $\text{C}_{20}\text{H}_{20}$ is extremely complicated and consists of 23 reaction steps [169]. It is not plausible to synthesize $\text{Si}_{20}\text{H}_{20}$ with the same procedure because the chemistry of silicon does not permit some of the possible intermediates.

To propose a solution, we employ a fingerprint distance (FP)- based exploration of the PES of $\text{Si}_{20}\text{H}_{20}$, using a recently developed method [36, 37], and we compare it to an analogue calculation on the $\text{C}_{20}\text{H}_{20}$ and C_{60} fullerene. The similarities and differences between the PES of the two systems are used to discuss why the global minimum is observed only for $\text{C}_{20}\text{H}_{20}$ and C_{60} .

¹D.S. De, B. Schaefer and S. Goedecker "The decahedral $\text{Si}_{20}\text{H}_{20}$ cage - where Levinthal's arguments do not lead to a paradox, but describe reality is under evaluation."

4.2.1 Co-relation between DFT and DFTB

The characteristics of an energy landscape are ultimately the key to understand the stability of a particular configuration, by providing the relationship of all the minima through their transition states (saddle points of the PES). Such a complete exploration of the PES is prohibitively expensive if performed at the DFT level for $\text{Si}_{20}\text{H}_{20}$, but it is feasible using DFTB. The similarity between the two levels of theory for 2000 structures of $\text{Si}_{20}\text{H}_{20}$, exemplified in Fig 4.1, suggests that we can use the DFTB energies as a fairly precise approximation of the DFT energy and of its PES. Fig 4.1 shows the correlation plot between DFT and DFTB energies for the lowest energy structures of $\text{Si}_{20}\text{H}_{20}$. Since the trends are similar, we have explored the PES at DFTB level.

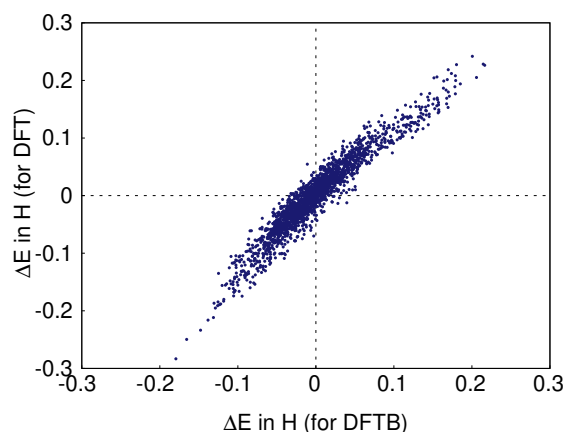


Figure 4.1: Correlation plot between DFT and DFTB energies of $\text{Si}_{20}\text{H}_{20}$.

4.2.2 Disconnectivity graph

We use disconnectivity graphs to visualize the energy landscapes, based upon samples of pathways linking local minima via transition states. Approximated, FP-based disconnectivity graphs are created according to a methodology recently introduced [36] based on fingerprint distances. The basic theory of fingerprint distances is given in the appendix C. It was noted that uphill barrier energies of transition states between directly connected minima tend to increase with increasing structural differences, that are directly quantifiable by a fingerprint distance between the two states. Such an observation allows to obtain qualitative topological information on a PES by post-processing trajectory data already available from MH runs, at a negligible additional cost. An FP-based disconnectivity plot was found to be a good representation of the computationally expensive explicit sampling of transition states in several cases, including Lennard-Jones, Si, NaCl and Au clusters [36].

4.2.3 Potential energy surface of C_{60}

In this section, we apply the idea of the FP-based disconnectivity graph to the PES of the C_{60} fullerene, whose PES has been analyzed in detail at several levels of theory [86, 171], and compare it to exact results. After this validation, we compare the topography of the C_{60} and $\text{C}_{20}\text{H}_{20}$ PES with that of $\text{Si}_{20}\text{H}_{20}$, to understand how their differences influence the journey of the cluster towards its most stable configuration. Previous studies found that the disconnectivity plot for C_{60} is of the weeping willow type, indicating that it is a structure seeker at high temperatures [86]. To construct the approximate FP-based PES represented in Fig 4.2 we considered 50,000 different C_{60} configurations, with almost all structures visited at least twice in a MH run. Multiple findings of the structures suggest a good sampling of the configurations within the energy range of interest. We did not constrain the search to include only structures connected through pyracylene rearrangements [172]: our set contains also structures with heptagonal and tetragonal carbon cycles. Previous simulations strongly suggest the role of such configurations in fullerene formation [173, 174].

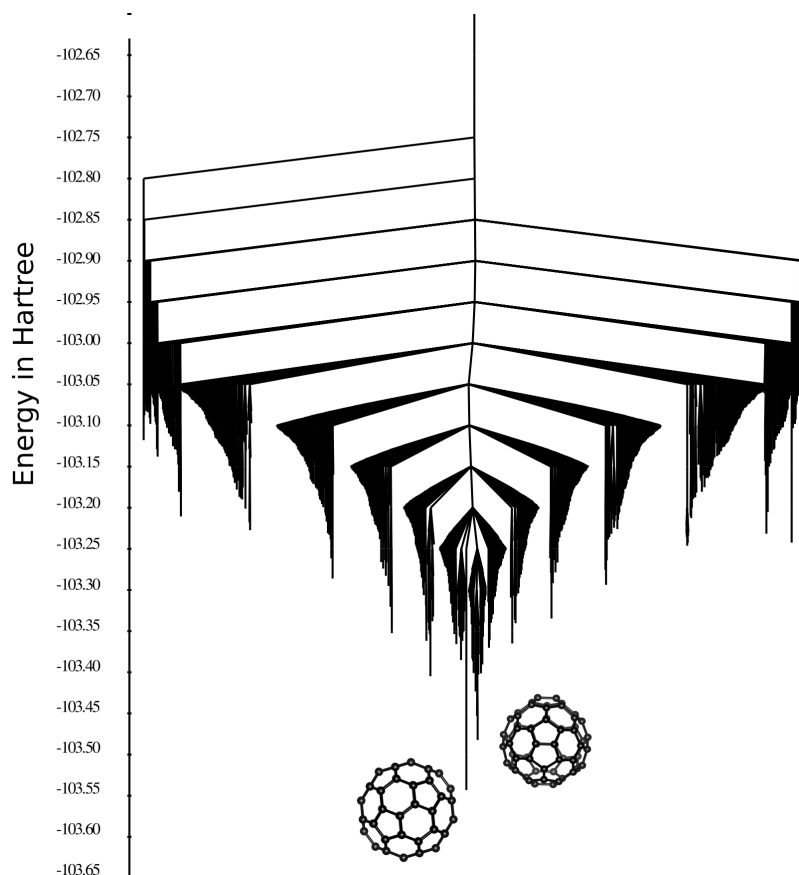


Figure 4.2: Disconnectivity plot for C_{60} from the approximate method.

The lowest total energy barrier of the pathway obtained through a trajectory-based connectivity database is shown for C_{60} to be a good approximation of the literature

value [175, 86]

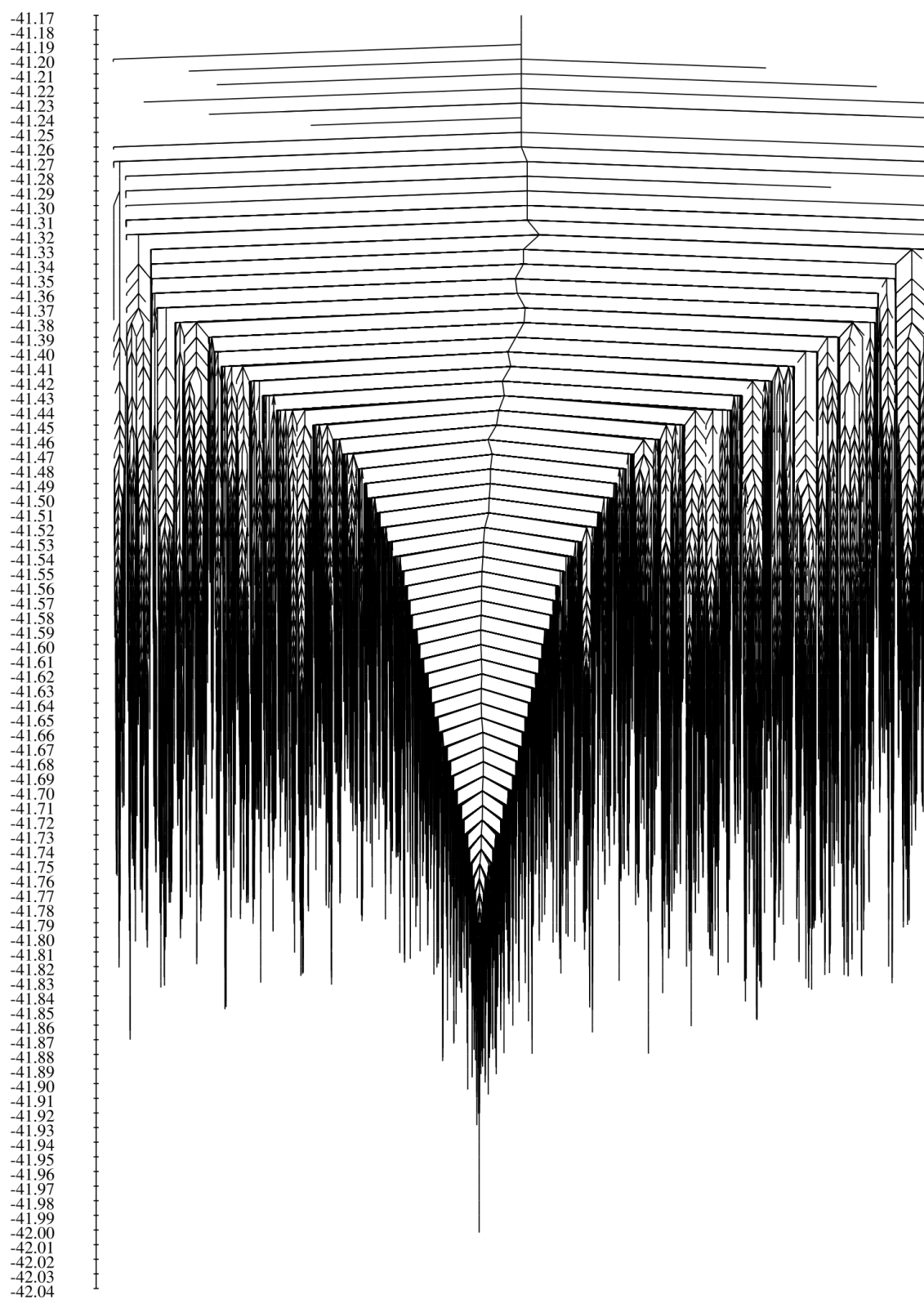


Figure 4.3: Disconnectivity plot for $C_{20}H_{20}$ from the approximate method.

The barrier height obtained from MHGPS between the ground state and the second lowest minimum (a structure with one Stone-Wales (SW) defect) is ≈ 0.25 Ha (6.7 eV), which is comparable with previous observation at DFTB level. However, previous studies suggests that an underestimation of barrier heights by empirical and some semiempirical interaction potentials is possible [86, 171]. With the approximate method, the barrier height is ≈ 0.32 Ha (8.64 eV), comparable with previous DFT results (7.3 eV) (Fig 4.4) [171].

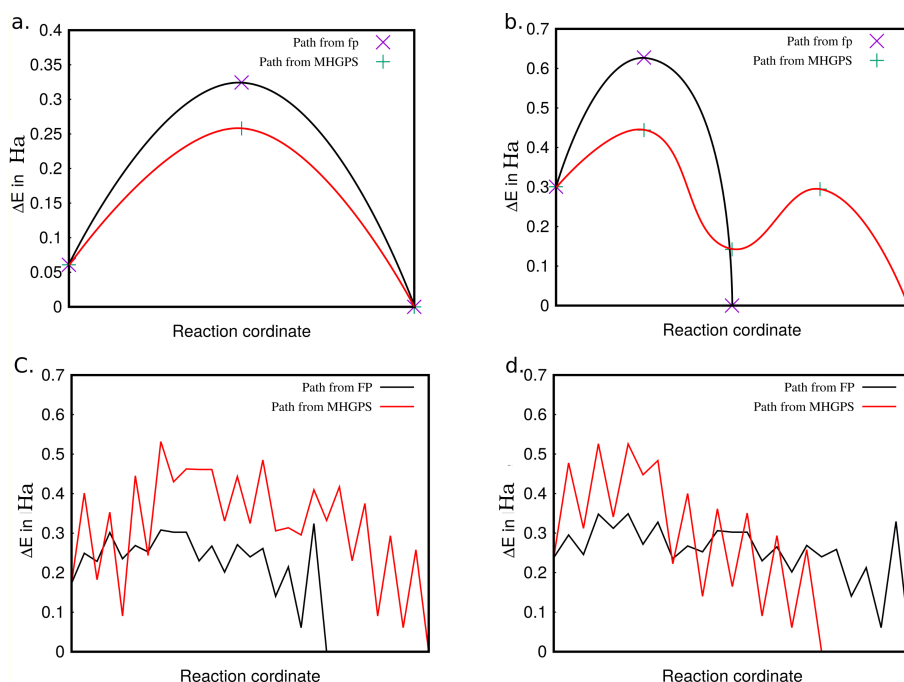


Figure 4.4: Comparison of the calculated pathways using the MHGPS method and the FP-based method

The topography of the PES of C_{60} does not have the characteristics that are associated with a readily obtainable minimum [176]. It does not have a single funnel nature, that can guide the relaxation; it has a rugged surface, *i.e.* there are high barriers between directly interconnected minima. In this situation, the evolution of the system can be considerably delayed by reaching “trapped states”. Despite these unfavorable characteristics, Walsh and Wales observe [86] that, by focusing on hierarchically classified defective structures based on the number of specific SW defects, it is possible to generate pathways that reach the minimum by iteratively remove defects. Such a mechanisms can generate sequences of minima that monotonically decrease in energy. Such an energy decrease is therefore associated with a energy gradient, that thermodynamically drives the system towards the global minimum, provided that it has the energy to overcome the energy barriers. Walsh and Wales estimate a timescale of the order of millisecond to obtain a statistically relevant fraction of the stable minimum.

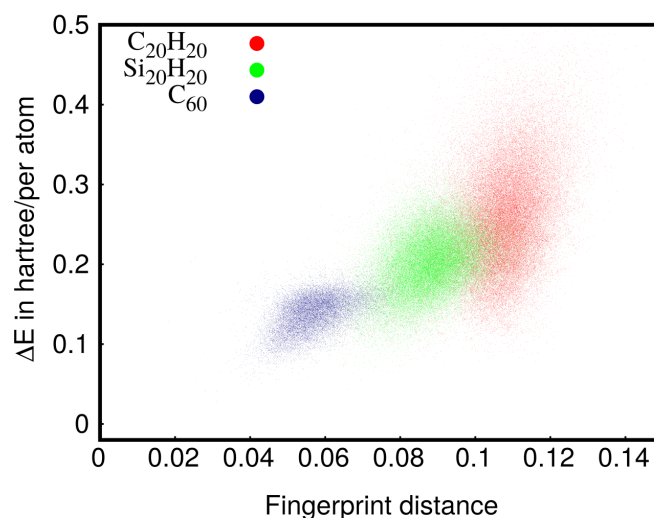


Figure 4.5: DE-plots for the investigated C_{60} , $C_{20}H_{20}$ and $Si_{20}H_{20}$ systems together with their ground state structures. Only the lowest 15000 configurations for C_{60} , 25000 configurations for $C_{20}H_{20}$ and 50000 configurations for $Si_{20}H_{20}$ are considered. Their slope is a measure for the average driving force towards the ground state.

4.2.4 Comparison of PES between different systems

While information about ruggedness of a PES can be understood at glance by looking at the disconnectivity graph, the gradient can be appreciated in a distance-energy (DE) plot [177], reported in Fig 4.5. In the graph we plot the energy difference between the global minimum and the the rest of the structures as a function of the fingerprint distance; such a representation have the additional advantage of not requiring the knowledge of the transition states. The lower edge of the DE-plot represents the structures which are the lowest in each funnel, *i.e.* the structures energetically closer to the ground state. The energy separation readily increases with the increase in fingerprint distance.

Let us now turn to the PES of $Si_{20}H_{20}$. To analyze it, we applied the FP-based method to obtain an approximate disconnectivity plot, using 99,000 minima to construct the tree shown in Fig 4.6. A complete construction of the connectivity between such a high number of minima is unfeasible with an exhaustive transition pathway search, due to the computational costs. The MHGPS has therefore only been applied to sample pathways to the global minimum.

$Si_{20}H_{20}$ is a high temperature structure seeker, as evinced from its distinct ground state that is separated from all the other conformations by very high energy barriers. In this context, we have also compared the disconnectivity plot of $C_{20}H_{20}$ with $Si_{20}H_{20}$. The global minima for both system have similar configuration and symmetry (I_h) (Fig. 4.7). Each vertex is a C/Si atom that bonds to three neighbouring C/Si atoms. Each C and Si atom is bonded to a hydrogen atom as well. However, $C_{20}H_{20}$ is possible to experimentally synthesize whereas $Si_{20}H_{20}$ not [170]. Thus, it

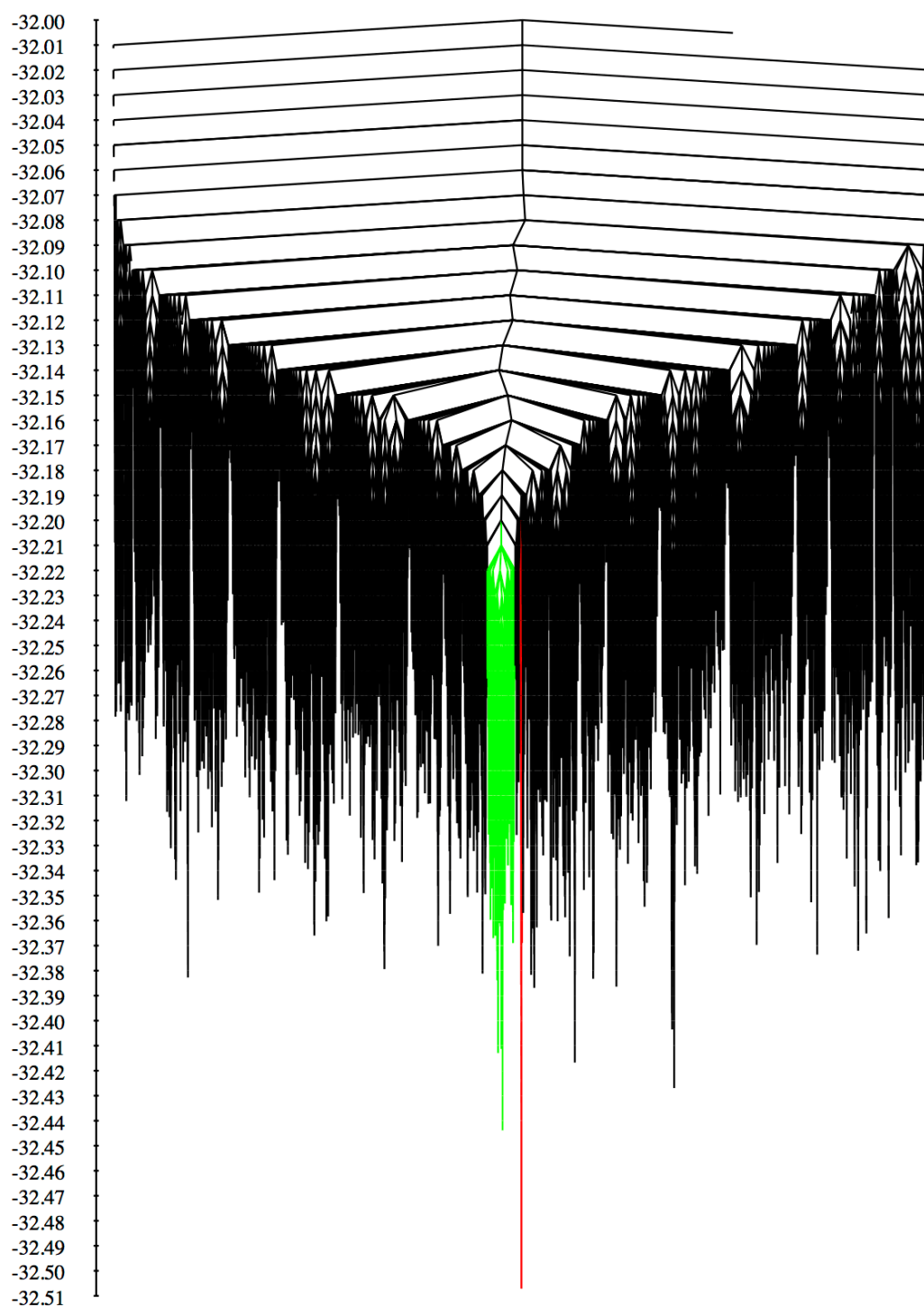


Figure 4.6: $\text{Si}_{20}\text{H}_{20}$ disconnectivity plot for from the FP-method. The configurations colored in green represent the biggest funnel, with ≈ 2000 structures. The global minima belong to the funnel colored in red, that contains 127 structures.

bodes well to look at the PES of both framework and comprehend the conceivable contrast. As in the case of C_{60} and $C_{20}H_{20}$, the PES has certain characteristics of a weeping willow diagram, but there are some important differences with $Si_{20}H_{20}$. By zooming into each funnel, (see appendix E) we observe that each they resembles the banyan tree. This pattern arises from a hierarchical structure. It is a sets of minima are dynamically associated by transition states of increasing energy, like a fractal [87, 37].

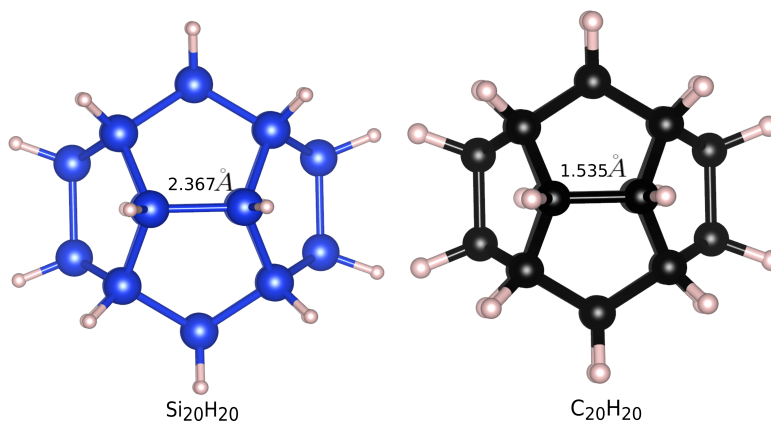


Figure 4.7: $Si_{20}H_{20}$ and $C_{20}H_{20}$ dodecahedron configuration.

All the structure below a particular node depending on the energy cutoff (green and red, for instance) are considered to be part of same funnel. The global potential energy minimum is the dodecahedron (lowest energy structure in the red funnel in Fig. 4.6), but the configuration space corresponding to the funnel in green in Fig. 4.6 is favored by entropy. The biggest funnel consists of more than 2000 structures whereas the funnel that contains the global minimum has 127 structures. The rearrangement mechanisms interconverting different minima include both cooperative and localized processes, and the resulting energy barriers are relatively large compared to the energy available at the temperatures used in experiments.

The PES of $Si_{20}H_{20}$ visibly has a myriad of different funnels, of various size, separated by high barriers. The PES of $C_{20}H_{20}$ is likewise comprise of different funnels however the greatest funnel is where the ground state is (4.3). It is unmistakable from the PES that the energy gradient is towards the global minimum.

A glaring difference with respect to C_{60} in the DE plot in Fig 4.5 is in the almost flat lower edge of the minima: within the limits of our approximations, the energy gradient towards the minimum is almost flat, resulting in a considerably reduced thermodynamic drive towards the dodecahedral structure. The difference in FP-distance of the low energy configurations and the global minimum of C_{60} and $C_{20}H_{20}$ is smaller than the $Si_{20}H_{20}$.

The overall problems with the high energy barriers and the flatness of the gradient is exacerbated by the length of the trajectories connecting two minima. The relaxation needs to go through several hundreds of intermediate structures, crossing barriers

of different energy scales. Such a behavior is shown in Fig 4.8, for the FP-based approximation (a) and the MHGPS search (b). With both methods, the structure goes through a flat (although not identical) energy region. In this region, the PES is glassy: there are several possible paths, leading to different end structures very similar energy. From this point of view, we see the effect of a PES with a low gradient: having too many energy equivalent choices, the structure does not reach the thermodynamically stable minimum in an experimentally accessible time, and can effectively be trapped in entropically more favorable conformations.

Eyring’s theory can be used to estimate the transition rate out of a minimum across a transition state along a single reaction path way [178]. The transition rate k_{mt} from of a minimum m with energy E_m through a transition state t with energy E_t at temperature T is given by

$$k_{mt} = \left(\frac{k_B T}{h} \right) \left(\frac{q_t}{q_m} \right) \exp \left(-\frac{E_t - E_m}{k_B T} \right) \quad (4.1)$$

where q_t is the partition function of the transition state for coordinates normal to the reaction coordinate, q_m is the partition function of the minimum, k_B is the Boltzmann constant, and h is Planck’s constant. For simplicity, we assume the partition functions in the above formula to be equal, in order to obtain an estimate of k_{mt} . For an energy difference of 0.25 Ha, corresponding to the approximated barrier between the two lowest minima of Si₂₀H₂₀, this correspond to a rate of $2 \times 10^8 \text{ s}^{-1}$.

A statistical analysis of the different low energy pathways from the lowest energy structure from different funnels to the global minima are shown in appendix F. In each case, the pathways have similar property. For each starting point, there are multiple lowest energy pathways to reach from the lowest energy structure of a funnel to the global minima (see appendix F). This suggests that the structure has to come across multiple barriers which are similar in energy in its PES space. Due to the multiple possibility, the structure might be lost in the glassy region and not able to reach the global minima.

In the canonical ensemble, each point x will be sampled with a probability proportional to its energy $E(x)$ by the Boltzmann weight, $\exp(-E(x)/k_B T)$. Thus, the Boltzmann factor favors low-energy conformations. Therefore, we can begin to see the vital role played by the potential energy surface. This role extends beyond purely thermodynamic considerations to the dynamics but the topography and connectivity of the PES naturally leads the system towards or away from the global minimum.

LJ₃₈ (Lennard Jones cluster) has one of the most complex PES which consists of two funnels. The PES can be imagined to be two basins of similar energies separated by a high barrier. The global minimum basin is narrower compared to the basin with the icosahedral core. This system has been well studied [179, 180, 71] and it was concluded that the difference in the width of the funnels (*i.e.* the number of structures in each funnel) leads to a much lower free energy barrier for passage from

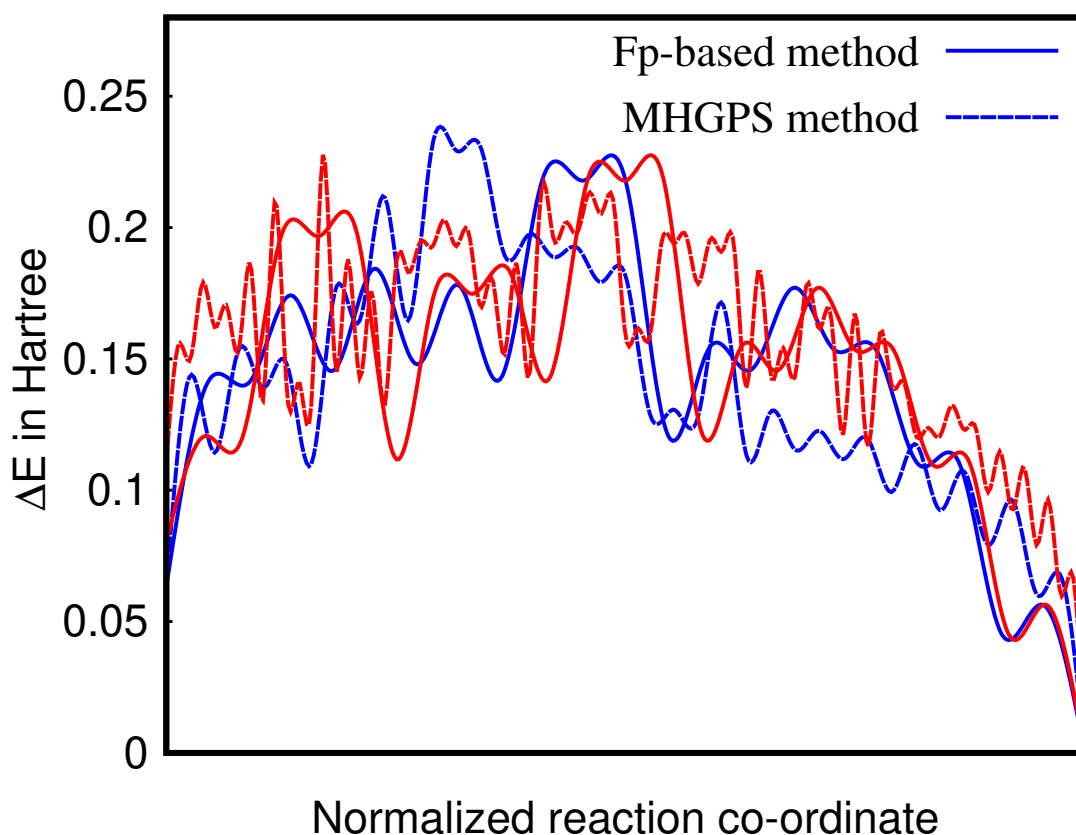


Figure 4.8: The pathway between the lowest energy structure of a funnel and the global minima. The pathway from approximate method is shown by solid lines and the pathway from MHGPS is shown by dashed lines. In each case structure goes through a flat region before it reaches the ground state. The y-axis represents the energy with respect to the ground state whereas x-axis represents the structures.

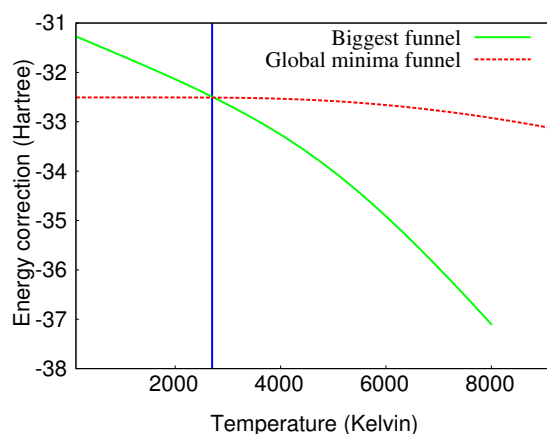


Figure 4.9: Energy correction of the ground state for two different funnel (red and green funnel in Fig. 4.6) with respect to the temperature due to the configurational entropy.

the liquid like state into the icosahedral funnel. This was confirmed by the master equation approach, which suggested that high energy distributions relaxed favorably into the secondary funnel of icosahedral minima rather than the close-packed funnel surrounding the global minimum [181].

The PES of Si₂₀H₂₀ displays a similar behavior. The disconnectivity plot in Fig. 4.6 consists of multiple funnels: all the structures below a particular node (green and red in Fig. 4.6) are considered to be part of same funnel. The biggest funnel consists of more than 2000 structures whereas the funnel that contains the global minima have 127 structures. This will lead to the correction in free energies of the lowest energy structures of different funnels due to the effects of configurational entropy.

Here we assume that the funnels are well sampled. The correction equation is given by

$$E_{\text{entropy}} = -k_B T \ln \left(\sum_i C(E_i) \exp \left(-\frac{\Delta E_i}{k_B T} \right) \right) \quad (4.2)$$

where E_{entropy} is the configurational entropy correction to the ground state of a funnel, k_B is the Boltzmann constant, T is the temperature in Kelvin.

If all structures in a MH calculation are visited more than once, then we can assume that the PES of Si₂₀H₂₀ was properly sampled. Unfortunately, in our calculations, most of them visited only once (even though we have more than 90,000 structures). This means that we need to run MH for a longer time to sample all the configurations. This procedure is computationally expensive and time consuming.

Therefore, $C(E_i)$ is a factor that provides a rough estimation of the number of possible configurations that has not been explored yet in a certain energy range. $C(E_i)$ is estimated in the following way:

Let us assume there is an unknown number of structures N in a certain energy interval. The probability of finding the same structure twice is then given by

$$1 - (N - 1)/N = 1/N \quad (4.3)$$

So if we have found M structures in the interval, the expectation value for the number of doubly found structures is M/N (assuming triply, ... found structures to be negligible). We know the ratio of doubly to singly found structures in our data – lets us call this ratio f . Therefore $M/N = f$, and solving for N we get the estimation $N = M/f$. From N we can calculate $C(E_i)$ for different energy range.

In Fig 4.9, we plotted the energy of the global minimum and the lowest energy configuration of the biggest funnel after the correction in free energy due to the configurational entropy at the different temperatures. The correction in Fig 4.9 clearly shows that at higher temperature the system will be driven towards bigger funnel. The cross over temperature is at around 2600K.

Adsorption of H on a Si_{20} surface is an exothermic process. The energy released during the adsorption of one hydrogen atom on $\text{Si}_{20}\text{H}_{20}$ is 0.17 eV, which equivalent to a temperature of 2000 K. Since the barrier height is considerable, we performed a short NVT MD simulation at that temperature, to understand whether the dodecahedron structure can survive this temperature and, conversely, whether this temperature is sufficient to interconvert a structure from a different funnel into the dodecahedron motif. We observed the dodecahedron structure to be quite stable up to 2500 K. The morphology of the other structures was also not affected. This suggests that the local temperature change due to the reaction is not high enough for the system to escape from one funnel to another. At high temperature, $\text{Si}_{20}\text{H}_{20}$ dissociate into $\text{Si}_{20}\text{H}_{18}$ and H_2 . This transformation is actually one of the required steps to jump from one funnel to another. From an experimental point of view, this imply a tight control of the hydrogen and temperature present in an experiment. If the amount of hydrogen is too low, as soon as a hydrogen molecule separates from the cluster, the probability of hydrogen molecule to dissociate again on Si surface and form Si–H bond is reduced. On the contrary, if the amount is too high, the Si_{20} can transform into configurations where it can take more than 20 H [182].

4.2.5

Conclusions

In conclusion, we have shown that the complicated pathways between the $\text{Si}_{20}\text{H}_{20}$ clusters lead to the lack of observation of the global minima in the experiment. Hence we have shown the importance of exploration of the PES of any structure. The FP-based method is efficient enough to provide a qualitative understanding of the PES without any computationally expensive transition state calculations. Even though the DE-plot and the disconnectivity plot suggests that $\text{Si}_{20}\text{H}_{20}$ is a high temperature structure seeker but the configurational entropy and the transition pathways leads to a different structural minima.

4.3 Stability of $[\text{Si}_{32}\text{Cl}_{45}]^-$ and $[\text{Si}_{32}\text{Br}_{45}]^-$ clusters with Si_{20} core

An one step synthesis procedure to synthesize $[\text{Si}_{32}\text{Cl}_{45}]^-$ cluster which consists of a Si_{20} dodecahedral core with an endohedral Cl^- ion has been developed by Telmann *et al.* [168]. They also performed Density functional theory (DFT) calculations to guess the possible structure. After geometry optimization, a hand-made structure will lead to the closest local minima on a Born-Oppenheimer potential energy surface. Starting multiple geometry optimizations from several different configurations or using several stages of symmetry constraints may provide some information; however, if exploration for PES is not systematic, the reliability of the retrieved structure is uncertain. For this reason, we have re-examined by carrying out a systematic and unbiased search for low-energy minima for the stoichiometries of $[\text{Si}_{32}\text{Cl}_{45}]^-$ and $[\text{Si}_{32}\text{Br}_{45}]^-$.

4.3.1 PES of $\text{Si}_{32}\text{Cl}_{45}^-$

A natural starting point of our investigation of the structural stability of $[\text{Si}_{32}\text{Cl}_{45}]^-$ cluster which consists of a Si_{20} dodecahedral core with an endohedral Cl^- ion, *i.e.* the symmetric structure considered by Tillmann *et al.* [168]. We represent Cl decorated Si as Si_0 and SiCl_3 decorated Si as Si_1 . We also swiped the positions of the decorative Cl atom and SiCl_3 and obtained some new configurations. In order to be sure that we have found a new configuration after swiping the atoms, we compared the energy as well as fingerprint distance from the initial structure. To speed up our exhaustive configurational search, we started MHM runs from either the initial configuration or the new configurations.

Among our $[\text{Si}_{32}\text{Cl}_{45}]^-$ clusters obtained in this way, we found that the starting high symmetry configuration structure is indeed the lowest energy structure. Our configurations agree with Tillmann *et al.* and lowest energy structures are cage-like structure. Si_{20} dodecahedral can be stabilized by Cl^- ion and SiCl_3 .

The DE plots for $[\text{Si}_{32}\text{Cl}_{45}]^-$ and $[\text{Si}_{32}\text{Br}_{45}]^-$ are shown in Fig 4.10. Its structure seeker character can be deduced from the fact that the first metastable structure is much higher in energy than the ground state, but not too far in configurational distance. This observation suggests that the barrier for jumping from the first metastable structure into the ground state is relatively small and that there is in general a strong driving force towards the ground state. Even though we found that the energy differences between the initial structure and the other structures are quite small, it is still possible to stabilize such structures by kinetic stability.

The low-energy part of the energy spectrum that we have explored is shown in Fig. 4.11, along with three of the low energy structures. It also has been found that

removal of SiCl_2 or SiCl_4 does not break the cage.

The distance between the central Cl^- ion and Si from the Si_{20} dodecahedral core depends on the decorative atoms and molecules: if a Si atom is decorated by Cl atom, the distance is 3.293 Å; if it is decorated by SiCl_3 the distance is 3.365 Å.

The Si–Si bond length in dodecahedral also depends on the decorative atoms: $\text{Si}_0\text{--Si}_1$ and $\text{Si}_1\text{--Si}_1$ bond lengths are 2.383 Å and 2.378 Å respectively. For the lowest energy structure, each pentagon consists of one $\text{Si}_1\text{--Si}_1$ bond and four $\text{Si}_0\text{--Si}_1$ bonds. Twelve Cl_3Si groups are arranged pairwise towards the vertices of an octahedron.

For neutral $\text{Si}_{32}\text{Cl}_{45}$, Si–Si bonds in Si_{20} varies. Each pentagon has three different bondlengths, whereas for charged $[\text{Si}_{32}\text{Cl}_{45}]^-$ Si–Si bondlengths are comparable. Hence, the charged structure is more symmetric.

The distance from the Cl^- to a Si atom is not the same as the lowest energy structure, but in this cases also, the distance between them depends on the decorative atoms on Si. This also effects the bond length between Si–Si in Si_{20} dodecahedral. This may be the reason of stability for the above structure.

Structure number	Relative	Gap (eV)	Formation Energy (eV)/atom	Space group	fp distance
1	0.000	1.84	-0.1675	D_{2h}	0
2	0.2485	1.84	-0.1673	C_1	0.0214
3	0.2893	1.84	-0.1673	C_1	0.0225
4	0.3035	1.74	-0.1672	C_s	0.0236
5	0.3410	1.79	-0.1671	C_1	0.0253
6	0.3421	1.95	-0.1669	C_2	0.0274
7	0.3765	1.88	-0.1669	C_1	0.0267
8	0.3799	1.68	-0.1668	C_1	0.0269
9	0.3831	1.89	-0.1667	C_1	0.0252

Table 4.1: Properties of different isomers of $[\text{Si}_{32}\text{Cl}_{45}]^-$

Table 4.1 provides some more information about the isomers of $[\text{Si}_{32}\text{Cl}_{45}]^-$. In the first column we tabulated the energy separation ΔE of the configurations with respect to the lowest energy structure. We can see that the ground state energy is 0.248 eV lower than the second lowest state. In the second column, we present the energy difference between the Highest Occupied Molecular Orbital and the Lowest Unoccupied Molecular Orbital (HOMO-LUMO) of the structures. The value lies in the ranges between 1.68 and 1.95 eV. The gaps are smaller than $\text{Si}_{20}\text{H}_{20}$ [160] and also they do not exhibit any special pattern. The fact that the lowest energy structure does not exhibit the largest gap might be unexpected but is also found in numerous other systems [183].

The next column shows the formation energies per atom ΔH with respect to the

bulk conformations of silicon and chlorine, which is defined as

$$\Delta H = \frac{E - n_{\text{Si}}E_{\text{Si}} - n_{\text{Cl}}E_{\text{Cl}}}{n_{\text{Si}} + n_{\text{Cl}}}$$

where E is the energy of the compound and E_x and n_x are the energy per atom of the reference configuration and number of atom respectively.

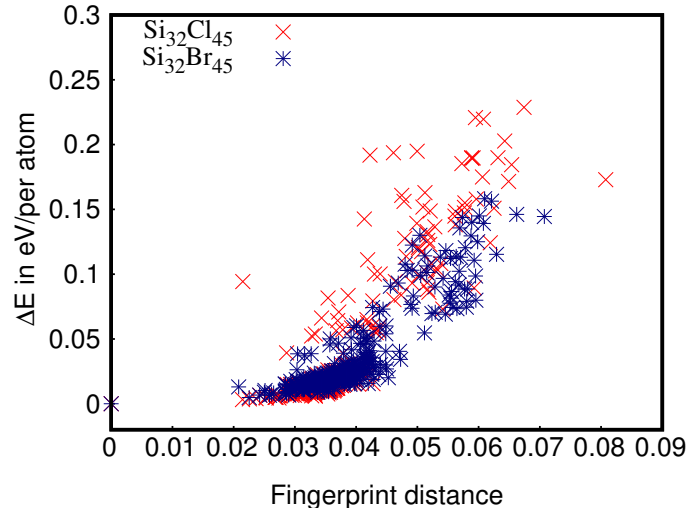


Figure 4.10: DE plots for $\text{Si}_{32}\text{Cl}_{45}^-$ and $\text{Si}_{32}\text{Br}_{45}^-$ cluster.

In the next column we have presented the point groups of the structures. The lowest energy structure is highly symmetric (D_{2h}) whereas the other structures display much lower symmetry (C_s , C_1 and C_2). The last column represents the fingerprint distance with respect to the lowest energy structure. In the fingerprint approach, an overlap matrix is calculated for an atom centered Gaussian basis set. The vector formed by the eigenvalues of this matrix defines a global fingerprint that characterizes the entire structure. The Euclidean norm of the difference vector between two structures is the configurational distance between them and satisfies the properties of a metric. The configurations are structurally quite similar to lowest energy structure but energetically quite different.

System	dissociation energy	
	PBE eV	PBE0 eV
With Charge	1.466	1.666
No Charge	1.142	1.756
No Center	1.526	1.719

Table 4.2: Dissociation energy of SiCl_2 from $[\text{Si}_{32}\text{Cl}_{45}]^-$, $\text{Si}_{32}\text{Cl}_{45}$ and $\text{Si}_{32}\text{Cl}_{44}$ in PBE and PBE0.

In here, we tried to understand the effect of this additional charge. We placed an extra electron on the encapsulated Cl atom and optimized the charge density. A

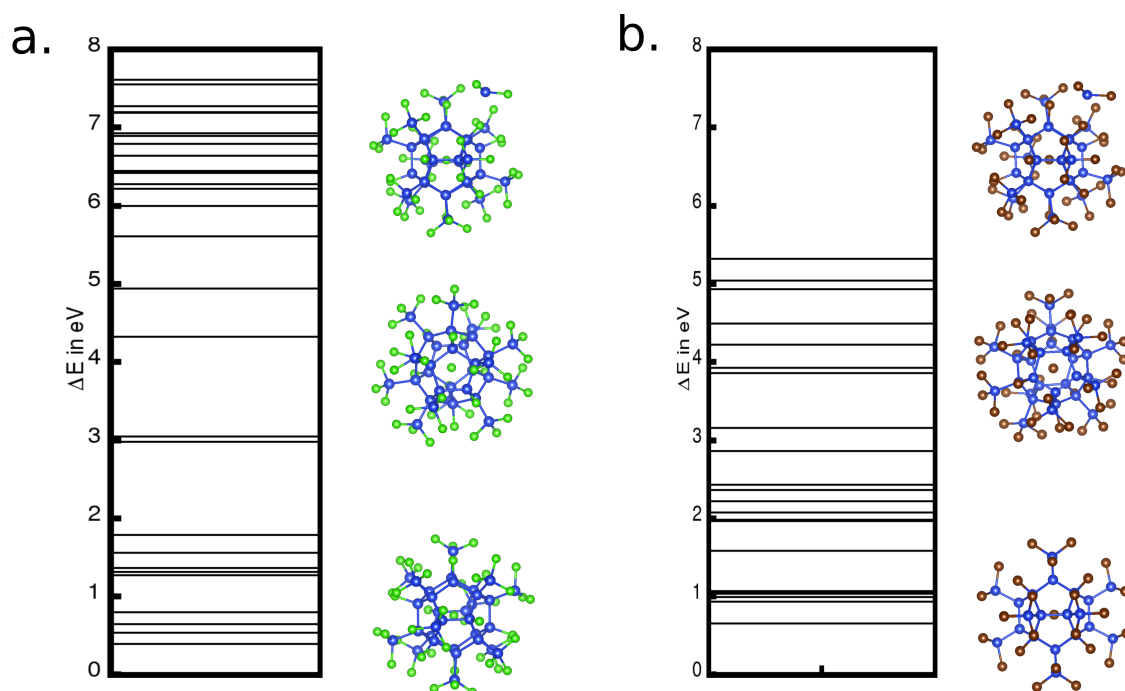


Figure 4.11: The low-energy part of the spectrum for $[\text{Si}_{32}\text{Cl}_{45}]^-$ and $[\text{Si}_{32}\text{Br}_{45}]^-$, together with figures of the 3 energetically lowest structures,

Bader charge analysis shows that the center Cl ion loses an electron. The extra electron of the center Cl ion get distributed over the Si cage.

This electronic delocalization therefore explains the stability of the cluster, irrespective of the position of the extra charge. The difference in charge density of charged $[\text{Si}_{32}\text{Cl}_{45}]^-$ and neutral $\text{Si}_{32}\text{Cl}_{45}$ is given in Fig 4.12a. Yellow colour represents a negative value, which means presence of extra electronic charge. Conversely, blue is a sign of positive charge, which suggests electron deficiency. The figure shows that Cl as well as some Si–Si bonds in the Si_{20} cage gains some electrons in the expense of loosing electron from some other Si–Si bonds. Hence this explains the equivalent bond length for Si–Si in the case of charged $[\text{Si}_{32}\text{Cl}_{45}]^-$ which we observed before. In Fig. 4.12b, we have plotted electron localization function (ELF) at a value of 0.88.

The $\text{ELF}=0.7$ map shows the silicon core surrounded by three chlorine valence domains; the bonding attractor are responsible for the bulges towards the Si center. A further bifurcation occurs for $\text{ELF}=0.82$, giving rise to bonding point attractors and non bonding ring attractor domains ($\text{ELF}=0.88$). Each ring is itself resolved midpoints between the center and the vertices positions respectively. The chlorine valence domain which is almost spherical at lower ELF values shows a hole in front of the chlorine core; increasing the threshold leads to a single attractor lying on the internuclear axis on the side of the chlorine core. This ringlike attractor correspond to lone pair on Cl.

The caged Cl atom prefers to stay at the center. We shifted Cl atom at different position of the cage but center position is most energetically stable. The dipole for the system along X, Y, Z direction is quite small and same (0.009 D). The average dipole moment is (0.01D). If any of the decorated atom or molecule is removed, a high dipole moment as well as a quadrupole moment arises along the direction. This may be the reason why Cl atom prefer to stay at the center of the caged structure. To understand the effect of the center Cl^- ion, we calculated dissociation energy of SiCl_2 from the cluster. We consider the reaction, $\text{Si}_{32}\text{Cl}_{45} \longrightarrow \text{Si}_{31}\text{Cl}_{43} + \text{SiCl}_2$, where $\text{Si}_{32}\text{Cl}_{45}$ is negatively charged in one case and not charged in other case. The dissociation energy is 1.46 eV and 1.14 eV respectively: the negatively charged cluster is much more stable than the neutral cluster. PBE0 gives a totally different order of dissociation energy.

We also considered the dissociation energy of SiCl_2 for the cluster without any center Cl atom or ion. The dissociation energy for such a system is 1.514 eV (PBE) and 1.719 eV (PBE0) which is larger than in the previous cases.

Using laser-desorption ionization(LDI) MS(-) observations, a fragmentation of $[\text{Si}_{32}\text{Cl}_{45}]^-$ is experimentally observed. A major fragmentation cascade is seen due to the extrusions of SiO_2 . From MH runs, we have also identified fragmented structures as in the experiments. SiCl_3 is substituted by Cl and SiCl_2 comes out from the system. The energy difference between $[\text{Si}_{32}\text{Cl}_{45}]^-$ and the first fragmented structure where one SiCl_2 got separated and replaced by Cl is 1.9 eV. This observation additionally suggests that to form a SiCl_2 , 1.9 eV of energy are required.

The energy difference between the ground state configurations and a fragmented structure with two SiCl_2 fragments is 2.9 eV. It is possible to remove SiCl_2 from the surface under gas phase without breaking the dodecahedron Si_{20} cage and in the expanse of small amount of energy.

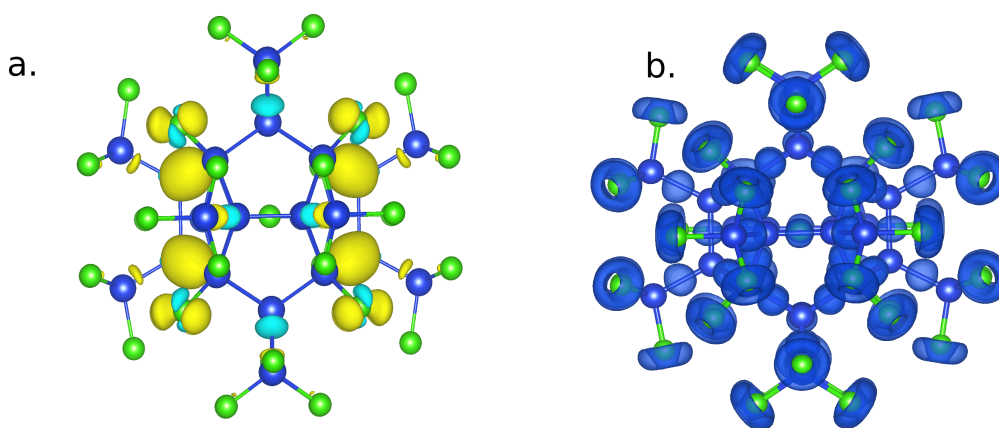


Figure 4.12: a) Charge density difference between neutral and charged $[\text{Si}_{32}\text{Cl}_{45}]^-$. b) ELF of $[\text{Si}_{32}\text{Cl}_{45}]^-$ at $\eta=0.88$.

4.3.2

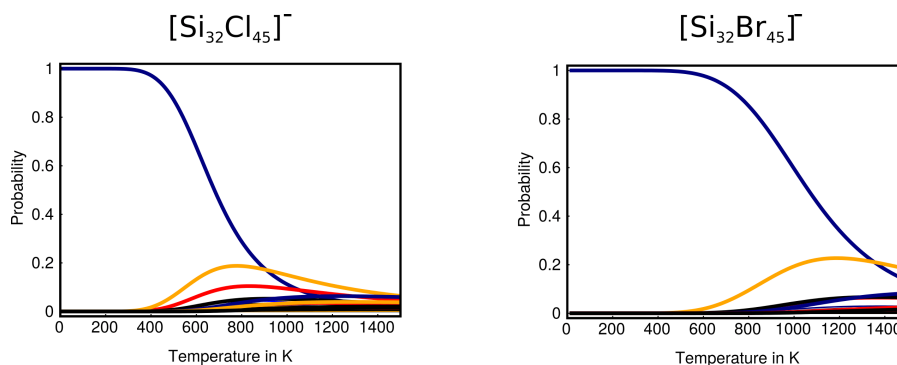
PES of $[\text{Si}_{32}\text{Br}_{45}]^-$ 

Figure 4.13: Boltzmann probability distribution at different temperature for $[\text{Si}_{32}\text{Cl}_{45}]^-$ and $[\text{Si}_{32}\text{Br}_{45}]^-$.

Structure number	Relative	Gap (eV)	Formation Energy (eV)/atom	Space group	fp distance
1	0.000	2.342	-0.1519	D _{2h}	0
2	0.3706	2.370	-0.1516	C ₁	0.0225
3	0.5042	2.373	-0.1514	C ₁	0.0258
4	0.5177	2.321	-0.1514	C ₁	0.0242
5	0.5188	2.328	-0.1514	C ₂	0.0289
6	0.5757	2.315	-0.1511	C _s	0.0261
7	0.6245	2.008	-0.1510	C ₁	0.0286
8	0.6358	2.315	-0.1509	C ₁	0.0265
9	0.6442	2.350	-0.1507	C ₁	0.0337

Table 4.3: Properties of different isomers of $[\text{Si}_{32}\text{Br}_{45}]^-$

As the previous study concluded that Br is most suited to synthesize $\text{Si}_{20}\text{H}_{20}$, we also wanted to see the effects of bromine in this system [162]. We replaced all Cl atoms by Br atoms from the first 10 low energy configurations of $[\text{Si}_{32}\text{Cl}_{45}]^-$, optimized them and then started 10 different MH runs. We found that the symmetric structure is again the lowest in energy. The low-energy part of the spectrum is shown in Fig. 4.11. The next lowest energy isomeric structure is much higher in energy than the lowest energy structure, in contrast with the Cl study, where the isomeric structures were energetically quite similar. In Table 4.3 we present some more information about the structures shown in Fig. 4.11. The HOMO-LUMO gaps are bigger than the ones for $[\text{Si}_{32}\text{Cl}_{45}]^-$; again there is no notable correlation between the structure stability and the HOMO-LUMO gap. The formation energy is higher than Cl counterpart, indicating that it is more likely to encounter experimentally the stoichiometry $[\text{Si}_{32}\text{Br}_{45}]^-$ than $[\text{Si}_{32}\text{Cl}_{45}]^-$. The fp-distance from the lowest energy structure (Table 4.3) does not correlate with the stability of the system.

We have additionally calculated Boltzmann probability factors in Fig 4.13. The symmetric configuration for $[\text{Si}_{32}\text{Cl}_{45}]^-$ and $[\text{Si}_{32}\text{Br}_{45}]^-$ are the most probable at the room temperature. Fig 4.13 also shows that symmetric $[\text{Si}_{32}\text{Br}_{45}]^-$ is more probable than $[\text{Si}_{32}\text{Cl}_{45}]^-$ at high temperature.

4.3.3 Cluster interactions

After we present the energy landscapes of the $[\text{Si}_{32}\text{Cl}_{45}]^-$ and $[\text{Si}_{32}\text{Br}_{45}]^-$, next we wanted to see how the ground state structure interact with each other. For this purpose, we placed the two clusters close to each other at a distance comparable to the bondlength between Si-Cl and did a local geometry optimization. Since the ground state configuration is highly symmetric, We considered three possible scenario where the cluster can attach to each other. If we consider that the center of the cluster is the origin of a cartesian coordinate system then we placed another cluster along the x, z axis and at an angle of 45° with the x-axis in the xy plane(x-y direction). We calculated the binding energy for the system, that is defined as

$$E_b = E_{tot} - 2 \times E_{ind} \quad (4.4)$$

where E_b is the binding energy, E_{tot} is the total energy of the two clusters together and E_{ind} is the energy of an individual cluster. It turns out that the $[\text{Si}_{32}\text{Cl}_{45}]^-$ and $[\text{Si}_{32}\text{Br}_{45}]^-$ clusters are inert in nature. In each case for $[\text{Si}_{32}\text{Cl}_{45}]^-$ dimer, the binding energy is positive (0.6-0.7 eV/atom) . wheres, for $[\text{Si}_{32}\text{Br}_{45}]^-$ dimer, the binding energy along X-Y direction is 0.08 ev/atom and along X, Y, Z direction is 0.07 eV/atom. This suggests that they do not prefer to interact with each other directly, although it might be possible to attach them with a ligand.

4.3.4 Conclusion

In conclusion, we have shown the ground state of $[\text{Si}_{32}\text{Cl}_{45}]^-$ and $[\text{Si}_{32}\text{Br}_{45}]^-$ and explored different isomers of the structure. For $[\text{Si}_{32}\text{Cl}_{45}]^-$, it is possible to synthesize the other isomers at very high temperature. We have also observed that formation energy for $[\text{Si}_{32}\text{Cl}_{45}]^-$ is much lower than $[\text{Si}_{32}\text{Br}_{45}]^-$. It suggests that $[\text{Si}_{32}\text{Cl}_{45}]^-$ is much easier to form than $[\text{Si}_{32}\text{Br}_{45}]^-$. We have also found that the extra charge from encapsulated Cl^- ion transfers to the Si cage. This extra electron makes the structure more symmetric. These clusters also do not prefer to bond to each other. This study will help us to understand the stabilizing mechanism for Si_{20} clusters.

CHAPTER 5

Applications to the surface and interfaces

In the previous chapters, we have shown detailed study of the PES for different clusters. The following chapter focuses in the exploration of PES for periodic systems *i.e.* surfaces and interfaces. This chapter is organized as follows:

First we discuss about the SiC/SiO₂ interface. There has been a long standing argument on the shape and size of the carbon clusters at interface of SiC/SiO₂ during the oxidation of SiC surface. In this section(Sec. 5.1)¹, we have employed an unbiased structure prediction method at the tight binding density functional theory (DFTB) level to explore different stable configurations of 4H-SiC in different environments such as oxygen, nitric oxide (NO) and nitrous oxide (N₂O) forming different carbon clusters at the SiO₂ /4H-SiC interface. We also checked the stability of such structures within DFT. Experimental Raman spectra and atomic force microscopy (AFM) results were done to support our prediction. This project was executed in the collaboration with Dipanwita Dutta from the Paul Scherrer Institut (PSI) in Switzerland, who performed all the experiments regarding this material under the supervision of Prof. Thomas A. Jung.

The second part of the chapter, we concentrate on understanding the formation boron 2d layer on Si substrate. Although boron atoms have high solubility limit in Si crystal, they tend to segregate on the surface of the Si [184, 185, 186, 187, 188, 189] at very high concentration, due to their high diffusivity. The above fact motivates us to consider semi conductors *i.e.* Si as a substrate to grow 2d boron structures. In this section(Sec. 5.2)², we have explored this possibility. we have shown that it

¹Dipanwita Dutta, Deb Sankar De *et al.* "Evidence for carbon nucleates compromising the channel mobility of thermal gate oxides in SiC" is under evaluation.

²D.S. De, J. A. Flores-Livas, M. Amsler, and S. Goedecker "Growth of 2D-boron layer on Si

is possible to obtain not only metallic boron mono layers but also 2d boron semiconductors on Si surface. By controlling the concentration of boron and depending upon the choice of Si surface, we can grow monolayer, icosahedral sheet or a layered configuration, a wide range of 2d configurations.

5.1 Formation of carbon cluster in 4H-SiC/SiO₂ interface

In the atmospheres of carbon rich red giant stars and by supernova remnants, silicon carbide (SiC) is synthesized naturally. On earth, SiC can be found naturally in Moissanite crystal, which is a rare mineral. Jons Jacob Berzelius was most probably the first to synthesize SiC in laboratory, and published his result in a paper as early as 1824[190].

Silicon carbide (SiC), a wide-bandgap semiconductor (3.3 eV), is considered as the major enabling material for advanced high power and high temperature electronic applications. In contrast to the commercially available SiC Schottky rectifier technology, SiC power MOSFETs are still affected by low channel mobilities and threshold voltage instabilities due to the poor quality of the SiC/SiO₂ interface. The reason for these defects can be attributed to the complicated oxidation process, that necessitates the removal of carbon in the form of CO and CO₂. Different defects in SiC crystals (dangling bonds, carbon clusters, near-interface traps, etc.) due to thermal oxidation of the crystal modifies the electronic properties of the inversion channel and deteriorate the field-effect mobility.

Until now more than 250 SiC polytypes have been identified [191]. The basic unit of each of the SiC polytypes consists of a Si or C atom centered tetrahedron with four covalently bonded C or Si. The bond length between the Si–C atoms is approximately 1.89 Å. The distance between the Si–Si or C–C atoms is approximately 3.08 Å. These tetrahedra are joined to one another by the corners to form the SiC crystals and have threefold symmetry around the axis parallel to the stacking direction. The crystal structures of SiC can be cubic, hexagonal or rhombohedral. In Fig. 5.1, we have shown some of the polytypes of SiC. The nomenclature of the SiC polytypes is based on the specific type of stacking. The labels 3C, 4H, 6H, 9R in Fig. 5.1 refer to the repeat stacking distance in the different unit cells. C, H, R refers to a cubic, hexagonal and rhombohedral lattices, respectively, while 3, 4, 6, 9, etc., refers to the number of C-Si dimers that are stacked.

4H-silicon carbide is the most promising polytype for power electronic devices thanks to its favorable properties. In contrast to silicon (Si), 4H-SiC exhibits a wide band gap of 3.3 eV (1.1 eV in Si) and a high breakdown electric field, that allow devices to operate at high voltage (10 kV), high frequency (20 kHz), and at temperatures above

substrate is under evaluation.

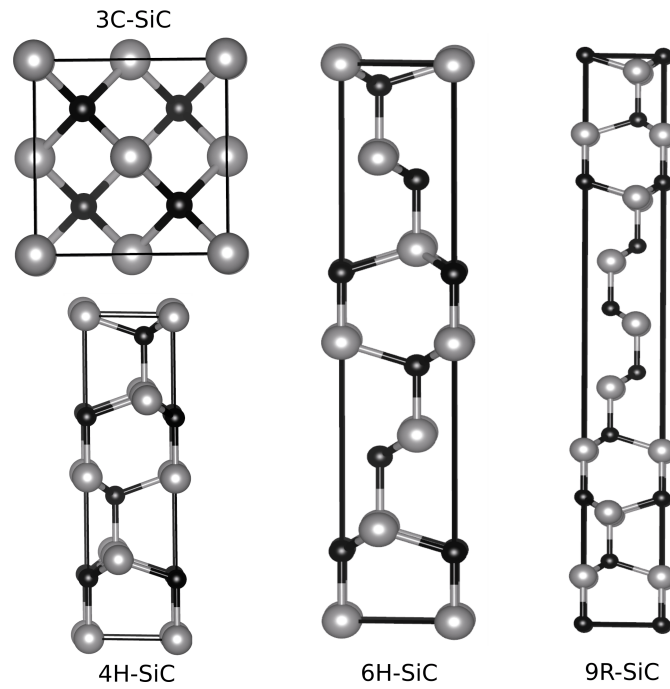


Figure 5.1: Different polymorph of SiC.

Table 5.1: Main physical and electronic properties of bulk 4H-SiC and Si. The bulk moduli for 4H-SiC and Si result from different ab-initio calculations. [2, 3]

physical and electronic properties	4H-SiC	Si
Bulk modulus (GPa)	217-224	98
Band gap (eV)	3.26	1.12
Breakdown electric field ($10^5 \text{V}\cdot\text{cm}^{-1}$)	22	3
Saturated electron drift velocity ($10^7 \text{cm}\cdot\text{sec}^{-1}$)	2	1.40
Thermal conductivity ($\text{W}\cdot\text{cm}^{-1}\cdot\text{K}^{-1}$)	4.90	1.30

175°C [192, 193, 194, 195]. In this thesis, we focus only one type of polymorph, namely 4H-SiC. The lattice parameter a along the $[10\bar{1}0]$ is 3.08 Å and c along $[0001]$ is 10.06 Å for 4H-SiC [2]. Hereon, we will refer to 4H-SiC as SiC unless otherwise specified.

SiC is the only wide band gap material with a native oxide (silicon dioxide, SiO_2) that can be grown in an industrially affordable, thermal process. Unfortunately however, the thermal oxidation of SiC – in contrast to Si – curtails the carrier mobility in the near interface region of the SiC, an effect that has been attributed to the presence of carbon-related defects formed at the interface during the chemically complex oxidation process, leading to carrier mobilities merely below 90 cm^2/Vs (compared to 900 cm^2/Vs in Si) [196, 197, 198]. Extensive efforts have been undertaken to reduce the near-interface mobilities, *e.g.* via surface conditioning or passivation of the SiC surface in the fabrication procedure.

The introduction of post-oxidation annealing in nitric oxide or nitrous oxide ambient was comprised a breakthrough for improving the SiC MOS performance [199, 200], but nevertheless the microscopic origin of the passivation mechanism is not yet fully understood.

5.1.1 Methods

A common way to search for new crystal structures is to perform a systematic survey of the enthalpy surface using some sophisticated structure prediction method. Here, Minima hopping method (MHM) simulations were performed using the MINHOCAO package on the DFTB scheme to evaluate the potential energy landscape [15]. The structural searches were conducted with surface slabs along the [0001] direction with a supercell sizes of 1x1 and 4x4, scanning several hundreds of different structures. Initial SiC/SiO₂ structures were randomly allowed to generate in an unbiased way. The surface model was constructed with a 10 Å vacuum gap perpendicular to the surface.

Density-Functional-Theory (DFT) calculations were performed within the projector augmented wave framework as implemented in the VASP package, to refine the geometries and energetic ranking of the most promising candidate structures [84]. We used the generalized gradient approximation with the PBE parametrization of the exchange-correlation functional [201]. A plane-wave cutoff energy of 500 eV was used together with a sufficiently dense k -point mesh, resulting in total energies converged to less than 1 meV/atom. The atomic structures were relaxed until the forces on the atoms were less than 3 meV/Å and the stresses were less than 0.1 eV/Å. All supercell relaxations were performed using $k=6\times6\times1$ MP meshes, while $4\times4\times1$ (PBE and HSE06) Γ -centered meshes were employed for final DOS calculations. The normal modes were calculated using the DFTB scheme. The Raman spectra were constructed with the RAMAN-PY package, which depends on the output from VASP calculations [202].

5.1.2 Oxidation models

To model the oxidation procedure in the oxygen environment, we use two different chemical configurations to model two distinct conditions during the oxidation process.

- **In model A** we provide an excess of oxygen at the SiC surface, more than required to oxidize the first surface layer, which corresponds to a one-step oxidation process.
- **In model B** we create an oxygen deficient reaction environment to mimic a two-step oxidation process. Thereby, the surface is first oxidized with half of

the oxygen required to convert the topmost layer into a stoichiometric SiO_2 pattern before more oxygen is added.

5.1.3 Identification of carbon clusters at the interface

The MHM simulations of both models show that the low-energy portion of the corresponding energy landscapes comprise structures which exhibit carbon nucleating in form of clusters, with varying size and geometry. While model *A* results in nucleates both at the interface and within the SiO_2 layer, model *B* produced nucleates only at the interface. The structural features of the carbon nucleates are similar in both models, and consist of characteristic five (C_5) and six (C_6) membered rings.

In presence of sufficient oxygen (model *A*), these carbon rings form covalent bonds to the surrounding Si atoms in the SiC or SiO_2 matrix (Fig. 5.4). On the other hand, the oxygen-deficient model *B* leads initially to chain-like carbon structures, which subsequently convert in a second step to interlinked chains of carbon rings as the MHM simulation progresses (chains of C_7 -Si ring (Fig. 5.2a) or of C_9 -Si-rings (Fig. 5.2c), and zig-zag carbon chains $[\text{C}-(\text{Si}-\text{R})_2]_n$ (Fig. 5.2b)). These chain structures exhibit an especially high energetic stability at specific interface sites: the periodic silicon carbide matrix anchors/passivates the chains and ribbons from the bottom, while the Si atoms from the SiO_2 layer bond from the top.

Occasionally the simulation finds cases where the carbon atoms contained in the unit cell do not nucleate (Fig. 5.2d), but form merely CO and CO_2 as the oxidation products. In fact, carbon nucleates only form when no CO_2 is formed in an initial stage, and CO diffuses away from the interface through the SiO_2 layer to the surface. The oxidized carbon is expected to diffuse to the surface through the growing SiO_2 layer and to be released as CO/ CO_2 into the process gas. The diffusion of C and O continuously in the oxidation process also modifies the solid matrix and leaves defects behind that broaden the interface and also affect the structural integrity of the SiO_2 and the near-interface region of the SiC.

We have encountered two types of defects, a C_7 -Si polycycle and a C_9 -Si polycycle. The C_7 -Si defect consists of a pentagonal carbon ring fused with a 4-ring carbon cluster and one Si atom; the C_9 -Si ring consists of a naphthalene-like structure, with a 6-carbon-atom ring fused to a ring made out of a 5 carbon atoms and one Si atom. In the pentagonal carbon ring, there are both sp^2 - and sp^3 -hybridized carbon atoms. In the C_4 -Si ring, C-C and C-Si bonds are single bonds where these C-C bonds act as a linker between C_5 and C_4 -Si rings, and two units of C_7 -Si rings are connected by a C=C double bond. The carbon atoms are anchored to the Si atoms of the SiC surface (bond length 1.8 Å) and are also bonded to the Si atoms in the oxide. A similar behavior can be observed for the C_9 -Si ring.

In the oxide, a variety of chemical bonds of Si and O are present. We observe two-fold coordinated oxygen atoms (Si-O-Si) and three-fold coordinated oxygen atoms.

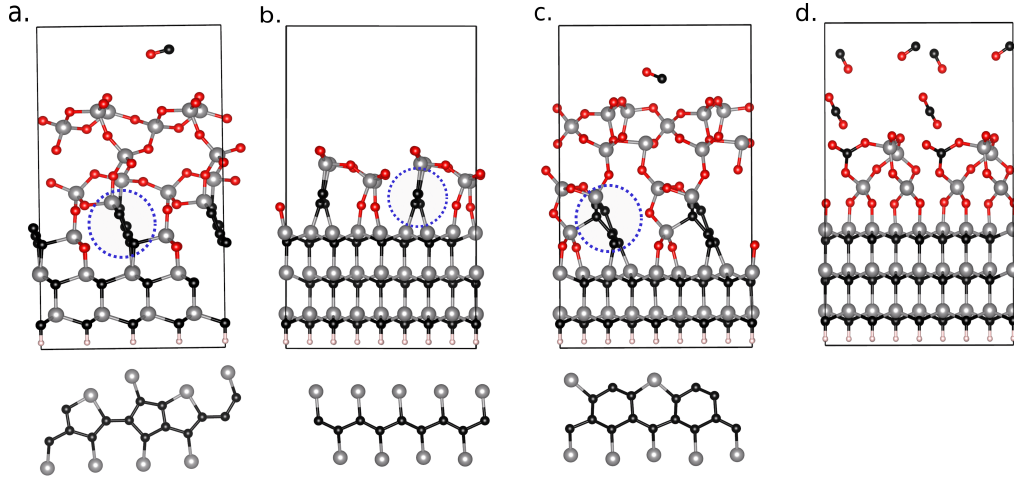


Figure 5.2: (a-d) Computationally predicted atomic structures of the interface after oxidation and subsequent oxide removal. The carbon nucleates are anchored via Si to the interface (a-c).

Some oxygen atoms change their chemical environment from three-fold coordination to two-fold. In this transition, however, by changing these chemical bonds around the oxygen atoms, (from three-fold to two-fold coordinated), some silicon atoms inevitably are left with dangling bonds. In order to reduce the number of the aforementioned dangling bonds, these Si atoms bond to carbon clusters. The oxygen atoms from SiO₂ are anchored at the Si atoms on the SiC surface providing a link between the SiC and the SiO₂ at the interface.

To investigate the role of the SiC/SiO₂ interface and the anchoring Si atoms, the carbon chains were moved from the interface towards the SiO₂ before a second round of minima hopping was performed. Consistently with the phenomenon of carbon accumulation at the interface, the carbon in this case is found to condensate in the form of quasi planar structures in SiO₂ away from the interface (Fig. 5.3). Note that these structures are higher in energy than the chain-like structure. The energies with respect to the chain like structure at the interface, of quasi-planar structure and free standing chain in SiO₂ matrix are 0.0952 eV/atom and 0.165 eV/atom, respectively. This observation suggests that although quasi-planar carbon structures may be considerably stable in SiO₂, the system prefers to nucleate carbon clusters or chains at the SiO₂/SiC interface. Furthermore, it is important to note that the anchoring Si atoms stabilize these chains, as we do not observe “free standing” carbon clusters in the solid matrix around the SiC/SiO₂ interface.

The stability of the chains was checked by giving increasingly higher initial velocities along x and y direction on the chains during the MD steps of minima hopping runs, which helped to break them; however, after evaluation of a few hundred structures, it was perceived that the chain-like structures were more stable than the distorted configurations.

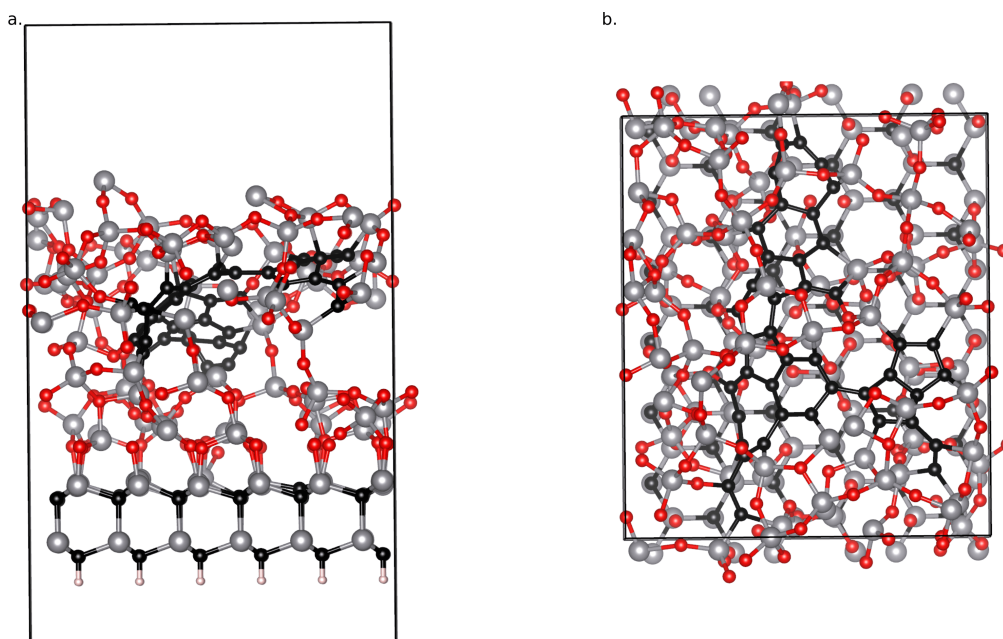


Figure 5.3: Side and top view of shifted carbon cluster in the SiO_2 matrix. The chains ruptured in SiO_2 matrix and the carbon atoms migrate and form a quasi-planar configuration.

During simulations according to Model A, we found carbon clusters inside the SiO_2 . A different amount of oxygen in the oxidation procedure results in different type of carbon clusters. In this case (Model A), we found some polycyclic carbon clusters which consist of 6-ring carbon clusters at the interface of SiC/SiO_2 . Structurally these clusters are different than the 6 ring clusters (Fig. 5.2c) that we observed in Model B. We also found that small carbon clusters are produced in SiO_2 ; this was not observed in the previous case. Many different kinds of carbon clusters are evolved inside the SiO_2 and at the interface. Some of the carbon clusters also migrate towards the surface of SiO_2 . 5-ring carbon clusters can be noticed at the surface of the SiO_2 . A list of the different configurations we encountered are reported in Fig. 5.4.

We additionally employed DFTB and MHM to understand the effect of ozone (O_3) on the carbon clusters decorating the SiC/SiO_2 interface. For this purpose, all SiO_2 was first removed from the optimized models (we used Fig. 5.2a,c configurations). The dangling bonds created by this operation were passivated with atomic hydrogen. In the next step, we optimized the configuration at DFT level and then the hydrogenated model surface was exposed to ozone, using MH calculations at the DFTB level.

We observe that ozone molecules attack the carbon cluster rather than the SiC surface. The carbon chains are broken into smaller clusters, and CO is released, as shown in Fig. 5.5. This hopping migration – where the chemical bonding partner of carbon is not changing – is consistent with our experimental Raman analysis (vide

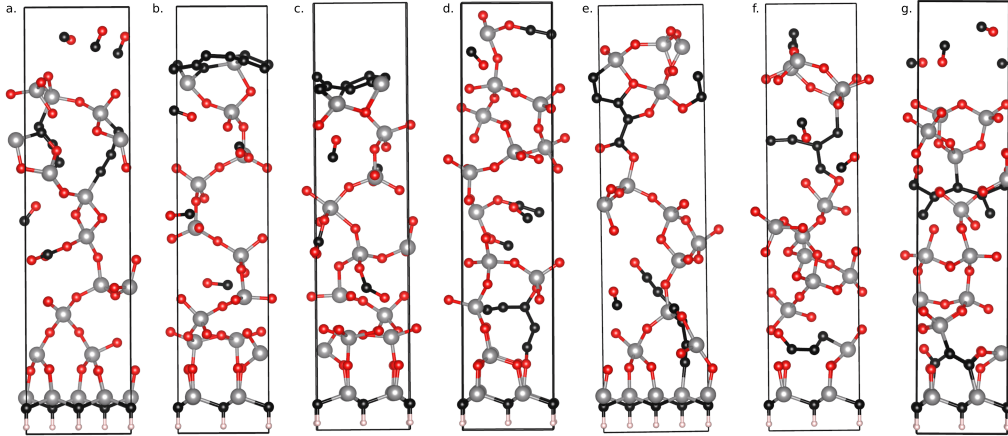


Figure 5.4: (a-g) Computed structures of the characteristic carbon nucleates obtained by an oxygen-rich process (Model A). a) Carbon nucleate only in SiO₂. b)-c) carbon nucleates at the surface of SiO₂. d)-g) carbon nucleates in SiO₂ as well as at the interface of SiO₂ and SiC.

infra): no shift of the position of the carbon peaks, *i.e.* no change in the bonding, has been observed; only the peak intensity is reduced. The nucleates present at SiC/SiO₂ interfaces could be removed by ozone. We attribute the behavior to the fact that the nucleates are carbon clusters, an observation in our own findings that is in agreement with an earlier report [203].

5.1.4

Density of states analysis

With the PBE functional, the calculated Kohn-Sham band gap of SiC is 2.2 eV, a value which severely underestimates the experimental value (3.3 eV), as usual at this level of theory. Hybrid-functional calculations, which include a fraction of the exact Hartree-Fock exchange, are often seen to improve the band gaps of semiconducting materials. The PBE0 hybrid functional yields a band gap of 4.0 eV, overestimating the experimental band gap by 0.7 eV. The band gap of SiC, calculated using HSE06 hybrid functional (3.4 eV) is comparable with the experimental value (3.3 eV). In this work, we use HSE06 to perform DOS calculations for large super cells.

The band gap calculated for 4H-SiC/SiO₂ interfaces depends also on the methods used [204]. We first calculated a pure interface between 4H-SiC and amorphous SiO₂ without any defect atoms at the interface. The band gap of such system is 2.84 eV using the PBE potential. This is comparable with PBE band gap value of pure SiC. With different hybrid potentials such as PBE0 the band gap is calculated to be 4.1 eV, and by using the HSE06 potential it is 3.4 eV which is also comparable to the value of the 4H-SiC band gap from DFT calculations with HSE06. This result indicates that the perfect abrupt interface structure does not produce defect states. We used the DOS of defect free SiC/SiO₂ as a reference for rest of our calculations.

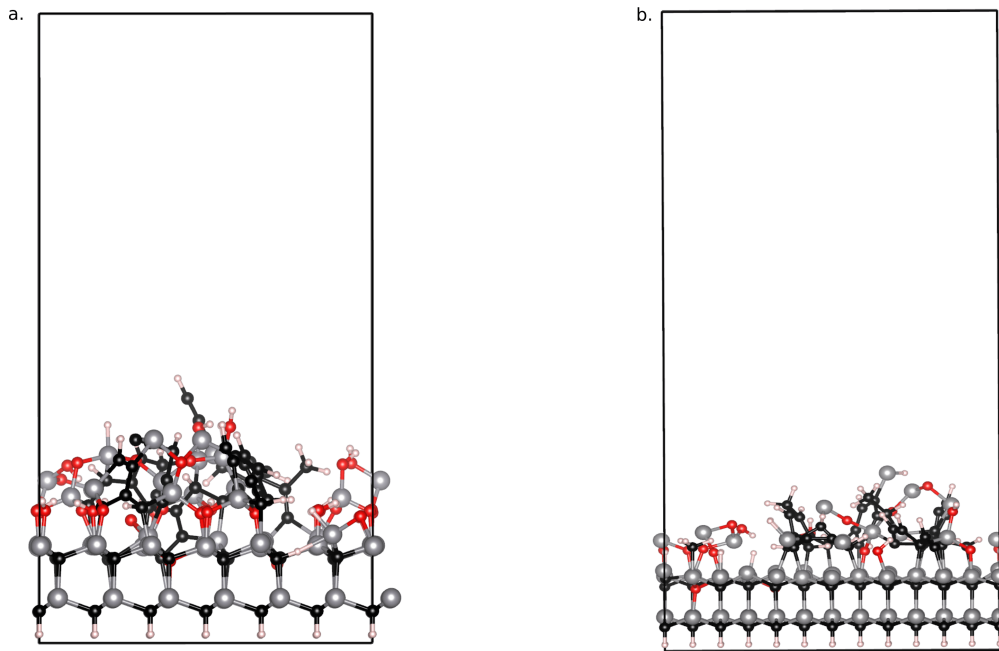


Figure 5.5: MH-DFTB simulations of a carbon chain exposed to ozone. In a) a 5 carbon ring chain and in b) a 6 carbon ring chain are disintegrated by the reaction with ozone and smaller carbon nucleates remain on the surface.

We find that the bandgap of structures which contain carbon nucleates is reduced. There are new states formed near the valence band and some mid-gap states are also observed depending on the nucleate shape. For 5-ring C nucleates (C_7 -Si in Fig. 5.6 and Fig. 5.7), the valence band edge is shifted up and the conduction band edge is shifted down, significantly reducing the band gap to 2.3 eV. In addition, a very stable defect state occupying the mid-gap state appears at -0.5 eV which is above the shifted valence band edge. The most important contribution for these new states comes from overlapping p_x states between the neighboring carbon atoms in the nucleates; a smaller contribution originates from p_y and p_z states. The occupied levels appear due to the p-p interaction between the nearest neighbor carbon atoms in the carbon nucleate.

For 6-ring carbon nucleates (C_9 -Si in Fig. 5.6 and Fig. 5.7) at the interface, the valence band is shifted upwards by 0.5 eV and the conduction band edge is shifted downward by 1.3 eV. The contribution for these new states, both at conduction and valence band edge, arises from the carbon nucleates at the interface; partially oxidized Si at the interface also contributes to the new states.

After analyzing the partial Density of States (pDOS) for all atoms, we observe that the major contribution comes from the p_y states of the carbon nucleates at the interface; p_z and p_x also contribute to those states, as can be seen in Fig. 5.7. No mid-gap state is obtained in this case. Different numerical simulations based on different model assumptions for the interface structure show a continuous distribution of

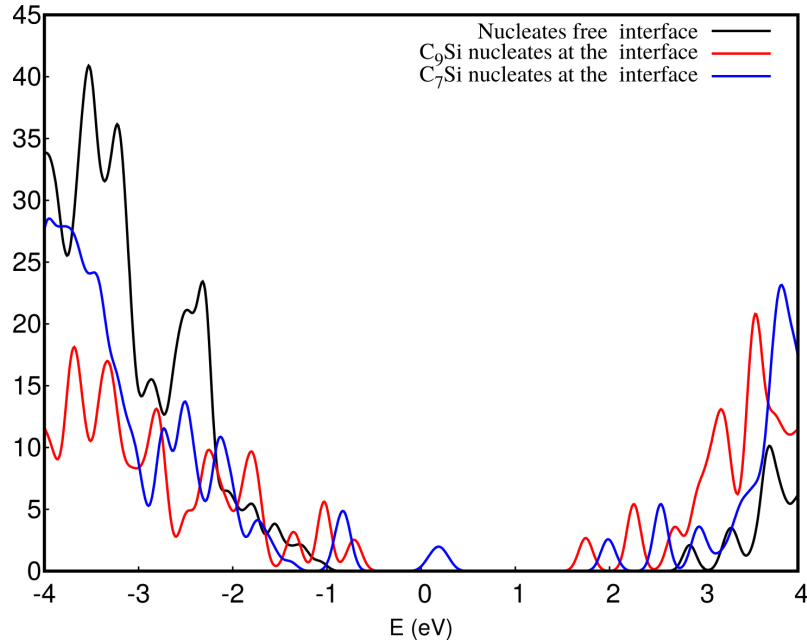


Figure 5.6: DOS of SiC/SiO₂ interface structures with different carbon nucleates: The interface without any carbon nucleates, with 5-atom carbon ring (C₇-Si) and 6 carbon ring (C₉-Si) nucleates. Initially, in the absence of nucleates the energy gap is around 3.1 eV. New states arise near the valence band edge if carbon nucleates are present at the interface.

states rising towards the band edges. The sensitivity of these model calculations is dependent on the energy with respect to the band edges. Therefore, the position of these structures (or even the presence or absence of peaks) should be regarded with some caution. Nonetheless, most of the experiments confirm a peak at 0.8 eV and at 2.7 eV above the valence band edge. These peaks are consistently observed in our DOS calculations, see Fig. 5.6.

5.1.5 Nitrogen passivation

The post oxidation annealing process of SiC in NO, NO₂, NH₃ ambient, or the direct growth of oxide on SiC in nitrogen environment is called nitrogen passivation. It has been observed that partial passivation of interface states could be accomplished by nitridation, either by post oxidation annealing or by oxidation in a gas mixture containing nitrogen [205, 206]. Atomic nitrogen was also shown to be effective in the form of a nitridation radical irradiation [207, 208] or by nitrogen implantation prior to oxidation [209]. The mechanism of nitridation is not yet fully understood; it has been suggested that nitrogen might compensate the unpaired electrons, or helps to remove the carbon from the interface by breaking down the carbon clusters. One possibility is that nitrogen saturates the Si dangling bonds and replace oxygen in strained Si-O-Si bonds. Due to the oxidation in nitrogenated environment a reduc-

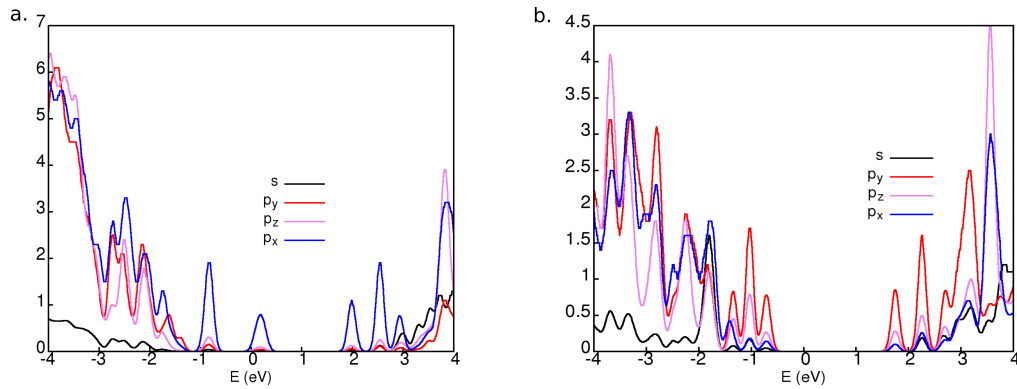


Figure 5.7: pDOS for the carbon from 5-atom carbon nucleates in the new state is shown here. It is emerging from the p_y state of carbon. The s , p_x and p_z orbitals contribute less to the new state. A similar situation is observed for the system comprising a C_6 nucleate at the interface.

tion in dangling bonds as well as a stronger decrease in the interface trap density near the conduction band of 4H-SiC is observed by Afanas'ev *et al.* [200]. This improves significantly the electron mobility at the oxidized 4H-SiC surfaces [210].

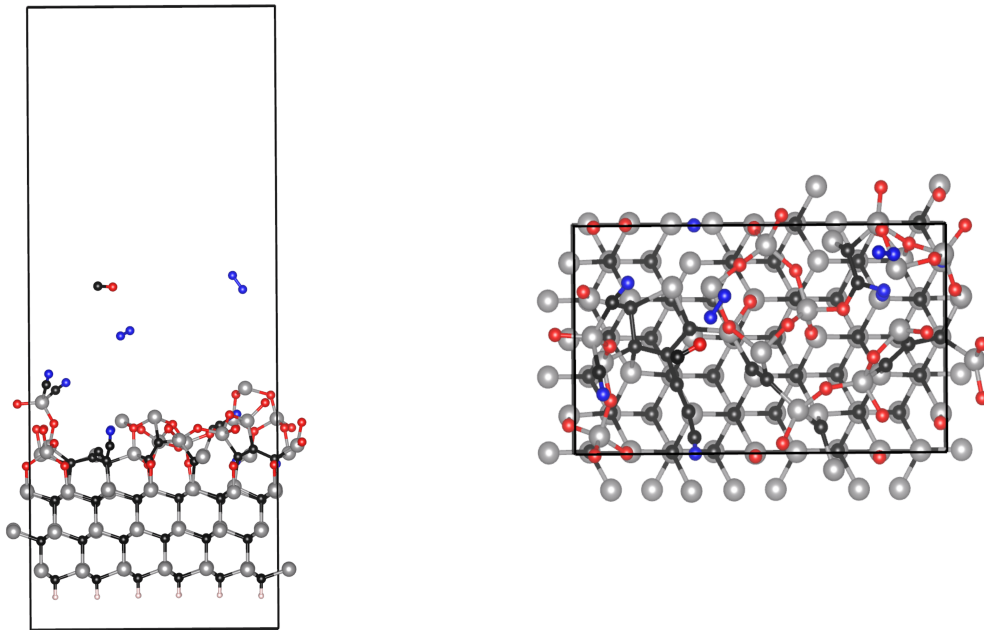


Figure 5.8: Side and top view of nitrogen passivated SiC/SiO₂.

To model the oxidation procedure in the NO and N₂O environment, we want to create an oxygen deficient reaction environment to mimic a two-step oxidation process (like model B in Subsec. 5.1.2). To achieve this, the surface is first oxidized with the full amount of the NO and N₂O, required to convert the topmost layer into a stoichiometric SiO₂ pattern, before the same amount of NO and N₂O is added again.

In the initial oxidation procedure, the NO and N₂O oxidizes the surface of the SiC and the SiO₂/SiC interface. As a product, N₂ and CO is formed. Interestingly, in the first step of oxidation any nitrogen is not incorporated within SiC or SiO₂ matrix either by NO or N₂O. In N₂O environment, N₂O dissociates into NO and N on the SiC surface; the atomic N migrates and react with another atomic N to forms N₂, whereas the NO oxidizes the surface. If more N₂O/NO is added, more of the SiC layer get oxidized. We also observed CO and CO₂ formation along with N₂. Few of the atomic nitrogen atoms get trapped in SiO₂ matrix: they migrate in the matrix and bonds with the under-coordinated Si and C atoms. The atomic nitrogen mostly forms C≡N bonds, with an average bond length of 1.15 Å. This CN molecules further bond with either an oxygen or a silicon of SiO₂. Some nitrogen atoms are observed to saturate dangling bonds by Si=N formation and replace oxygen in a strained Si–O–Si bonds.

Nitrogen atom can also be in a carbon site. There are two possible bond configurations of N at the C sites. From the XPS results, Xu *et al.* concluded that most of the N atoms are bonded with three Si atoms [208], whereas, Umeda *et al.* reported that the N donors (tetra-coordinated N) occupying substitutional C sites [211]. These nitrogen atoms are observed in the channel region after post-nitridation annealing. However, the reported amount of tetra-coordinated N is $5 \times 10^{17} \text{ cm}^{-3}$ ([212]), which is lower than the detection limit of XPS. Experimentally measured photoelectron intensity angular distribution (PIAD) pattern by Mori *et al.* is qualitatively similar with the simulated PIAD pattern for the atomic arrangement of around N atom [213]. This result supports the conclusions, given by Xu *et al.*

In our calculated structures, we also observed that some of the nitrogen atoms partially replace the C atoms in the top layer and directly bond to three Si atoms, while the Si atoms bond to the remaining C atom sites; this supports the previous experimental data [213, 208]. The average bond length is around 1.75 Å, comparable with the Si–N bond length measured in the gas phase. The Si–N bond length has been determined experimentally by photodiffraction experiments to be $1.730 \pm 0.08 \text{ Å}$, which agrees very well with our results [214]. The Si–N bond length is shorter than the Si–C in the SiC matrix. Due to the difference in the bond length between Si–C and Si–N, interfacial N causes interface strain within SiC at the SiO₂/SiC interface [215]. The formation of CN molecules means that only few small carbon clusters are formed at the interface. However, it also leads to the presence of carbon atom in the SiO₂ matrix. It is also observed that this CN molecules eventually attach with oxygen and extracts CO as a byproduct and leave behind the nitrogen atoms. Interestingly, previous experimental studies also reached a similar conclusion [200, 216]. Similar type of bonding is also observed when SiC is oxidized in an N₂O environment. Small carbon clusters are formed and Si bonds are saturated, leading to a better mobility in SiC/SiO₂. This observation is consistent with experimental findings [217, 218].

Hence, the results in this study indicate that there is a trade-off relationship between interfacial N reducing the interface defects by capping the Si dangling bonds and

the interfacial strain degrading the inversion layer mobility.

5.1.6

Raman spectra

The signatures for carbon clusters can be gathered from our measurements of Raman spectroscopy. These experiments were carried out at 300 K using the micro Raman spectroscopy setup based on a 532 nm single mode continuous wave laser and an inverted microscope (Leica DM5000 equipped with a 100x NA=0.9 objective, Germany) with Raman filter (Semrock, Rochester, U.S.A.) with 40 μm slit.

In order to obtain a thorough understanding on the composition of these nucleates, a second order Raman spectroscopy measurements to identify the chemical bonds involved in the observed nucleates is used, thus allowing distinction of sp^2 sites within a matrix of sp^3 SiC [219]. The used sample were on the same TGO and pTGO after the oxide was removed from the top. To facilitate the identification of the carbon bonds at the interface and after incomplete oxidation of SiC, the background/ reference spectra from the TGO spectra is subtracted. The resulting Raman spectrum after the background correction with a clean SiC wafer exhibits ten sharp peaks corresponding to vibrational excitation modes of bonds associated with the different carbon species in different bonding states (Table 5.2) [220].

Experimental Results	Theoretical Results	Literature Review [221, 222, 223, 224]	Association of each peak
1477		1470	benzene related vibrations in finite size crystal
1524	1523	1530 1523	3 coordinated amorphous C; polyene
1543	1530	1554	G band for C film with low sp^3 content
1573	1554	1594 1582	G band shift of the graphitic band (1582) due to epitaxial strain for graphene on SiC
1605			aromatic $\text{CB}=\text{C}$ stretching
1622	1622	1622	Aromatic $\text{CB}=\text{C}$ and sp^2 dimers in sp^3 phase
1653		1660	G band for ta-c
1688	1686	1686	$\text{C}=\text{C}$ or $\text{C}=\text{O}$
1713	1717	1712 1720	$\text{C}=\text{O}$ stretch symmetric stretching carbonyl / Benzene related
1740		1735	asymmetric stretching of carbonyl $\text{C}=\text{O}$

Table 5.2: Comparison of experimental and theoretical Raman signals with literature values and the corresponding, most plausible undesired/defective carbon bonds

Finite size carbon crystals and/or benzene-like rings are associated with the Raman peak at 1477 cm^{-1} . Furthermore, our Raman analysis provides clear evidence for the simultaneous presence of both graphitic and amorphous (a-C) bands in the nucleate rich region close to the interface. The graphitic carbon is recognized by the graphitic band or G-band @ 1622 cm^{-1} , corresponding to C–C vibrations of sp^2 dimers embedded in an sp^3 environment; The amorphous carbon is recognized by the virtual absence of the defective graphite or D-band characterized by a peak maximum @ 1573 cm^{-1} [221, 222, 223, 224]. The peak assignments have been provided in Table 5.2.

The interpretation of the experimental Raman spectra is supported by the computed frequencies of the normal vibrational modes [Table 5.2] for all the structures (oxygen rich (model A) and oxygen deficient (model B) simulation) where carbon rings are formed. Notably, a numerical calculation of the full Raman spectrum is not feasible due to the very large number of atoms. Further on, laser heating or quantum confinement may lead to certain shifts in the value between theory and measured Raman peak position. The selection of the Raman active modes is based on identification of corresponding frequencies in numerical and experimental Raman data in consistency with symmetry considerations. In this way, we can attribute some experimental peaks such as 1523 cm^{-1} , 1622 cm^{-1} and 1686 cm^{-1} to the vibrational modes of 1524 cm^{-1} , 1622 cm^{-1} , and 1688 cm^{-1} respectively (Table 5.2). Further, the two distinct modes from our simulations at 1530.18 cm^{-1} and 1554.51 cm^{-1} are close enough to be associated with the experimentally observed 1543 cm^{-1} peak, while the computed mode at 1717.71 cm^{-1} can be identified with the experimental peak at 1713 cm^{-1} .

A reduction of 6.5% in the Raman intensity of all the monitored (non-SiC) carbon peaks for the HF dipped samples is observed after the samples are exposed to HF. This provides evidence for the reduced carbon content by HF-etching. This finding confirms the reduction in the number of particles/nucleates already observed in the AFM experiment, and provides additional evidence that these defects contain carbon. In the experiments the intensity of the Raman peaks changes after the pure oxygen processed sample has been cleaned using Ozone. There is a drop in the intensity of the carbon peak due to the smaller amount of non-SiC carbon bonds or the size of these defects becoming smaller which is in agreement with our simulation. The AFM results also supports our predictions. The details of the experiment can be found in this reference [225].

5.1.7

Conclusions

Extensive atomistic simulations provide a detailed understanding on the origin of the carbon nucleates such as graphitic (sp^2) and amorphous (sp^3 mixed in sp^2) carbon. Simulation of oxidation of SiC by MHM at DFTB level proved that there is a strong bond between carbon nucleates and the surrounding matrix via Si-C and O-C

bonds. Our Raman results along with DFT/DFTB normal mode analysis further provide conclusive affirmation of the presence of aromatic and amorphous carbon (sp^3 mixed in an sp^2 environment) which is different from the carbon contained in the SiC matrix. Further, the DFT calculations also confirm the impact of the defective carbon accumulations on the electronic structure at the interface. However, after the interface gets passivated with nitrogen during the oxidation of SiC surface in NO/N₂O environment, we have observed smaller carbon clusters at the interface. This study motivates further research to investigate the carbon accumulation mechanisms contributing to the experimentally observed larger nucleates, and towards the role of passivating agents.

5.2 Growth of 2d boron on Si substrates

The discovery of graphene [226, 153], the thinnest, one-atom-thick, planar carbon material, has fueled interest in other reduced dimensionality systems which may have transpiring properties (*i.e.* very high thermal conductivity, electrical conductivity, current densities than their bulk counterparts) [227, 228, 229, 230, 231, 232, 233]. In this context, boron is an appealing element in the periodic table since it is next to the carbon and considered as a potential candidate for 2d material. Bonding between boron atoms is more complex than in carbon; for instance, both two- and three-center B-B bonds can be observed [234]. Thus, boron has an extremely complicated chemistry and structural behavior in its bulk allotropes [235, 236].

2d boron exhibits many unique structures owing to its electron deficiency. It is different from other well-known 2d materials. Generally, 2d boron crystals can be classified into three categories:

- Graphene-like atomically monolayered boron sheets [237, 238].
- 2d boron structures with thickness of a few layers [239].
- 2d boron structures with icosahedral configurations [240, 241, 242, 243].

5.2.1 A brief overview of previous work on 2d boron

The prediction of the B₈₀ buckyball has garnered extensive interest due to its structural similarity to the C₆₀ [244, 245] which opens up the possibility of 2d boron sheet to exist. Borophene was coined to refer to a general class of atomically thin boron sheets [246]. It was followed immediately by the proposal of stable 2d boron sheets with triangular and hexagonal motifs (named as α sheet) [247]. Since then, various buckled and unbuckled monolayer structures of boron, which include the different α -sheets, β -sheets, γ -sheets, $\eta_{1/8}$ and $\eta_{2/15}$ -sheets, triangular sheet, or graphene-like hexagonal sheet have been predicted from ab initio computations [248, 249]. The

absence of layered boron bulk materials makes it difficult to mechanically exfoliate the corresponding 2d sheet, as successfully realized in other 2d materials [230]. As a result, thermal evaporation deposition, chemical vapor deposition and molecular beam epitaxy should be the potential techniques to experimentally produce a 2d boron sheet. The choice of substrate is critical for the synthesis of 2d B. After careful considerations and theoretical calculations, different metal *i.e.* Cu, Ag, Al and Au were selected as substrate [250, 251]. Recently two experimental groups confirmed the predictions by synthesizing boron monolayer on Ag substrate [237, 238].

2d multilayer boron sheet which is semiconductor (bandgap of 2.35 eV) has been synthesized by chemical vapor deposition method on Cu substrate [239]. Whereas, 2d semimetallic multi-layered boron sheet was predicted to grow on Pb (110) substrate only by manipulating the surface thickness [252].

2d icosahedral boron sheets have also been topic of interest in this decade. Various groups have proposed 2d icosahedral boron sheets based on B_{12} structures [253, 254]. Recently, four discrete boron icosahedral structures, namely, the icosahedral chain and three icosahedral sheets (referred as the icosahedral α , δ_4 , and δ_6 sheets, respectively) were predicted by Kah et al. using semi-empirical Hamiltonian method [241], deeming δ_6 -icosahedral sheet as the most stable structure among them.

5.2.2 Boron doping in silicon

To modify the electrical features of Si for Si-based electrical device, B is used as a p-type dopant due to its very high solid solubility. Boron atoms also have a high diffusivity rate which tends them to form clusters in Si sub surface and on surface layers. Various experimental studies showed that at high concentration of boron and at high temperature B atoms have a strong tendency for segregation at sub-surface layer [255, 256]. However, by controlling different parameter, B accumulates on the surface [184, 189, 257]. PurB³ is another method which has been used to form boron layers on (100) Si surface [185, 186]. Depending upon the temperature and pressure the thickness of the boron layer can be controlled from few nanometer to atomically thin layer [187, 188].

Above experimental results motivate us to consider semi conductors *i.e.* Si as a substrate to grow boron 2d structures.

5.2.3 Silicon surfaces

Silicon surfaces reconstruction of (100), (111), (113) and (110) were explored in our study. The final configuration for each of the surfaces is shown in Fig. 5.9. Each of the surfaces are passivated at the bottom with H. Experimentally, the

³Based on chemical vapor deposition (CVD) method

reported stability of the Si surfaces is as follows: (111)>(001)>(113)>(110) (at the low temperature) and (001)>(113)>(110)>(111) (at high temperature) [258]. Their respective electronic band structure is shown in Fig. 5.10 and it shows that Si(100) and Si(111) surface has a small bandgap whereas Si(110) and Si(113) are metallic.

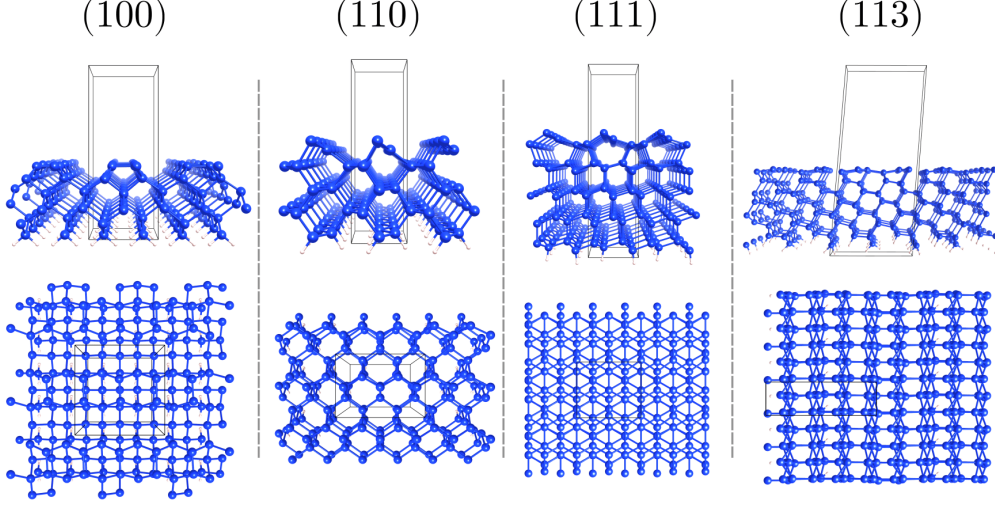


Figure 5.9: Silicon surfaces reconstruction obtained in this work (top and side views).

Because of the computational limitation, we considered only MH runs with B doping Si surfaces as follows: 4 layers of Si for all surfaces except for Si(111) (3 layers). In each case a vacuum of 10 Å along z-direction was used. 2d boron configurations obtained from our MH runs are re-optimized with more Si layers so that we can obtain a proper stability order of the 2d layer as well as their chemical properties. In order to explore the dependence on boron content, MH runs were extended from 1 to 24 atoms for the respective 4 Si-surfaces. The formation energy of doping B atoms in Si surfaces is defined as:

$$\Delta E_f = (E_{tot}(SiB) - E_{tot}(0))/n_B - E_{ref} \quad (5.1)$$

where

$$\Delta E(ref) = E_{tot}(D) - E_{tot}(0) + n_{Si}E_{tot}(Si) \quad (5.2)$$

Here, $E_{tot}(D)$ is the total energy of a supercell with one B complex and $E_{tot}(0)$ is the total energy of the same supercell, but without the B complex (i.e. only Si surface). n_{Si} is the number of Si atoms transferred to the chemical reservoir (taking as bulk Si). $E_{tot}(Si)$ is the total energy per atom in bulk Si, respectively and $E_{tot}(SiB)$ is the energy of the total system. The formation energy of the isolated boron sheet was computed according to

$$E_f = (E_{sheet}/N - E_{at}) \quad (5.3)$$

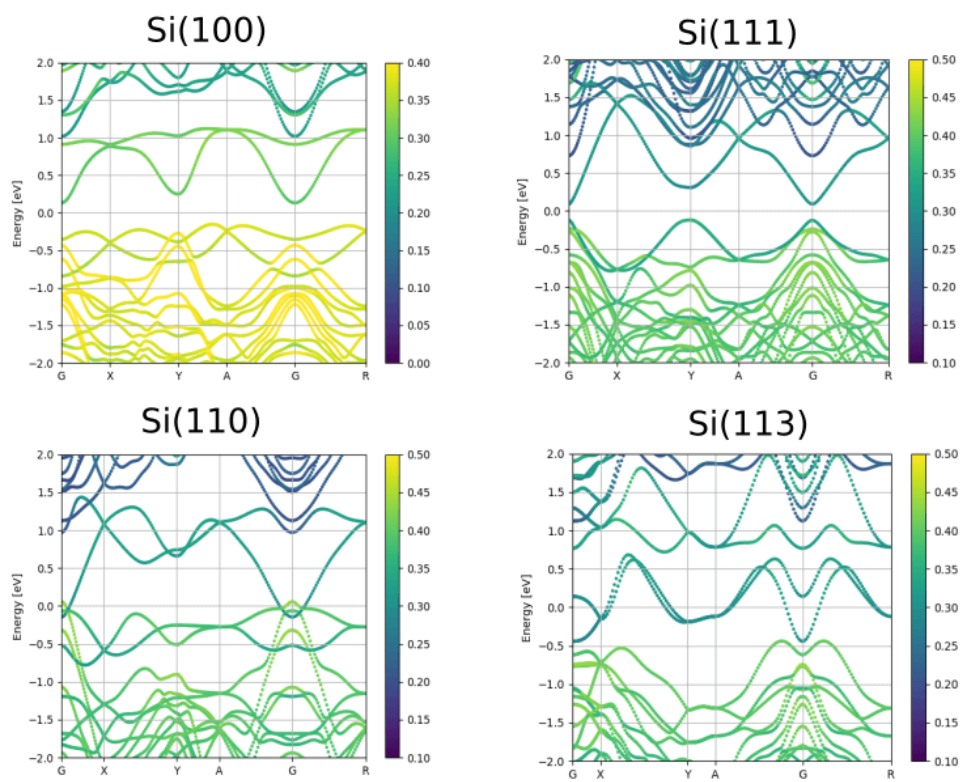


Figure 5.10: Electronic band structure of silicon surfaces reconstruction considered in this work.

where E_{sheet} is the total energy of the sheet with n atoms, and E_{at} is the energy of a single spin-polarized boron atom.

5.2.4 B on Si (100) surface:

The crystal explorations used 2×1 asymmetric buckled dimer reconstruction on rectangular supercell of 3 layers of Si (100) surface. The symmetric dimer reconstruction is higher than the asymmetric buckled dimer reconstruction in energy as observed in previous studies [259]. Our study reveals that single boron atom prefers to substitute one Si atom from the first sub-surface layer. This was also observed from previous theoretical and experimental results [256, 260, 261]. The second boron atom also prefers to substitute another Si atom from the first sub-surface layer. The substitutional impurities in the near-surface layer, resulting in the ejection of two host Si atoms, which move into the ad-layer. For more than 2 boron atom, few of them substitute the Si atoms and form clusters.

As we increase the number of B atoms to 16, the atoms prefer to stay on the surface. None of them substitute surface or sub-surface Si atoms. 20 boron atom on Si (100) surface forms a stable monolayer of 2d-boron structure. The formation energy for different number of boron atoms on Si (100) substrate is plotted in Fig. 5.11. The formation energy decreases with increasing N , which means that 2D structures become more stable with increasing boron concentration as they approach to the bulk state. It remains nearly constant (0.38 eV/atom) when N is greater than or equal to twelve atoms per unit cell. The number of boron atoms increased gradually. The lowest monolayer have $P12/m1$ symmetry (Fig. 5.12a). The lattice constants for the $P12/m1$ symmetry boron are $a=7.368 \text{ \AA}$, $b=7.725 \text{ \AA}$, and $\beta=94.36805^\circ$ (unique axis b). The bond length between two boron is 1.8 \AA . The 2d boron surface buckled up on top of Si (100) surface and the B-B bond lengths range from $1.8-2.1 \text{ \AA}$. The band structure of Si (100) surface with 2×1 asymmetric buckled dimer reconstruction, is shown in Fig. 5.10. An indirect band gap of 0.2 eV can be observed. In previous experimental and theoretical studies also predict that this type of reconstruction is semi conductor [262, 263]. From Fig. 5.13, we can see that Boron/Si(100) system behaves like a metal at PBE level and HSE06 calculation also supports the conclusion. Interestingly, the Si surface prefers to have 2×1 symmetric dimer reconstruction when boron layer is formed on top of the surface. The surface states due to the reconstructions from the midgap region is removed after boron adsorption. Hydrogen adsorbed 2×1 symmetric dimer reconstruction on Si (100) surface have the similar behavior. It has been observed that the surface states are removed and a gap opens up [264]. The contribution of the new states in the band gap region of Si (100) surface is due to the boron (Fig. 5.13). Few other 2D boron configurations which are slightly higher in energy (0.0006-0.0049 eV/atom) than the lowest energy configuration for boron 20 atoms, are shown in Fig. 5.15(a,b,c). As we increase the number of boron atoms, they start to form layered structures with $P1$ symmetry.

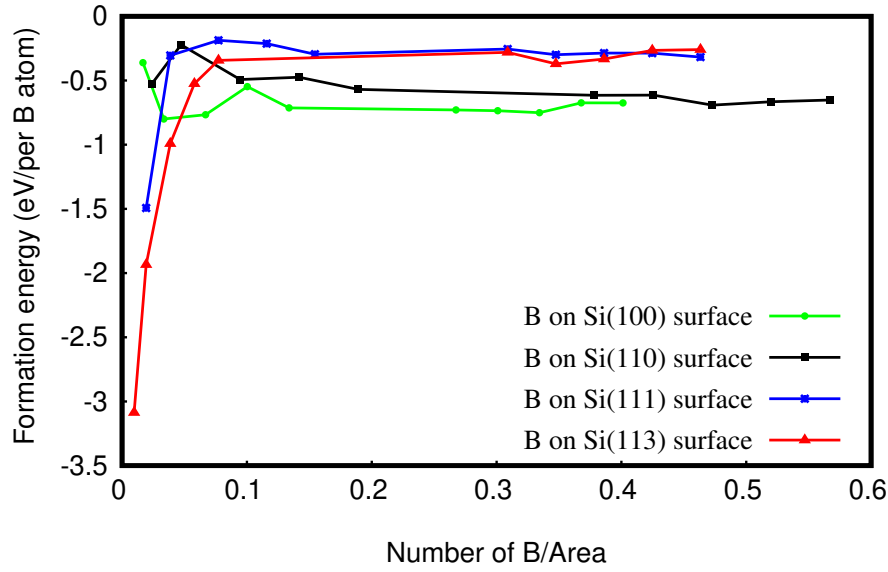


Figure 5.11: Formation energy of different number of boron atom vs the number of boron atom per unit area on different Si surfaces.

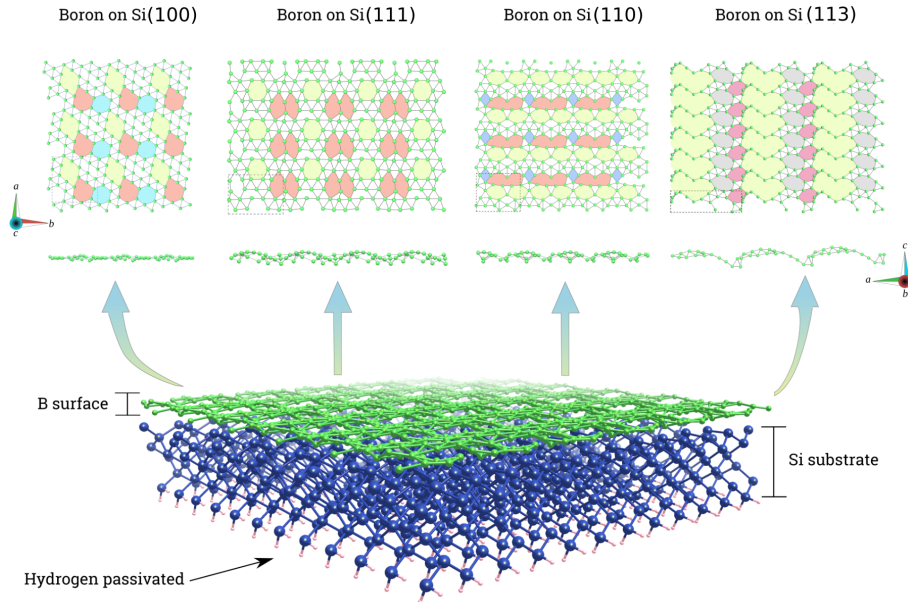


Figure 5.12: Boron monolayer with maximum number of boron on different Si surfaces. If we add more boron atoms, they transform into layered configuration or icosahedral boron surfaces. a. 20 boron atoms on Si (100) surface with P12/m1 symmetry b. 20 boron atoms Si (111) surface with Pm symmetry. c. 18 boron atoms on Si (110) surface with P1m1 symmetry d. 16 boron atoms on Si (113) surface with P1 symmetry.

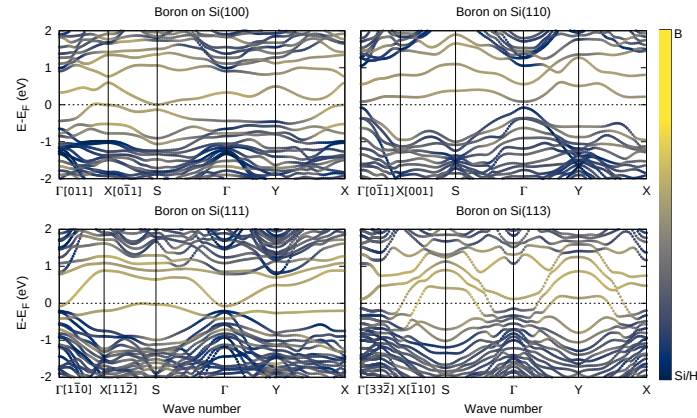


Figure 5.13: Band structure of boron monolayers with Si substrates. Here the boron contribution to the different bands is also shown.

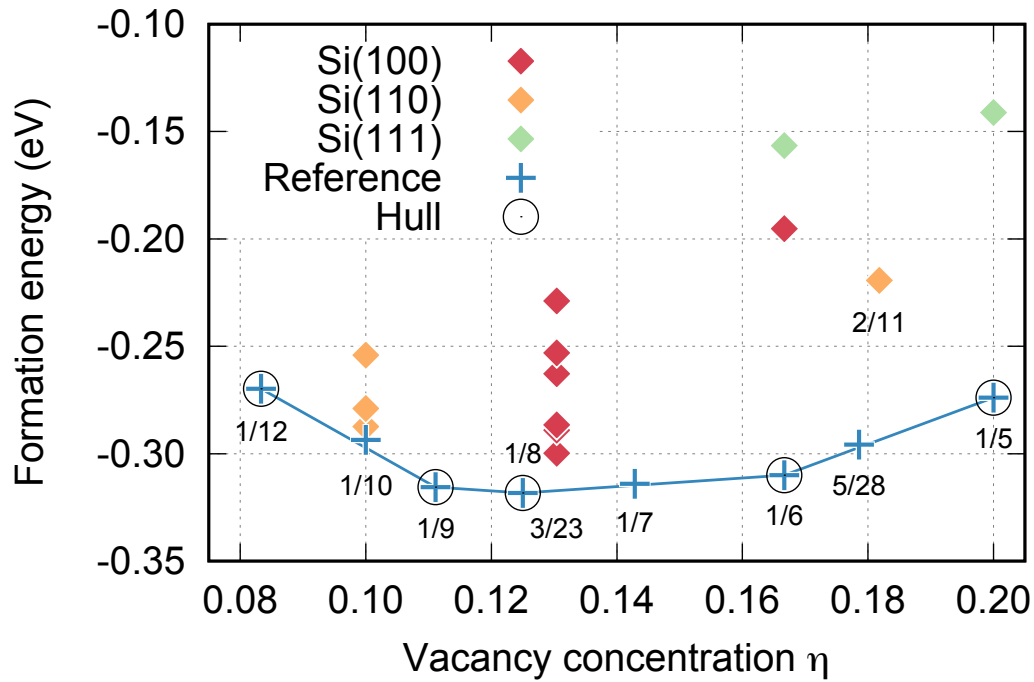


Figure 5.14: Convex hull for 2d boron. The convex hull as defined by the hole concentrations. The blue line represents the lowest energy 2d boron configurations at particular hole concentrations. The other points represent the formation energy of exfoliated 2d Boron stabilised on different Si surfaces.

5.2.5

B on Si (111) surface

Si (111) surface is the second most stable surface of Si in low temperature. Here we have considered Si 2×1 reconstruction. It is a semiconductor (Fig. 5.10) as observed previously [263]. The lowest energy configuration that we obtained from single B atom on Si (111) surface is similar as B-Si(111)- $(\sqrt{3} \times \sqrt{3})R30^\circ$ surface [265]. Two

types of dangling bonds were observed previously: a passivated Si dangling bond with a sub-surface B atom underneath and a Si dangling bond with a sub-surface Si atom underneath which we also observed in our calculation [266]. As we increase the number of boron atoms, they start to substitute other Si atoms or occupy interstitial positions and form cluster at the sub surface region.

12 boron atoms segregate on top of Si substrate. 20 Boron atoms form a single layer on Si (111) surface with P1m1 symmetry (Fig. 5.12). If we add more boron atoms, then 2nd boron layer starts to form with same symmetry or the isomers of P1 symmetry. The formation energies after 16 boron atoms remain constant (Fig. 5.11). The DOS and the bandstructure suggests that the boron monolayer with the Si substrate is metal (Fig. 5.13). The band gap opens if we add more boron atoms to the system. The contribution to the new surface states are not only from the boron but also from the surface Si atoms at the valance band edge. However, the 2×1 reconstruction is removed. The Si-B bond length is around 2.3 Åslightly more than the Si-B bond length during the intrinsic doping (2.1 Å).

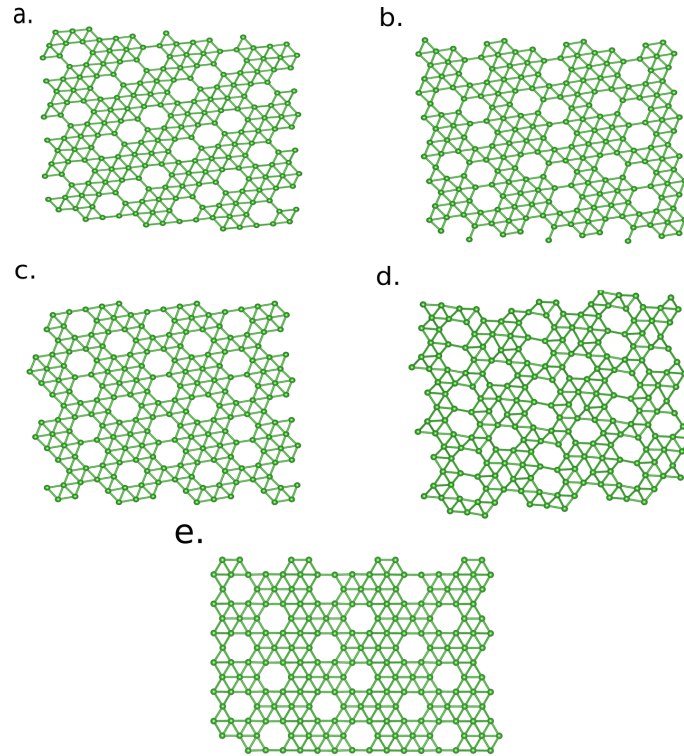


Figure 5.15: different Boron monolayers on different Si surfaces. a. 20 boron atoms on Si (100) surface with P1 symmetry b. 20 boron atoms Si (100) surface with Pm symmetry. c. 20 boron atoms on Si (100) surface with P2/m symmetry d. 20 boron atoms on Si (111) surface with P1 symmetry. e. 18 boron atoms on Si (110) surface with P222₁ symmetry.

5.2.6

B on Si (110) surface:

For Si (110) surface, we started our calculation with 1×1 reconstruction and with four layers. Fig. 5.12c is the lowest energy boron monolayer structure on Si (110) surface with 18 boron atoms and have P1m1 symmetry. There are few other different type of boron moronlayer which are slightly higher in energy (Fig. 5.15e). If we increase the number of boron atoms on Si (110) surface the icosahedral sheets start to form (Fig. 5.16).

B–B bondlength in an isolated icosahedron B_{12} is 1.61-1.75 Å. In our case, the B–B bondlength in the icosahedral sheet (Fig. 5.16a) which is formed by 20 boron atoms, is 1.70-1.88 Å. The icosahedral are connected through a bond length of 1.79 Å which is bigger (0.12 Å) than α -B. They are also connected through a six boron atoms cluster. The size of the B_6 cluster starts to increase as we increase the number of boron atoms into the system. For 22 boron atoms, a B_8 cluster is formed and for 24 boron atoms, B_{11} cluster is formed. The bond length between the two icosahedron is increased (1.87 Å) as we increase the number of boron atoms indicating a weaker interaction.

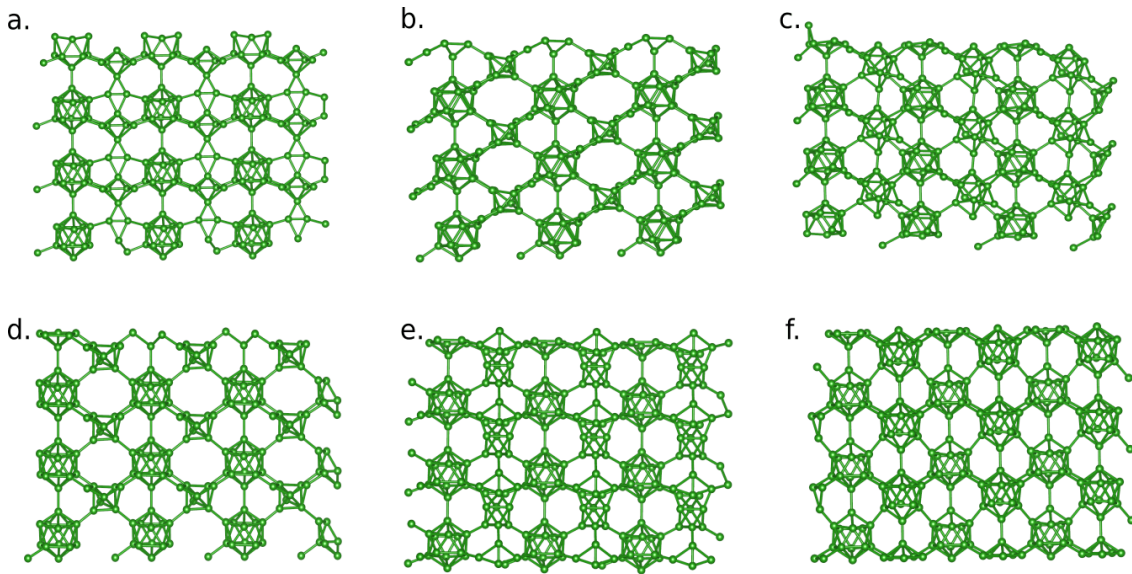


Figure 5.16: Icosahedral boron surfaces on Si (110) surface. The Lowest energy structure by a. 20 boron atoms b. 22 boron atoms c. 24 boron atoms on Si (110) surface. d.-f. metastable boron icosahedral sheets on Si (110) surface.

The monolayer and the icosahedral sheets with Si(110) surface are semi conductors. Clean Si (110) surface with 1×1 reconstruction is metallic (Fig. 5.10c) and the dangling bonds of the atoms of the top layer create new surface states close to the Fermi levels as observed in previous literature [267]. Fig. 5.19 and Fig. 5.13 is the DOS and the band structure for Fig. 5.12c. The band gap is 0.4eV in PBE but according to the hybrid HSE06 calculation, the band gap is 0.6eV. It is not stable

as a free standing layer but transform into β_1^s . The contribution to the valance band edge is still due to the surface Si atoms whereas new states arise near the conduction band edge due to the boron atoms. The 1×1 reconstruction is removed due to the adsorption of boron atoms. There is no dangling bonds present and hence, the surface states from the midgap region is removed.

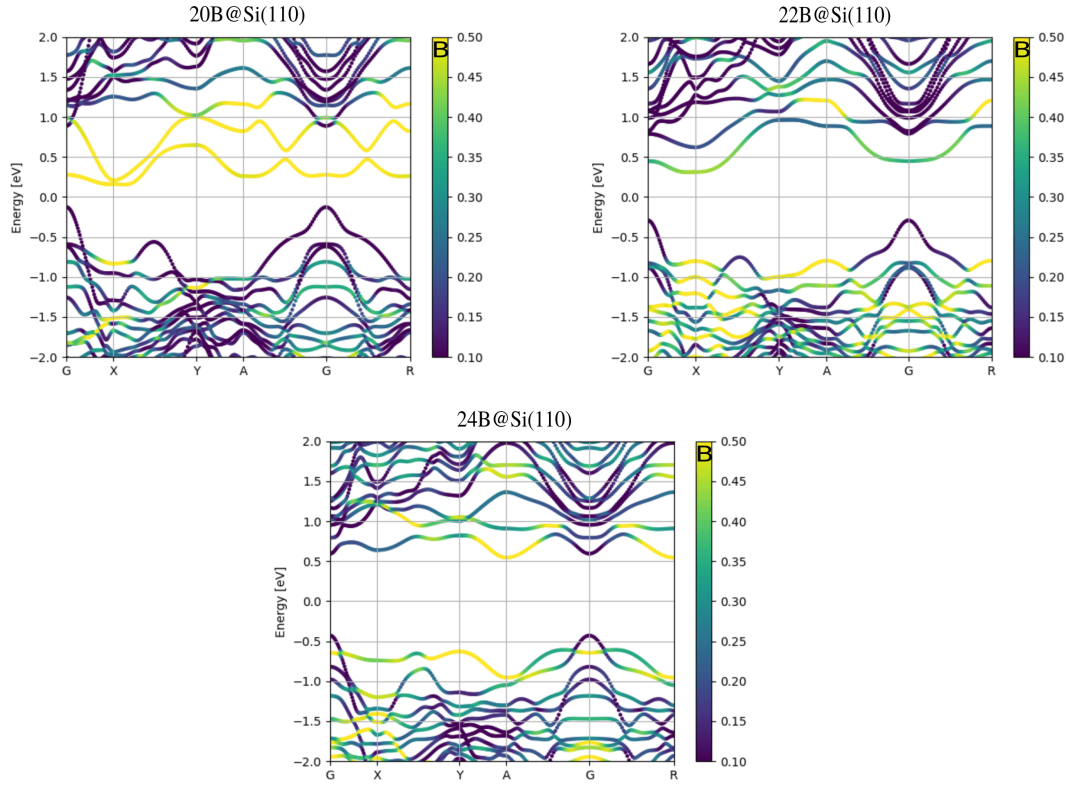


Figure 5.17: Band structure of the boron icosahedral layers (from Fig. 5.16a-c) on Si (110) surface.

The band gap for icosahedral sheets varies from 0.3 to 0.5 eV in PBE and 1.3 to 1.69 eV in HSE06. The DOS and the band structure plots are given in Fig. 5.19 and Fig. 5.17.

Calculated phonon spectra of planer Fig. 5.12C and icosahedral sheets Fig. 5.16a-c are plotted in Fig 5.18 , showing that all four sheets are stable without giving any negative frequencies.

The DOS and Si-B COHP curves for different number of boron atom on Si surface is shown in Fig. 5.19. For boron monolayer on Si(110) surface, most of the Si-B interaction states below the Fermi level is bonding in nature except a small region. As we increase the number of boron atoms, the structural change happens and the monolayer transforms into icosahedral sheets. This transformation opens the bandgap as well as the anti-bonding states disappear. This suggests that there is a strong interaction between the surface Si atoms and the boron atoms.

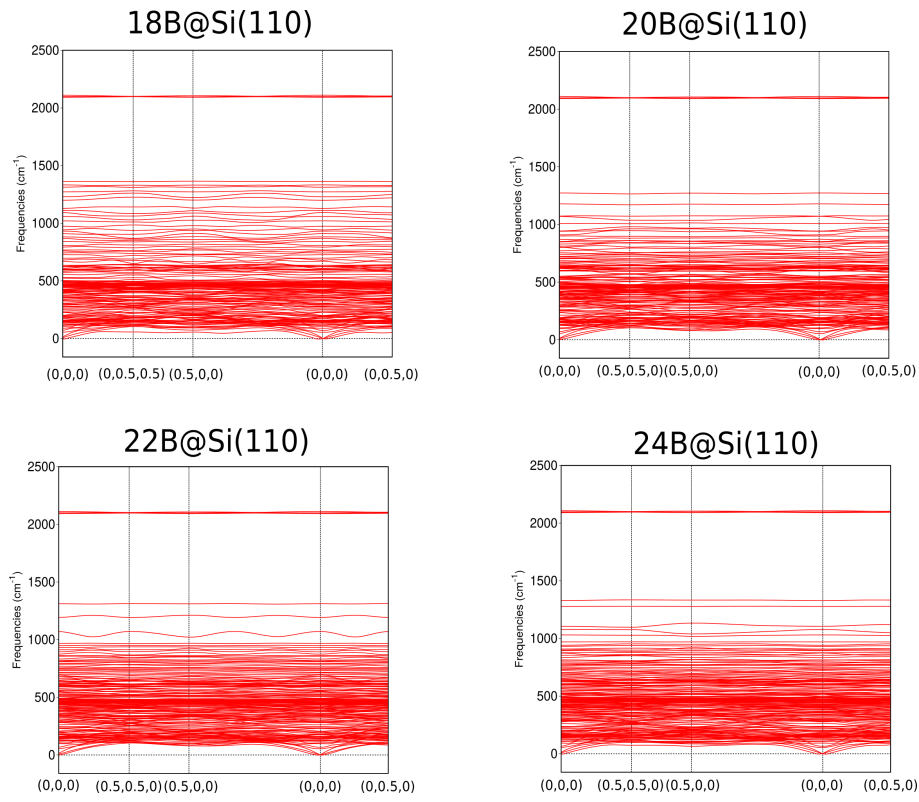


Figure 5.18: Calculated phonon spectra of monolayer (from Fig. 5.12c) and icosahedral layers (from Fig. 5.16a-c) on Si (110) surface.

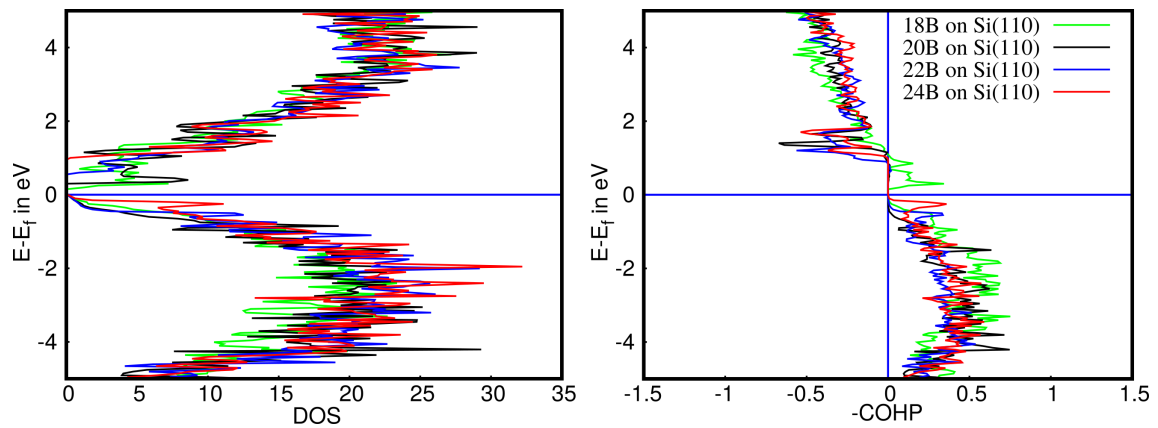


Figure 5.19: DOS and COHP curves 18, 20, 22, 24 boron atoms on Si(110) surface. All curves are shifted so that the Fermi level lies at 0 eV. For COHP, we plotted the surface Si and B interactions.

5.2.7 Si (113) surface:

Until 8 boron atoms on Si (113) surface, boron atoms prefer to be at the subsurface layer, as observed previously in experiments and theory [268, 257]. As we increase the number of boron, they start to accumulate on the surface. With 16 boron atoms, they form a monolayer with P1 symmetry on Si (113) surface. Beyond that number of boron atoms on Si (113) surface, they form layered configurations with P1 symmetry (Fig. 5.15d). The monolayer and the layered configurations are metallic and semiconductors respectively in PBE as well as in HSE06.

5.2.8 Conclusions:

It is important to mention that all the experimental and theoretical investigations so far have only considered metallic substrate to grow boron sheets. In this work, we proposed a different approach, namely to use the rapidly available silicon substrates to synthesized exotic boron layers. By selecting the Si surface and carefully controlling the concentration of boron atoms, we are able to build boron layers with desired electronic properties from semiconducting to metallic. Furthermore our result points towards the stabilization of complex layered configurations and 2d-icosahedral boron structures. More importantly all these structure are not only kinetically but also dynamically stable, which suggests that are likely to be accessible experimentally.

CHAPTER 6

Conclusions and outlook

This thesis is predominantly on the exploration of configurational space of different materials of different dimensions using *ab initio* techniques. We focus on understanding the predicted geometrical configurations and their electronic properties. For this purpose, we employed MHM to explore the PES as well as identify putative low lying energy structures. We have also employed an approximate fp-method and MHGPS to locate transition states. A brief summary of the conclusions is listed below.

Exoheadrally decorated atoms on C_{60} . In Chapter 3, we conducted an unbiased and systematic search for configurations of exohedrally decorated fullerenes with the alkali metals, alkaline-earth metals and other elements. In addition to supporting previous experimental results, our study provided new putative ground states and determined the maximum number of atoms that can homogeneously be distributed on the fullerene surface. Moreover, using the ELF as a descriptor, we were able to scan 64 different elements for homogeneous distributions with up to a maximum of 32 atoms. These results determined that Li, Na, K, Rb, Cs, Ca, Sr, Ba, Sc, Y and La are suited for homogeneous distribution. Among them, Li, Na, K, Rb, Cs, Ca, Sr and Ba elements are already observed in experiments. Interestingly, Y, Sc and La have not yet contemplated experimentally and we predict that these elements should follow an homogeneous distribution on C_{60} .

Exohedrally decorated C_{60} in the presence of the electric field. Experimentally observed dipole moment has been utilized to identify the possible configurations of decorated C_{60} . Inspired by this fact and from the previous section of this chapter, we inspected the change in PES of Li and K decorated C_{60} in the presence of electric fields. We have simulated the similar range of the strengths of the electric

field as can be obtained in the experiment, for instance, near the tip in a scanning microscopes. Our results suggest that some of the metastable configurations can be further stabilize at certain electric fields. A considerable change in PES is implied by these results. One can convert from one structure to the other just by increasing or decreasing the strength of the electric field which can be used in different applications *i.e.* molecular switch. In certain fields and temperature, multiple configurations are degenerate in energy. This will lead to a significant contribution to the experimentally measured dipole moment. Hence, caution must be taken during the theoretical prediction of the structures based on the experimental results.

Metal decorated $C_{48}B_{12}$. The last part of this chapter contains the exploration of metal decorated boron-carbon heterofullerenes. Previous computational studies suggested that homogeneously coated dilute $C_{48}B_{12}$ cage are very stable which contradicts our findings. The decoration destroys the dilute $C_{48}B_{12}$ cage with the exception of Li. The bonding between such destroyed configurations are difficult to generalize. The results provide valuable informations for experimental efforts of synthesis such heterofullerenes. Our results also suggest the adequacy of the PES search.

Exploration of $Si_{20}H_{20}$ cluster PES. The first part In Chapter 4 is about the stability of $Si_{20}H_{20}$. Even though the theoretical dodecahedron configuration of $Si_{20}H_{20}$ has been established as a global minima a decade ago, still it is not possible to synthesize. Here we compared the fp based disconnectivity plots of $Si_{20}H_{20}$ and other fullerene configurations *i.e.* $C_{20}H_{20}$ and C_{60} which are experimentally realized. Despite the high energy barrier between the intermediate states and the global minima, similar as $Si_{20}H_{20}$, the funnel gradient and the configurational entropy will lead to global minima of those configurations. Whereas, $Si_{20}H_{20}$ will get lost in their fractal shaped funnels. Hence as a summary of this work, we can say that the complicated pathways between the $Si_{20}H_{20}$ clusters lead to the lack of observation of the global minima in the experiment.

Unbiased search of $[Si_{32}Cl_{45}]^-$ and $[Si_{32}Br_{45}]^-$. The last part of Chapter 4, we have explored PES of $[Si_{32}Cl_{45}]^-$ and $[Si_{32}Br_{45}]^-$ which contains a Si_{20} core. Even though the ground state of $[Si_{32}Cl_{45}]^-$ is stable but according to Boltzmann statics other isomers are possible to synthesize at very high temperature. The symmetric decoration of Si_{20} provides the stability of the system. The extra charge is distributed over the cluster, providing similar type of bonds and bond lengths. The clusters are inert in nature and can only be attached to each other by some ligands. This study provides a further understanding in stabilizing mechanism of Si_{20} .

Analysis of carbon defect assessment at the SiC/SiO₂ interface. In the first section of Chapter 5, we provided the size, structure and the characteristic of carbon nucleates at the SiC/SiO₂ interface. We oxidized the SiC surface in diluted as well as rich environment of oxygen, NO and N₂O. Different environment provides different type of carbon nucleates such as graphitic (sp^2) and amorphous (sp^3 mixed in sp^2) carbon at different position of the SiC/SiO₂ matrix. A strong bond between carbon nucleates and the surrounding matrix via Si-C and O-C bonds is observed

after the MHM runs at DFTB level and local optimization by DFT. Fused carbon rings and small carbon clusters are obtained at the interface whereas semi-planar graphene like configurations are formed in SiO₂ matrix. Oxidation in nitride species environment incorporated nitrogen at the interface, resulting in small carbon clusters. Raman results and AFM studies which were done by Dipanwita Dutta from the Paul Scherrer Institut (PSI) supports our prediction. The reduction in band gap observed experimentally and confirmed theoretically is due to the carbon nucleates.

Growth of 2d B structures on Si substrates. The last section of Chapter 5 provides a study of 2d boron nucleations on Si substrates. Previous experimental and theoretical studies have considered only metal substrates to grow 2d boron. Herein for the first time, we have shown that different type of boron layered structures can be stabilized on Si substrates. The high solubility of boron atoms on Si surface might be a challenge but the high diffusivity helps to segregate on the surface by controlling the temperature in experiments. By considering different Si-substrates and boron density, one can stabilize particular boron layers. Not only metallic monolayers, which are usually common for this system, but also semi conducting layers are possible to stabilize. Furthermore, increasing the number of boron results on more complex icosahedral- and multi- layer sheets that are likely to be synthesizable. Finally, all the structures that were studied in detail in this thesis, are kinetically as well as dynamically stable which suggests that they are experimentally synthesizable.

In retrospect, we have shown the successful application of a powerful method to explore the PES in a wide range of materials systems, from low dimensional clusters, to surfaces, to interfaces and to large periodic bulk systems. The importance of a complete and thorough search of PES was highlighted for different materials. We explained the reasons behind the lack of experimental confirmation of some theoretical predictions. Such prediction schemes are very promising and powerful tools, and we expect them to lead to significant advances *in silico* material design, a domain still in blossom stages. Finally, the studies presented in this work offer a guidance for current experimental efforts and provide a glance into the future for synthesizing new materials based on our predictions.

APPENDIX A

Minima hopping guided path search (MHGPS)

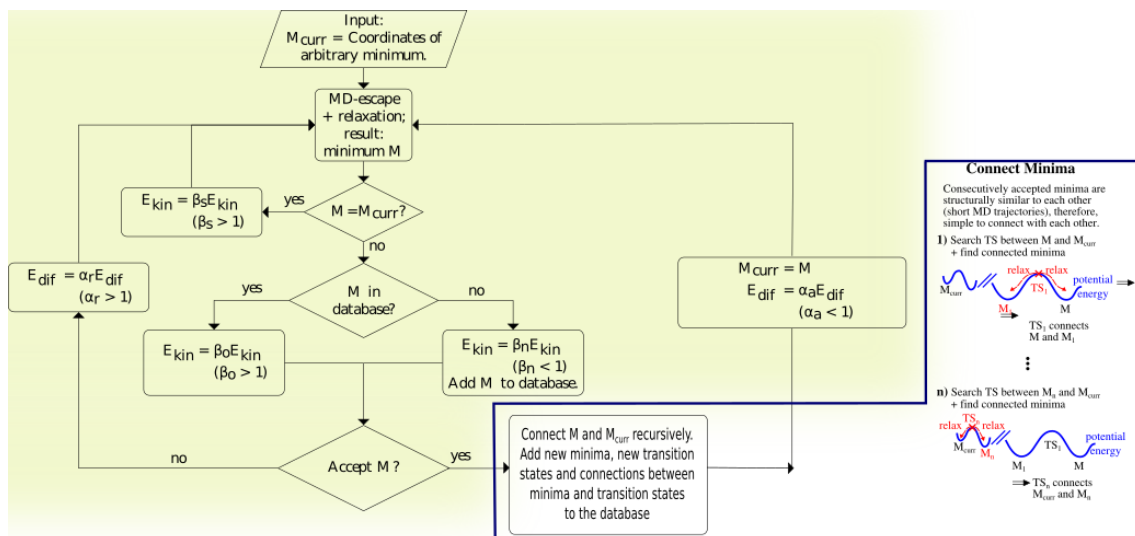


Figure A.1: MHGPS approach for reaction pathway sampling. The shaded region represents MHM algorithm.

APPENDIX B

Electron localization function (ELF)

Becke and Edgecombe introduced ELF to measure the electronic localization in the atomic and molecular system [269]. The original formula is based on the Taylor expansion of the spherically averaged conditional same-spin pair probability density to find an electron close to a same-spin reference electron. According to Hartree-Fock (HF) approximation:

$$P_2(r, r') = \rho(r)\rho(r') - |\rho_1(r, r')|^2 \quad (\text{B.1})$$

where $P_2(r, r')$ is the probability density to simultaneously find two like spin electrons at positions r and r' . $\rho(r)$ and $\rho(r')$ are the electron densities. $\rho_1(r, r')$ is the one-particle density matrix of the HF determinant.

$$\rho(r, r') = \sum_i^{\sigma} \psi_i(r')\psi_i(r) \quad (\text{B.2})$$

where the summation runs over all occupied σ -spin (i.e. either up or down spin) orbitals $\psi_i(r)$. Now we can define the conditional probability as the probability density to find an electron at some position r' if a like-spin reference electron is located with certainty at position r .

$$P_{cond}(r, r') = \rho(r') - |\rho_1(r, r')|^2 / \rho(r) \quad (\text{B.3})$$

the localization of an electron with the probability density to find a second like-spin electron near the reference point is given by

$$D(r) = \sum_i^{\sigma} |\nabla \psi_i(r)|^2 - \frac{1}{4} \frac{|\nabla \rho(r)|^2}{\rho(r)} \quad (\text{B.4})$$

Here the Pauli repulsion is described by the smallness of the $D(r)$ which is a measure of electron localization. Using this factor for uniform electron gas Becke and Edgecombe defined ELF as follows:

$$\eta(r) = \frac{1}{[1 + \chi_{BE}^2(r)]} \quad (\text{B.5})$$

where

$$\chi_{BE}(r) = \frac{D(r)}{D_h(r)} \quad (\text{B.6})$$

Since the pair density is not explicitly defined the original formulation of ELF derived from the pair density is not applicable. However, Savin et al. observed that the Kohn-Sham orbital representation of the Pauli kinetic energy density has the same formal structure as the expression of Becke and Edgecombe. This DFT-ELF approach evaluates the Pauli kinetic energy density based on the diagonal elements of the one-particle density matrix (the electron density) [270]. The Pauli kinetic energy is the energy due to the redistribution of the electrons in accordance with the Pauli principle and is the integral of the Pauli kinetic energy density:

$$t_P(r) = t(r) + \frac{1}{8} \frac{|\Delta\rho(r)|^2}{\rho(r)} \quad (\text{B.7})$$

It is the more or less arbitrary division of $t_P(r)$ by the kinetic energy density of a uniform electron gas of the same electron density (with the Fermi constant $c_F = \frac{3}{10}(3\pi^2)^{\frac{2}{3}}$).

$$t_h(r) = c_F \rho(r)^{\frac{5}{3}} \quad (\text{B.8})$$

For a closed shell system the ratio

$$\chi_S(r) = \frac{t_P(r)}{t_h(r)} \quad (\text{B.9})$$

$\chi_S(r)$ is identical with the ratio $\chi_{BE}(r)$. This identity holds also for an open shell system, when the kinetic energy densities are computed for the corresponding spin part only. $\text{ELF} = 1$ corresponding to perfect localization and $\text{ELF} = \frac{1}{2}$ corresponding to the electron gas.

APPENDIX C

Measuring structural difference

The identification of two structures of N atoms based on their energies is not sufficient for many cases. The enthalpy degeneracy within the short range potentials requires some additional method to distinguish different structures. The most natural way to calculate the difference by root-mean-square displacement (RMSD) by shifting and rotating the two geometries and by permuting the indices of the atoms. The RMSD is given by

$$RMSD(\mathbf{R}^A, \mathbf{R}^B) = \frac{1}{\sqrt{N}} \min_{U, P} \|\mathbf{R}_1 - U \mathbf{R}_2 P\| \quad (C.1)$$

where \mathbf{R}_i^A and \mathbf{R}_i^B are the coordinates of two N atom configurations measured from their respective centroids. P and U are a $N \times N$ permutation and rotation matrix respectively. The RMSD value is minimal if the two structures are similar. The rotation and permutation is codependent. Hence it is problematic to find an optimal value for them especially for geometrically distinct systems. This problem was solved by Monte Carlo method but it is limited due to the time scales exponentially with the number of permutable atoms. Because of this reason Sadghi *et al.* introduced another quantity to distinguish the structure which is called as fingerprint distance. The configurational fingerprints are given by the eigenvalues of an overlap matrix [271].

$$O_{ij} = \int \phi_i^l(\mathbf{r}) \phi_j^{l'}(\mathbf{r}) d\mathbf{r} \quad (C.2)$$

where ϕ_i are the Gaussian type orbitals centered on the atom at position \mathbf{r}_i and is

given by

$$\phi_i^{\mathbf{l}}(\mathbf{r}) \propto (x - x_i)^{l_x} (y - y_i)^{l_y} (z - z_i)^{l_z} \exp(-\alpha_i |\mathbf{r} - \mathbf{r}_i|^2) \quad (\text{C.3})$$

Here $\mathbf{l}=(l_x, l_y, l_z)$ is an angular momentum $L=l_x + l_y + l_z$. The orbitals are classified depending on their value of L *i.e.* s -type orbital is $L=0$, p -type orbital is $L=1$, or d -type orbital is $L=2$. α_i is the orbital width and they are inversely proportional to the covalent radius of the atoms on which the orbitals are centered on. The structural difference is given by the root mean square difference of the two fingerprint vectors. This fingerprint distance is invariant under translations, rotations, reflections as well as under the permutation of the atomic indices. They are computationally cheap and reliable to distinguish distinct geometrical configurations.

APPENDIX D

ELF for all decorated C_{60} configurations

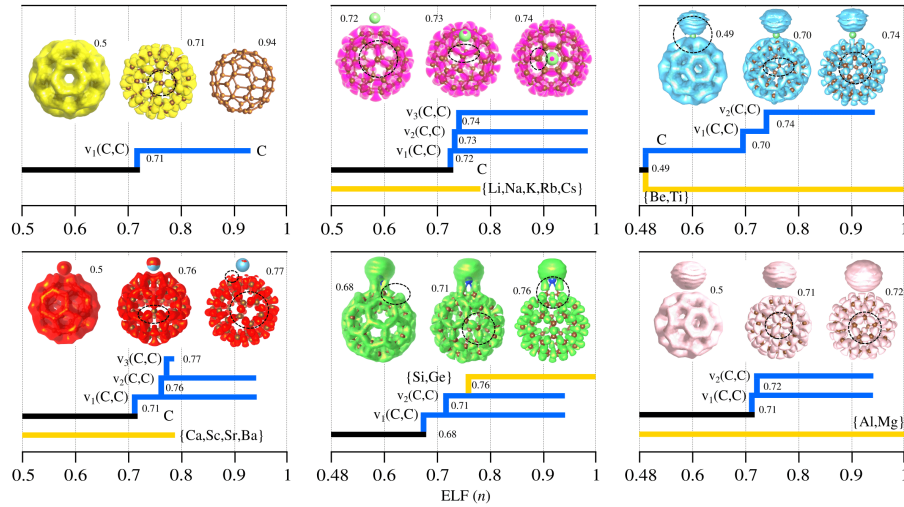


Figure D.1: different ELF-prints we have found for different single atom adsorbed on C_{60}

The elements in white in periodic table can be sub grouped in few different classes. One of the distinct class involves p-block elements, and more generally those elements that covalently interact with carbon in C_{60} . Fig. D.1 depicts the typical picture found with Si, Ge, etc. The C–C bonding starts to bifurcate at lower values of η (0.68) which contains only two carbon attractors, the carbon-silicon bonding (purely covalent) is split only for larger values above 0.76. Be and Ti (Fig. D.1) are of particular interest, for values of 0.5 (free electron type interaction) as the s-electrons are shared and forms bonds which retains a particular topology. The

bifurcation suggests that the metal atom volume (yellow line in diagram) is split at 0.49 initially and further the carbon-carbon volume are split at high values 0.70 and 0.74. They are marked with dashed-black circles the volume separation for the corresponding regions in the C_{60} .

APPENDIX E

Si₂₀H₂₀ disconnectivity plot for different number of low energy
structures

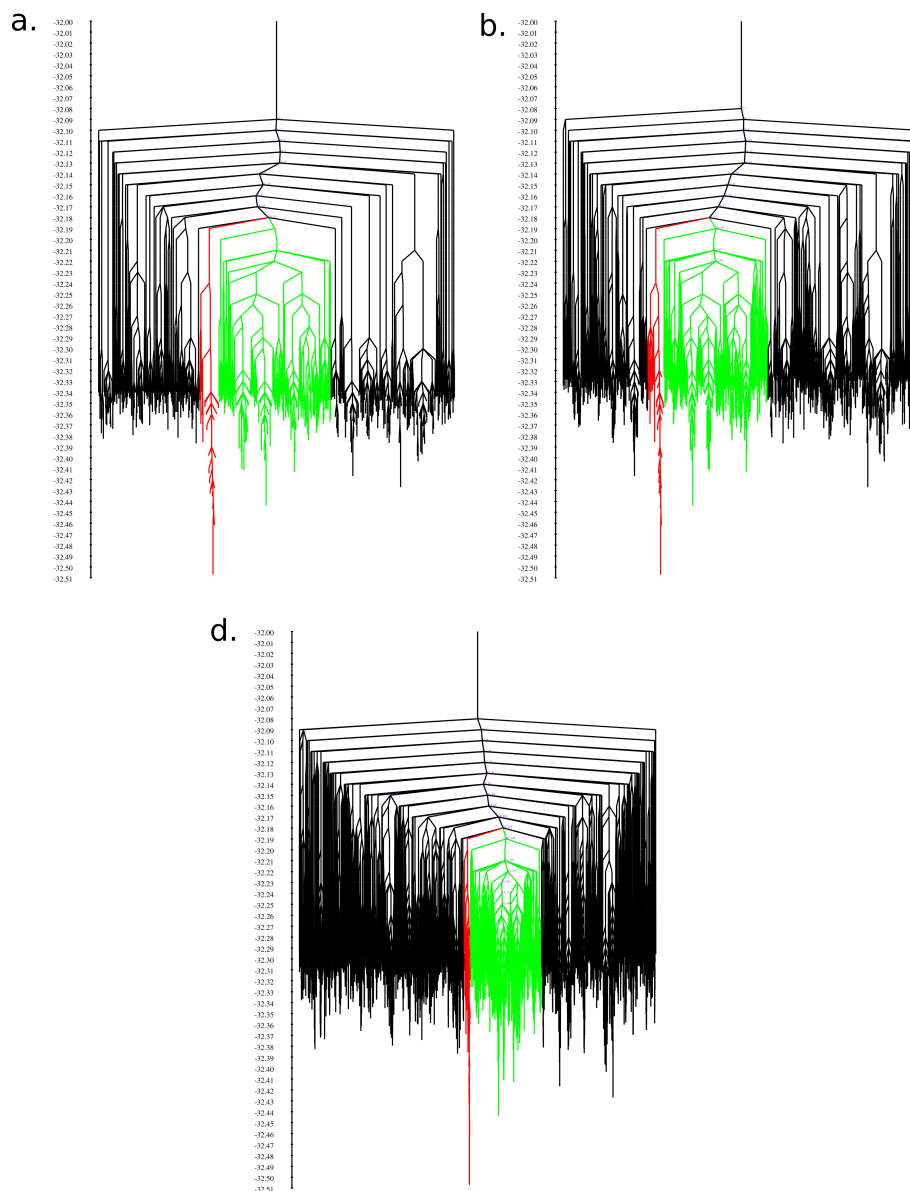


Figure E.1: Disconnectivity plot for different number of low energy configurations. a) 900 b) 1600 c) 8000 configurations are considered. The green funnel represents the biggest funnel and the global minimum is in the red funnel.

APPENDIX F

Lowest energy pathway from the lowest energy structure of
one funnel to the global minimum of $\text{Si}_{20}\text{H}_{20}$

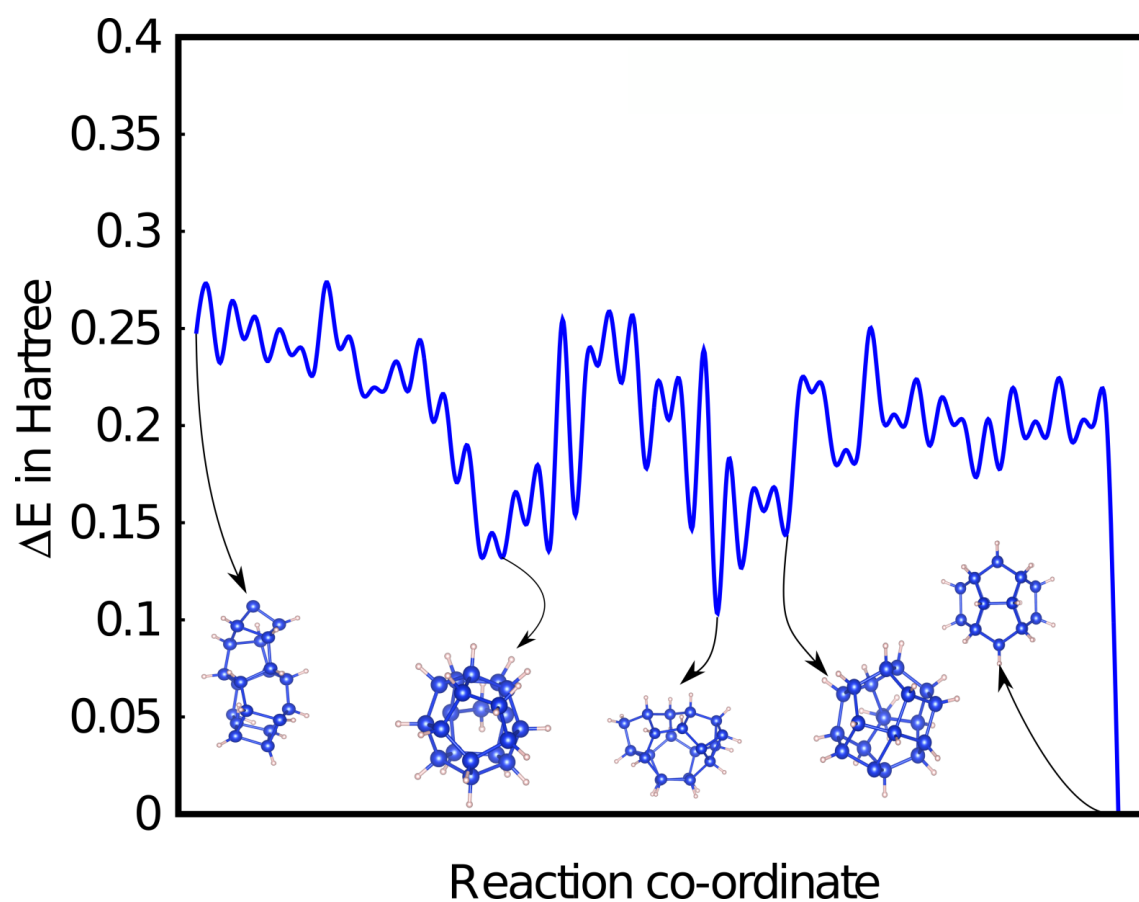


Figure F.1: A possible reaction pathway path from the hydrogenated Si_{20} global minimum structure of Si_{20} to the dodecahedron $\text{Si}_{20}\text{H}_{20}$ ground state configuration found by BMHPGS. The shown energies are the energies from the physical potential energy surface without the bias.

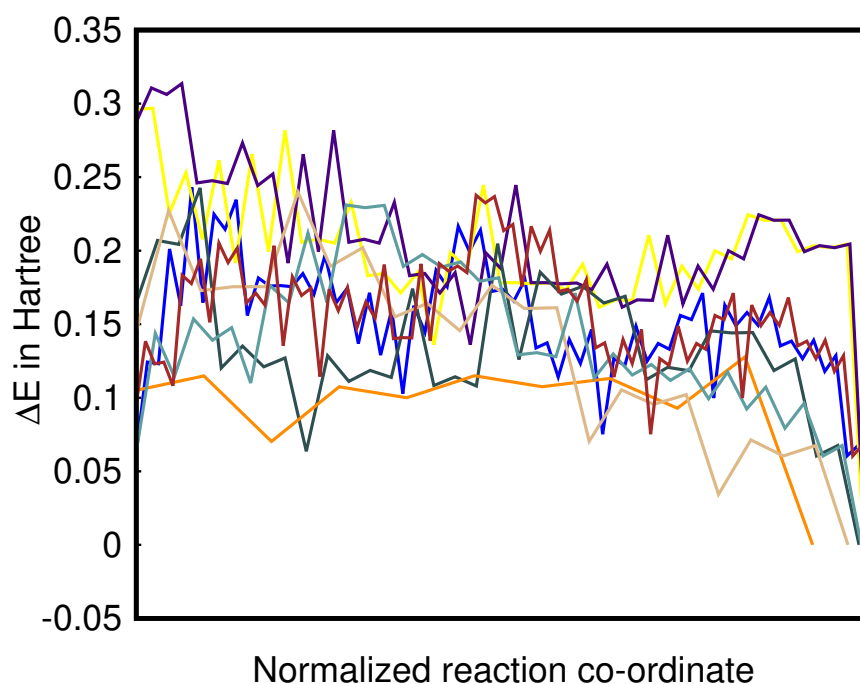


Figure F.2: Pathway from 8 different local minima to the ground state configuration of $\text{Si } 20 \text{ H } 20$. All the initial structures are in the energy difference range of 0.05-0.1 Ha and are the bottoms of different superbasis. Only the orange path was started in the superbasis containing the global minimum. For this reason this path does not have to overcome the higher barriers between superbasis, that have a height of 0.08 Ha or more. In each case the system goes through a flat region of potential energy surface before it reaches to global minimum funnel.

Bibliography

- [1] R. C. Weast, M. Astle, and W. Beyer, "CRC handbook of chemistry and physics," 1985. [2](#), [46](#)
- [2] R. K. Willardson and E. R. Weber, *SiC materials and devices*, vol. 52. Academic Press, 1998. [6](#), [89](#)
- [3] M. S. Shur, *Handbook series on semiconductor parameters*, vol. 1. World Scientific, 1996. [6](#), [89](#)
- [4] Y. Wang, J. Lv, L. Zhu, and Y. Ma, "Crystal structure prediction via particle-swarm optimization," *Physical Review B*, vol. 82, no. 9, p. 094116, 2010. [7](#)
- [5] R. Eberhart and J. Kennedy, "A new optimizer using particle swarm theory," in *Micro Machine and Human Science, 1995. MHS'95., Proceedings of the Sixth International Symposium on*, pp. 39–43, IEEE, 1995. [7](#)
- [6] R. Kennedy, "J. and eberhart, particle swarm optimization," in *Proceedings of IEEE International Conference on Neural Networks IV, pages*, vol. 1000, 1995. [7](#)
- [7] J. H. Holland, *Adaptation in natural and artificial systems: an introductory analysis with applications to biology, control, and artificial intelligence*. MIT press, 1992. [7](#), [27](#)
- [8] S. Woodley, P. Battle, J. Gale, and C. A. Catlow, "The prediction of inorganic crystal structures using a genetic algorithm and energy minimisation," *Physical Chemistry Chemical Physics*, vol. 1, no. 10, pp. 2535–2542, 1999. [7](#)
- [9] S. Kirkpatrick, C. D. Gelatt, and M. P. Vecchi, "Optimization by simulated annealing," *science*, vol. 220, no. 4598, pp. 671–680, 1983. [7](#), [26](#)

-
- [10] V. Černý, “Thermodynamical approach to the traveling salesman problem: An efficient simulation algorithm,” *Journal of optimization theory and applications*, vol. 45, no. 1, pp. 41–51, 1985. [7](#), [26](#)
- [11] M. Deem and J. Newsam, “Determination of 4-connected framework crystal structures by simulated annealing,” *Nature*, vol. 342, no. 6247, p. 260, 1989. [7](#), [26](#)
- [12] J. Pannetier, J. Bassas-Alsina, J. Rodriguez-Carvajal, and V. Caignaert, “Prediction of crystal structures from crystal chemistry rules by simulated annealing,” *Nature*, vol. 346, no. 6282, p. 343, 1990. [7](#), [26](#)
- [13] F. Jensen, *Introduction to computational chemistry*. John Wiley & sons, 2017. [7](#), [26](#), [28](#)
- [14] S. Goedecker, “Minima hopping: An efficient search method for the global minimum of the potential energy surface of complex molecular systems,” *The Journal of chemical physics*, vol. 120, no. 21, pp. 9911–9917, 2004. [7](#), [8](#), [24](#), [27](#), [33](#), [62](#)
- [15] M. Amsler and S. Goedecker, “Crystal structure prediction using the minima hopping method,” *The Journal of chemical physics*, vol. 133, p. 224104, Dec. 2010. [7](#), [8](#), [29](#), [90](#)
- [16] S. E. Schönborn, S. Goedecker, S. Roy, and A. R. Oganov, “The performance of minima hopping and evolutionary algorithms for cluster structure prediction,” *The Journal of chemical physics*, vol. 130, no. 14, p. 144108, 2009. [7](#)
- [17] D. J. Wales, “Locating stationary points for clusters in cartesian coordinates,” *Journal of the Chemical Society, Faraday Transactions*, vol. 89, no. 9, pp. 1305–1313, 1993. [8](#)
- [18] D. J. Wales, “Rearrangements of 55-atom lennard-jones and (C₆₀) 55 clusters,” *The Journal of chemical physics*, vol. 101, no. 5, pp. 3750–3762, 1994. [8](#)
- [19] G. Mills and H. Jónsson, “Quantum and thermal effects in H₂ dissociative adsorption: evaluation of free energy barriers in multidimensional quantum systems,” *Physical review letters*, vol. 72, no. 7, p. 1124, 1994. [8](#)
- [20] G. Henkelman and H. Jónsson, “Improved tangent estimate in the nudged elastic band method for finding minimum energy paths and saddle points,” *The Journal of chemical physics*, vol. 113, no. 22, pp. 9978–9985, 2000. [8](#)
- [21] G. Henkelman, B. P. Uberuaga, and H. Jónsson, “A climbing image nudged elastic band method for finding saddle points and minimum energy paths,” *The Journal of chemical physics*, vol. 113, no. 22, pp. 9901–9904, 2000. [8](#)
- [22] G. Henkelman and H. Jónsson, “A dimer method for finding saddle points on high dimensional potential surfaces using only first derivatives,” *The Journal of chemical physics*, vol. 111, no. 15, pp. 7010–7022, 1999. [8](#)
-

-
- [23] R. Olsen, G. Kroes, G. Henkelman, A. Arnaldsson, and H. Jónsson, "Comparison of methods for finding saddle points without knowledge of the final states," *The Journal of chemical physics*, vol. 121, no. 20, pp. 9776–9792, 2004. [8](#)
- [24] S. Sakong, C. Mosch, A. Lozano, H. F. Busnengo, and A. Groß, "Lowering energy barriers in surface reactions through concerted reaction mechanisms," *ChemPhysChem*, vol. 13, no. 15, pp. 3467–3471, 2012. [8](#)
- [25] B. Schaefer, S. Mohr, M. Amsler, and S. Goedecker, "Minima hopping guided path search: An efficient method for finding complex chemical reaction pathways," *The Journal of chemical physics*, vol. 140, no. 21, p. 214102, 2014. [8](#)
- [26] B. Schaefer, R. Pal, N. S. Khetrpal, M. Amsler, A. Sadeghi, V. Blum, X. C. Zeng, S. Goedecker, and L.-S. Wang, "Isomerism and structural fluxionality in the Au_{26} and Au_{26}^- nanoclusters," *ACS nano*, vol. 8, no. 7, pp. 7413–7422, 2014. [8](#)
- [27] S. Roy, S. Goedecker, M. J. Field, and E. Penev, "A minima hopping study of all-atom protein folding and structure prediction," *The Journal of Physical Chemistry B*, vol. 113, no. 20, pp. 7315–7321, 2009. [8](#)
- [28] P. Pochet, L. Genovese, D. Caliste, I. Rousseau, S. Goedecker, and T. Deutsch, "First-principles prediction of stable SiC cage structures and their synthesis pathways," *Physical Review B*, vol. 82, no. 3, p. 035431, 2010. [8](#)
- [29] A. Willand, M. Gramzow, S. Alireza Ghasemi, L. Genovese, T. Deutsch, K. Reuter, and S. Goedecker, "Structural metastability of endohedral silicon fullerenes," *Phys. Rev. B*, vol. 81, p. 201405, May 2010. [8](#), [67](#)
- [30] S. De, S. A. Ghasemi, A. Willand, L. Genovese, D. Kanhere, and S. Goedecker, "The effect of ionization on the global minima of small and medium sized silicon and magnesium clusters," *The Journal of chemical physics*, vol. 134, no. 12, p. 124302, 2011. [8](#)
- [31] S. De, A. Willand, M. Amsler, P. Pochet, L. Genovese, and S. Goedecker, "Energy landscape of fullerene materials: a comparison of boron to boron nitride and carbon," *Physical review letters*, vol. 106, no. 22, p. 225502, 2011. [8](#)
- [32] P. Pochet, L. Genovese, S. De, S. Goedecker, D. Caliste, S. A. Ghasemi, K. Bao, and T. Deutsch, "Low-energy boron fullerenes: Role of disorder and potential synthesis pathways," *Physical Review B*, vol. 83, no. 8, p. 081403, 2011. [8](#)
- [33] M. Amsler, J. A. Flores-Livas, L. Lehtovaara, F. Balima, S. A. Ghasemi, D. Machon, S. Pailhes, A. Willand, D. Caliste, S. Botti, *et al.*, "Crystal structure of cold compressed graphite," *Physical review letters*, vol. 108, no. 6, p. 065501, 2012. [8](#)
-

-
- [34] J. A. Flores-Livas, L. Lehtovaara, M. Amsler, S. Goedecker, S. Pailhes, S. Botti, A. San Miguel, and M. A. Marques, "Raman activity of sp^3 carbon allotropes under pressure: A density functional theory study," *Physical Review B*, vol. 85, no. 15, p. 155428, 2012. [8](#)
- [35] J. A. Flores-Livas, M. Amsler, T. J. Lenosky, L. Lehtovaara, S. Botti, M. A. Marques, and S. Goedecker, "High-pressure structures of disilane and their superconducting properties," *Physical review letters*, vol. 108, no. 11, p. 117004, 2012. [8](#)
- [36] B. Schaefer and S. Goedecker, "Computationally efficient characterization of potential energy surfaces based on fingerprint distances," *The Journal of chemical physics*, vol. 145, no. 3, p. 034101, 2016. [9](#), [68](#), [69](#)
- [37] O. M. Becker and M. Karplus, "The topology of multidimensional potential energy surfaces: Theory and application to peptide structure and kinetics," *The Journal of Chemical Physics*, vol. 106, no. 4, pp. 1495–1517, 1997. [9](#), [24](#), [31](#), [68](#), [75](#)
- [38] D. Wales, *Energy landscapes: Applications to clusters, biomolecules and glasses*. Cambridge University Press, 2003. [11](#), [24](#), [26](#), [31](#)
- [39] C. B. Anfinsen, "Principles that govern the folding of protein chains," *Science*, vol. 181, no. 4096, pp. 223–230, 1973. [11](#)
- [40] F. Stillinger and T. Weber, "Structural aspects of the melting transition," in *Proceedings of the Tenth Mexican Winter Meeting on Statistical Mechanics, Bell Laboratories. Kinam, Cocoyoc, Mexico*, pp. 159–171, 1981. [11](#)
- [41] F. H. Stillinger and T. A. Weber, "Hidden structure in liquids," *Physical Review A*, vol. 25, no. 2, p. 978, 1982. [11](#)
- [42] M. Born and R. Oppenheimer, "Zur quantentheorie der molekeln," *Annalen der Physik*, vol. 389, no. 20, pp. 457–484, 1927. [12](#)
- [43] A. Szabo and N. S. Ostlund, *Modern quantum chemistry: introduction to advanced electronic structure theory*. Courier Corporation, 2012. [14](#)
- [44] P. Hohenberg and W. Kohn, "Phys rev 136: B864," *Kohn W, Sham LJ (1965) Phys Rev*, vol. 140, p. A1133, 1964. [14](#)
- [45] W. Kohn and L. J. Sham, "Self-consistent equations including exchange and correlation effects," *Physical review*, vol. 140, no. 4A, p. A1133, 1965. [15](#)
- [46] J. C. Slater, "A simplification of the hartree-fock method," *Physical Review*, vol. 81, no. 3, p. 385, 1951. [17](#)
- [47] S. H. Vosko, L. Wilk, and M. Nusair, "Accurate spin-dependent electron liquid correlation energies for local spin density calculations: a critical analysis," *Canadian Journal of physics*, vol. 58, no. 8, pp. 1200–1211, 1980. [17](#)
-

-
- [48] J. P. Perdew, K. Burke, and M. Ernzerhof, "Generalized gradient approximation made simple," *Physical review letters*, vol. 77, no. 18, p. 3865, 1996. [17](#)
- [49] J. Tao, J. P. Perdew, V. N. Staroverov, and G. E. Scuseria, "Climbing the density functional ladder: Nonempirical meta-generalized gradient approximation designed for molecules and solids," *Physical Review Letters*, vol. 91, no. 14, p. 146401, 2003. [17](#)
- [50] C. Adamo and V. Barone, "Toward reliable density functional methods without adjustable parameters: The PBE0 model," *The Journal of chemical physics*, vol. 110, no. 13, pp. 6158–6170, 1999. [17](#)
- [51] A. D. Becke, "Density-functional thermochemistry. III. the role of exact exchange," *The Journal of chemical physics*, vol. 98, no. 7, pp. 5648–5652, 1993. [17](#)
- [52] J. P. Perdew and K. Schmidt, "Jacob's ladder of density functional approximations for the exchange-correlation energy," *AIP Conference Proceedings*, vol. 577, no. 1, pp. 1–20, 2001. [17](#)
- [53] F. F. Abraham, R. Walkup, H. Gao, M. Duchaineau, T. D. De La Rubia, and M. Seager, "Simulating materials failure by using up to one billion atoms and the world's fastest computer: Brittle fracture," *Proceedings of the National Academy of Sciences*, vol. 99, no. 9, pp. 5777–5782, 2002. [17](#)
- [54] K. Kadau, T. C. Germann, P. S. Lomdahl, and B. L. Holian, "Microscopic view of structural phase transitions induced by shock waves," *Science*, vol. 296, no. 5573, pp. 1681–1684, 2002. [17](#)
- [55] G. Seifert, H. Eschrig, and W. Bieger, "An approximation variant of LCAO-X-alpha methods," *Zeitschrift Fur Physikalische Chemie-Leipzig*, vol. 267, no. 3, pp. 529–539, 1986. [18](#)
- [56] W. M. C. Foulkes and R. Haydock, "Tight-binding models and density-functional theory," *Phys. Rev. B*, vol. 39, pp. 12520–12536, Jun 1989. [18](#)
- [57] T. Frauenheim, G. Seifert, M. Elsterner, Z. Hajnal, G. Jungnickel, D. Porezag, S. Suhai, and R. Scholz, "A self-consistent charge density-functional based tight-binding method for predictive materials simulations in physics, chemistry and biology," *physica status solidi (b)*, vol. 217, no. 1, pp. 41–62, 2000. [19](#)
- [58] D. Porezag, T. Frauenheim, T. Köhler, G. Seifert, and R. Kaschner, "Construction of tight-binding-like potentials on the basis of density-functional theory: Application to carbon," *Physical Review B*, vol. 51, no. 19, p. 12947, 1995. [19](#)
- [59] M. Elstner, D. Porezag, G. Jungnickel, J. Elsner, M. Haugk, T. Frauenheim, S. Suhai, and G. Seifert, "Self-consistent-charge density-functional tight-binding method for simulations of complex materials properties," *Physical Review B*, vol. 58, no. 11, p. 7260, 1998. [19](#)
-

-
- [60] P. G. Mezey, "Catchment region partitioning of energy hypersurfaces, I," *Theoretica chimica acta*, vol. 58, no. 4, pp. 309–330, 1981. [23](#)
- [61] L. C. W. Dixon, "The global optimization problem. an introduction," *Toward global optimization*, vol. 2, pp. 1–15, 1978. [23](#)
- [62] E. Bitzek, P. Koskinen, F. Gähler, M. Moseler, and P. Gumbsch, "Structural relaxation made simple," *Physical review letters*, vol. 97, no. 17, p. 170201, 2006. [25](#)
- [63] C. G. Broyden, "The convergence of a class of double-rank minimization algorithms 1. general considerations," *IMA Journal of Applied Mathematics*, vol. 6, no. 1, pp. 76–90, 1970. [25](#)
- [64] R. Fletcher, "A new approach to variable metric algorithms," *The computer journal*, vol. 13, no. 3, pp. 317–322, 1970. [25](#)
- [65] D. Goldfarb, "A family of variable-metric methods derived by variational means," *Mathematics of computation*, vol. 24, no. 109, pp. 23–26, 1970. [25](#)
- [66] D. F. Shanno, "Conditioning of quasi-newton methods for function minimization," *Mathematics of computation*, vol. 24, no. 111, pp. 647–656, 1970. [25](#)
- [67] K. Ryan, J. Lengyel, and M. Shatruk, "Crystal structure prediction via deep learning," *Journal of the American Chemical Society*, 2018. [26](#)
- [68] J. Graser, S. K. Kauwe, and T. D. Sparks, "Machine learning and energy minimization approaches for crystal structure predictions: A review and new horizons," *Chemistry of Materials*, vol. 30, no. 11, pp. 3601–3612, 2018. [26](#)
- [69] C. C. Fischer, K. J. Tibbetts, D. Morgan, and G. Ceder, "Predicting crystal structure by merging data mining with quantum mechanics," *Nature materials*, vol. 5, no. 8, p. 641, 2006. [26](#)
- [70] D. J. Wales and J. P. Doye, "Global optimization by basin-hopping and the lowest energy structures of lennard-jones clusters containing up to 110 atoms," *The Journal of Physical Chemistry A*, vol. 101, no. 28, pp. 5111–5116, 1997. [26](#)
- [71] J. P. Doye and D. J. Wales, "Thermodynamics of global optimization," *Physical review letters*, vol. 80, no. 7, p. 1357, 1998. [26](#), [52](#), [76](#)
- [72] D. J. Wales and H. A. Scheraga, "Global optimization of clusters, crystals, and biomolecules," *Science*, vol. 285, no. 5432, pp. 1368–1372, 1999. [26](#)
- [73] D. E. Goldberg, K. Milman, and C. Tidd, "Genetic algorithms: A bibliography," *IlliGAL Report*, vol. 92008, 1992. [27](#)
- [74] T. Bush, C. R. A. Catlow, and P. Battle, "Evolutionary programming techniques for predicting inorganic crystal structures," *Journal of Materials Chemistry*, vol. 5, no. 8, pp. 1269–1272, 1995. [27](#)
-

-
- [75] J. Mestres and G. E. Scuseria, "Genetic algorithms: A robust scheme for geometry optimizations and global minimum structure problems," *Journal of Computational Chemistry*, vol. 16, no. 6, pp. 729–742, 1995. [27](#)
- [76] A. R. Oganov and C. W. Glass, "Crystal structure prediction using ab initio evolutionary techniques: Principles and applications," *The Journal of chemical physics*, vol. 124, no. 24, p. 244704, 2006. [27](#)
- [77] C. W. Glass, A. R. Oganov, and N. Hansen, "Uspex-evolutionary crystal structure prediction," *Computer physics communications*, vol. 175, no. 11-12, pp. 713–720, 2006. [27](#)
- [78] G. Trimarchi and A. Zunger, "Global space-group optimization problem: Finding the stablest crystal structure without constraints," *Physical Review B*, vol. 75, no. 10, p. 104113, 2007. [27](#)
- [79] W. Bi, Y. Meng, R. Kumar, A. Cornelius, W. Tipton, R. Hennig, Y. Zhang, C. Chen, and J. Schilling, "Pressure-induced structural transitions in europium to 92 gpa," *Physical Review B*, vol. 83, no. 10, p. 104106, 2011. [27](#)
- [80] S. Roy, S. Goedecker, and V. Hellmann, "Bell-evans-polanyi principle for molecular dynamics trajectories and its implications for global optimization," *Physical Review E*, vol. 77, no. 5, p. 056707, 2008. [28](#)
- [81] M. Parrinello and A. Rahman, "Crystal structure and pair potentials: A molecular-dynamics study," *Phys. Rev. Lett.*, vol. 45, pp. 1196–1199, Oct 1980. [31](#)
- [82] B. Aradi, B. Hourahine, and T. Frauenheim, "DFTB+, a sparse matrix-based implementation of the DFTB method," *The Journal of Physical Chemistry A*, vol. 111, no. 26, pp. 5678–5684, 2007. [31](#)
- [83] L. Genovese, A. Neelov, S. Goedecker, T. Deutsch, S. A. Ghasemi, A. Wiland, D. Caliste, O. Zilberberg, M. Rayson, A. Bergman, and R. Schneider, "Daubechies wavelets as a basis set for density functional pseudopotential calculations," *The Journal of Chemical Physics*, vol. 129, no. 1, p. 014109, 2008. [31](#)
- [84] G. Kresse and J. Furthmüller, "Efficiency of ab-initio total energy calculations for metals and semiconductors using a plane-wave basis set," *Computational Materials Science*, vol. 6, no. 1, pp. 15 – 50, 1996. [31](#), [90](#)
- [85] D. J. Wales, "Energy landscapes: calculating pathways and rates," *International Reviews in Physical Chemistry*, vol. 25, no. 1-2, pp. 237–282, 2006. [31](#)
- [86] T. R. Walsh and D. J. Wales, "Relaxation dynamics of C₆₀," *The Journal of Chemical Physics*, vol. 109, no. 16, pp. 6691–6700, 1998. [31](#), [70](#), [71](#), [72](#)
- [87] D. J. Wales, M. A. Miller, and T. R. Walsh, "Archetypal energy landscapes," *Nature*, vol. 394, no. 6695, p. 758, 1998. [31](#), [75](#)
-

-
- [88] M. Miller, D. Wales, and V. de Souza, “disconnectionDPS.” <http://www-wales.ch.cam.ac.uk/software.html>. 31
- [89] H. W. Kroto, J. R. Heath, S. C. O’Brien, R. F. Curl, and R. E. Smalley, “C₆₀: Buckminsterfullerene,” *Nature*, vol. 318, no. 6042, p. 162, 1985. 34
- [90] L. Pan, M. B. Sander, X. Huang, J. Li, M. Smith, E. Bittner, B. Bockrath, and J. K. Johnson, “Microporous metal organic materials: promising candidates as sorbents for hydrogen storage,” *Journal of the American Chemical Society*, vol. 126, no. 5, pp. 1308–1309, 2004. 35
- [91] L. Schlapbach and A. Züttel, “Hydrogen-storage materials for mobile applications,” *Nature*, vol. 414, no. 6861, pp. 353–358, 2001. 35
- [92] B. Bogdanović and M. Schwickardi, “Ti-doped alkali metal aluminium hydrides as potential novel reversible hydrogen storage materials,” *Journal of alloys and compounds*, vol. 253, pp. 1–9, 1997. 35
- [93] T. Yildirim, J. Íñiguez, and S. Ciraci, “Molecular and dissociative adsorption of multiple hydrogen molecules on transition metal decorated C₆₀,” *Physical Review B*, vol. 72, no. 15, p. 153403, 2005. 35
- [94] K. Chandrakumar and S. K. Ghosh, “Alkali-metal-induced enhancement of hydrogen adsorption in C₆₀ fullerene: an ab initio study,” *Nano letters*, vol. 8, no. 1, pp. 13–19, 2008. 35
- [95] Q. Wang, Q. Sun, P. Jena, and Y. Kawazoe, “Theoretical study of hydrogen storage in Ca-coated fullerenes,” *Journal of Chemical Theory and Computation*, vol. 5, no. 2, pp. 374–379, 2009. 35
- [96] M. Yoon, S. Yang, C. Hicke, E. Wang, D. Geohegan, and Z. Zhang, “Calcium as the superior coating metal in functionalization of carbon fullerenes for high-capacity hydrogen storage,” *Phys. Rev. Lett.*, vol. 100, p. 206806, 2008. 35
- [97] B. Rao and P. Jena, “Hydrogen uptake by an alkali metal ion,” *EPL (Europhysics Letters)*, vol. 20, no. 4, p. 307, 1992. 35
- [98] H. Tanaka, S. Osawa, J. Onoe, and K. Takeuchi, “Formation process of Si-coated C₆₀,” *The Journal of Physical Chemistry B*, vol. 103, no. 29, pp. 5939–5942, 1999. 35
- [99] F. Rabilloud, R. Antoine, M. Broyer, I. Compagnon, P. Dugourd, D. Rayane, F. Calvo, and F. Spiegelman, “Electric dipoles and susceptibilities of alkali clusters/fullerene complexes: experiments and simulations,” *The Journal of Physical Chemistry C*, vol. 111, no. 48, pp. 17795–17803, 2007. 35, 51, 52, 54, 56, 57
- [100] N. Hamamoto, J. Jitsukawa, and C. Satoko, “Electronic and geometric properties of alkali-C₆₀ molecules,” *The European Physical Journal D-Atomic, Molecular, Optical and Plasma Physics*, vol. 19, no. 2, pp. 211–221, 2002. 35, 45
-

-
- [101] J. Roques, F. Calvo, F. Spiegelman, and C. Mijoule, "Wetting-to-nonwetting transition in metal-coated C_{60} ," *Phys. Rev. Lett.*, vol. 90, p. 075505, 2003. [35](#)
- [102] J. Roques, F. Calvo, F. Spiegelman, and C. Mijoule, "Nucleation of a sodium droplet on C_{60} ," *Phys. Rev. B*, vol. 68, p. 205412, 2003. [35](#)
- [103] P. Weis, R. D. Beck, G. Bräuchle, and M. M. Kappes, "Properties of size and composition selected gas phase alkali fulleride clusters," *The Journal of chemical physics*, vol. 100, no. 8, pp. 5684–5695, 1994. [35](#)
- [104] A. Tang, Z. Shang, Q. Teng, Y. Pan, Z. Cai, X. Zhao, and J. Feng, "Theoretical study on the structures and electron spectra of $C_{60}M_{12}$ ($M = \text{Li, Na, Be}$)," *International journal of quantum chemistry*, vol. 73, no. 6, pp. 505–509, 1999. [35](#)
- [105] Z. Slanina, C. Miyajima, X. Zhao, F. Uhlík, L. Adamowicz, and E. sawa, "Metal-coated fullerenes $C_{60}M_n$: Calculations for $M = \text{Be, Mg, Al}$ and $n = 12, 20, 32$," *Fullerene science and technology*, vol. 8, no. 4-5, pp. 385–402, 2000. [35](#)
- [106] H. Lee, B. Huang, W. Duan, and J. Ihm, "Ab initio study of beryllium-decorated fullerenes for hydrogen storage," *Journal of Applied Physics*, vol. 107, no. 8, 2010. [35](#)
- [107] Y. Zhao, Y.-H. Kim, A. Dillon, M. Heben, and S. Zhang, "Hydrogen storage in novel organometallic buckyballs," *Physical review letters*, vol. 94, no. 15, p. 155504, 2005. [35](#), [41](#)
- [108] R. Guirado-López, "Stability and electronic properties of Si-doped carbon fullerenes," *Phys. Rev. B*, vol. 65, p. 165421, 2002. [35](#)
- [109] H. Le and N. Pham, "A density functional theory investigation of Ni_n, Pd_n, Pt_n clusters ($n = 1-4$) adsorbed on buckminsterfullerene (C_{60})," *ChemPhysChem*, 2017. [35](#)
- [110] Z.-Y. Tian and S.-L. Dong, "Yttrium-dispersed C_{60} fullerenes as high-capacity hydrogen storage medium," *The Journal of chemical physics*, vol. 140, no. 8, p. 084706, 2014. [35](#)
- [111] L. Genovese, A. Neelov, S. Goedecker, T. Deutsch, S. A. Ghasemi, A. Willand, D. Caliste, O. Zilberberg, M. Rayson, A. Bergman, and R. Schneider, "Daubechies wavelets as a basis set for density functional pseudopotential calculations," *The Journal of Chemical Physics*, vol. 129, no. 1, 2008. [35](#)
- [112] J. P. Perdew, K. Burke, and M. Ernzerhof, "Generalized gradient approximation made simple," *Phys. Rev. Lett.*, vol. 77, pp. 3865–3868, 1996. [35](#)
- [113] B. Silvi, A. Savin, *et al.*, "Classification of chemical bonds based on topological analysis of electron localization functions," *Nature*, vol. 371, no. 6499, pp. 683–686, 1994. [35](#)
-

-
- [114] G. Kresse and J. Furthmüller, “Efficient iterative schemes for ab initio total-energy calculations using a plane-wave basis set,” *Physical review B*, vol. 54, no. 16, p. 11169, 1996. [36](#)
- [115] G. Henkelman, A. Arnaldsson, and H. Jónsson, “A fast and robust algorithm for Bader decomposition of charge density,” *Computational Materials Science*, vol. 36, no. 3, pp. 354–360, 2006. [36](#)
- [116] E. Sanville, S. D. Kenny, R. Smith, and G. Henkelman, “Improved grid-based algorithm for Bader charge allocation,” *Journal of computational chemistry*, vol. 28, no. 5, pp. 899–908, 2007. [36](#)
- [117] W. Tang, E. Sanville, and G. Henkelman, “A grid-based Bader analysis algorithm without lattice bias,” *Journal of Physics: Condensed Matter*, vol. 21, no. 8, p. 084204, 2009. [36](#)
- [118] U. Zimmermann, N. Malinowski, A. Burkhardt, and T. Martin, “Metal-coated fullerenes,” *Carbon*, vol. 33, no. 7, pp. 995–1006, 1995. [40](#), [41](#)
- [119] M. Ohara, Y. Nakamura, Y. Negishi, K. Miyajima, A. Nakajima, and K. Kaya, “Behavior of silicon and germanium clusters on a C₆₀ fullerene,” *The Journal of Physical Chemistry A*, vol. 106, no. 18, pp. 4498–4501, 2002. [42](#)
- [120] F. Rabilloud, “Structure and electronic properties of alkali- C₆₀ nanoclusters,” *The Journal of Physical Chemistry A*, vol. 114, no. 26, pp. 7241–7247, 2010. [45](#), [52](#), [58](#)
- [121] F. Rabilloud, “Electronic and geometric properties of exohedral potassium-fullerenes,” *Computational and Theoretical Chemistry*, vol. 964, no. 1, pp. 213–217, 2011. [45](#)
- [122] M. Calatayud, J. Andrés, A. Beltrán, and B. Silvi, “The hierarchy of localization basins: a tool for the understanding of chemical bonding exemplified by the analysis of the VO_x and VO_x⁺ (x= 1-4) systems,” *Theoretical Chemistry Accounts*, vol. 105, no. 4-5, pp. 299–308, 2001. [47](#)
- [123] A. Savin, B. Silvi, and F. Coionna, “Topological analysis of the electron localization function applied to delocalized bonds,” *Canadian journal of chemistry*, vol. 74, no. 6, pp. 1088–1096, 1996. [47](#)
- [124] R. Rousseau and D. Marx, “Exploring the electronic structure of elemental lithium: from small molecules to nanoclusters, bulk metal, and surfaces,” *Chemistry—A European Journal*, vol. 6, no. 16, pp. 2982–2993, 2000. [47](#)
- [125] Y. Grin, A. Savin, and B. Silvi, “The elf perspective of chemical bonding,” *The Chemical Bond: Fundamental Aspects of Chemical Bonding*, pp. 345–382, 2014. [50](#)
- [126] M. Broyer, R. Antoine, E. Benichou, I. Compagnon, P. Dugourd, and D. Rayane, “Structure of nano-objects through polarizability and dipole measurements,” *Comptes Rendus Physique*, vol. 3, no. 3, pp. 301–317, 2002. [51](#)
-

-
- [127] P. Dugourd, R. Antoine, G. Breaux, M. Broyer, and M. F. Jarrold, "Entropic stabilization of isolated β -sheets," *Journal of the American Chemical Society*, vol. 127, no. 13, pp. 4675–4679, 2005. [51](#)
- [128] H.-L. Cheng, W.-Y. Chou, C. Kuo, F.-C. Tang, and Y.-W. Wang, "Electric field-induced structural changes in pentacene-based organic thin-film transistors studied by *in situ* micro-Raman spectroscopy," *Applied physics letters*, vol. 88, no. 16, p. 161918, 2006. [51](#)
- [129] K. Kotsuki, S. Obata, and K. Saiki, "Electric-field-assisted position and orientation control of organic single crystals," *Langmuir*, vol. 30, no. 47, pp. 14286–14291, 2014. [51](#)
- [130] N. D. Gurav, S. P. Gejji, L. J. Bartolotti, and R. K. Pathak, "Encaged molecules in external electric fields: A molecular "tug-of-war"," *The Journal of chemical physics*, vol. 145, no. 7, p. 074302, 2016. [51](#)
- [131] H. Shen, "Geometrical configuration and electronic structure of C_{60} fullerene molecule under external electric field," *International Journal of Nanoscience*, vol. 4, no. 03, pp. 389–397, 2005. [51](#)
- [132] J.-y. Sorimachi and S. Okada, "Electrostatic properties of fullerenes under an external electric field: First-principles calculations of energetics for all IPR isomers from C_{60} to C_{78} ," *Chemical Physics Letters*, vol. 659, pp. 1–5, 2016. [51](#)
- [133] D. Rayane, R. Antoine, P. Dugourd, E. Benichou, A. Allouche, M. Aubert-Frécon, and M. Broyer, "Polarizability of KC_{60} : Evidence for potassium skating on the C_{60} surface," *Physical review letters*, vol. 84, no. 9, p. 1962, 2000. [51](#), [60](#)
- [134] R. Antoine, D. Rayane, E. Benichou, P. Dugourd, and M. Broyer, "Electric dipole moment and charge transfer in alkali-C molecules," *The European Physical Journal D-Atomic, Molecular, Optical and Plasma Physics*, vol. 12, no. 1, pp. 147–151, 2000. [51](#)
- [135] P. Dugourd, R. Antoine, D. Rayane, I. Compagnon, and M. Broyer, "Enhanced electric polarizability in metal C_{60} compounds: Formation of a sodium droplet on C_{60} ," *The Journal of Chemical Physics*, vol. 114, no. 5, pp. 1970–1973, 2001. [51](#)
- [136] D. S. De, J. A. Flores-Livas, S. Saha, L. Genovese, and S. Goedecker, "Stable structures of exohedrally decorated C_{60} -fullerenes," *Carbon*, vol. 129, pp. 847–853, 2018. [52](#), [58](#), [62](#), [64](#)
- [137] J. Ochterski, "Thermochemistry in gaussian, gaussian, inc., wallingford ct, 2000," 2010. [56](#)
- [138] A. Rosén and B. Wästberg, "Calculations of the ionization thresholds and electron affinities of the neutral, positively and negatively charged C_{60} —"follene-
-

- 60",” *The Journal of Chemical Physics*, vol. 90, no. 4, pp. 2525–2526, 1989. [58](#)
- [139] K. E. Geckeler, *Advanced macromolecular and supramolecular materials and processes*. Springer, 2003. [58](#)
- [140] V. Cammarata, T. Guo, A. Illies, L. Li, and P. Shevlin, “Gas-phase observation of multiply charged C_{60} anions,” *The Journal of Physical Chemistry A*, vol. 109, no. 12, pp. 2765–2767, 2005. [58](#)
- [141] S. Tomita, J. U. Andersen, H. Cederquist, B. Concina, O. Echt, J. Forster, K. Hansen, B. Huber, P. Hvelplund, J. Jensen, *et al.*, “Lifetimes of C_{60}^{2-} and C_{70}^{2-} dianions in a storage ring,” *The Journal of chemical physics*, vol. 124, no. 2, p. 024310, 2006. [58](#)
- [142] C. Yannouleas and U. Landman, “Stabilized-jellium description of neutral and multiply charged fullerenes $C_{60}^{x\pm}$,” *Chemical physics letters*, vol. 217, no. 3, pp. 175–185, 1994. [58](#)
- [143] U. Zimmermann, N. Malinowski, A. Burkhardt, and T. Martin, “Metal-coated fullerenes,” *Carbon*, vol. 33, no. 7, pp. 995 – 1006, 1995. [58](#)
- [144] M. Riad Manaa, H. A. Ichord, and D. W. Sprehn, “Predicted molecular structure of novel $C_{48}B_{12}$,” *Chemical Physics Letters*, vol. 378, pp. 449–455, 2003. [61](#)
- [145] S. Mohr, P. Pochet, M. Amsler, B. Schaefer, A. Sadeghi, L. Genovese, and S. Goedecker, “Boron aggregation in the ground states of boron-carbon fullerenes,” *Physical Review B*, vol. 89, no. 4, p. 041404, 2014. [61](#)
- [146] Q. Sun, Q. Wang, and P. Jena, “Functionalized heterofullerenes for hydrogen storage,” *Applied Physics Letters*, vol. 94, no. 1, p. 013111, 2009. [61](#), [64](#)
- [147] Y. Gao, X. Wu, and X. C. Zeng, “Designs of fullerene-based frameworks for hydrogen storage,” *Journal of Materials Chemistry A*, vol. 2, no. 16, pp. 5910–5914, 2014. [61](#)
- [148] Y. Zhao, Y.-H. Kim, A. Dillon, M. Heben, and S. Zhang, “Hydrogen storage in novel organometallic buckyballs,” *Physical review letters*, vol. 94, no. 15, p. 155504, 2005. [61](#), [64](#)
- [149] S. Er, G. A. de Wijs, and G. Brocks, “Improved hydrogen storage in Ca-decorated boron heterofullerenes: a theoretical study,” *Journal of Materials Chemistry A*, vol. 3, no. 15, pp. 7710–7714, 2015. [61](#), [64](#)
- [150] P. Qi and H. Chen, “Theoretical study of hydrogen adsorption on Ca-decorated $C_{48}B_{12}$ clusters,” *AIP Advances*, vol. 5, no. 9, p. 097158, 2015. [61](#), [64](#)
- [151] H. Lee, B. Huang, W. Duan, and J. Ihm, “Ab initio study of beryllium-decorated fullerenes for hydrogen storage,” *Journal of Applied Physics*, vol. 107, no. 8, p. 084304, 2010. [61](#), [62](#), [64](#)
-

-
- [152] H. W. Gibson, R. J. Weagley, R. A. Mosher, S. Kaplan, W. M. Prest, and A. J. Epstein, "Molecular structure of 'trans'-polyacetylene: The presence of remnant cis units and their influence on soliton formation and diffusion," *Phys. Rev. B*, vol. 31, pp. 2338–2342, Feb 1985. [67](#)
- [153] K. S. Novoselov, A. K. Geim, S. V. Morozov, D. Jiang, M. I. Katsnelson, I. V. Grigorieva, S. V. Dubonos, and A. A. Firsov, "Two-dimensional gas of massless dirac fermions in graphene," *Nature*, vol. 438, no. 7065, pp. 197–200, 2005. [67](#), [101](#)
- [154] P. Boul, J. Liu, E. Mickelson, C. Huffman, L. Ericson, I. Chiang, K. Smith, D. Colbert, R. Hauge, J. Margrave, and R. Smalley, "Reversible sidewall functionalization of buckytubes," *Chemical Physics Letters*, vol. 310, no. 3, pp. 367–372, 1999. [67](#)
- [155] R. D. Miller and J. Michl, "Polysilane high polymers," *Chemical Reviews*, vol. 89, no. 6, pp. 1359–1410, 1989. [67](#)
- [156] H. Okamoto, Y. Kumai, Y. Sugiyama, T. Mitsuoka, K. Nakanishi, T. Ohta, H. Nozaki, S. Yamaguchi, S. Shirai, and H. Nakano, "Silicon nanosheets and their self-assembled regular stacking structure," *Journal of the American Chemical Society*, vol. 132, no. 8, pp. 2710–2718, 2010. PMID: 20121277. [67](#)
- [157] K.-M. Ho, A. A. Shvartsburg, B. Pan, Z.-Y. Lu, C.-Z. Wang, J. G. Wacker, J. L. Fye, and M. F. Jarrold, "Structures of medium-sized silicon clusters," *Nature*, vol. 392, no. 6676, pp. 582–585, 1998. [67](#)
- [158] Q. Sun, Q. Wang, T. M. Briere, V. Kumar, Y. Kawazoe, and P. Jena, "First-principles calculations of metal stabilized Si₂₀ cages," *Phys. Rev. B*, vol. 65, p. 235417, May 2002. [67](#)
- [159] C. W. Earley, "Ab initio investigation of strain in group 14 polyhedrane clusters (M_nH_n: n = 4, 6, 8, 10, 12, 16, 20, 24)," *The Journal of Physical Chemistry A*, vol. 104, no. 28, pp. 6622–6627, 2000. [67](#)
- [160] A. D. Zdetsis, "High-symmetry high-stability silicon fullerenes: A first-principles study," *Phys. Rev. B*, vol. 76, p. 075402, Aug 2007. [67](#), [81](#)
- [161] C. Y. Zhang, H. S. Wu, and H. Jiao, "Structure and stability of endohedral X@Si₂₀H₂₀ complexes (X= Li^{0/+}, Na^{0/+}, K^{0/+}, Be^{0/2+}, Mg^{0/2+}, Ca^{0/2+})," *Chemical physics letters*, vol. 410, no. 4-6, pp. 457–461, 2005. [67](#)
- [162] F. Pichierri, V. Kumar, and Y. Kawazoe, "Encapsulation of halide anions in perhydrogenated silicon fullerene: X-@Si₂₀H₂₀ (X=F, Cl, Br, I)," *Chemical Physics Letters*, vol. 406, no. 4, pp. 341 – 344, 2005. [67](#), [85](#)
- [163] D. Palagin and K. Reuter, "Evaluation of endohedral doping of hydrogenated Si fullerenes as a route to magnetic Si building blocks," *Phys. Rev. B*, vol. 86, p. 045416, Jul 2012. [67](#)
-

-
- [164] V. Kumar and Y. Kawazoe, "Hydrogenated silicon fullerenes: Effects of H on the stability of metal-encapsulated silicon clusters," *Physical review letters*, vol. 90, no. 5, p. 055502, 2003. [67](#)
- [165] M. Pouchard, C. Cros, P. Hagemuller, E. Reny, A. Ammar, M. Ménétrier, and J.-M. Bassat, "A brief overview on low sodium content silicides: are they mainly clathrates, fullerenes, intercalation compounds or zintl phases?," *Solid State Sciences*, vol. 4, no. 5, pp. 723–729, 2002. [68](#)
- [166] S. Yamanaka, "Silicon clathrates and carbon analogs: high pressure synthesis, structure, and superconductivity," *Dalton Trans.*, vol. 39, pp. 1901–1915, 2010. [68](#)
- [167] E. Reny, S. Yamanaka, C. Cros, and M. Pouchard, "High pressure synthesis of an iodine doped silicon clathrate compound," *Chem. Commun.*, pp. 2505–2506, 2000. [68](#)
- [168] J. Tillmann, J. H. Wender, U. Bahr, M. Bolte, H.-W. Lerner, M. C. Holthausen, and M. Wagner, "One-step synthesis of a [20]silafullerane with an endohedral chloride ion," *Angewandte Chemie International Edition*, vol. 54, no. 18, pp. 5429–5433, 2015. [68](#), [80](#)
- [169] L. A. Paquette, R. J. Ternansky, D. W. Balogh, and G. Kentgen, "Total synthesis of dodecahedrane," *Journal of the American Chemical Society*, vol. 105, no. 16, pp. 5446–5450, 1983. [68](#)
- [170] R. J. Ternansky, D. W. Balogh, and L. A. Paquette, "Dodecahedrane," *Journal of the American Chemical Society*, vol. 104, no. 16, pp. 4503–4504, 1982. [68](#), [73](#)
- [171] H. F. Bettinger, B. I. Yakobson, and G. E. Scuseria, "Scratching the surface of buckminsterfullerene: the barriers for stonewales transformation through symmetric and asymmetric transition states," *Journal of the American Chemical Society*, vol. 125, no. 18, pp. 5572–5580, 2003. [70](#), [72](#)
- [172] A. Stone and D. Wales, "Theoretical studies of icosahedral C₆₀ and some related species," *Chemical Physics Letters*, vol. 128, no. 5, pp. 501–503, 1986. [70](#)
- [173] I. László, "Formation of cage-like C₆₀ clusters in molecular-dynamics simulations," *EPL (Europhysics Letters)*, vol. 44, no. 6, p. 741, 1998. [70](#)
- [174] F. Pietrucci and W. Andreoni, "Fate of a graphene flake: A new route toward fullerenes disclosed with ab initio simulations," *Journal of Chemical Theory and Computation*, vol. 10, no. 3, pp. 913–917, 2014. PMID: 26580170. [70](#)
- [175] Y. Kumeda and D. J. Wales, "Ab initio study of rearrangements between C₆₀ fullerenes," *Chemical Physics Letters*, vol. 374, no. 1, pp. 125 – 131, 2003. [71](#)
-

-
- [176] P. E. Leopold, M. Montal, and J. N. Onuchic, "Protein folding funnels: a kinetic approach to the sequence-structure relationship," *Proceedings of the National Academy of Sciences*, vol. 89, no. 18, pp. 8721–8725, 1992. [72](#)
- [177] S. De, B. Schaefer, A. Sadeghi, M. Sicher, D. G. Kanhere, and S. Goedecker, "Relation between the dynamics of glassy clusters and characteristic features of their energy landscape," *Phys. Rev. Lett.*, vol. 112, p. 083401, Feb 2014. [73](#)
- [178] H. Eyring, "The activated complex in chemical reactions," *The Journal of Chemical Physics*, vol. 3, no. 2, pp. 107–115, 1935. [76](#)
- [179] J. P. Doye, M. A. Miller, and D. J. Wales, "The double-funnel energy landscape of the 38-atom Lennard-Jones cluster," *The Journal of Chemical Physics*, vol. 110, no. 14, pp. 6896–6906, 1999. [76](#)
- [180] J. Neirotti, F. Calvo, D. L. Freeman, and J. Doll, "Phase changes in 38-atom Lennard-Jones clusters. I. A parallel tempering study in the canonical ensemble," *The Journal of Chemical Physics*, vol. 112, no. 23, pp. 10340–10349, 2000. [76](#)
- [181] M. A. Miller, J. P. Doye, and D. J. Wales, "Structural relaxation in atomic clusters: Master equation dynamics," *Physical Review E*, vol. 60, no. 4, p. 3701, 1999. [78](#)
- [182] N. Matsko, "Study of volume and surface plasmons in small silicon–hydrogen nanoclusters using the GW method," *Physical Chemistry Chemical Physics*, 2018. [79](#)
- [183] F. Li, P. Jin, D.-e. Jiang, L. Wang, S. B. Zhang, J. Zhao, and Z. Chen, " B_{80} and $B_{101-103}$ clusters: Remarkable stability of the core-shell structures established by validated density functionals," *The Journal of Chemical Physics*, vol. 136, no. 7, p. 074302, 2012. [81](#)
- [184] A. Vailionis, G. Glass, P. Desjardins, D. G. Cahill, and J. Greene, "Electrically active and inactive B lattice sites in ultrahighly B doped Si (001): An x-ray near-edge absorption fine-structure and high-resolution diffraction study," *Physical review letters*, vol. 82, no. 22, p. 4464, 1999. [87](#), [102](#)
- [185] F. Sarubbi, T. L. Scholtes, and L. K. Nanver, "Chemical vapor deposition of α -boron layers on silicon for controlled nanometer-deep p^+n junction formation," *Journal of electronic materials*, vol. 39, no. 2, pp. 162–173, 2010. [87](#), [102](#)
- [186] K. Mok, V. Mohammadi, L. Nanver, W. de Boer, and A. Vlooswijk, "Low-pressure chemical vapor deposition of pureb layers on silicon for p^+n junction formation," in *Junction Technology (IWJT), 2012 12th International Workshop on*, pp. 113–116, IEEE, 2012. [87](#), [102](#)
- [187] V. Mohammadi and S. Nihtianov, "Lateral gas phase diffusion length of boron atoms over Si/B surfaces during CVD of pure boron layers," *AIP Advances*, vol. 6, no. 2, p. 025103, 2016. [87](#), [102](#)
-

-
- [188] V. Mohammadi, S. Nihtianov, and C. Fang, "A doping-less junction-formation mechanism between n-silicon and an atomically thin boron layer," *Scientific reports*, vol. 7, no. 1, p. 13247, 2017. [87](#), [102](#)
- [189] A. Fissel, J. Krügener, and H. Osten, "Towards controlled molecular beam epitaxial growth of artificially stacked Si: Study of boron adsorption and surface segregation on Si(1 1 1)," *Journal of Crystal Growth*, vol. 323, no. 1, pp. 144–149, 2011. [87](#), [102](#)
- [190] J. Berzelius, "Untersuchungen über die flussspathsäure und deren merkwürdigsten verbindungen," *Annalen der Physik*, vol. 77, no. 6, pp. 169–230, 1824. [88](#)
- [191] G. Fisher and P. Barnes, "Towards a unified view of polytypism in silicon carbide," *Philosophical Magazine B*, vol. 61, no. 2, pp. 217–236, 1990. [88](#)
- [192] V. Šimonka, A. Hössinger, J. Weinbub, and S. Selberherr, "Growth rates of dry thermal oxidation of 4H-silicon carbide," *Journal of Applied Physics*, vol. 120, no. 13, p. 135705, 2016. [89](#)
- [193] G. Brezeanu, "Silicon carbide (SiC): a short history. an analytical approach for SiC power device design," in *Semiconductor Conference, 2005. CAS 2005 Proceedings. 2005 International*, vol. 2, pp. 345–348, IEEE, 2005. [89](#)
- [194] A. Hefner, "Status of high-voltage, high-frequency silicon-carbide power devices," in *31st GOMACTech Conf*, pp. 232–235, 2006. [89](#)
- [195] J. Ortiz-Rodriguez, T. Duong, A. Rivera-Lopez, and A. Hefner, "High-voltage, high-frequency SiC power mosfets model validation," in *Power Electronics Specialists Conference, 2007. PESC 2007. IEEE*, pp. 1018–1022, IEEE, 2007. [89](#)
- [196] J. Campi, Y. Shi, Y. Luo, F. Yan, and J. H. Zhao, "Study of interface state density and effective oxide charge in post-metallization annealed SiO₂/-SiC structures," *IEEE Transactions on Electron Devices*, vol. 46, no. 3, pp. 511–519, 1999. [89](#)
- [197] E. Pippel, J. Woltersdorf, H. Ö. Ólafsson, and E. Ö. Sveinbjörnsson, "Interfaces between 4H-SiC and SiO₂: Microstructure, nanochemistry, and near-interface traps," *Journal of applied physics*, vol. 97, no. 3, p. 034302, 2005. [89](#)
- [198] V. V. Afanas'ev, F. Ciobanu, S. Dimitrijević, G. Pensl, and A. Stesmans, "SiC/SiO₂ interface states: properties and models," in *Materials Science Forum*, vol. 483, pp. 563–568, Trans Tech Publ, 2005. [89](#)
- [199] T. Sakai, M. Hemmi, Y. Murata, T. Yamakami, R. Hayashibe, Y. Onuma, and K. Kamimura, "Effect of direct nitridation of 4H-SiC surface on MOS interface states," in *Silicon Carbide and Related Materials 2011*, vol. 717 of *Materials Science Forum*, pp. 725–728, Trans Tech Publications, 6 2012. [90](#)
- [200] V. Afanas'ev, A. Stesmans, F. Ciobanu, G. Pensl, K. Cheong, and S. Dimitrijević, "Mechanisms responsible for improvement of 4H-SiC/SiO₂ interface
-

- properties by nitridation,” *Applied Physics Letters*, vol. 82, no. 4, pp. 568–570, 2003. [90](#), [97](#), [98](#)
- [201] J. P. Perdew, K. Burke, and M. Ernzerhof, “Generalized gradient approximation made simple,” *Physical review letters*, vol. 77, no. 18, p. 3865, 1996. [90](#)
- [202] A. Fonari and S. Stauffer, *vasp_raman.py*. <https://github.com/raman-sc/VASP/>, 2013. [90](#)
- [203] C. Harris and V. Afanas’ev, “SiO₂ as an insulator for SiC devices,” *Micro-electronic engineering*, vol. 36, no. 1-4, pp. 167–174, 1997. [94](#)
- [204] F. Devynck, A. Alkauskas, P. Broqvist, and A. Pasquarello, “Defect levels of carbon-related defects at the SiC/SiO₂ interface from hybrid functionals,” *Physical Review B*, vol. 83, no. 19, p. 195319, 2011. [94](#)
- [205] P. Jamet, S. Dimitrijević, and P. Tanner, “Effects of nitridation in gate oxides grown on 4H-SiC,” *Journal of Applied Physics*, vol. 90, no. 10, pp. 5058–5063, 2001. [96](#)
- [206] P. Jamet and S. Dimitrijević, “Physical properties of N₂O and NO-nitrided gate oxides grown on 4H-SiC,” *Applied Physics Letters*, vol. 79, no. 3, pp. 323–325, 2001. [96](#)
- [207] Y. Maeyama, H. Yano, Y. Furumoto, T. Hatayama, Y. Uraoka, and T. Fuyuki, “Improvement of SiO₂/SiC interface properties by nitrogen radical irradiation,” *Japanese journal of applied physics*, vol. 42, no. 6A, p. L575, 2003. [96](#)
- [208] Y. Xu, X. Zhu, H. Lee, C. Xu, S. Shubeita, A. Ahyi, Y. Sharma, J. Williams, W. Lu, S. Ceesay, *et al.*, “Atomic state and characterization of nitrogen at the SiC/SiO₂ interface,” *Journal of Applied Physics*, vol. 115, no. 3, p. 033502, 2014. [96](#), [98](#)
- [209] F. Moscatelli, A. Poggi, S. Solmi, and R. Nipoti, “Nitrogen implantation to improve electron channel mobility in 4H-SiC mosfet,” *IEEE Transactions on Electron Devices*, vol. 55, no. 4, pp. 961–967, 2008. [96](#)
- [210] R. Schörner, P. Friedrichs, D. Peters, D. Stephani, S. Dimitrijević, and P. Jamet, “Enhanced channel mobility of 4H-SiC metal-oxide-semiconductor transistors fabricated with standard polycrystalline silicon technology and gate-oxide nitridation,” *Applied physics letters*, vol. 80, no. 22, pp. 4253–4255, 2002. [97](#)
- [211] T. Umeda, K. Esaki, R. Kosugi, K. Fukuda, T. Ohshima, N. Morishita, and J. Isoya, “Behavior of nitrogen atoms in SiC-SiO₂ interfaces studied by electrically detected magnetic resonance,” *Applied physics letters*, vol. 99, no. 14, p. 142105, 2011. [98](#)
- [212] F. Matsui, T. Matsushita, and H. Daimon, “Stereo atomscope and diffraction spectroscopy – atomic site specific property analysis,” *Journal of Electron Spectroscopy and Related Phenomena*, vol. 178-179, pp. 221 – 240, 2010.
-

- Trends in X-ray Photoelectron Spectroscopy of solids (theory, techniques and applications). [98](#)
- [213] D. Mori, Y. Oyama, T. Hirose, T. Muro, and F. Matsui, “Local structural determination of N at SiO₂/SiC (0001⁻) interfaces by photoelectron diffraction,” *Applied Physics Letters*, vol. 111, no. 20, p. 201603, 2017. [98](#)
- [214] N. Franco, J. Avila, M. Davila, M. Asensio, D. Woodruff, O. Schaff, V. Fernandez, K. Schindler, and A. Bradshaw, “Structure determination of using scanned-energy mode photoelectron diffraction,” *Journal of Physics: Condensed Matter*, vol. 9, no. 40, p. 8419, 1997. [98](#)
- [215] J. Houston Dycus, W. Xu, D. J. Lichtenwalner, B. Hull, J. W. Palmour, and J. M. LeBeau, “Structure and chemistry of passivated SiC/SiO₂ interfaces,” *Applied Physics Letters*, vol. 108, no. 20, p. 201607, 2016. [98](#)
- [216] V. Afanas’ev, F. Ciobanu, S. Dimitrijević, G. Pensl, and A. Stesmans, “Band alignment and defect states at SiC/oxide interfaces,” *Journal of Physics: Condensed Matter*, vol. 16, no. 17, p. S1839, 2004. [98](#)
- [217] K. Y. Cheong, S. Dimitrijević, J. Han, and H. B. Harrison, “Electrical and physical characterization of gate oxides on 4H-SiC grown in diluted N₂O,” *Journal of applied physics*, vol. 93, no. 9, pp. 5682–5686, 2003. [98](#)
- [218] Y.-H. Tseng, T.-H. Wu, B.-Y. Tsui, C.-T. Yen, C.-C. Hung, and C.-Y. Lee, “A comprehensive study on the oxidation of 4H-SiC in diluted N₂O ambient,” *Japanese Journal of Applied Physics*, vol. 56, no. 4S, p. 04CR02, 2017. [98](#)
- [219] W. Lu, L. Feldman, Y. Song, S. Dhar, W. Collins, W. Mitchel, and J. Williams, “Graphitic features on SiC surface following oxidation and etching using surface enhanced raman spectroscopy,” *Applied physics letters*, vol. 85, no. 16, pp. 3495–3497, 2004. [99](#)
- [220] P. Borowicz, T. Gutt, T. Małachowski, and M. Latek, “Carbonic inclusions on SiC/SiO₂ interface investigated with raman scattering,” *Diamond and Related Materials*, vol. 20, no. 5-6, pp. 665–674, 2011. [99](#)
- [221] U. Starke, J. Bernhardt, J. Schardt, and K. Heinz, “SiC surface reconstruction: Relevancy of atomic structure for growth technology,” *Surface Review and Letters*, vol. 6, no. 06, pp. 1129–1141, 1999. [99](#), [100](#)
- [222] T. Kimoto, A. Itoh, and H. Matsunami, “Step-controlled epitaxial growth of high-quality SiC layers,” *physica status solidi (b)*, vol. 202, no. 1, pp. 247–262, 1997. [99](#), [100](#)
- [223] J. Epler, T. Jung, and H. Schweizer, “Evolution of monolayer terrace topography on (100) GaAs annealed under an arsine/hydrogen ambient,” *Applied physics letters*, vol. 62, no. 2, pp. 143–145, 1993. [99](#), [100](#)
- [224] J. Bokor, “Ultrafast dynamics at semiconductor and metal surfaces,” *Science*, vol. 246, no. 4934, pp. 1130–1134, 1989. [99](#), [100](#)
-

-
- [225] D. Dutta, D. S. De, D. Fan, S. Roy, G. Alfieri, M. Camarda, M. Amsler, J. Lehmann, H. Bartolf, S. Goedecker, and T. A. Jung, “Evidence for carbon nucleates compromising the channel mobility of thermal gate oxides in SiC,” *submitted*, 2018. [100](#)
- [226] K. S. Novoselov, A. K. Geim, S. V. Morozov, D. Jiang, Y. Zhang, S. V. Dubonos, I. V. Grigorieva, and A. A. Firsov, “Electric field effect in atomically thin carbon films,” *science*, vol. 306, no. 5696, pp. 666–669, 2004. [101](#)
- [227] J. Zhao, H. Liu, Z. Yu, R. Quhe, S. Zhou, Y. Wang, C. C. Liu, H. Zhong, N. Han, J. Lu, *et al.*, “Rise of silicene: A competitive 2D material,” *Progress in Materials Science*, vol. 83, pp. 24–151, 2016. [101](#)
- [228] V. Tran, R. Soklaski, Y. Liang, and L. Yang, “Layer-controlled band gap and anisotropic excitons in few-layer black phosphorus,” *Physical Review B*, vol. 89, no. 23, p. 235319, 2014. [101](#)
- [229] H. Liu, A. T. Neal, Z. Zhu, Z. Luo, X. Xu, D. Tománek, and P. D. Ye, “Phosphorene: an unexplored 2D semiconductor with a high hole mobility,” *ACS nano*, vol. 8, no. 4, pp. 4033–4041, 2014. [101](#)
- [230] N. Mounet, M. Gibertini, P. Schwaller, D. Campi, A. Merkys, A. Marrazzo, T. Sohler, I. E. Castelli, A. Cepellotti, G. Pizzi, *et al.*, “Two-dimensional materials from high-throughput computational exfoliation of experimentally known compounds,” *Nature nanotechnology*, vol. 13, no. 3, p. 246, 2018. [101](#), [102](#)
- [231] S. Cahangirov, M. Topsakal, E. Aktürk, H. Şahin, and S. Ciraci, “Two-and one-dimensional honeycomb structures of silicon and germanium,” *Physical review letters*, vol. 102, no. 23, p. 236804, 2009. [101](#)
- [232] Y.-H. Lee, X.-Q. Zhang, W. Zhang, M.-T. Chang, C.-T. Lin, K.-D. Chang, Y.-C. Yu, J. T.-W. Wang, C.-S. Chang, L.-J. Li, *et al.*, “Synthesis of large-area MoS₂ atomic layers with chemical vapor deposition,” *Advanced materials*, vol. 24, no. 17, pp. 2320–2325, 2012. [101](#)
- [233] A. J. Mannix, B. Kiraly, M. C. Hersam, and N. P. Guisinger, “Synthesis and chemistry of elemental 2D materials,” *Nature Reviews Chemistry*, vol. 1, no. 2, p. 0014, 2017. [101](#)
- [234] M. Fujimori, T. Nakata, T. Nakayama, E. Nishibori, K. Kimura, M. Takata, and M. Sakata, “Peculiar covalent bonds in α -rhombohedral boron,” *Physical review letters*, vol. 82, no. 22, p. 4452, 1999. [101](#)
- [235] B. Albert and H. Hillebrecht, “Boron: elementary challenge for experimenters and theoreticians,” *Angewandte Chemie International Edition*, vol. 48, no. 46, pp. 8640–8668, 2009. [101](#)
- [236] A. R. Oganov, J. Chen, C. Gatti, Y. Ma, Y. Ma, C. W. Glass, Z. Liu, T. Yu, O. O. Kurakevych, and V. L. Solozhenko, “Ionic high-pressure form of elemental boron,” *Nature*, vol. 457, no. 7231, p. 863, 2009. [101](#)
-

-
- [237] A. J. Mannix, X.-F. Zhou, B. Kiraly, J. D. Wood, D. Alducin, B. D. Myers, X. Liu, B. L. Fisher, U. Santiago, J. R. Guest, *et al.*, “Synthesis of borophenes: Anisotropic, two-dimensional boron polymorphs,” *Science*, vol. 350, no. 6267, pp. 1513–1516, 2015. [101](#), [102](#)
- [238] B. Feng, J. Zhang, Q. Zhong, W. Li, S. Li, H. Li, P. Cheng, S. Meng, L. Chen, and K. Wu, “Experimental realization of two-dimensional boron sheets,” *Nature chemistry*, vol. 8, no. 6, p. 563, 2016. [101](#), [102](#)
- [239] G. Tai, T. Hu, Y. Zhou, X. Wang, J. Kong, T. Zeng, Y. You, and Q. Wang, “Synthesis of atomically thin boron films on copper foils,” *Angewandte Chemie*, vol. 127, no. 51, pp. 15693–15697, 2015. [101](#), [102](#)
- [240] X.-F. Zhou, A. R. Oganov, Z. Wang, I. A. Popov, A. I. Boldyrev, and H.-T. Wang, “Two-dimensional magnetic boron,” *Physical Review B*, vol. 93, no. 8, p. 085406, 2016. [101](#)
- [241] C. Kah, M. Yu, P. Tandy, C. Jayanthi, and S. Wu, “Low-dimensional boron structures based on icosahedron B₁₂,” *Nanotechnology*, vol. 26, no. 40, p. 405701, 2015. [101](#), [102](#)
- [242] N. Karmodak and E. D. Jemmis, “Metal templates and boron sources controlling borophene structures: An Ab Initio Study,” *The Journal of Physical Chemistry C*, vol. 122, no. 4, pp. 2268–2274, 2018. [101](#)
- [243] X.-B. Li, S.-Y. Xie, H. Zheng, W. Q. Tian, and H.-B. Sun, “Boron based two-dimensional crystals: theoretical design, realization proposal and applications,” *Nanoscale*, vol. 7, no. 45, pp. 18863–18871, 2015. [101](#)
- [244] H. Kroto, J. Heath, S. O’Brien, R. Curl, and R. Smalley, “This week’s citation classic®,” *Nature*, vol. 318, pp. 162–3, 1985. [101](#)
- [245] N. G. Szwacki, A. Sadrzadeh, and B. I. Yakobson, “B₈₀ fullerene: an ab initio prediction of geometry, stability, and electronic structure,” *Physical review letters*, vol. 98, no. 16, p. 166804, 2007. [101](#)
- [246] Z. A. Piazza, H.-S. Hu, W.-L. Li, Y.-F. Zhao, J. Li, and L.-S. Wang, “Planar hexagonal B₃₆ as a potential basis for extended single-atom layer boron sheets,” *Nature communications*, vol. 5, p. 3113, 2014. [101](#)
- [247] H. Tang and S. Ismail-Beigi, “Novel precursors for boron nanotubes: the competition of two-center and three-center bonding in boron sheets,” *Physical review letters*, vol. 99, no. 11, p. 115501, 2007. [101](#)
- [248] X. Wu, J. Dai, Y. Zhao, Z. Zhuo, J. Yang, and X. C. Zeng, “Two-dimensional boron monolayer sheets,” *ACS nano*, vol. 6, no. 8, pp. 7443–7453, 2012. [101](#)
- [249] X. Yu, L. Li, X.-W. Xu, and C.-C. Tang, “Prediction of two-dimensional boron sheets by particle swarm optimization algorithm,” *The Journal of Physical Chemistry C*, vol. 116, no. 37, pp. 20075–20079, 2012. [101](#)
-

-
- [250] Y. Liu, E. S. Penev, and B. I. Yakobson, "Probing the synthesis of two-dimensional boron by first-principles computations," *Angewandte Chemie International Edition*, vol. 52, no. 11, pp. 3156–3159, 2013. [102](#)
- [251] L. Zhang, Q. Yan, S. Du, G. Su, and H.-J. Gao, "Boron sheet adsorbed on metal surfaces: Structures and electronic properties," *The Journal of Physical Chemistry C*, vol. 116, no. 34, pp. 18202–18206, 2012. [102](#)
- [252] X.-L. He, X.-J. Weng, Y. Zhang, Z. Zhao, Z. Wang, B. Xu, A. R. Oganov, Y. Tian, X.-F. Zhou, and H.-T. Wang, "Two-dimensional boron on Pb (110) surface," *FlatChem*, vol. 7, pp. 34 – 41, 2018. [102](#)
- [253] K. C. Lau and R. Pandey, "Stability and electronic properties of atomistically-engineered 2D boron sheets," *The Journal of Physical Chemistry C*, vol. 111, no. 7, pp. 2906–2912, 2007. [102](#)
- [254] I. Higashi and T. Ishii, "Two-dimensional icosahedral B₁₂ networks in boron-rich crystals," *Forma*, vol. 16, no. 3, pp. 187–207, 2001. [102](#)
- [255] G. Glass, H. Kim, P. Desjardins, N. Taylor, T. Spila, Q. Lu, and J. Greene, "Ultrahigh B doping ($< \sim 10^{22} \text{ cm}^{-3}$) during Si (001) gas-source molecular-beam epitaxy: B incorporation, electrical activation, and hole transport," *Physical Review B*, vol. 61, no. 11, p. 7628, 2000. [102](#)
- [256] G. Glass, H. Kim, M. Sardela, Q. Lu, J. Carlsson, J. Abelson, and J. Greene, "Effects of high B-doping on Si(001) dangling bond densities, H desorption and film growth kinetics during gas-source molecular beam epitaxy," *Surface science*, vol. 392, no. 1-3, pp. L63–L68, 1997. [102](#), [105](#)
- [257] Z. Zhang, K. Sumitomo, and F. Lin, "Observation of B segregation on Si (113) by scanning tunneling microscopy," *Ultramicroscopy*, vol. 105, no. 1-4, pp. 16–21, 2005. [102](#), [112](#)
- [258] G.-H. Lu, M. Huang, M. Cuma, and F. Liu, "Relative stability of Si surfaces: A first-principles study," *Surface science*, vol. 588, no. 1-3, pp. 61–70, 2005. [103](#)
- [259] A. Ramstad, G. Brocks, and P. Kelly, "Theoretical study of the Si (100) surface reconstruction," *Physical Review B*, vol. 51, no. 20, p. 14504, 1995. [105](#)
- [260] M. Ramamoorthy, E. Briggs, and J. Bernholc, "Chemical and strain effects on boron-doped Si (100)," *Physical Review B*, vol. 59, no. 7, p. 4813, 1999. [105](#)
- [261] X. Luo, S. Zhang, and S.-H. Wei, "Understanding ultrahigh doping: The case of boron in silicon," *Physical review letters*, vol. 90, no. 2, p. 026103, 2003. [105](#)
- [262] D. Chadi, "Atomic and electronic structures of reconstructed Si (100) surfaces," *Physical Review Letters*, vol. 43, no. 1, p. 43, 1979. [105](#)
-

-
- [263] D. E. Eastman, "Geometrical and electronic structure of Si (001) and Si (111) surfaces: A status report," *Journal of Vacuum Science and Technology*, vol. 17, no. 1, pp. 492–500, 1980. [105](#), [107](#)
- [264] H. Raza, "Theoretical study of isolated dangling bonds, dangling bond wires, and dangling bond clusters on a H: Si (001)-(2× 1) surface," *Physical Review B*, vol. 76, no. 4, p. 045308, 2007. [105](#)
- [265] R. Headrick, I. Robinson, E. Vlieg, and L. Feldman, "Structure determination of the Si (111): B (3× 3) r30° surface: Subsurface substitutional doping," *Physical review letters*, vol. 63, no. 12, p. 1253, 1989. [107](#)
- [266] H. Shi, M. Radny, and P. Smith, "Electronic structure of the Si (111) 3× 3 R 30°- B surface," *Physical Review B*, vol. 66, no. 8, p. 085329, 2002. [108](#)
- [267] V. Brázdová and D. R. Bowler, "Si atom adsorption and diffusion on Si (110)-(1× 1) and (2× 1)," *Physical Review B*, vol. 81, no. 16, p. 165320, 2010. [109](#)
- [268] L. Long-Zhong, L. Zheng-Hui, and Z. Zhao-Hui, "Structural features of boron-doped Si (113) surfaces simulated by ab initio calculations," *Chinese Physics Letters*, vol. 25, no. 6, p. 2177, 2008. [112](#)
- [269] A. D. Becke and K. E. Edgecombe, "A simple measure of electron localization in atomic and molecular systems," *The Journal of chemical physics*, vol. 92, no. 9, pp. 5397–5403, 1990. [118](#)
- [270] A. Savin, O. Jepsen, J. Flad, O. K. Andersen, H. Preuss, and H. G. von Schnering, "Electron localization in solid-state structures of the elements: the diamond structure," *Angewandte Chemie International Edition in English*, vol. 31, no. 2, pp. 187–188, 1992. [119](#)
- [271] A. Sadeghi, S. A. Ghasemi, B. Schaefer, S. Mohr, M. A. Lill, and S. Goedecker, "Metrics for measuring distances in configuration spaces," *The Journal of Chemical Physics*, vol. 139, no. 18, p. 184118, 2013. [120](#)
-

Deb Sankar De

Curriculum Vitae

I consider myself as an enthusiastic person with problem solving ability within a group or independently.

Personal Information

Date of Birth 12th April, 1988
Nationality India
Cell Phone +41 78 920 63 20
Email debsankar.de@unibas.ch
Postal Address Oberwilerstrasse 124, CH-4054 Basel Switzerland

Education

Nov. 2014– Dec. 2018 **Ph.D in Physics**, *University of Basel*, Basel, Switzerland.
Thesis Title: Structure prediction for nano materials.
Supervisor: Prof. Stefan Goedecker
Aug. 2008 – May. 2010 **M.Sc. Physics**, *Jawaharlal Nehru University (J.N.U)*, New Delhi, India.
Thesis Title: Theoretical Study of Disordered Spin Dimers and G-L Theory of Superconductivity.
Supervisor: Dr. Brijesh Kumar
July, 2005 – July, 2008 **B.Sc.(Hons.) Physics**, *Krishnagar Government College, University of Kalyani*, Krishnagar, India.

Work experience

January 2019 – present **Post doc.**, *University of Basel*, Basel, Switzerland.
Project Title: Understanding Complex Molecular Crystals: Structures and Properties using machine learning.
July. 2012 – Nov. 2014 **Research Associate**, *Indian Institute of Technology, Kanpur*, Kanpur, India.
Project Title: Ab initio calculation for catalytic and photoelectrocatalytic systems.
Jan. 2011 – May. 2012 **Research Assistant**, *TSU, JNCASR, Bangalore*, Bangalore, India.
Project Title: Optimization of computer memory and execution time for ising model using multispin coding technique and graph cut technique. Simulation of charge transport in organic solar cell using Kinetic Monte Carlo.

Technical skills

Language:

Programming Fortran, C, Python
Scripting UNIX Shell Scripting
Markup \LaTeX , (X)HTML

Specialized Software MATLAB, Mathematica, Jupiter notebook, TensorFlow

Skills

All Electron Code FHIaims
PAW or Pseudopotential based DFT Codes BigDFT, Quantum Espresso, VASP, NWChem, gamess
Structure Prediction Methods Minima hopping method (MHM)
Other ASE, DFTB+, CHAMP, Lammmps

Publications

1. *Two scale simulation of surface stress in solids and its effects*
Ganesh Iyer, **Deb De**, Arun Kumar, Raj Pala, Anandh Subramaniam
Applied Surface Science 371, 343–348, (2016)
2. *Poisson effect driven anomalous lattice expansion in metal nanoshells*
Ganesh Iyer, Suboohi Shervani, Gargi Mishra, **Deb De**, Arun Kumar, Sri Sivakumar, Kantesh Balani, Raj Pala, and Anandh Subramaniam
Applied Physics Letter 110, 131603 (2017)
3. *Stable structures of exohedrally decorated C_{60} -fullerenes*
Deb Sankar De, José A. Flores-Livas, Santanu Saha, Luigi Genovese, Stefan Goedecker
Carbon, 2018, 129, pp 847-853
4. *Influence of an external electric field on the potential-energy surface of alkali-metal-decorated C_{60}*
Deb Sankar De, Santanu Saha, Luigi Genovese, Stefan Goedecker
Physical Review A 97, 063401 (2018)
5. *Evidence for carbon nucleates compromising the channel mobility of thermal gate oxides in SiC*
Dipanwita Dutta, **Deb Sankar De**, Dr. Daniel Fan, Dr. Shantanu Roy, Dr. Giovanni

Alfieri, Dr. Massimo Camarda, Dr. Maximilian Amsler, Dr. Jörg Lehmann, Dr. Holger Bartolf, Prof. Stefan Goedecker, Prof. Thomas Andreas Jung
Applied Physics Letters 115, 101601 (2019) (Editor's Pick)

6. *Finding optimal atomic index permutations for chemical reaction pathways*
Deb Sankar De, Marco Krummenacher, Bastian Schaefer, and Stefan Goedecker
Physical Review Letters 123, 206102 (2019)
7. *Comment on the stability of decorated $C_{48}B_{12}$ heterofullerene*
Deb Sankar De, Santanu Saha, Luigi Genovese, Stefan Goedecker
arXiv preprint arXiv:1802.03763 (2018)
8. *Stability of $[Si_{32}Cl_{45}]^-$ and $[Si_{32}Br_{45}]^-$ with Si_{20} dodecahedron core*
Deb Sankar De, Santanu Saha, Luigi Genovese, and Stefan Goedecker
Under Review in **Physical Chemistry Chemical Physics**
9. *The $Si_{20}H_{20}$ fullerene - where Levinthal's arguments do not lead to a paradox, but describe reality*
Deb Sankar De, Bastian Schaefer and Stefan Goedecker
submitted
10. *Growth of 2D-boron layer on Si substrate*
Deb Sankar De, José A. Flores-Livas, Stefan Goedecker, Maximilian Amsler
submitted
11. *$(Si(NH)_{0.5}O_{1.5})_n$ ($n=20,24$) cages: A polyatomic fullerene*
Santanu Saha, Bastian Schaefer, **Deb Sankar De**, Luigi Genovese and Stefan Goedecker
submitted

Poster Presentations

- International Workshop on Computational Design and Discovery of Novel Materials – Laussane, Switzerland September 2018
- MARVEL Site visit – Laussane, Switzerland April 10-11, 2018
- Marvel Junior Retreat – Pura, Lugano, Switzerland July 03-06 2017
- MARVEL 3rd Review – Laussane April. 2017
- SNI's Annual Meeting – Lenzerheide, Switzerland 15-16 September 2016
- Total Energy and Force Methods 2016, International Workshop on Computational Physics and Material Science – Luxembourg 11-13 Jan. 2016
- International conference on nano science and technology (ICONSAT) Chandigarh March 2014
- Winter school on Photoelectro chemistry IIT Madras December 2013

- DAE-BRNS 2nd National Workshop on Materials Chemistry NWMC-2013 (CAT-MAT) Bhabha Atomic Research Centre Mumbai November 22 - 23, 2013
- SERC School-cum-Symposium on Molecular Simulation – IIT Kanpur, India, November 27-30 2012.
- Modern Computational Science 2012 - Optimization – Germany August 20-31, 2012.

Oral Presentations

- “2D Boron Growth on Si Surfaces” Marvel Junior Retreat – Fieschertal, Switzerland July 17 - 20 2018 ([link](#))
- “Unbiased potential energy surface exploration for metal atom decorated C₆₀ with and without electric field” E-MRS 2018 – Warsaw, Poland September 17 - 20 2018 ([link](#)) (won Graduate student awards)
- “Utilizing finger prints to construct the disconnectivity graph” APS March meeting 2019 - Boston, Massachusetts, USA
- “Comparison of potential energy surface between carbon based and silicon based fullerene configurations” Atomistic Simulation of Carbon-Based Materials (ASCM) Workshop 2019 - Helsinki, Finland 10th-12th April 2019. [link](#)

Teaching Experience

- Computational Physics, University of Basel
 - Tutorial Assistant
 - Graded Assignments
- Electronic Structure, University of Basel
 - Tutorial Assistant
- Statistical Mechanics for Nanosciences, University of Basel
 - Tutorial Assistant
 - Graded Assignments and exam sheets